DEPARTAMENT OF CHEMISTRY

TRANSDERMAL DELIVERY SYSTEMS BASED ON NATURAL POLYMERIC BIOMATERIALS

DIANA FILIPA VIEIRA ARAÚJO

Master in Biotechnology

DOCTORATE IN CHEMICAL AND BIOLOGICAL ENGINEERING

NOVA University Lisbon

September, 2023

NOVA SCHOOL OF
SCIENCE & TECHNOLOGY

DEPARTAMENT OF CHEMISTRY

TRANSDERMAL DELIVERY SYSTEMS BASED ON NATURAL POLYMERIC BIOMATERIALS

DIANA FILIPA VIEIRA ARAÚJO

Master in Biotechnology

Adviser: Maria Filomena Andrade de Freitas
Assistant Professor, NOVA School of Science and Technology, NOVA University Lisbon

Co-advisers: Maria Alexandra Núncio de Carvalho Ramos Fernandes
Associate Professor with habilitation, *NOVA School of Science and Technology,* NOVA University Lisbon
Ana Carolina Cardoso Marques
Junior Researcher, *NOVA School of Science and Technology,* NOVA University Lisbon

Examination Committee:

Chair: José Paulo Barbosa Mota,
Full Professor, NOVA School of Science and Technology, NOVA University Lisbon

Rapporteurs: Carmen Sofia da Rocha Freire Barros,
Principal Researcher, University of Aveiro
Miguel Ângelo Parente Ribeiro Cerqueira,
Researcher, International Iberian Nanotechnology Laboratory

Adviser: Maria Filomena Andrade de Freitas,
Assistant Professor, NOVA School of Science and Technology, NOVA University Lisbon

Members: Ana Catarina Beco Pinto Reis,
Assistant Professor with habilitation, University of Lisbon
Pedro Miguel Ribeiro Viana Baptista,
Full Professor, NOVA School of Science and Technology, NOVA University Lisbon
José Paulo Barbosa Mota,
Full Professor, NOVA School of Science and Technology, NOVA University Lisbon

DOCTORATE IN CHEMICAL AND BIOLOGICAL ENGINEERING

NOVA University Lisbon
September 2023

Transdermal delivery systems based on natural polymeric biomaterials

Copyright © Diana Filipa Vieira Araújo, NOVA School of Science and Technology, NOVA University Lisbon.

The NOVA School of Science and Technology and the NOVA University Lisbon have the right, perpetual and without geographical boundaries, to file and publish this dissertation through printed copies reproduced on paper or on digital form, or by any other means known or that may be invented, and to disseminate through scientific repositories and admit its copying and distribution for non-commercial, educational or research purposes, as long as credit is given to the author and editor.

To my guardian angel,

ACKNOWLEDGMENTS

Um doutoramento é uma jornada longa, cheia de emoções, e marcada por desafios intelectuais e pessoais. Exige uma dedicação constante, perseverança e paixão inigualável. No entanto, ao longo desta jornada vão aparecendo pessoas sem as quais este caminho não seria possível, retratando de forma inalterável o provérbio "se quer ir depressa vá sozinho, mas se quiser chegar longe vá acompanhado".

Em primeiro lugar gostaria de deixar um agradecimento muito especial à minha orientadora, Prof. Dr. Filomena Freitas, por ter depositado em mim toda a confiança, e ter acreditado nas minhas capacidades para desenvolver este trabalho. Agradecer-lhe pela transmissão de conhecimento, exemplo de dedicação única, pensamento crítico, e por me trazer calma e serenidade nas alturas mais críticas. Obrigada Filomena, pela orientadora exemplar, e pela contribuição diária para a minha evolução como cientista e pessoa. Obrigada por tudo!

À Prof. Maria Ascensão Reis, gostaria de agradecer todas as oportunidades que me foi dando ao longo do meu percurso, pela disponibilização de todos os recursos e, por me deixar fazer parte da família BIOENG há 10 anos.

Quero estender os meus agradecimentos às minhas coorientadoras, por me darem a conhecer novas áreas e me desafiarem a integrar novos mundos. À Prof. Alexandra Fernandes, pela orientação na parte de ciências da vida, por me ajudar a desenhar e interpretar os resultados das experiências celulares, pela envolvência no trabalho, e por estar sempre disponível para dar sugestões. Foi muito gratificante trabalhar sob a sua orientação. À Prof. Elvira Fortunato, pela orientação na parte de ciência dos materiais, por me ter disponibilizado o acesso a todos os recursos integrantes dos laboratórios, e por sempre acreditar na excelência e ambição impostos neste trabalho. Quero agradecer à Dr. Carolina Marques por ter assumido a responsabilidade da coorientação após o desvinculo da Prof. Elvira, e por toda a ajuda dada ao longo deste meu percurso.

À Fundação para a Ciência e Tecnologia pelo suporte financeiro (SFRH/BD/140829/2018) que me permitiu desenvolver este trabalho de investigação científica.

Ao Prof. Vítor Alves por me receber sempre de braços abertos no Instituto Superior de Agronomia, por todos os ensinamentos e disponibilidade demonstrada ao longo do trabalho.

À Prof. Salete Reis e à Dr. Sofia Lima por me terem dado a conhecer a Faculdade de Farmácia da Universidade do Porto, e por possibilitarem a minha integração no seu grupo de

investigação. Foram meses de grande aprendizagem e de saída da minha zona de conforto que se proporcionaram crescimento não só profissional como também pessoal.

À Dr. Catarina Rodrigues, pela disponibilidade demonstrada e pela prontidão em ajudar a realizar todos os ensaios celulares realizados ao longo deste trabalho.

Ao Thomas Rodrigues e à Matilde Martins, que desempenharam um papel crucial como estudantes de mestrado, contribuindo significativamente para a realização das experiências deste projeto. Sem a dedicação deles, este trabalho não teria alcançado tantos progressos.

A todos os meus colegas do BIOENG, agradeço a boa disposição, entreajuda e companheirismo demonstrado ao longo dos anos. Ao João Pereira pela ajuda incansável em tudo e mais alguma coisa. À Patrícia Reis, por partilhar a sua inteligência e por nos mostrar que existem mesmo "Messis" desta vida. Ao grupo dos "miúdos" do 407, especialmente à Ana Teresa, Rita Bernardino e Cátia Gil, pelas gargalhadas e pelo ótimo ambiente que vivemos dentro e fora do laboratório.

À Eliana Guarda, por partilhar o momento de entrega da tese, e mesmo assim me ter dado um suporte gigante nesta última e tão difícil fase deste trabalho. Estamos juntas miúda!

Às minhas queridas irmãs, por serem suporte absoluto, pelo apoio inesgotável, e por estarem sempre disponíveis para me ajudar em todas as fases da minha vida.

Ao Fábio, expresso a minha profunda gratidão pelo amor, carinho e apoio inestimável. Agradeço por seres a minha âncora, meu parceiro de todos os momentos, meu melhor amigo e pela dedicação à nossa família. É um prazer partilhar a vida contigo.

À minha adorável filha Maria, por ter trazido luz e alegria à minha vida, por me ter ensinado o verdadeiro significado do amor incondicional, e por me demonstrar a importância dos pequenos gestos e detalhes.

Finalmente, quero fazer um agradecimento muito especial, à minha querida mãe. Apesar de não estar presente fisicamente, a sua presença continua a moldar a minha vida e a dar-me forças para continuar. Agradeço por todos os momentos, lições de vida, pelo amor incondicional, e pela dádiva de a ter tido como mãe. Obrigada mãe, continuarei a seguir o meu caminho com a certeza de que estarás sempre orgulhosa.

Um sincero agradecimento a todos.

"*If you can dream it, you can do it.*"

(Walt Disney)

ABSTRACT

The human skin provides a unique delivery pathway for therapeutic and other active agents. Although several approaches have been proposed and implemented, including the use of synthetic and natural polymers, there is a persistent pursuit of alternative biomaterials for enhancing the development of transdermal delivery systems. Therefore, in this study, natural polymers, namely the chitin-glucan complex (CGC), FucoPol, and polyhydroxyalkanoates (PHA), have been prospected for use as biomaterials for the fabrication of hydrogels and microneedles (MN) arrays, two innovative approaches for efficient and controlled drug delivery through the skin.

CGC was solubilized using NaOH/urea solvent systems through a freeze/thaw procedure, overcoming its previous insolubility challenge. This approach resulted in a significant solubilization rate of 63–68%, yielding a chitosan-glucan complex (ChGC). Based on this process, hydrogels were fabricated using different alkali solvent systems, NaOH and KOH solutions, via a freeze-thaw procedure. The hydrogels exhibited varying microstructures, viscoelastic properties, and textures depending on the type of solvent used and their ionic strength. Furthermore, the hydrogels were biocompatible. Subsequently, optimization of the process parameters allowed the reduction of the time needed to prepare the CGC hydrogels, and the optimized structures demonstrated a spontaneous swelling ratio and good water retention capacity. When loaded with caffeine, hydrogels' mechanical and rheological properties were significantly affected, and the caffeine release rate depended on the pH and ionic strength of the surrounding solution. Additionally, it was shown that increasing the CGC concentration led to the formation of hydrogels with a denser and tighter microstructure and increased their mechanical and rheological parameters. The hydrogels were loaded with different types of active pharmaceutical ingredients (APIs), exhibiting permeation fluxes through artificial membranes correlated to the APIs' physicochemical characteristics.

FucoPol was used as a structuring agent to fabricate hydrogel membranes (HMs) using Fe^{3+} as a crosslinker. It was demonstrated that, after a threshold of 1.5 g/L, Fe^{3+} concentration had a limited effect on HMs strength, while varying the concentration of FucoPol significantly influenced their properties. Three FucoPol concentrations (1.0, 1.75, and 2.5wt%) combined with Fe^{3+} (1.5 g/L) resulted in HMs with varying microstructures, swelling ratios, and hardness values. These HMs were non-cytotoxic and exhibited anti-inflammatory properties. Additionally, the

FucoPol HMs were loaded with caffeine or diclofenac sodium using different methods to assess drug loading capacity. The results showed that the loading method had an impact on the mechanical and rheological properties of the HMs and led to distinct drug release profiles.

PHAs with different compositions, including homopolymer poly(3-hydroxybutyrate) (PHB), copolymer poly(3-hydroxybutyrate-co-3-hydroxyvalerate) (PHBHV) with varying HV content (14, 43, and 87wt%), and terpolymer poly(3-hydroxybutyrate-co-3-hydroxyvalerate-co-3-hydroxyhexanoate) (PHBVHx), were used to fabricate MNs through a micromolding process. While these biopolymers were successfully utilized for MN fabrication, their distinct physicochemical properties led to MNs with differing characteristics. PHB, PHBV (43% HV), and PHBVHx produced sharp MNs with similar failure forces (~5.5 N), suggesting the ability to pierce the human skin. PHBVHx MNs displayed greater deformation resistance and insertion studies in Parafilm multilayer systems revealed their ability to penetrate up to 396 μm without breaking. Furthermore, diclofenac sodium was coated onto PHBVHx MNs and the resulting coated MNs exhibited comparable failure forces, decreased mechanical stiffness, and a rapid drug release profile.

Overall, this work demonstrated that the natural polymers CGC, FucoPol, and PHAs can be used as structuring agents for the development of novel biomaterials, namely, hydrogels and MNs, with very promising properties, thus contributing to the sustainable fabrication of improved transdermal delivery systems.

Keywords: Biopolymers, Hydrogels, Microneedles arrays, Drug delivery, Transdermal drug delivery systems.

RESUMO

A pele humana proporciona uma via de administração única para agentes terapêuticos e outros compostos ativos. Embora várias abordagens tenham sido propostas e implementadas, incluindo o uso de polímeros sintéticos e naturais, persiste a procura por biomateriais alternativos para melhorar o desenvolvimento de sistemas de administração transdérmica. Assim, nesta tese foram utilizados biomateriais naturais, nomeadamente o complexo quitina-glucano (CQG), FucoPol e polihidroxialcanoatos (PHAs), na fabricação de hidrogéis e matrizes de microagulhas (MN), duas abordagens inovadoras para entrega eficiente e controlada de fármacos através da pele.

CQG foi solubilizado utilizando sistemas de solventes NaOH/ureia através de um procedimento de congelamento/descongelamento, superando seu desafio de insolubilidade. Esta abordagem resultou em uma taxa de solubilização significativa de 63–68%, produzindo um complexo quitosano-glucano (ChGC). Com base nesse processo, foram fabricados hidrogéis utilizando diferentes sistemas de solventes alcalinos, nomeadamente soluções de NaOH e KOH, por meio de um procedimento de congelamento/descongelamento. Esses hidrogéis apresentaram microestruturas, propriedades viscoelásticas e texturas variáveis, dependendo do tipo de solvente utilizado e da sua força iónica. Além disso, os hidrogéis demonstraram ser biocompatíveis. Posteriormente, a otimização dos parâmetros do processo permitiu a redução do tempo necessário para preparar os hidrogéis, e as estruturas otimizadas demonstraram absorção de água espontânea, bem como uma boa capacidade de retenção de água. Quando carregados com cafeína, as propriedades mecânicas e reológicas dos hidrogéis foram significativamente afetadas, e a taxa de liberação de cafeína dependeu do pH e da força iónica da solução de libertação. Além disso, foi demonstrado que o aumento da concentração de CQG levou à formação de hidrogéis com uma microestrutura mais densa e compacta, e ao aumento dos parâmetros mecânicos e reológicos. Os hidrogéis de CQG foram capazes de ser carregados com diferentes tipos de ingredientes farmacêuticos ativos (APIs), exibindo fluxos de permeação através de membranas artificiais correlacionados com as características físico-químicas dos APIs.

FucoPol foi utilizado como agente estruturante no fabrico de membranas de hidrogel (HMs) usando Fe^{3+} como reticulante. Foi demonstrado que, acima de um valor de 1,5 g/L, a concentração de Fe^{3+} tem um efeito limitado na resistência das membranas, enquanto a variação da concentração de FucoPol influenciou significativamente suas propriedades. Três concentrações de FucoPol (1,0, 1,75 e 2,5%) combinadas com Fe^{3+} (1,5 g/L) resultaram em membranas com diferentes microestruturas, capacidade de absorção de água e propriedades mecânicas. As membranas demonstraram ser biocompatíveis, exibindo propriedades anti-inflamatórias. Além disso, as membranas de FucoPol foram carregadas com cafeína ou diclofenac de sódio através de diferentes métodos para avaliar a sua capacidade de incorporação de fármacos. Os resultados demostraram que o método de incorporação utilizado teve impacto nas propriedades mecânicas e reológicas das membranas, levando a perfis distintos de libertação.

PHAs com diferentes composições, incluindo PHB, PHBV com diferentes conteúdos em 3HV (14, 43 e 87%), e PHBVHx, foram usados para fabricar MNs através de um processo de micromoldagem por fusão. Embora estes biopolímeros tenham sido bem-sucedidos no fabrico das MNs, as suas distintas propriedades físico-químicas resultaram em MNs com características diferentes. PHB, PHBV contendo 43% em 3HV, e PHBVHx produziram MNs pontiagudas com forças de falha semelhantes (~5,5 N), sugerindo capacidade de perfurar a pele humana. As MNs de PHBVHx exibiram maior resistência à deformação e estudos de inserção em sistemas multicamadas de Parafilm revelaram a sua capacidade de penetrar até 396 μm sem quebrar. Além disso, diclofenac de sódio foi utilizado para revestir MNs de PHBVHx, sendo que as MNs revestidas apresentaram forças de falha comparáveis às MNs não revestidas, rigidez mecânica diminuída e um perfil de libertação rápida do fármaco.

No geral, esta tese demonstrou que os polímeros naturais CGC, FucoPol e PHAs podem ser usados como agentes de estruturação para o desenvolvimento de novos biomateriais, nomeadamente, hidrogéis e MNs, com propriedades muito promissoras, contribuindo, assim, para a fabricação sustentável de melhores sistemas de administração transdérmica.

Palavas chave: Biopolímeros, Hidrogéis, Matrizes de microagulhas, Libertação de fármacos, Sistemas de administração transdérmica.

CONTENTS

ACKNOWLEDGMENTS VI

ABSTRACT X

RESUMO XII

CONTENTS XIV

LIST OF FIGURES XXII

LIST OF TABLES XXX

ACRONYMS XXXII

SYMBOLS XXXVI

I. BACKGROUND AND MOTIVATION 1

- I.1. Background 1
  - 1.1. Introduction 1
  - 1.2. Human Skin 2
  - 1.3. Transdermal Drug Delivery Systems 4
- I.2. Motivation 6
- I.3. Thesis Outline 7

II. HYDROGELS 11

- 1. Polysaccharide Hydrogels 11
  - 1.4. Hydrogels 11
  - 1.5. Polysaccharides 14
  - 1.6. Hydrogels Based on Polysaccharides 16
  - 1.7. Conclusions and Perspective 21
- 2. Chitin-glucan complex Hydrogels 23
  - 2.1. Low Temperature dissolution of yeast chitin-glucan complex and characterization of the regenerated polymer 23

2.1.1. Introduction 24
2.1.2. Materials and Methods 25
2.1.2.1. Materials 25
2.1.2.2. CGC Dissolution in NaOH/Urea Solvent Systems 25
2.1.2.3. Polymer Regeneration 26
2.1.2.4. Rheological Properties of the Polymer Solutions 26
2.1.2.5. Characterization of the Regenerated Polymer 26
2.1.2.5.1. Elemental Analysis and Degree of Acetylation 26
2.1.2.5.2. Fourier Transform Infrared Spectroscopy 27
2.1.2.5.3. X-ray Diffraction Profiles 27
2.1.2.5.4. Thermal Properties 27
2.1.3. Results and Discussion 27
2.1.3.1. Preparation of CGC Solutions in NaOH/urea Solvent Systems 27
2.1.3.2. Rheological Behavior of the Solutions 29
2.1.3.3. Characterization of the Regenerated Polymer 32
2.1.3.3.1. Elemental Analysis and Degree of Acetylation 32
2.1.3.3.2. Fourier Transform Infrared Spectroscopy 33
2.1.3.3.3. XRD Analysis 34
2.1.3.3.4. Thermal Properties 36
2.1.4. Conclusions 37
2.2. Novel hydrogel based on yeast chitin-glucan complex: characterization and safety assessment 39
2.2.1. Introduction 40
2.2.2. Materials and Methods 41
2.2.2.1. Materials 41
2.2.2.2. Preparation of CGC hydrogels 41
2.2.2.3. Chemical characterization of CGC hydrogels 41
2.2.2.4. Rheological properties 42
2.2.2.5. Texture profile analysis 42
2.2.2.6. Cryo-Scanning Electron Microscopy 42
2.2.2.7. Cytotoxicity tests 42
2.2.3. Results and Discussion 43
2.2.3.1. Hydrogels formation 43
2.2.3.2. Morphological characterization 45

2.2.3.3. Rheological properties 47
2.2.3.4. Texture profile analysis 49
2.2.3.5. Cytotoxicity of the CGC hydrogels 50
2.2.4. Conclusions 51
2.3. Chitin-glucan complex hydrogels: optimization of gel formation and demonstration of drug loading and release ability 53
2.3.1. Introduction 54
2.3.2. Materials and Methods 55
2.3.2.1. Materials 55
2.3.2.2. Preparation of CGC hydrogels 55
2.3.2.3. CGC hydrogels characterization 55
2.3.2.3.1. Chemical characterization 55
2.3.2.3.2. Morphology, density and porosity 55
2.3.2.3.3. Compressive mechanical analysis 56
2.3.2.3.4. Rheological properties 56
2.3.2.3.5. Swelling and water retention behavior 56
2.3.2.4. Drug loading 57
2.3.2.5. Characterization of the loaded hydrogels 57
2.3.2.6. *In vitro* drug release studies 58
2.3.2.7. Statistical analysis 58
2.3.3. Results and Discussion 58
2.3.3.1. Hydrogel formation 58
2.3.3.2. Chemical Characterization of the Hydrogels 60
2.3.3.3. Morphological Characterization 60
2.3.3.4. Hydrogels' Porosity and Density 61
2.3.3.5. Mechanical Properties 62
2.3.3.6. Rheological Properties 64
2.3.3.7. Swelling Behavior and Water Retention Kinetics 65
2.3.3.8. Hydrogels Loading and Release Ability 66
2.3.3.8.1. Loading Na51* Hydrogels with Caffeine 66
2.3.3.8.2. Characterization of the Na5$_1$* Loaded Hydrogels 67
2.3.3.8.3. Release of Caffeine from the Na5$_1$* Hydrogels 70
2.3.4. Conclusions 72

2.4. Chitin-glucan complex hydrogels: physical-chemical characterization, stability *In vitro* drug permeation, and biological assessment in primary cells......73
2.4.1. Introduction......75
2.4.2. Materials and Methods......75
2.4.2.1. Materials......75
2.4.2.2. Preparation of the CGC hydrogels......75
2.4.2.3. CGC hydrogels characterization......76
2.4.2.3.1. Chemical characterization......76
2.4.2.3.2. Morphology, density and porosity......76
2.4.2.4. Compressive mechanical analysis......76
2.4.2.5. Rheological properties......77
2.4.2.6. Swelling and water retention behavior......77
2.4.2.7. Preparation of API-Loaded CGC Hydrogels......77
2.4.2.8. *In Vitro* Drug Release Studies......77
2.4.2.9. *In Vitro* Drug Permeation Studies......78
2.4.2.10. CGC Hydrogels Effect on Fibroblasts......78
2.4.2.11. Statistical Analysis......79
2.4.3. Results and Discussion......79
2.4.3.1. Hydrogels Fabrication......79
2.4.3.2. Morphological Characterization......81
2.4.3.3. Mechanical properties......82
2.4.3.4. Rheological properties......84
2.4.3.5. Swelling ratio and water retention behavior......85
2.4.3.6. Hydrogels loading and release ability......88
2.4.3.6.1. Loading of API......88
2.4.3.6.2. *In vitro* release studies......89
2.4.3.6.3. *In vitro* permeation studies......91
2.4.3.7. Effect of CGC hydrogels in fibroblasts......93
2.4.4. Conclusions......95
3. FucoPol Hydrogel Membranes......97
3.1. Novel hydrogel membranes based on the bacterial polysaccharide FucoPol: Design, characterization, and biological properties......97
3.1.1. Introduction......98

3.1.2. Materials and Methods 99
  3.1.2.1. Materials 99
  3.1.2.2. Preparation of FucoPol HMs........ 100
  3.1.2.3. Rheological Properties 100
  3.1.2.4. FucoPol HMs Characterization 100
  3.1.2.4.1. Chemical Characterization........ 101
  3.1.2.4.2. Morphology........ 101
  3.1.2.4.3. Porosity 101
  3.1.2.4.4. FT-IR Spectroscopy 101
  3.1.2.4.5. XRD Analysis 101
  3.1.2.4.6. TGA Analysis 102
  3.1.2.4.7. Compressive Mechanical Analysis........ 102
  3.1.2.4.8. Water Retention Capacity........ 102
  3.1.2.4.9. Swelling Behavior 102
  3.1.2.4.10. Gel Fraction 103
  3.1.2.5. Biological Assays........ 103
  3.1.2.5.1. Cell Culture and Culture Media 103
  3.1.2.5.2. Cytotoxicity Tests........ 103
  3.1.2.5.3. Anti-Inflammatory Activity........ 104
  3.1.2.6. Statistical Analysis 104
3.1.3. Results and Discussion........ 105
  3.1.3.1. Fabrication of FucoPol HMs........ 105
  3.1.3.1.1. Effect of Fe^{3+} Concentration 105
  3.1.3.1.2. Effect of FucoPol Concentration........ 106
  3.1.3.2. Morphological Characterization........ 107
  3.1.3.3. Chemical Characterization of FucoPol HMs 109
  3.1.3.3.1. Composition 109
  3.1.3.3.2. FT-IR Spectroscopy 110
  3.1.3.3.3. XRD Analysis........ 112
  3.1.3.3.4. Thermogravimetric Analysis 113
  3.1.3.3.5. Mechanical Properties 114
  3.1.3.3.6. Water Retention Capacity........ 116
  3.1.3.3.7. Swelling Behavior and Gel Fraction........ 118
  3.1.3.3.8. Cytotoxicity of FucoPol HMs 120

3.1.3.3.9. Anti-Inflammatory Activity 121

3.1.4. Conclusions 122

3.2. Exploring the drug loading and release ability of FucoPol hydrogel membranes 125

3.2.1. Introduction 126

3.2.2. Materials and Methods 127

3.2.2.1. Materials 127

3.2.2.2. Preparation of HM1 membranes 127

3.2.2.3. Loading of the HM1 membranes with APIs 128

3.2.2.4. Characterization of the loaded hydrogel membranes 129

3.2.2.4.1. FT-IR Spectroscopy 129

3.2.2.4.2. Mechanical properties 129

3.2.2.4.3. Rheological properties 129

3.2.2.4.4. *In vitro* release studies 129

3.2.3. Results and Discussion 129

3.2.3.1. Loading of APIs 129

3.2.3.2. Characterization of the loaded HM1 132

3.2.3.2.1. FT-IR Spectroscopy 132

3.2.3.2.2. Mechanical properties 133

3.2.3.2.3. Rheological properties 135

3.2.3.3. *In vitro* release studies 137

3.2.4. Conclusions 140

III. MICRONEEDLES ARRAYS 141

4. Microneedles Arrays based on natural polymers 141

4.1.1. MNs arrays: Fabrication methods, materials and design 142

4.1.2. Biodegradable MNs 146

4.1.3. Dissolving MNs 148

4.1.4. Hydrogel-forming MNs 150

5. Development of PHA-based Microneedles Arrays 153

5.1.1. Introduction 154

5.1.2. Materials and Methods 155

5.1.2.1. PHAs Production, Extraction and Purification 155

5.1.2.2. PHA Characterization 156

5.1.2.2.1. Monomer composition 156
5.1.2.2.2. Molecular mass distribution 157
5.1.2.2.3. Thermal Properties 157
5.1.2.3. Fabrication of MNs Arrays Molds 157
5.1.2.4. Preparation of PHA MNs Arrays 158
5.1.2.5. PHA MNs Arrays Characterization 159
5.1.2.5.1. Morphology 159
5.1.2.5.2. Compressive axial mechanical analysis 159
5.1.2.5.3. Insertion studies 159
5.1.2.6. Preparation of loaded MNs 159
5.1.2.6.1. Loading of the PHBVHx MNs 159
5.1.2.6.2. Characterization of the coated PHBVHx MNs 160
5.1.2.6.3. *In vitro* drug release studies 160
5.1.3. Results and Discussion 160
5.1.3.1. Biopolymers' Physical and Chemical Properties 160
5.1.3.2. Fabrication of the PHA MNs arrays 162
5.1.3.3. Morphological characterization 165
5.1.3.4. Mechanical Characteristics of the MNs 166
5.1.3.5. Insertion studies 168
5.1.3.6. Preparation of loaded PHBVHx MNs 171
5.1.3.7. Characterization of the DS-coated PHBVHx MNs 171
5.1.3.7.1. Morphology 171
5.1.3.7.2. Mechanical properties 172
5.1.3.7.3. *In vitro* drug release studies 173
5.1.4. Conclusions 174
IV. CONCLUSIONS AND FUTURE WORK 177
IV.1. Conclusions 177
IV.2. Future Work 178
REFERENCES 181
APPENDIX 215

LIST OF FIGURES

Figure I.1.1 - Schematic representation of the structure of human skin presenting the (A) three main layers and (B) sublayers of the epidermis (reproduced from [15]). 2

Figure I.1.2 - Schematic representation of different pathways through drug skin permeation (adapted from [20]) 3

Figure 1.1 - Schematic representation of classification of hydrogels. 12

Figure 1.2 - Schematic representation of the fabrication of chemical and physical crosslinked hydrogels (adapted from [55]). 13

Figure 1.3 - Illustration of the "egg-box" model between alginate G-blocks and Ca^{2+} ions (adapted from [86]) 18

Figure 2.1 — Macroscopic aspect of: (**A**) initial CGC suspensions in the three NaOH/urea solvent systems; (**B**) the CGC solutions obtained after removal of the insoluble fraction by centrifugation; (**C**) the corresponding CGC solutions after dialysis against deionized water. Solvent systems 1, 2 and 3 are represented by the numbers 1, 2 and 3, respectively 28

Figure 2.2 — Apparent viscosity of first soluble fractions of CGC1 (■), CGC2 (▲) and CGC3 (◆), and solvent systems 1 (□), 2 (△) and 3 (◇), measured at 20 °C. 30

Figure 2.3 — Viscoelastic properties of first soluble fractions of CGC1 (■), CGC2 (▲) and CGC3 (◆). Mechanical spectrum storage [G′ (full symbols)] and loss moduli [G″ (open symbols)]. 31

Figure 2.4 — FTIR spectra of CGC$_0$ and the polymer regenerated from the soluble fractions of CGC in: (**A**) solvent system 1 (CGC$_{1.1}$ and CGC$_{1.2}$), (**B**) solvent system 2 (CGC$_{2.1}$ and CGC$_{2.2}$) and (**C**) solvent system 3 (CGC$_{3.1}$ and CGC$_{3.2}$). 34

Figure 2.5 — X-ray diffraction profiles of CGC$_0$ and the polymer regenerated from the soluble fractions of CGC in: (**A**) solvent systems 1 (CGC$_{1.1}$ and CGC$_{1.2}$), (**B**) solvent systems 2 (CGC$_{2.1}$ and CGC$_{2.2}$) and (**C**) solvent systems 3 (CGC$_{3.1}$ and CGC$_{3.2}$). 35

Figure 2.6 —Thermogravimetric analysis (TGA) of the polymers: CGC1 (**A**), CGC2 (**B**) and CGC3 (**C**). Continuous line represents CGC$_0$; Dotted and dashed lines correspond to first and second soluble fractions, respectively. 36

Figure 2.7 —Schematic illustration of CGC hydrogels preparation, comprising polymer suspension in the alkali systems, application of freeze-thaw cycles for polymer dissolution and dialysis for polymer gelation. 44

Figure 2.8 — Photographs of: (A) the CGC solutions obtained by the freeze-thaw procedure in the alkali solvent systems: NaOH 1 mol/L (Na1 hydrogel) and 5 mol/L (Na5 hydrogel) and in KOH 1 mol/L (K1 hydrogel) and 5 mol/L (K5 hydrogel); (B) the corresponding CGC hydrogels obtained by dialysis of the alkali solutions against deionized water........44

Figure 2.9 — SEM images of the K1 hydrogel prepared with KOH 1 mol/L (a, b) and of the K5 hydrogel prepared with 5 mol/L (c, d). Hydrogels' regions observed under magnification 500× (b, d) were expanded from images presented under magnification 150× (a, c)........46

Figure 2.10 — SEM images of the Na1 hydrogels prepared with NaOH 1 mol/L (a, b), and of the Na5 hydrogels prepared 5 mol/L (c, d). Hydrogels' regions observed under magnification 500× (b, d) were expanded from images presented under magnification 150× (a, c)........47

Figure 2.11 — Rheological properties of CGC hydrogels using (a) NaOH (Na1 and Na5 hydrogels) and (b) KOH (K1 and K5 hydrogels). Mechanical spectrum storage (G′, solid symbols) and loss moduli (G′′, open symbols)........48

Figure 2.12 — Texture Profile Analysis parameters for hydrogels prepared with NaOH 1 mol/L (Na1) and 5 mol/L (Na5), and with KOH 1 mol/L (K1) and 5 mol/L (K5): (A) hardness, (B) springiness and (C) cohesiveness........49

Figure 2.13 — L929 fibroblasts and HaCaT keratinocytes viability when exposed to different concentrations of freeze dried CGC hydrogels dissolved in NaOH 1mol/L, for 24 h. The dotted line at 70% represents the viability limits for non-toxic condition (ISO 10993-5, 2009)........51

Figure 2.14 — Macroscopic aspect and SEM images of (A) $Na5_1$, (B) $Na5_2$, (C) $Na5_3$, and (D) $Na5_1$* hydrogels under magnification 500×; (E) chemical structure of CGC and schematic representation of the CGC hydrogel........59

Figure 2.15 — Porosity (▬) and density (○) of the CGC hydrogels........62

Figure 2.16 — Compressive mechanical properties of the CGC hydrogels compressive stress: (**A**) stress–strain curves, (**B**) hardness, (C) compressive modulus, and (**D**) toughness........63

Figure 2.17 — Rheological properties of the (**A**) $Na5_1$* hydrogel, (**B**) $Na5_1$* rehydrated hydrogel, and (**C**) $Na5_1$* loaded hydrogel, at 25 °C. Mechanical spectrum storage (G′, solid symbols) and loss moduli (G′′, open symbols)........64

Figure 2.18 — Swelling behavior of (**A**) $Na5_1$* hydrogels in PBS (■), NaCl 0.9% (▲) and deionized water (◆), water retention kinetics of (**B**) water-swollen hydrogels, at 37 °C, and (**C**) macroscopic aspect of hydrogels after the two processes........65

Figure 2.19 — Macroscopic aspect of $Na5_1$* hydrogels loaded with caffeine........67

Figure 2.20 — FTIR spectra of (**A**) caffeine, (**B**) $Na5_1^*$ hydrogels, and (**C**) $Na5_1^*$ loaded hydrogels. 68

Figure 2.21 — Caffeine release profile of $Na5_1^*$ hydrogel in PBS (■) and NaCl 0.9% (▲), at 37 °C. 70

Figure 2.22 — Plot of ln (Mt/M∞) vs. ln (t) for the caffeine release from $Na5_1^*$ loaded hydrogels in PBS (■) and NaCl 0.9% (▲) solutions, following the Korsmeyer–Peppas model. 72

Figure 2.23 — $Na5_1^{*4}$ and $Na5_1^{*6}$ hydrogels: (A) immediately after dialysis, (B) after being cut with cylindrical mold and (C, D) SEM images of the hydrogels. Hydrogel regions observed under magnification 1500× (D) were expanded from images presented under magnification 500× (C). 81

Figure 2.24 — Compression stress-strain curves of $Na5_1^*$ (blue line), $Na5_1^{*4}$ (orange line), and $Na5_1^{*6}$ (black line) hydrogels 82

Figure 2.25 — Loading-unloading curves of (A) $Na5_1^{*4}$ and (B) $Na5_1^{*6}$ hydrogels, under 50% strain. 84

Figure 2.26 — Rheological properties of the $Na5_1^{*4}$ (▲) and $Na5_1^{*6}$ (●) hydrogels at 25 ºC: (A) Mechanical spectrum storage (G′, solid symbols) and loss moduli (G″, open symbols), (B) Loss tangent (Tan δ) 84

Figure 2.27 — Macroscopic appearance of (A) freeze-dried and (B) swollen CGC hydrogel samples 86

Figure 2.28 — Swelling ratio (A) after 10 min and water retention capacity (B) after 30 min incubation of the $Na5_1^{*4}$ (dark grey) and the $Na5_1^{*6}$ (light grey) hydrogels, in deionized water, PBS, and NaCl 0.9%, at 37 ºC. 86

Figure 2.29 — Cumulative release profile of caffeine (▲, blue line), diclofenac sodium (◆, green line), salicylic acid (■, orange line), and ibuprofen sodium (●, yellow line) of $Na5_1^{*4}$ hydrogels in PBS, at 37 ºC. 90

Figure 2.30 — Cumulative amount profiles of (A) caffeine, (B) diclofenac sodium, (C) salicylic acid and (D) ibuprofen sodium from $Na5_1^{*4}$ hydrogels 92

Figure 2.31 —Representative images of the wound healing assay (A) at 0 h and 12 h after performing a scratch in a Fibroblasts monolayer in the presence of a CGC hydrogel (CGC hydrogel) or absence (control); Percentage of remission (B) after 12 h exposure to CGC hydrogel, or untreated (control). Bars represent the mean ± SEM of two independent experiments. Aspect of fibroblasts (C) in the absence (control) or presence (CGC hydrogel) of the CGC hydrogel. Cells were exposed for 12h to the freeze-dried CGC hydrogel sample, fixed with 4% (w/v) formaldehyde, and then actin filaments were stained with Phalloidin conjugated with AlexaFluor 488 (green fluorescence) and nuclei stained with Hoechst 33258 (blue fluorescence). The presented images are representative of 5 images acquired with a Confocal microscope Zeiss LSM710. 94

Figure 3.1 — Schematic illustration of Fucopol HMs preparation, comprising polymer dissolution in deionized water, immersion in $FeCl_3$ solution for polymer gelation and washing step. 100

Figure 3.2 — Effect of Fe^{3+} concentration ((A) 0.05 g/L, (B) 1.5 g/L, (C) 5 g/L, (D) 8.5 g/L and (E) 9.95 g/L) on the storage (G′, solid symbols) and loss (G″, open symbols) moduli of FucoPol HMs prepared using 1wt% of FucoPol. 106

Figure 3.3 — Effect of FucoPol concentration ((A) 0.5wt%, (B) 1.5wt%, (C) 1.75wt% and (D) 2.5wt%) on the storage (G′, solid symbols) and loss (G″, open symbols) moduli of FucoPol HMs prepared using 1.5 g/L of Fe^{3+}. 107

Figure 3.4 — FucoPol HMs: (**A**) macroscopic aspect and corresponding SEM images under (**B**) 500× and (**C**) 1000× magnifications. 108

Figure 3.5 —FTIR spectra of $FeCl_3.6H_2O$, FucoPol, HM1, HM2 and HM3. 111

Figure 3.6 — X-ray diffraction patterns of FucoPol and HM1, HM2 and HM3 HMs. 112

Figure 3.7 — Thermogravimetric curves of FucoPol and HM1, HM2 and HM3 HMs. 113

Figure 3.8 — Compression stress–strain curves of HM1 (dashed green line), HM2 (square dotted orange line) and HM3 (dash-dotted blue line) HMs. Insert graph highlights the initial linear deformation of the samples. 115

Figure 3.9 — Macroscopic appearance of HM1, HM2 and HM3 HMs samples after being subjected to all the conditions for the study of water retention ability. 116

Figure 3.10 — Water retention behavior of HM1 (▲), HM2 (■) and HM3 (●) HMs at (**A**) 20 °C and (**B**) 30 °C under 55% (dashed lines) and 99% (full lines) relative humidity. 117

Figure 3.11 — Macroscopic appearance of (**A**) freeze-dried, (**B**) water-swollen and (**C**) NaCl 0.9% swollen HM samples. 118

Figure 3.12 — Swelling behavior of HM1 (▲), HM2 (■), and HM3 (●) HMs in (**A**) deionized water and (**B**) NaCl 0.9%, at room temperature. 119

Figure 3.13 — Swelling ratio (columns) after 24 h and gel fraction (●) of HM1, HM2 and HM3 HMs in deionized water (light grey) and NaCl 0.9% (dark grey) determined at room temperature. 120

Figure 3.14 — Acute monocytic leukemia cell line, THP1 (light grey bars) and normal dermal fibroblasts (dark grey bars) cell viability (percentage) after 24 h of exposure to HM1, HM2 and

HM3 HMs and 500 µg/mL of FucoPol. Bars represent the average ± SD of three independent experiments. ns—non-statistically significant. 121

Figure 3.15 —Effect of HMs on *TNF-α* expression levels in THP1 cells. Inflammation in THP1 cells was stimulated for 2 h via the addition of 7 µg/mL lipopolysaccharides (LPS), and then the HMs or 500 µg/mL of FucoPol were added. In parallel, cells were submitted to the same treatment but without LPS. (**A**) *TNF-α* expression after 2 h, 2h30 and 5 h in LPS-treated samples calculated with $2^{-\Delta\Delta Ct}$ using the *RNA 18S* and corresponding LPS untreated samples as reference. (**B**) *TNF-α* expression after 2 h 30 and 5 h in LPS-treated samples that were exposed to the HMs and FucoPol for 30 min (2h30 samples) and 3 h (5 h samples), calculated with $2^{-\Delta\Delta Ct}$ using the *RNA 18S* and corresponding LPS control samples as reference. (**C**) Percentage of reduction in *TNF-α* expression in HM-treated samples relative to the respective control sample (treated with LPS and collected at the same time point). (**D**) *TNF-α* expression after 2h30 and 5 h in LPS untreated samples that were exposed to the HMs and FucoPol for 30 min (2h30 samples) and 3 h (5 h samples), calculated with $2^{-\Delta\Delta Ct}$ using the *RNA 18S* and corresponding control samples as reference. (**E**) *TNF-α* expression after 2 h in samples that were simultaneously submitted to LPS and to the HMs or FucoPol, calculated with $2^{-\Delta\Delta Ct}$ using the *RNA 18S* and corresponding LPS untreated samples as reference. Bars are the average ± SD of three independent experiments. **p*-value below 0.05 relative to control; ns—non-statistically significant. 122

Figure 3.16 - Macroscopic aspect of the freeze-dried FucoPol hydrogel membranes loaded with caffeine (A and B) prepared by diffusion ($\mathrm{HM1\_D_{CAF}}$) or mixing ($\mathrm{HM1\_M_{CAF}}$) methods, respectively, and loaded with diclofenac sodium (C and D) prepared by diffusion ($\mathrm{HM1\_D_{DS}}$) or mixing ($\mathrm{HM1\_M_{DS}}$) methods, respectively. 130

Figure 3.17 - FTIR spectra of HM1 loaded with (A) caffeine and (B) diclofenac sodium by diffusion (HM1_D) and mixing (HM1_M) methods. 133

Figure 3.18 - Compression stress-strain curves of the HM1 membranes (light grey dashed line) and the HM1 membranes loaded with (A) caffeine and (B) diclofenac sodium by diffusion (full line) and mixing (dotted line) methods. 134

Figure 3.19 - Rheological properties of the HM1 membranes (grey symbols) and the HM1 membranes loaded with caffeine using (A) diffusion and (C) mixing method, and with diclofenac sodium using (B) diffusion and (D) mixing method, at 25 ºC. Mechanical spectrum storage (G′, solid symbols) and loss moduli (G′′, open symbols). 136

Figure 3.20 - Cumulative release profile of membranes (A) $\mathrm{HM1\_D_{CAF}}$ (🟧) and $\mathrm{HM1\_D_{DS}}$ (🟦) and (B) $\mathrm{HM1\_M_{CAF}}$ (🔴) and $\mathrm{HM1\_M_{DS}}$ (🟢), in deionized water, at 37 ºC. 138

Figure 4.1 - A schematic representation of five different MN types used to facilitate transdermal drug delivery. (A) Solid MNs increase the permeability of a drug formulation by creating micro-holes across the skin. (B) Coated MNs for rapid dissolution of the coated drug into the skin. (C) Dissolvable MNs for rapid or controlled release of the drug incorporated within the microneedles. (D) Hollow MNs used to puncture the skin and enable the release of a liquid drug following active infusion or diffusion of the formulation through the needle bores. (E) Hydrogel-forming MNs take up interstitial fluids from the tissue, inducing diffusion of the drug located in a patch through the swollen microprojections (reproduced from [21]).......... 143

Figure 4.2 - Schematic illustration of polymeric MNs fabrication via PDMS micromolding (reproduced from [369]). 145

Figure 4.3 - Schematic illustration of polymeric MNs behavior in contact with the dermal interstitial fluid. 146

Figure 5.1 - Images of the (A) cultivation broth, before and after centrifuging, (B) the cell pellet, (C) the freeze-dried cell pellet, (D) the milled biomass, and (E) the dried biopolymer, following Soxhlet extraction with chloroform, precipitation in ice-cold ethanol and freeze-drying. 156

Figure 5.2 - Schematic illustration of the PDMS mold preparation (adapted from [412]). 158

Figure 5.3 - Schematic illustration of the fabrication process used for the preparation of PHA MNs arrays (adapted from [412]). 158

Figure 5.4 - Schematic illustration of the preparation of DS-coated PHA MNs. 160

Figure 5.5 - Thermogravimetric curves of PHB, copolymers $PHBV_{14}$, $PHBV_{43}$, and PHBV87, and terpolymer PHBVHx. 163

Figure 5.6 - Differential scanning calorimetry (DSC) thermogram of $PHBV_{43}$ comprising the first (blue line) and the second (red line) heating scan. 164

Figure 5.7 - Three-step process for the MNs array fabrication: (A) $PHBV_{43}$ sample over the PDMS mold, (B) filling the mold microcavities with molten polymer, and (C) demolding process and obtaining MNs array. 164

Figure 5.8 - Macroscopically appearance of MNs arrays fabricated using different types of PHAs. 165

Figure 5.9 - Optical images of MNs arrays fabricated using PHB, copolymers $PHBV_{14}$, $PHBV_{43}$, and $PHBV_{87}$, and terpolymer PHBVHx, in a side view. 166

Figure 5.10 - (A) Compression stress-strain curves of the MNs arrays fabricated from PHB (grey line), $PHBV_{43}$ (green line), and PHBVHx (orange line), and (B) optical images of MNs based on PHB (1), $PHBV_{43}$ (2) and PHBVHx (3) after the compression test. 167

Figure 5.11 - Parafilm insertion studies: (A) Optical image of the set-up (B) Percentage of holes created in each Parafilm layer using PHBVHx MNs, and (C) optical images of parafilm layers after insertion. 170

Figure 5.12 - SEM images of PHBVHx based MNs: (A) before and (B) after insertion in Parafilm. 171

Figure 5.13 - SEM image of DS-coated PHBVHx MNs. 172

Figure 5.14 - Compression stress-strain curves of the DS-coated PHBVHx MNs (blue line) and non-coated PHBVHx MNs (orange line). 173

Figure 5.15 - Cumulative release profile of DS from coated PHBVHx MNs. 174

Figure A1 - A1. L929 fibroblasts and HaCaT keratinocytes viability when exposed to different concentrations of NaOH, for 24 h. The dotted line at 70% represents the viability limits for non-toxic condition (ISO 10993-5, 2009). 215

Figure A2 - Differential scanning calorimetry (DSC) thermogram of polymers (A) $PHBV_{14}$, (B) $PHBV_{43}$ and (C) $PHBV_{87}$. 216

LIST OF TABLES

Table 1.1 - Examples of natural polysaccharides used to fabricate hydrogels. 17

Table 2.1 — Solubilized CGC mass, polymer concentration and overall solubilization of the soluble fractions in different NaOH/urea solvent systems. 28

Table 2.2 — Elemental characterization of the original CGC (CGC_0) and polymer samples regenerated from the NaOH/urea solvent systems (DA, degree of acetylation). 32

Table 2.3 — Degradation temperature (T_{deg}) and crystallinity index (CI) of the original. CGC (CGC_0) and polymer samples regenerated from the NaOH/urea solvent systems. 35

Table 2.4 — Chemical characterization of CGC hydrogels (n.d. – not detected). 45

Table 2.5 — Chemical characterization of CGC hydrogels obtained by different number of freeze–thaw cycles: 1 cycle ($Na5_1$ hydrogel), 2 cycles ($Na5_2$ hydrogel), 3 cycles ($Na5_3$ hydrogel) and 1 cycle with reduced freezing time ($Na5_1$* hydrogel); n.a., data not available. 60

Table 2.6 — Effect of caffeine on the mechanical and rheological properties of the $Na5_1$* hydrogel. 69

Table 2.7 —Chemical characterization, compressive mechanical properties (under 80% strain), and dissipation energies (cycles under 50% strain) of $Na5_1{*}^4$ and $Na5_1{*}^6$ hydrogels....80

Table 2.8 —Concentration of loading solutions, drug loading (DL, mg/cm^3), entrapment efficiency (EE, %) and Korsmeyer-Peppas model parameters obtained from the *in vitro* release kinetics of $Na5_1{*}^4$ hydrogels; R^2, regression coefficient; *n*, release exponent. 88

Table 3.1 — Physical and chemical characterization and mechanical properties (under 90% strain) of FucoPol HMs prepared from the gelation of FucoPol with Fe^{3+} (1.5 g/L) using polymer concentrations of 1.0wt% (HM1), 1.75wt% (HM2) and 2.5wt% (HM3). 109

Table 3.2 — Thermal degradation steps and degradation temperature (T_{deg}) of FucoPol and FucoPol HMs. 114

Table 3.3 - APIs concentrations in the loading solutions, drug loading (DL) capacity, entrapment efficiency (EE), and API content in the HM1 membranes. 131

Table 3.4 - Mechanical properties (under 90% strain) and storage (G′) and loss (G′′) moduli (measured at 1 Hz) of the HM1 membranes loaded with caffeine ($HM1\_D_{CAF}$ and $HM1\_M_{CAF}$) or diclofenac sodium ($HM1\_D_{DS}$ and $HM1\_M_{DS}$), compared to the non-loaded membranes (HM1). 135

Table 3.5 - Korsmeyer–Peppas model parameters obtained from the *in vitro* release kinetics of HM1 membranes; R^2, regression coefficient; *n*, release exponent. 139

Table 5.1 - Composition, molecular mass distribution, and thermal properties of different PHA used (3HB, 3-hydroxybutyrate; 3HV, 3-hydroxyvalerate; 3HHx, 3-hydroxyhexanoate; M_w, molecular weight; PDI, polydispersity index; T_g, glass transition temperature; Tm, melting temperature; $T_{5\%}$, the temperature at which 5% weight loss occurs; ΔHm, melting enthalpy, χc, degree of crystallinity; n.d., not detected). 162

ACRONYMS

AES	Atomic emission spectrometry
API	Active pharmaceutical ingredient
ATCC	American Type Culture Collection
ATR	Attenuated total reflectance
BC	Bacterial cellulose
CAF	Caffeine
CGC	Chitin-glucan complex
ChCsGC	Chitin/chitosan-glucan complex
ChGC	Chitosan-glucan complex
CI	Crystallinity index
CMC	Carboxymethylcellulose
CPS	Capsular polysaccharides
DA	Degree of acetylation
DAC	2,3-Dialdehyde cellulose
DES	Deep eutectic solvents
DL	Drug loading
DMEM	Dulbecco's Modified Eagle Medium
DS	Diclofenac sodium
DSC	Differential scanning calorimetry
EE	Entrapment efficiency
EPS	Exopolysaccharide
FT-IR	Fourier transform infrared spectroscopy
FBS	Fetal bovine serum

GC	Gas chromatography
HA	Hyaluronic acid
HB	3-Hydroxybutyrate
HHx	3-Hydroxyhexanoate
HM	Hydrogel membrane
HPLC	High-performance liquid chromatography
HV	3-Hydroxyvalerate
ILs	Ionic liquids
ICP	Inductively coupled plasma
IPN	Interpenetrating polymeric network
LPS	Lipopolysaccharide
LCST	Low critical solution temperature
mcl	Medium chain length
MeHA	Methacrylate hyaluronic acid
MMC	Mixed microbial culture
MN	Microneedle
Mn	Number molecular weight
Mw	Molecular weight
MWCO	Molecular weight cut-off
NSAID	Nonsteroidal anti-inflammatory drug
PBS	Phosphate buffered saline
PCL	Polycaprolactone
PCLA	Polycaprolactone-co-lactide
PDI	Polydispersity index
PDMS	Polydimethylsiloxane

PEEK	Polyether ether ketone
PEG	Poly(ethylene glycol)
PEGDA	Poly(ethylene glycol)-diacrylate
PEO	Polyethylene oxide
PHAs	Polyhydroxyalkanoates
PHB	Poly(3-hydroxybutyrate)
PHBV	Poly(3-hydroxybutyrate-co-3-hydroxyvalerate)
PHBVHx	Poly(3-hydroxybutyrate-co-3-hydroxyvalerate-co-3-hydroxyhexanoate
PLA	Poly(lactic acid)
PPDO	Poly(p-dioxanone)
PVA	Poly(vinyl alcohol)
RH	Relative humidity
RPMI	Roswell park memorial institute
scl	Short-chain length
SD	Standard deviation
SEM	Scanning electron microscopy
Tan δ	Loss tangent of delta
TDDS	Transdermal drug delivery systems
Tdeg	Degradation temperature
Tg	Glass transition temperature
TGA	Thermogravimetry analysis
Tm	Melting temperature
TNF-α	Tumor necrosis factor alpha
TPA	Texture profile analysis
Xc	Crystallinity

XRD	X-ray diffraction

SYMBOLS

ΔHm	Melting enthalpy (J/g)
G'	Storage modulus (Pa)
G''	Loss modulus (Pa)
Jss	Steady-state flux (µg/cm^2/h)
k	Kinetic constant
n	Release exponent
P	Partition coefficient
Q	Chitin content (%)
ρ	Density (g/cm^3)
R^2	Regression coefficient

I. BACKGROUND AND MOTIVATION

I.1. Background

1.1. Introduction

Drug delivery plays a crucial role in healthcare, and its extensive application in modern medicine has integrated it into our daily lives. It can be defined as the process of administering therapeutic substances such as drugs, to a specific site of the body for the purpose of achieving a therapeutic effect [1]. According to the delivery route, several modalities are available, including the enteral route (e.g., oral, sublingual, rectal), the parenteral route (e.g., intramuscular, subcutaneous, intravenous, intradermal injections), the topical route (e.g., epidermal, mucosal), and the inhalation route (e.g., vaporization, gas inhalation) [2]. For centuries, drug administration has been done conventionally through oral and intravenous routes [3,4]. Although the oral route remains the most convenient method since drugs can be self-administrated and portable, and doses are pre-determined, there is of low bioavailability due to their enzymatic degradation and poor absorption in the gastrointestinal tract [5,6]. On the other hand, the intravenous route allows the administration of macromolecules, such as proteins and peptides, but is limited by pain, risk of infection, and needle phobia [7,8]. Both these routes have additional limitations since drugs have to be administered multiple times per day and the introduction of the drug into the body occurs at once [9].

To mitigate these drawbacks and limitations, the search for alternative routes for drug delivery has been the subject of intensive research. Taking advantage of the unique delivery pathway for therapeutics provided by the human skin, transdermal drug delivery systems emerged as an attractive approach. These systems are pharmaceutical formulations and devices designed to administer drugs through the skin into the systemic circulation for systemic or localized therapeutic effects [7,10].

1.2. Human Skin

The human skin is the body's largest organ, representing around 15% of the body mass. It is a complex organ that acts as a protective barrier to the external environment, preventing the invasion of foreign pathogens, while also hosting beneficial commensal microbiota [11,12]. It also provides thermal regulation and sensory perception, is involved in the synthesis of vitamin D, and possesses immune-neuroendocrine functions that contribute to the body's homeostasis [13,14].

The human skin comprises three main layers: the epidermis, the dermis, and the subcutaneous tissue, also known as hypodermis, each with distinct functions and structures (Fig. I.1.1).

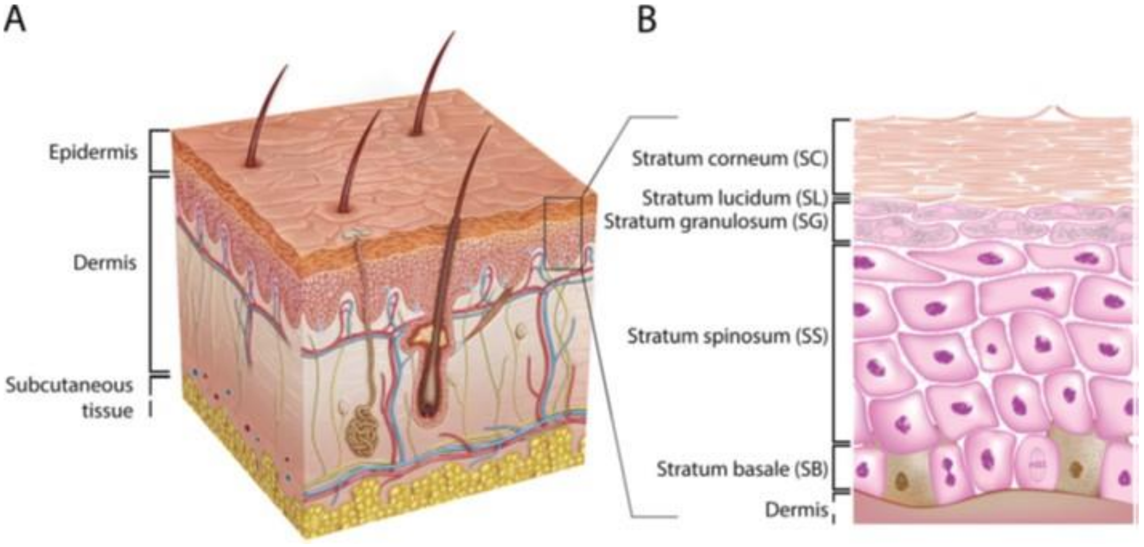

Figure I.1.1 - Schematic representation of the structure of human skin presenting the (A) three main layers and (B) sublayers of the epidermis (reproduced from [15]).

The epidermis, the outermost layer of the skin, is mainly composed of specialized epithelial cells, so-called keratinocytes, and secondarily it also has melanocytes, Langerhans cells, and Merkel cells [7,11]. It consists of several sublayers, with the outermost being the *stratum corneum*, composed of flattened dead cells (corneocytes) that form a protective barrier against environmental factors and moisture loss. Beneath it lies the *stratum granulosum*, where cells undergo keratinization, producing the protein keratin for strength and waterproofing. Then, the *stratum spinosum* contains living keratinocytes that provide structural support, while the *stratum basale* accommodates actively dividing cells that continually replenish the upper layers. Additionally, melanocytes in the basal layer produce melanin, responsible for skin pigmentation and UV protection. Langerhans cells, part of the immune system, are also scattered throughout the epidermis, contributing to the skin's defense mechanisms [16,17]. The dermis, the second layer of the skin, is mainly composed of fibroblasts that synthesize collagen and elastin fibers, crucial for skin firmness, elasticity, and structural support. It also contains macrophages and mast cells that contribute to immune responses and healing processes. This layer includes blood vessels, nerves, hair follicles, and glands, essential for functions such as hair growth, thermoregulation, and skin hydration [7,11]. The innermost skin layer is the hypodermis, it is mainly composed of adipose tissue, it serves mainly as a support structure and thermal insulator. The hypodermis also plays a role in energy storage, and it contains blood vessels that supply the skin and underlying tissues [11,17].

Skin penetration by micro and macromolecules involves either the transepidermal pathway, including intercellular and intracellular routes, or the transappendageal pathway, resulting in the topical delivery to the skin or the transdermal delivery into the systemic circulation (Fig. I.1.2) [7,18]. The transepidermal pathway implies the drug permeation across the epidermis, more specifically through the *stratum corneum*. It can be performed by the intercellular route where small hydrophobic drugs (usually with a molecular weight < 500 Da) diffuse within the lipid matrix between the corneocytes cells [19]. Drugs can also permeate directly through the keratinized corneocytes in a so-called intracellular route. This route allows the diffusion of small hydrophilic or moderately lipophilic molecules [7]. On the other hand, the transappendageal pathway involves drug permeation through structures associated with skin appendages such as sweat glands and hair follicles. This pathway is especially followed by large hydrophilic molecules [19].

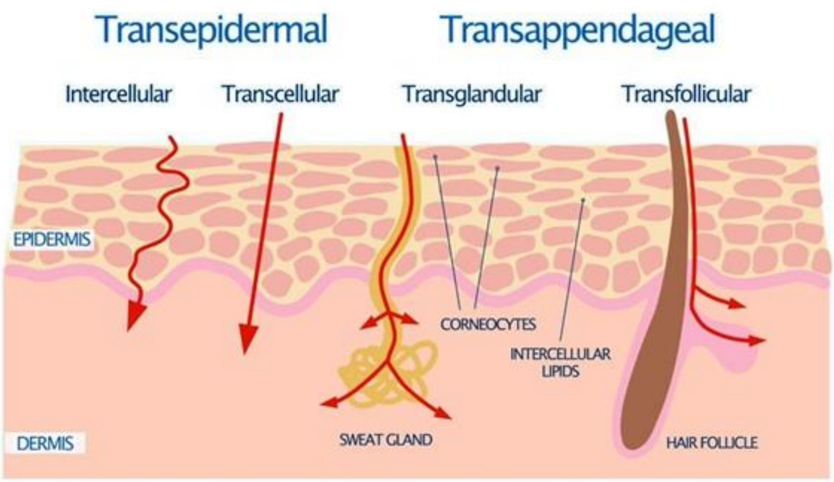

Figure I.1.2 - Schematic representation of different pathways through drug skin permeation (adapted from [20]).

1.3. Transdermal Drug Delivery Systems

Contrary to topical drug delivery that aims to treat dermatological conditions working primarily within the superficial skin layers, transdermal drug delivery allow the drug administration through the skin to achieve systemic circulation. Transdermal drug delivery represents an attractive alternative to oral and intravenous delivery, providing several advantages that include avoidance of the first pass hepatic metabolism, prevention of gastrointestinal degradation and food-related inconsistency in absorption, the possibility of enhanced bioavailability, elimination of pain and discomfort, and improved patient compliance [4,7,18]. However, only a limited number of drugs can penetrate the lipophilic *stratum corneum*, which is the most superficial layer of the skin and provides the main barrier to exogenous substances. Successful drugs should have optimal physicochemical properties, such as low molecular weight, reasonable lipophilicity, and low melting point, correlating with good solubility [18,21,22]. In the last decades, several strategies for transdermal delivery have been developed to improve the delivery of hydrophilic drugs, peptides, and macromolecules [4,7].

Nowadays, transdermal drug delivery systems (TDDS) can act through two different methodologies: passive/chemical and active/physical delivery technologies. Passive delivery is characterized by modification of the *stratum corneum* without its disruption, influenced by drug-vehicle interactions and optimization of formulation. These delivery systems are based on particulate systems (e.g., liposomes, transferosomes, emulsions, nanoparticles) and chemical enhancers (e.g., glycols, fatty acids) [23]. However, passive approaches have disadvantages as the small size of the molecules that can be delivered and the extensive time in drug release [7,24]. To overcome the poor drug transport via the skin and the drawbacks of passive delivery, active delivery systems have been developed. Active delivery is characterized by the physical disruption of the *stratum corneum* or the use of external energy to act as a drug transport across the skin. These methods are more effective in transdermal delivery, allowing a wide class of drugs to be delivered into the skin and overcoming lag times in drug release when compared with passive methods [7]. In this way, electrically based techniques, such as sonophoresis (ultrasound) and electroporation, allow the formation of aqueous pores in the lipid bilayers of the *stratum corneum*, while iontophoresis has been used to drive drugs through the transappendageal route. Mechanical methodologies, including tape stripping and MNs, are also used and involve either removing or piercing the *stratum corneum*, respectively [23].

Hydrogels have emerged as versatile and promising materials as TDDS. These three-dimensional, water-rich networks of polymers possess unique properties that make them ideal candidates for delivering a wide range of therapeutic agents through the skin [25,26]. Hydrogels can be tailored to control the release of drugs in a sustained and controlled way, ensuring therapeutic efficacy while minimizing side effects. Their biocompatibility, ease of application, and ability to maintain skin hydration contribute to patient comfort and adherence [27]. Additionally, the customizable nature of hydrogels allows for fine-tuning their mechanical and chemical properties, making them suitable for various drug formulations and applications. One notable example is the use of hydrogel patches for the delivery of pain relief medications such as lidocaine [28] and diclofenac [29]. These patches adhere comfortably to the skin and slowly release the drug over time, providing localized pain relief without the need for frequent reapplication. Another example is the use of hydrogel-based dressings for wound care. As dressings, hydrogels offer distinct advantages essentially due to their adaptability to match wound type and stage, while meeting crucial criteria including exudate absorption, maintenance of moist wound environment, thermal insulation, preservation of gas exchanges, painless removal, and ease of handling [30]. Moreover, hydrogel dressings can present antimicrobial activity or be loaded with antimicrobial agents preventing infection [31]. Overall, the use of hydrogels as TDDS represents a promising avenue for improving drug delivery, enhancing patient outcomes, and advancing the field of transdermal therapeutics. In this thesis, the fundamental principles of hydrogel design and their specific advantages in drug delivery through the skin will be explored and detailed in Section II, where the polysaccharides chitin-glucan complex (CGC) and FucoPol, will be used as innovative biomaterials for the development of these structures.

A cutting-edge innovation in the field of TDDS are the MN arrays. These microscopic needles, barely visible to the naked eye, have opened up new horizons in drug delivery by providing a minimally invasive means to transport therapeutic agents through the skin [32,33]. MNs puncture the *stratum corneum* creating microchannels that enable precise and controlled drug administration. Their potential for painless and efficient drug delivery makes them a topic of increasing interest and exploration across the fields of pharmaceuticals, cosmetics, and beyond. Generally, these promising technologies are under development for the delivery of biomacromolecules including proteins, peptides, hormones, vaccines, and genes [34,35]. In the field of vaccination, MNs arrays have undergone extensive research and were found to be on par with traditional methods of administration, overcoming some drawbacks associated with pain, needle phobia, self-administration, and safety [36,37]. Initially employed for the delivery of vaccines against influenza, the use of MNs to deliver vaccines to a diverse range of viral and bacterial infections, as well as immunotherapy for cancer treatment has been reported in several studies [38,39]. In the cosmetic industry, MN arrays have also gained significant relevance in recent times, particularly for applications related to skin moisturization and anti-aging treatments. For this application, most of the MNs are composed of hyaluronic acid which dissolves into the skin upon application. These MNs provide skin hydration and facilitate the delivery of active ingredients for enhancing skin health through their gradual dissolution [33,40]. In this thesis, the fascinating world of MN arrays will be explored in Section III where design principles, properties, and promising use of the biopolymers polyhydroxyalkanoates will be investigated.

I.2. Motivation

Considering that the biomedical and pharmaceutical fields are continuously evolving, several challenges in these TDDS have been taken into consideration. Although significant progress has been made in enhancing biocompatibility, drug loading, drug release mechanisms, and treatment duration in hydrogel-based drug delivery systems, challenges related to their practical clinical application persist. Issues such as shelf life, sterilization methods, user compliance, and scalability must be effectively addressed prior to the deployment of these systems for therapeutic agent delivery to patients [41]. Regarding MN arrays, the translation from academic research to viable products in the market requires the consideration of some challenges in crucial fields including safety (e.g., skin irritation, patient compliance), regulation (e.g., clinical adaptation, regulatory approval), compatibility (e.g., biocompatibility, stability), manufacture (e.g., reproducibility, packaging, cost) and loading (e.g., dose accuracy, stability) [33].

The use of biopolymers for the fabrication of TDDS is mainly driven by their biocompatibility, biodegradability, and safety properties. Different from synthetic materials, biopolymers are derived from natural sources, making them more biocompatible and reducing the risk of adverse reactions or toxicity. These macromolecules can often be metabolized over time, minimizing the accumulation of foreign substances within the body. Additionally, biopolymers are environmentally friendly and sustainable, aligning with the growing focus on green and sustainable technologies in various industries, including healthcare. They offer a promising alternative to traditional materials that may have environmental concerns.

The motivation behind this thesis is rooted in the pursuit of innovative solutions to advance TDDS. Therefore, the potential of different microbial polymers to revolutionize transdermal drug delivery was studied by leveraging the unique properties of those natural polymers, specifically FucoPol, a fucose-rich bioactive bacterial polysaccharide, CGC, a yeast copolymer of chitin and glucan, and PHAs, natural biocompatible polyesters. These natural polymers possess unique and distinct functional properties that make them ideal candidates for the development of innovative TDDS that include two distinct delivery approaches: hydrogels and MN arrays. The investigation of both types of structures provides a comprehensive understanding of how these natural polymeric biomaterials can be tailored to suit various drug delivery needs.

Overall, the main goal was to contribute to the development of TDDS that are both effective and versatile, offering new possibilities for enhancing patient care, treatment outcomes, and safety while reducing environmental impact.

I.3. Thesis Outline

This PhD thesis is structured into four sections, encompassing nine chapters, designed as research papers or book chapters, which were either published or submitted for publication. Each chapter provides an introductory context, detailing the materials and methods utilized, and discussing the obtained results and key conclusions. The specific methodology applied in each chapter is comprehensively described within the context of the subject and, where applicable, linked to methodologies employed in previous chapters. In this thesis, sections II and III focus on the investigation of hydrogels and microneedles arrays, respectively, based on natural polymeric biomaterials, as potential TDDS. Hence, the structure of this thesis has the following outline:

Section I presents the background, motivation, and main objectives of this thesis.

Section II describes the fabrication of hydrogels based on two polysaccharides, chitin-glucan complex (CGC) and FucoPol. This section is divided into three main chapters:

Chapter 1 provides a fundamental overview of the state of the art on polysaccharide hydrogels.

Chapter 2 focuses on the dissolution of the polysaccharide CGC and its ability for hydrogels' fabrication. This chapter is divided into four sub-chapters:

2.1 - Low temperature dissolution of yeast chitin-glucan complex and characterization of the regenerated polymer describes the use of non-toxic solvents to dissolve CGC and provides a detailed characterization of the regenerated biopolymer.

2.2 - Novel hydrogels based on yeast chitin glucan complex: characterization and safety assessment focus on the development of hydrogels using different solvent systems and polymer concentration.

2.3 - Chitin-glucan complex hydrogels: Optimization of gel formation and demonstration of drug loading and release ability describes the optimization of the hydrogel fabrication process regarding the number of freeze-thaw cycles and freezing time. Additionally, the hydrogel prepared under the optimized conditions was used to study their ability to load and release drugs.

2.4 - Chitin-glucan complex hydrogels: Physical-chemical characterization, stability, in vitro drug permeation, and biological assessment in primary cells reports the effect of polymer concentration on hydrogel preparation. The obtained hydrogels were characterized and their ability to load and release different types of drugs was assessed by *in vitro* release and permeation studies.

Chapter 3 demonstrates the use of the polysaccharide FucoPol to produce hydrogel membranes. This chapter is divided into two sub-chapters:

3.1 - Novel hydrogel membranes based on the bacterial polysaccharide FucoPol: Design, characterization, and biological properties demonstrated the preparation of hydrogel membranes using Fe^{3+} cations as crosslinking agent. The effect of polymer and Fe^{3+} concentration was evaluated, and the optimized conditions were used to prepare membranes that were further characterized. Additionally, the obtained membranes were evaluated regarding their cytotoxicity and anti-inflammatory activity.

3.2 - Exploring the drug loading and release ability of FucoPol hydrogel membranes focuses on the capacity of the prepared hydrogel membranes to be loaded with different drugs following two distinct loading methods. The loaded membranes were characterized, and the influence of the loading method was evaluated. Moreover, their ability to release the loaded drugs was assessed by *in vitro* release studies.

Section III focuses on the fabrication of MNs from polyhydroxyalkanoates. This section is divided into two chapters:

Chapter 4 provides a fundamental overview of the state of the art on MNs arrays fabrication.

Chapter 5 describes the preparation of microneedles arrays from different types of polyhydroxyalkanoates. The fabricated microneedles arrays were characterized and their ability to be coated was evaluated.

Section IV reports the main conclusions of this dissertation and provides suggestions for future work.

The work developed during this PhD resulted in several significant scientific outputs including two book chapters and six scientific papers. Additionally, there is an ongoing manuscript in preparation. The information regarding the publications is presented at the beginning of each respective chapter.

.

II. HYDROGELS

1. Polysaccharide Hydrogels

This chapter was adapted from the following published book chapter:

- Freitas, F., Torres, C.A.V., **Araújo, D.**, Farinha, I., Pereira, J. R., Concórdio-Reis, P., Reis, M.A.M. (2021) "Advanced Microbial Polysaccharides." In B. Rehm & M. F. Moradali (Eds.), Biopolymers for Biomedical and Biotechnological Applications (1st ed., pp. 19–62). Wiley. DOI: 10.1002/9783527818310.ch2

1.4. Hydrogels

Hydrogels represent a class of materials composed of a three-dimensional, hydrophilic polymeric network able to absorb large amounts of water or biological fluids [42,43]. Their tunable properties, functionalities, and versatile fabrication methods allow their application in a wide range of applications in several fields such as food and agriculture [44], cosmetics [45], biomedicine [46], soft robotics [47], and wastewater treatment [48]. Hydrogels' unique properties, characterized by high water content and extracellular matrix-mimicking structure, render them potential to act as soft tissue biomaterials with application in various areas of biomedicine from tissue engineering scaffolds [49] and drug delivery systems [41] to soft contact lenses [50] and biosensors [51], among others. Hydrogels can be classified based on various parameters, including material source, crosslinking type, charge, composition, response characteristics, and structure/configuration (Fig. 1.1).

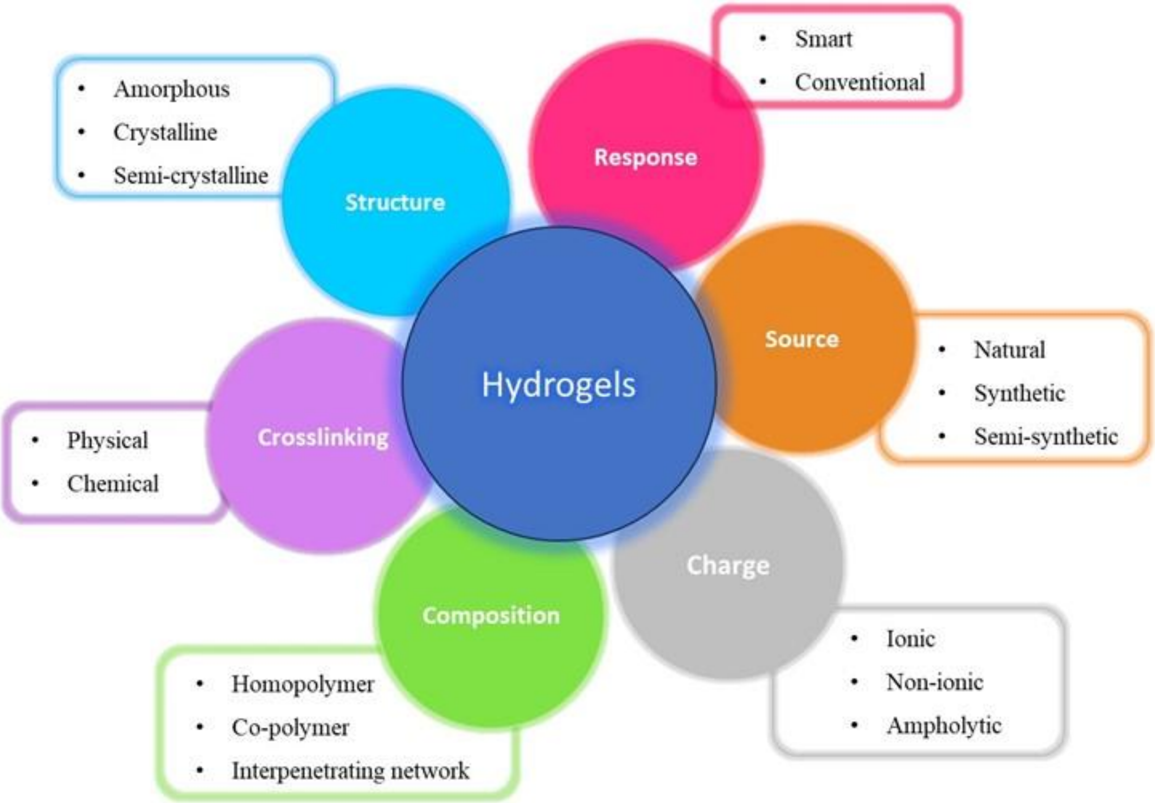
Smart
Conventional
Response
Amorphous
Crystalline
Semi-crystalline
Structure
Hydrogels
Source
Natural
Synthetic
Semi-synthetic
Physical
Chemical
Crosslinking
Charge
Ionic
Non-ionic
Ampholytic
Composition
Homopolymer
Co-polymer
Interpenetrating network

Figure 1.1 - Schematic representation of classification of hydrogels.

According to their preparation method and physical structure, hydrogels can be produced by physical or chemical crosslinking (Fig. 1.2) [52,53]. Physically crosslinked hydrogels are reversible under specific conditions, and polymer chains are weakly stabilized by secondary forces such as ionic interactions, hydrogen bonding, or hydrophobic interactions. On the other hand, chemically crosslinked hydrogels are irreversible and stable, with strong covalent bonds involving reactions of polymeric backbone with a crosslinking agent. Chemical hydrogels can be produced by different techniques, including radiation, graft copolymerization, or in the presence of a crosslinking agent [54].

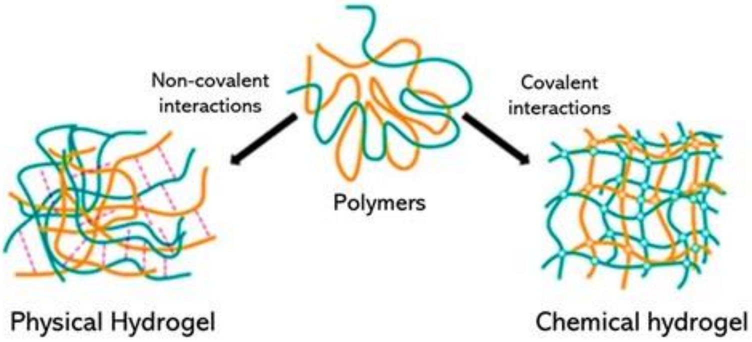

Figure 1.2 - Schematic representation of chemical and physical crosslinked hydrogels (adapted from [55]).

Depending on the polymers involved, hydrogels can be classified as homopolymer hydrogels, if composed of a single type of repeating unit (e.g., poly(ethylene glycol) (PEG)), copolymer hydrogels, if constituted by two or more different repeating units (e.g., poly(ethylene glycol)-diacrylate (PEGDA)), and interpenetrating polymeric network (IPN) hydrogels when two independent crosslinked networks intermesh each other in the presence of crosslinker. Therefore, hydrogels can be semi-IPN if one of the components is a non-crosslinked polymer [56,57].

Additionally, hydrogels can also be categorized based on their ionic charge as non-ionic (neutral), ionic (cationic or anionic), and ampholytic hydrogels. Such classification refers to the overall charge, namely no charge groups are present in neutral hydrogels, and cationic and anionic hydrogels are characterized by the presence of either positively or negatively charged groups, respectively. In the presence of both, negatively and positively charged groups, ampholytic hydrogels are produced [54,58]. Ionic and ampholytic hydrogels are also known as polyelectrolytes.

Considering their final application, hydrogels can be designed to be stimulus sensitive, responding distinctively towards external conditions such as temperature, pH, ionic strength, and magnetic or electric field [59,60]. In fact, the ability to respond to external stimuli makes them usually called “smart” or "stimuli-sensitive” hydrogels. Moreover, exhibiting “smart” characteristics is an advantage for biomedical applications such as controlled drug delivery [61,62] or agriculture [63].

Based on the source of the polymers used to fabricate the structures, hydrogels can be classified as natural, synthetic, or semi-synthetic hydrogels [56,64]. Natural hydrogels are fabricated from natural sources such as polysaccharides (e.g., alginate, chitosan, cellulose, hyaluronic acid) or proteins (e.g., collagen, gelatin). Natural polymers are generally biocompatible and biodegradable and often exhibit inherent bioactivity, a feature that renders them suitable for several biomedical applications [41,65]. Natural hydrogels demonstrate a remarkable resemblance to the natural extracellular matrix, providing an ideal environment for cell growth and tissue regeneration. However, poor mechanical properties and weak stabilization are identified as the main disadvantages of these structures [65]. Synthetic hydrogels are created from synthetic polymers such as poly(vinyl alcohol) (PVA), PEG, and polyacrylamide. These hydrogels are synthesized through chemical reactions allowing for precise tuning of their properties, namely improved mechanical properties and high stability [66]. Nonetheless, synthetic polymers are considered environmentally unfriendly due to their recalcitrancy to biological degradation, resulting in the accumulation of non-biodegradable solid waste materials [43]. Semi-synthetic hydrogels, also known as hybrid hydrogels, are hydrogel materials that are created by combining both natural and synthetic components. These hydrogels leverage the advantages of both natural and synthetic materials to achieve a balance of desirable properties for specific applications.

This chapter focuses on the use of natural polysaccharides to fabricate hydrogels. It starts with a brief overview of polysaccharides, followed by the role of these macromolecules in the hydrogel formation, detailing the currently more relevant polysaccharides for this purpose and describing their advantages and challenges.

1.5. Polysaccharides

Polysaccharides are high molecular weight molecules composed of repeated units of saccharide monomers linked together by glycosidic bonds [67]. The specific arrangement and the type of monosaccharides present in the macromolecule chain determine the type and properties of the polysaccharide. According to their chemical composition, polysaccharides can be classified as homopolysaccharides when composed of only one type of monosaccharide monomer (e.g., cellulose, starch) or heteropolysaccharides when composed of two or more different types of monosaccharides (e.g., hyaluronic acid, xanthan) [67,68]. Besides the presence of the most common monomers glucose, galactose, and mannose, other neutral sugars such as rhamnose, arabinose, and fucose, as well as uronic acids and aminosugars are also frequently found. Additionally, several other substituents including organic acyl groups (e.g., ester-linked groups, pyruvate ketals) and inorganic groups (e.g., sulfate, phosphate) are also common in their composition [68]. Most of these substituents are ionizable groups that confer the polysaccharides a polyelectrolyte character, greatly affecting their properties, as well as the nature and number of intra/intermolecular interactions. In fact, the possible multiple combinations of monomeric units in these macromolecules, along with the stereospecificity of glycosidic linkages (α or β anomers), leads to structural variations ranging from linear to highly branched structures. The most common glycosidic bonds between saccharide monomers are α-1,4 and β-1,4 characteristics of the linear backbone, and α-1,6 and β-1,6, responsible for branching the structure [69].

Polysaccharides are the most abundant naturally occurring macromolecules and are found in a variety of natural sources that include plants (e.g., starch, cellulose, pectin), animals (e.g., glycogen, chitin), seaweeds (e.g., alginate) and microorganisms (e.g., xanthan, glucans). Several key features of polysaccharides over synthetic materials include their biocompatibility, biodegradability, renewability, and abundance, making them valuable materials for a wide range of applications in various industries such as pharmaceuticals, food, and cosmetics [70–72]. Compared to other natural polysaccharides, those of microbial origin have been extensively studied due to their improved properties and easy production when compared to other natural polysaccharides [73]. For example, microorganisms usually have much higher growth rates than algae or plants, and their production processes can easily be manipulated to improve yields and productivity. Moreover, the production process is not climate- or seasonal-dependent and can rely on the use of low-cost by-products or wastes as raw materials [73–76].

Microbial polysaccharides, produced by bacteria, fungi, yeasts, and algae, can be found intracellularly in different cellular components and/or in the extracellular environment. Generally, intracellular polysaccharides are often reserve materials for energy and carbon sources (e.g., glycogen) and can be found within the cell cytoplasm, while cell-wall-associated polysaccharides are anchored to the cell-wall of the microbial cell, contributing to its structural integrity (e.g., CGC), and extracellular polysaccharides are secreted by the cells, forming either a capsule that remains associated with the cell surface (capsular polysaccharides, CPS) or a slime that is loosely bound to the cell surface (exopolysaccharides, EPS) [77]. CPS are mostly associated with the pathogenicity of the microorganism and include virulence-promoting factors [78], whilst EPS has been proposed to provide protection against environmental stress, cell adherence to surfaces, and carbon or water storage reserves [79].

Due to their functional properties, polysaccharides can be used as structuring agents, based on their ability to form polymeric structures (e.g., films, gels, emulsions, micro- and nanoparticles). Moreover, their inherent biological properties (e.g., anti-inflammatory, antitumor, immunomodulator, antiviral) make them valuable bioactive compounds in the development of novel pharmaceutical drugs [67,80–82].

1.6. Hydrogels Based on Polysaccharides

The potential use of polysaccharides in the biomedical field has gained considerable attention due to their biocompatibility, biodegradability, and nontoxicity. Moreover, the presence of several functional groups, as well as variable physicochemical properties and valuable biological activities, boosts the use of polysaccharides in numerous pharmaceutical areas, including drug delivery, wound healing, and tissue engineering [67,83].

Owing to their hydrophilicity and characteristic charge given by their functional groups, one of the polysaccharides' most valuable property is their ability to form hydrogels which have emerged as a new class of biomaterials [56]. Several polysaccharides, such as alginate, chitosan, hyaluronic acid, cellulose, dextran, and xanthan, either alone or in blends, have been used for the design and fabrication of hydrogels (Table 1.1).

Table 1.1 - Examples of natural polysaccharides used to fabricate hydrogels.

Polysaccharide	Charge	Sugar monomers	Chemical structure	Source	Properties	Biomedical Application	Reference
Alginate	Anionic	Guluronic acid Mannuronic acid	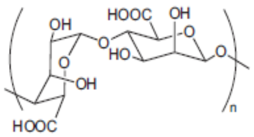	Brown seaweed (*Laminaria* sp., *Lessonia* sp.), Bacteria (*Azotobacter* sp., *Pseudomonas* sp.)	Water soluble Gel-forming ability	Drug delivery Wound dressing Tissue regeneration	[84–86]
Carrageenan	Anionic	Galactose	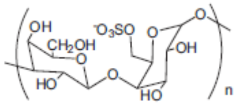	Red seaweed (*Kappaphycus* sp., *Chondrus* sp.)	Water soluble Gel-forming ability	Drug delivery Wound dressings Tissue engineering	[87,88]
Cellulose	Neutral	Glucose	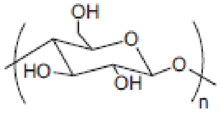	Plants, Bacteria (*Acetobacter* sp., *Rhizobium* sp.)	Water insoluble Chiral High crystallinity	Drug delivery Tissue regeneration Surgical material Wound dressing	[89,90]
Chitosan	Cationic	N-acetyl-glucosamine Glucosamine	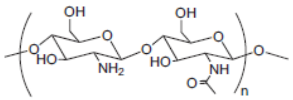	Deacetylation of chitin extracted from marine crustaceans, insects, yeasts, and fungi	Soluble in acidic media Mucoadhesive Antimicrobial	Drug delivery Wound dressing Tissue engineering Bioadhesive	[91–93]
Dextran	Neutral	Glucose	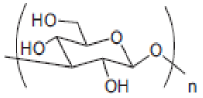	Bacteria (*Leuconostoc* sp., *Lactobacillus* sp., *Weissella* sp.)	Water soluble High stability	Drug delivery Tissue engineering Wound dressings Biosensing	[94,95]
Hyaluronic acid	Anionic	N-acetyl-glucosamine Glucuronic acid	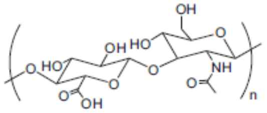	Animal (rooster comb), Bacteria (*Streptococcus* sp.)	Water soluble Viscoelastic behavior Antimicrobial	Drug delivery Tissue regeneration Wound healing	[96–98]
Pullulan	Neutral	Glucose	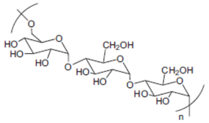	Fungi (Aureobasidium sp.)	Water soluble Film forming ability	Drug delivery Tissue engineering Imaging	[99,100]
Xanthan	Anionic	Glucose Mannose Glucuronic acid	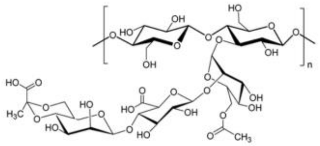	Bacteria (*Xanthomonas* sp.)	Water soluble High viscosity	Drug delivery Tissue engineering	[101,102]

As one of the major compounds of brown seaweed, alginate is a hydrophilic heteropolysaccharide that provides flexibility and strength to the organism [103]. Owing to their anionic nature, conferred by their constituent monomers guluronic and mannuronic acids, alginates form hydrogels when interacting with multivalent cations through a typical ionotropic gelation process [84]. The most well-known example of alginate hydrogel formation is in the presence of Ca^{2+} which crosslinks the polymeric chain by the "egg-box" model [104]. This model describes the interaction between the Ca^{2+} ions and two antiparallel blocks of guluronate residues (G-blocks) of alginate, creating a diamond-shaped cavity that binds the cation through multi-coordination involving the oxygen atoms of the carboxyl functional groups (Fig. 1.3) [86].

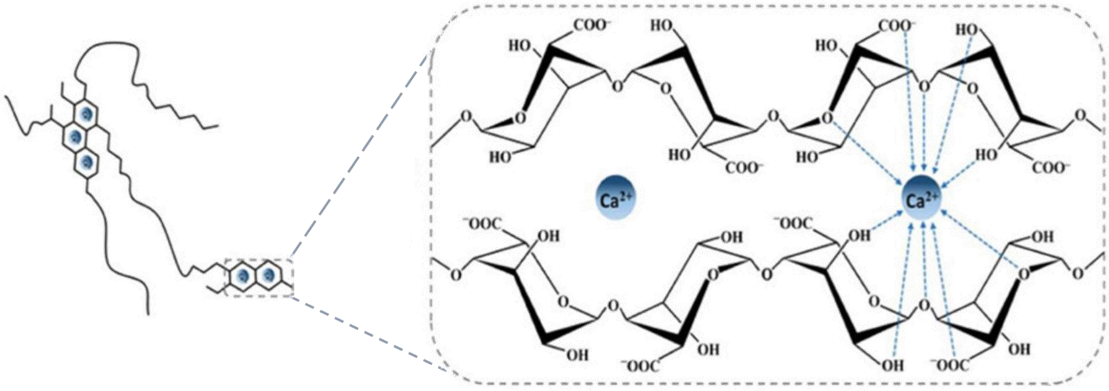

Figure 1.3 - Illustration of the "egg-box" model between alginate G-blocks and Ca^{2+} ions (adapted from [86]).

Alginate hydrogels have been extensively used as drug delivery vehicles, mainly due to the possibility of encapsulating drugs, increasing their bioavailability, under different physical structures that include microspheres [105], nanoparticles, and nanofibers [106]. Different types of drugs and bioactive molecules, such as doxorubicin [107], quercetin [108], and miltefosine [109], have been orally, parenterally, and transdermally delivered from alginate gel nanoparticles. Moreover, its specific biological and tissue-mimicking properties along with its intrinsic antibacterial activity [103], improve the injured skin tissue treatment, preventing bacterial infection. These features make alginate hydrogels potential biomaterials to be used as scaffolds in wound healing and tissue engineering [85,110].

Chitosan is another widely studied polysaccharide extensively used in hydrogel design and production. It is a semi-crystalline cationic polysaccharide obtained by the deacetylation of chitin extracted from marine crustaceans, insects, and the cell wall of yeasts and fungi [91]. Chitosan based hydrogels have been prepared either by physical or chemical crosslinked methods to develop materials suitable to be applied in the biomedical field as drug delivery systems or wound healing dressings [83,111].

It is well known that chitosan has low water solubility and can only be maintained in aqueous solution under acidic conditions. Consequently, the neutralization of a chitosan solution to a pH above 6.2 (amine pKa) displays the gelation phenomenon [112,113]. This unique behavior allows the utilization of chitosan to produce pH-sensitive hydrogels [114]. These hydrogels exhibit the ability to undergo reversible swelling in response to changes in the surrounding pH environment. Thus, at acid conditions (pH≤4), the protonation of the polymer's amino groups promotes hydrogel swelling, while under alkaline conditions (pH>7), the amino groups become deprotonated, leading to a reduction in positive charges, thus decreasing the hydrogels' swelling [115,116]. The pH-responsive behavior of chitosan hydrogels makes them particularly useful for drug delivery applications since drug release can be tailored to environments of specific pH values. For example, Jing et al. [117] developed hydrogel beads of sodium alginate/carboxymethyl chitosan that exhibited a pH-dependent release profile of the protein lactoferrin. The obtained beads maintained their structure during the loading and release processes and were able to prevent protein release in the gastric environment. Additionally, these types of hydrogels can also be used in wound dressing applications dealing with the changes in pH associated with infection. For this purpose, a chitosan/polyphenolic patch was designed to load a topical antibiotic (neomycin) and act as a wound dressing [118]. The results showed neomycin release concomitant with the environment's pH, being stimulated at pH 5.5 (normal skin environment) and sustained released at pH 7.5 (wound environment), demonstrating potential for chronic wound infection.

Chitosan hydrogels can also exhibit thermo-responsive behavior by incorporation of polyol- or sugar-phosphate salts such as glycerophosphate [113,119]. In this case, increasing the temperature disrupts the electrostatic attraction of the amino groups, and sodium glycerophosphate, dehydrating the chitosan chain into a gel [120]. Chitosan based thermo-reversible hydrogels have a low critical solution temperature (LCST) which means that below the LCST, a polymer solution presents low viscosity, and above an LCST a gel-like state is obtained [112]. This feature is interesting for biomedical applications since LCST is typically close to human body temperature, particularly for the preparation of injectable hydrogels [120]. Once injected into the body, the hydrogels undergo a *in situ* gelation process as the temperature increases to body temperature. This property is valuable for minimally invasive drug delivery systems and for tissue engineering applications. Ahsan et al. [121] prepared a chitosan/hyaluronic acid hydrogel for sustained delivery of disulfiram for anticancer treatment. These hydrogels exhibited high biocompatibility upon fast gelation at physiological temperature and demonstrated to be pH-responsive with selective drug release properties.

Hyaluronic acid is a naturally occurring polysaccharide found in the human body, particularly in articular cartilage and synovial fluid [97]. It belongs to a group of glycosaminoglycan heteropolysaccharides, consisting of N-acetyl-glucosamine and D-glucuronic acid linked by glycoside bonds. Hyaluronic acid, a key component of the extracellular matrix, plays a vital structural and functional role in various processes. It contributes to functions such as lubricating arthritic joints and regulating the viscoelastic properties of soft tissues [122]. Due to its intrinsic properties, such as high water retention and viscoelasticity, hyaluronic acid has been used for the fabrication of hydrogels [123]. To improve the mechanical properties as well as degradation rate, hyaluronic acid has been chemically modified (e.g., esterification) or crosslinked with several compounds (e.g., divinyl sulfone) [123]. Among several biomedical applications, hyaluronic acid based hydrogels have been widely used in tissue engineering and controlled drug release [98,122].

Regarding drug release applications, smart hydrogels have also been developed using hyaluronic acid. For this purpose, pH-sensitive hydroxyethyl cellulose/hyaluronic acid hydrogels were designed as transdermal delivery systems for skin lesion treatment [124]. In this case, hydroxyethyl cellulose provided structural support, while hyaluronic acid offered skin compatibility and pH-responsive properties. Various hydrogel formulations were synthesized and characterized, with the structures consisting of hydroxyethyl cellulose and hyaluronic acid at a mass ratio of 1:3, exhibiting optimal rheological and adhesive properties. This formulation demonstrated efficient drug release (>70%), at pH 7, and displayed antimicrobial activity against *Propionibacterium acnes*, making it a promising transdermal delivery system for acne treatment, primarily penetrating the skin through hair follicles. Jung et al. [125] explored the use of hyaluronic acid and the gelling agent Pluronic F-127, to prepare injectable thermossensitive hydrogels for treating arthritis by long-term delivery of a nonsteroidal anti-inflammatory drug. The results demonstrated that the incorporation of high molecular weight hyaluronic acid not only enhanced the hydrogel's mechanical strength but also facilitated sustained drug release. Notably, the critical gelation temperature of the prepared hydrogel was significantly lower than that of native Pluronic F-127. Moreover, the fabricated hydrogel exhibited both sustained drug release characteristics and superior bioavailability under physiological conditions. For cartilage tissue engineering, Park et al. [126] developed an innovative injectable hyaluronic acid hydrogel chemically crosslinked and containing cytomodulin-2 for chondrogenic differentiation. In this study, human periodontal ligament stem cells were employed as a cell source known for their tolerance to *ex vivo* manipulation. The fabricated hydrogel displayed notable stiffness and a porous interconnected structure with excellent biocompatibility, and it persisted *in vitro* and *in vivo* for an extended duration compared to unmodified hyaluronic acid.

Despite their numerous advantages including biocompatibility and biodegradability, polysaccharide-based hydrogels present several challenges in their development and application [127]. These include variability in biodegradability rates, mechanical weaknesses for some natural polysaccharides, and potential variability in the sourced materials. Moreover, the choice of cross-linking agents can impact their biocompatibility, pose regulatory constraints, and may difficult to achieve precise drug release control. Additionally, not all polysaccharides offer the same level of tunability as synthetic polymers, limiting their adaptability in certain applications. These challenges can be addressed through optimization, innovative cross-linking techniques, hybrid materials, and rigorous quality control to enhance the reliability and safety of polysaccharide-based hydrogels across various applications.

1.7. Conclusions and Perspective

Polysaccharide hydrogels represent a remarkable class of biomaterials with enormous potential in the biomedical and biotechnological fields. Driven by their inherent properties such as biocompatibility, non-toxicity, degradability, and swelling properties, they are highly attractive for a wide range of applications, including tissue engineering, wound healing, and controlled drug release systems. Several polysaccharides have been successfully used as materials for the design and fabrication of hydrogels under different physical forms such as beads, membranes, and films. In particular, the ability to deliver therapeutics in a controlled and targeted way, while providing a supportive environment for tissue regeneration, positions polysaccharide hydrogels at the forefront of cutting-edge biomedical advancements.

It is crucial to understand that several challenges remain associated with these structures and optimizations should be performed to overcome them. Regarding materials, more precise chemical modifications of polysaccharides, coupled with their combination with other polymers, could enhance the overall structural characteristics of these systems. Furthermore, the advancement of 3D printing and bioprinting technologies will enable the creation of highly reproducible and intricate structures using polysaccharide hydrogels. This includes the development of heterogeneous systems capable of achieving controlled release of biotherapeutics with precise temporal and spatial control.

2. Chitin-glucan complex Hydrogels

2.1. Low Temperature dissolution of yeast chitin-glucan complex and characterization of the regenerated polymer

The results shown in this chapter were adapted from the following publication:

- **Araújo, D**.; Alves, V.D.; Marques, A.C.; Fortunato, E.; Reis, M.A.M.; Freitas, F. Low temperature dissolution of yeast chitin-glucan complex and characterization of the regenerated polymer. Bioengineering 2020, 7, 28. https://doi.org/10.3390/bioengineering7010028

Summary

Chitin-glucan complex (CGC) is a copolymer composed of chitin and glucan moieties extracted from the cell-walls of several yeasts and fungi. Despite its proven valuable properties, which include antibacterial, antioxidant, and anticancer activity, the utilization of CGC in many applications is hindered by its insolubility in water and most solvents. In this study, NaOH/urea solvent systems were used for the first time for the solubilization of CGC extracted from the yeast *Komagataella pastoris*. Different NaOH/urea ratios (6:8, 8:4, and 11:4 (w/w), respectively) were used to obtain aqueous solutions using a freeze-thaw procedure. There was an overall solubilization of 63–68%, with the highest solubilization rate obtained for the highest tested urea concentration (8 wt%). The regenerated polymer, obtained by dialysis of the alkali solutions followed by lyophilization, formed porous macrostructures characterized by a chemical composition similar to that of the starting copolymer, although the acetylation degree decreased from 61.3% to 33.9–50.6%, indicating that chitin was converted into chitosan, yielding chitosan-glucan complex (ChGC). Consistent with this, there was a reduction in the crystallinity index and thermal degradation temperature. Given these results, this study reports a simple and green procedure to solubilize CGC and obtain aqueous ChGC solutions that can be processed as novel biomaterials.

2.1.1. Introduction

Chitin-glucan complex (CGC), a copolymer composed of chitin (N-acetyl-D-glucosamine polymer) and glucan (glucose homopolymer) moieties linked through β-(1,3) and β-(1,6) glycosidic linkages [128,129], is the main component of the inner cell wall of yeasts and fungi, contributing for the stiffness and stability of the cells [75,128]. Therefore, those microorganisms can be a source of CGC, whose biodegradability and biocompatibility, combined with its inherent bioactivity, render this biopolymer interesting for high-value applications. In fact, CGC of microbial origin has been reported to possess antibacterial [130], antioxidant [131], and anticancer activity [132], and has been used as an anti-aging component in cosmetics formulations [129], as a food additive [133], in wound dressing [134] and in pharmaceuticals for obesity and diabetes treatments [135].

Despite its proven properties, the utilization of CGC in a broader range of applications is still hindered by its insolubility in water and most organic and inorganic solvents [136,137]. Similarly to chitin and cellulose, CGC solubility is limited to toxic and/or corrosive polar solvents (e.g. dimethylacetamide/lithium chloride) [138,139] and the resulting solutions are often unstable, which difficulties their processing. CGC's insolubility is given by the inter- and intramolecular hydrogen bonds established between CGC chains and due to the strong covalent linkages between β-glucan and chitin [140]. In order to improve CGC solubility, chemical modification (e.g., carboxymethylation) [141,142], and physical methods (e.g., sonication) that induce depolymerization [136], have been developed. However, those modifications the physical-chemical properties of the original biopolymer, such as its biodegradability and bioactivity. Other strategies include the use of alternative "eco-friendly" solvents, such as ionic liquids (ILs) [143], for CGC solubilization.

In recent years, alkali solvent systems, mainly based on NaOH or KOH, have been proposed for the dissolution of crustacean chitin [144,145], β-glucans [146,147], and cellulose [148,149] from plant sources, and yeast CGC [150]. The addition of urea to the alkali solution was reported to enhance the polymers' solubilization by disrupting the inter- and intramolecular hydrogen bonds [151,152]. Moreover, it was reported that low temperature steps (below the freezing point of the solvent system) play an important role in the solubilization process. At such low temperatures, the hydrated alkali component disrupts the polymer chain matrix by breaking the hydrogen bonds and allowing the formation of new ones. This yields a stable structure composed of the polymer chain associated with the alkali component and water clusters [151,153]. The solubilization of the polymer chains is allowed by the volume expansion of the matrix upon freezing-induced strength and disruption of the hydrogen bonds.

In this study, NaOH/urea solvent systems were used for the first time for the solubilization of CGC extracted from *Komagataella pastoris* biomass and the preparation of aqueous solutions. Several concentrations of NaOH and urea were tested, and the rheological properties of the resulting solutions were studied. Moreover, the CGC was regenerated from such solutions, and the resulting polymers were characterized in terms of acetylation degree, structural and thermal properties.

2.1.2. Materials and Methods

2.1.2.1. Materials

Yeast biomass was obtained by cultivation of *Komagataella pastoris* DSM 70877 using glycerol as the sole carbon source, as described by Farinha et al. [154]. CGC was extracted from *K. pastoris* biomass by the hot alkaline extraction procedure described by Araújo et al. [155], with slight modifications. Briefly, 1 L culture broth was mixed with 1 L NaOH 2 mol/L (to yield a suspension with a NaOH concentration of 1 mol/L) and treated at 65 ºC for 2 h, under constant stirring. After centrifugation (13000×g, 15 min), the alkaline-insoluble material was re-suspended in deionized water (200 mL), neutralized with H_2SO_4 95%, and washed repeatedly until constant conductivity values were reached (below 50 µS/cm), keeping a neutral pH. The CGC thus obtained was freeze dried (ScanVac CoolSafe^{TM}, LaboGene, Lillerød, Denmark) at −110 °C for 48 h and stored at room temperature in a closed vessel. NaOH pellets (99% purity) and urea (99% purity) were purchased from AzkoNobel (Amsterdam, the Netherlands) and Panreac (Barcelona, Spain), respectively.

2.1.2.2. CGC Dissolution in NaOH/Urea Solvent Systems

Three different NaOH/urea solvent systems were prepared with varying concentrations of each solute (Table 2.1). The selected NaOH/urea ratios were reported for solubilization of crustacean chitin and/or cellulose [144,152,156–158]. For the dissolution experiments, the CGC powder (0.5 g) was dispersed in the solvent systems (25 g) and the suspensions were kept at −20 °C for 48 h. During this period, four freeze-thaw cycles were performed in which the thawed suspensions were extensively stirred (at 500 rpm, for 1 h), at room temperature. The insoluble fractions of the suspensions were separated from the soluble ones (first soluble fractions, coded as $CGC_{1.1}$, $CGC_{2.1}$, and $CGC_{3.1}$, for solvent systems 1, 2 and 3, respectively) by centrifugation (20,000× g, 30 min, 4 °C). The obtained insoluble fraction was re-suspended in fresh NaOH/urea solvent system and subjected to the same freeze-thaw process to obtain a second soluble fraction (coded as $CGC_{1.2}$, $CGC_{2.2}$ and $CGC_{3.2}$, for solvent systems 1, 2 and 3, respectively).

2.1.2.3. Polymer Regeneration

All soluble fractions were subjected to dialysis with a 12,000 molecular weight cut-off (MWCO) membrane (Nadir® dialysis tubing, Carl Roth, Karlsruhe, Germany) against deionized water until neutral pH and constant conductivity values (20 μS/cm) were achieved. The samples were freeze dried and kept in closed vessels, at room temperature.

The overall recovery yield (% recovery) in each solvent system was determined by equation (2.1.1):

$$\%\, recovery = \frac{W_1 + W_2}{W_{initial}} \times 100 \tag{2.1.1}$$

where W_1 is the weight (g) of the first soluble fraction, W_2 is the weight (g) of the second soluble fraction and $W_{initial}$ is the initial polymer weight (g). All experiments were performed in triplicate.

2.1.2.4. Rheological Properties of the Polymer Solutions

The rheological properties of solutions obtained with the three solvent systems were assessed using a controlled stress rheometer (HAAKE MARSIII, Thermo Scientific, Waltham, MA, USA) equipped with a cone-plate geometry (diameter 3.5 mm, angle 2°), with a gap of 0.1 mm. The samples were equilibrated at 20 °C, for 5 min, after which the flow curves were performed using a steady state flow ramp in the shear rate of 10–1000 s^{-1}. The viscoelastic properties were evaluated by carrying out stress sweeps at a constant frequency (1 Hz) for a stress range from 10^{-4} to 1000 Pa, and frequency sweeps at a constant tension within the linear viscoelastic region, for a frequency range from 10^{-3} to 1 Hz.

2.1.2.5. Characterization of the Regenerated Polymer

2.1.2.5.1. Elemental Analysis and Degree of Acetylation

Elemental analysis of the regenerated samples was performed by a Flash EA 1112 Series CHNS analyzer (Thermo Scientific). The chitin content (Q, %) was calculated based on the samples' nitrogen content (%), using the following formula (2.1.2) [159]:

$$Q = 14.199N \tag{2.1.2}$$

where N is the nitrogen content (%) in the sample.

The degree of acetylation (DA, %) was calculated by the following formula (2.1.3) [144]:

$$DA = \frac{(\frac{C}{N} \times Q) - 5.14}{1.72} \times 100 \qquad (2.1.3)$$

where C/N is the ratio (%) of carbon to nitrogen contents, as determined by elemental analysis and Q represents the chitin content.

2.1.2.5.2. Fourier Transform Infrared Spectroscopy

Fourier transform infrared spectroscopy (FT-IR) was performed using a Nicolet 6700 FT-IR (Thermo Electron Corporation, Waltham, MA, USA) with a diamond crystal attenuated total reflectance (ATR) accessory. The spectra were obtained between 500 and 4000 cm^{-1} after 10 scans, at room temperature.

2.1.2.5.3. X-ray Diffraction Profiles

X-ray diffraction (XRD) was performed with a diffractometer (X'Pert Pro, PANalytical, Almelo, The Netherlands) with a CuKα target and wavelength of 1.5406 Å. The crystallinity index (CI, %) of the samples was determined by the following equation (2.1.4) [154]:

$$CI = \frac{I_{110} - I_{am}}{I_{110}} \times 100 \qquad (2.1.4)$$

where I_{110} is the maximum intensity of the (110) peak at a 2θ angle around 19° and I_{am} is the intensity of the amorphous diffraction at 2θ ≈ 20°, corresponding to the minimum intensity.

2.1.2.5.4. Thermal Properties

Thermogravimetry analysis (DSC-TGA) was performed with a Simultaneous Thermal Analyser (STA 449 F3 Jupiter, NETZSCH Thermal Analysis, Wittelsbacherstraße, Germany), in an air atmosphere, with a heating rate of 20 °C/min, from 0 to 500 °C.

2.1.3. Results and Discussion

2.1.3.1. Preparation of CGC Solutions in NaOH/urea Solvent Systems

Previous studies reported the solubilization of yeast CGC, in alkali solutions (NaOH, KOH) for the preparation of hydrogels [150]. Moreover, it has been described that the addition of urea in aqueous alkali solutions improves the solubility and stability of cellulose [160] and crustacean chitin [144]. Therefore, in this study, three solvent systems based on NaOH and urea at different ratios (6:8, 8:4 and 11:4 wt%, for solvent systems 1, 2 and 3, respectively) (Table 2.1) were prepared and tested to obtain CGC aqueous solutions using freeze-thaw procedures described for solubilization of crustacean chitin [144,156,157] and cellulose [152,158].

CGC solubilization was observed for all tested solvent systems (Fig. 2.1), although with slightly different solubility rates (Table 2.1). As shown in Fig. 2.1, the obtained CGC solutions were opaque and presented a yellowish coloration (Fig. 2.1A). After the removal of the insoluble fraction, the solutions became translucid but kept the yellow color, which might be due to the presence of impurities (Fig. 2.1B). During the dialysis process, impurities were removed and CGC solutions became white and opaque (Fig. 2.1C).

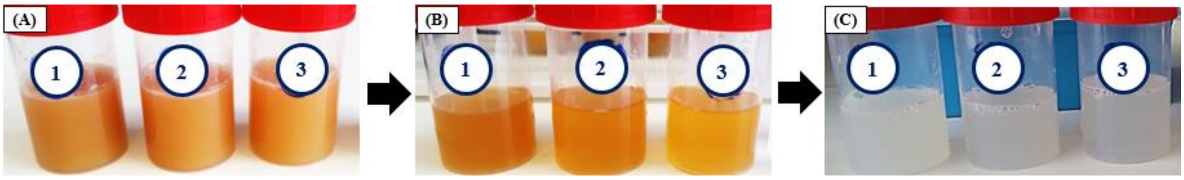

Figure 2.1 — Macroscopic aspect of: (**A**) initial CGC suspensions in the three NaOH/urea solvent systems; (**B**) the CGC solutions obtained after removal of the insoluble fraction by centrifugation; (**C**) the corresponding CGC solutions after dialysis against deionized water. Solvent systems 1, 2 and 3 are represented by the numbers 1, 2 and 3, respectively.

Table 2.1 — Solubilized CGC mass, polymer concentration and overall solubilization of the soluble fractions in different NaOH/urea solvent systems.

Solvent System	NaOH:Urea (wt%:wt%)	Starting Polymer Mass (mg)	Fraction Solution	Solubilized Polymer Mass (mg)	Polymer Concentration (wt%)	Recovery (%)	Overall recovery (%)
1	6:8	504.4 ± 5.1	$CGC_{1.1}$	275.8 ± 4.1	13.8 ± 0.2	54.7 ± 1.4	68.0 ± 1.7
			$CGC_{1.2}$	67.2 ± 0.9	3.4 ± 0.1	13.3 ± 0.3	
2	8:4	506.0 ± 4.7	$CGC_{2.1}$	275.4 ± 6.0	13.8 ± 0.3	54.4 ± 1.7	65.2 ± 0.3
			$CGC_{2.2}$	54.4 ± 10.8	2.7 ± 0.5	10.7 ± 2.0	
3	11:4	502.7 ± 1.2	$CGC_{3.1}$	258.3 ± 22.3	12.9 ± 1.1	51.4 ± 4.6	62.9 ± 3.1
			$CGC_{3.2}$	57.8 ± 7.5	2.9 ± 0.4	11.5 ± 1.5	

The highest overall recovery (68.0 ± 1.7%) was obtained from solvent system 1 that contained the highest urea concentration (8wt%) and the lowest NaOH concentration (6 wt%), suggesting that urea contributes to CGC solubilization. The same solvent system was reported to result in significantly lower solubility for shrimp shell chitin and cotton linter cellulose (30.0 and 36.1%, respectively) [144,152], even if only the first soluble fraction is considered (57.0 ± 1.4%).

The use of solvent systems 2 and 3, which had lower urea concentration (4wt%) and higher NaOH concentrations (8 and 11wt%, respectively), resulted in similar overall recovery values (65.2 ± 0.3 and 62.9 ± 3.1%, respectively) (Table 2.1). These results seem to indicate that increasing NaOH concentration in the solvent system, for the same urea concentration, has no significant impact on CGC solubilization. Hu et al. [144] and Zhou et al. [152] tested solvent system 2 for solubilization of shrimp shell chitin and cotton linter cellulose, respectively, achieving contrasting results. While a high solubility rate was reported for chitin in this solvent (85.0%) [144], a low solubility was obtained for cellulose (40.5%) [152].

These findings may be related to the differing nature of the macromolecules under study, namely, chitin, cellulose, and CGC, which have distinct composition and molecular structures. Moreover, different procedures were adopted for chitin and cellulose solubilization, namely, the initial polymer content, the number of freeze-thaw cycles, and the exposure time to the solvent at low temperatures, which have probably also influenced the reported results.

These results demonstrate that the tested NaOH/urea solvent systems were suitable to achieve high CGC solubilization, yielding solutions (first soluble fractions $CGC_{1.1}$, $CGC_{2.1}$ and $CGC_{3.1}$) with polymer concentrations of 12.9 ± 1.1wt% and 13.8 ± 0.2wt% (Table 2.1). Furthermore, most of the polymer was solubilized during the first solubilization step since lower polymer concentrations were obtained in the second soluble fractions (below 3.4 ± 0.1wt%).

The polymer concentration in the first soluble fractions for all tested solvent systems is within the range of those reported for crustacean chitin and cellulose using different types of solvents. In fact, a similar polymer concentration (14%) was reported for the solubilization of chitin crab shell in dimethylacetamide/lithium chloride [161]. Lower values were also obtained using green solvents, such as deep eutectic solvents (DES) and ILs. Sharma et al. [162] reported the dissolution of crab chitin and cellulose in DES that resulted in a concentration below 8wt%. On the other hand, shrimp chitin solubilization in 1-ethyl-3-methyl-imidazolium bromide ([Emim][Br]) resulted in polymer concentrations of 12% [163].

2.1.3.2. Rheological Behavior of the Solutions

The rheological behavior of the first soluble fractions of CGC in each NaOH/urea solvent system ($CGC_{1.1}$, $CGC_{2.1}$ and $CGC_{3.1}$) is shown in Fig. 2.2 and 2.3. The second soluble fraction was not analyzed due to their considerably low polymer concentrations.

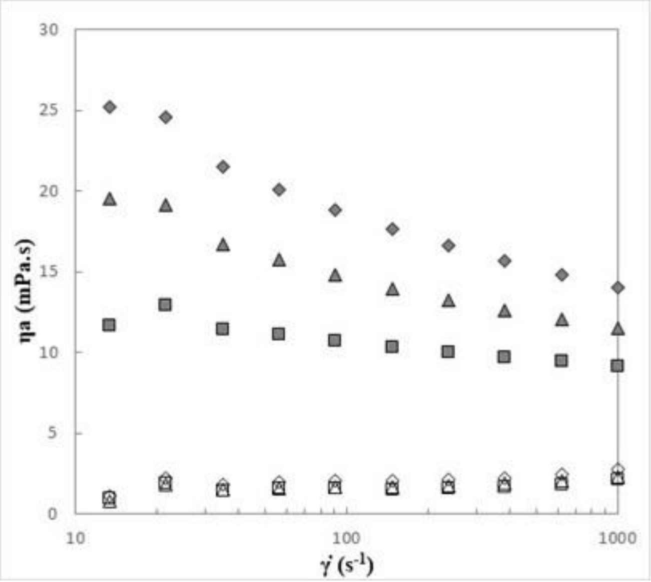

Figure 2.2 — Apparent viscosity of first soluble fractions of CGC1 (■), CGC2 (▲) and CGC3 (◆), and solvent systems 1 (□), 2 (△) and 3 (◇), measured at 20 °C.

The flow curves of the three solutions (Fig. 2.2) had a similar behavior with a constant apparent viscosity at low shear rates (characteristics of Newtonian fluids), followed by a slight decrease in apparent viscosity values with the increase of the shear rate (shear-thinning behavior). As shown in Fig. 2.2, solution $CGC_{1.1}$ approaches a Newtonian plateau at 11.6–12.9 mPa·s, while $CGC_{2.1}$ and $CGC_{3.1}$ solutions approached this plateau at higher values (19.1–19.5 and 24.6–25.2 mPa·s, respectively).

Similar flow behavior was reported by Hu et al. [144] for shrimp chitin solutions in NaOH/urea at a concentration of 2wt%. In that study, the solutions were reported to exhibit a Newtonian plateau at low shear rates (0.1–1.0 s^{-1}), followed by a shear-thinning behavior with the increase of shear rate [145]. The observed flow behavior of the polymer solutions was not due to the solvent systems that exhibited a quite low viscosity (below 2.2 mPa.s) and no shear thinning behavior (Fig. 2.2).

Fig. 2.2 shows that solution $CGC_{1.1}$ presented the lowest apparent viscosity values (11.7 mPa·s, at 13.3 s^{-1}), while $CGC_{2.1}$ and $CGC_{3.1}$ had slightly higher values (19.5 and 25.2 mPa·s at 13.3 s^{-1}, respectively). Since the polymer concentration was similar for all three solutions (12.91–13.79wt%), these results might suggest that the flow behavior was influenced by the solvent systems' composition. The low concentration of NaOH (6wt%) and high urea content (8wt%) present in solvent 1 might have prevented the interaction of the polymer macromolecules, thus decreasing the viscosity of solution $CGC_{1.1}$. Similar behavior was reported by Huber et al. [164] for cellulose solutions in NaOH/urea, in which a viscosity reduction of almost 40% was observed by increasing the urea concentration in the solvent.

On the other hand, increasing the concentration of NaOH in solvent systems 2 and 3 (to 8 and 11wt%, respectively) has apparently led to higher apparent viscosity in solutions CGC$_{2.1}$ and CGC$_{3.1}$ (Fig. 2.2). The increasing ionic strength of these solutions may have contributed to the higher apparent viscosity observed.

The mechanical spectra (Fig. 2.3) revealed that all the solutions presented a loss modulus (G'') considerably higher than the storage modulus (G'), both highly dependent on the frequency. This result is indicative of liquid-like fluid behavior since the polymer solutions show a higher viscous behavior than the elastic one. As the frequency increases, both moduli tend to the same value. A similar trend was reported for chitin in NaOH/urea aqueous solution. Hu et al. [165] demonstrated that chitin solutions with a concentration range from 0.5 to 1.5% also present values of G'' higher than G' for low frequency values. In the case of chitin solutions, at low concentrations (0.5 and 1%) both moduli have different values at a frequency 1 Hz which is consistent with a dilute solution. Once concentration is increased to 1.5%, analogous to the results obtained for CGC solutions, a cross-over is observed at a frequency below 1 Hz.

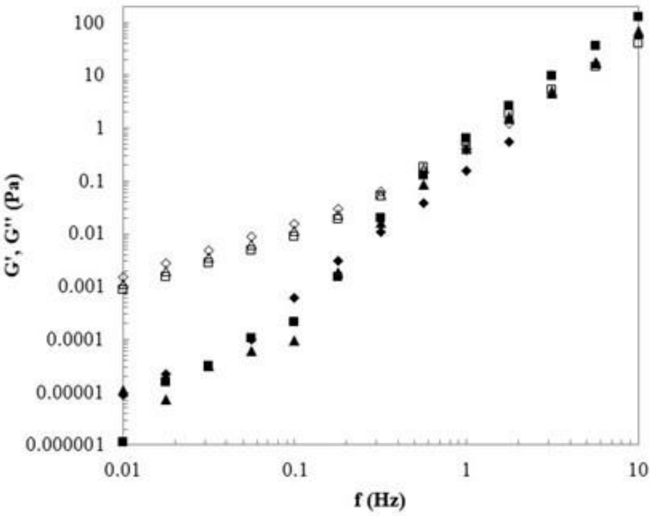

Figure 2.3 — Viscoelastic properties of first soluble fractions of CGC1 (■), CGC2 (▲) and CGC3 (◆). Mechanical spectrum storage [G' (full symbols)] and loss moduli [G'' (open symbols)].

2.1.3.3. Characterization of the Regenerated Polymer

2.1.3.3.1. Elemental Analysis and Degree of Acetylation

The polymers regenerated from the soluble fractions in solvent systems 1 (CGC$_{1.1}$ and CGC$_{1.2}$), 2 (CGC$_{2.1}$ and CGC$_{2.2}$) and 3 (CGC$_{3.1}$ and CGC$_{3.2}$) were characterized in terms of their physical and chemical composition. Table 2.2 shows the elemental characterization of the original CGC (CGC$_0$), and the polymers regenerated from all solutions.

Table 2.2 — Elemental characterization of the original CGC (CGC$_0$) and polymer samples regenerated from the NaOH/urea solvent systems (DA, degree of acetylation).

Sample	**Elemental Analysis (%)**			**Chitin Content (%)**	**DA (%)**
	C	**H**	**N**		
CGC$_0$	43.6 ± 0.05	7.2 ± 0.05	1.7 ± 0.01	23.8 ± 0.10	61.3 ± 0.41
CGC$_{1.1}$	40.4 ± 0.17	7.2 ± 0.05	1.3 ± 0.15	18.8 ± 2.11	34.5 ± 1.40
CGC$_{1.2}$	42.0 ± 0.09	7.2 ± 0.10	1.5 ± 0.03	21.7 ± 0.40	47.6 ± 0.76
CGC$_{2.1}$	40.3 ± 0.12	7.2 ± 0.09	1.5 ± 0.03	20.7 ± 0.40	33.9 ± 0.99
CGC$_{2.2}$	41.6 ± 0.35	7.0 ± 0.18	1.9 ± 0.16	26.5 ± 2.31	44.8 ± 2.86
CGC$_{3.1}$	41.2 ± 0.22	7.1 ± 0.06	1.7 ± 0.18	23.4 ± 2.61	41.6 ± 1.81
CGC$_{3.2}$	42.3 ± 0.12	6.9 ± 0.06	2.3 ± 0.11	32.8 ± 1.61	50.6 ± 0.99

The chitin content of the original CGC$_0$, as determined based on the elemental analysis data, was 23.8 ± 0.10%. The first soluble fractions (CGC$_{1.1}$, CGC$_{2.1}$ and CGC$_{3.1}$) had lower chitin contents (18.8 ± 2.11%, 20.7 ± 0.40% and 23.4 ± 2.61%, respectively, Table 2.2). Interestingly, the second soluble fractions (CGC$_{1.2}$, CGC$_{2.2}$ and CGC$_{3.2}$) were apparently richer in chitin, with higher content values (21.7 ± 0.40%, 26.5 ± 2.31% and 32.8 ± 1.61%, respectively) than the first soluble ones. This might be explained by the fact that the CGC$_0$ sample was probably composed of polymer chains of different composition in terms of chitin:glucan ratio, which may have been solubilized differently during the freeze-thaw procedure. It is likely that the macromolecule chains with lower chitin:glucan ratio were more easily solubilized, thus resulting in solutions with lower chitin content (i.e., the first soluble fractions CGC$_{1.1}$, CGC$_{2.1}$ and CGC$_{3.1}$), while the chains with higher chitin:glucan ratio only solubilized later, during the second solubilization step (i.e., the second soluble fractions CGC$_{1.2}$, CGC$_{2.2}$ and CGC$_{3.2}$).

On the other hand, it can be also observed that the chitin content of the regenerated polymers increased as the NaOH concentration in the solvent systems increased (Table 2.2). In fact, as the NaOH concentration increased (6, 8 and 11%, in solvents 1, 2 and 3, respectively), the chitin content of the corresponding regenerated polymers also increased (18.8 ± 2.11%, 20.7

± 0.40% and 23.4 ± 2.61% for the first soluble fractions, and 21.7 ± 0.40%, 26.5 ± 2.31% and 32.8 ± 1.61% for the second soluble fractions). These results are in accordance with the study reported by Hu et al. [144], in which the solubilization of chitin was improved from 30 to 85% by increasing the NaOH concentration by 2% in the NaOH/urea solvent system.

The dissolution process had a significant impact on the chitin acetylation degree. Initially, CGC_0 presented a DA of 61.3 ± 0.41%, while the regenerated polymers presented lower values of acetylation degree (between 33.9 ± 0.99 and 50.6 ± 0.99%) indicating that chitin was converted into chitosan, its soluble and N-deacetylated derivative [166,167]. Focusing on the regenerated polymers, concomitant with the values obtained for chitin content, the second soluble fractions display a higher degree of acetylation when comparing with the first ones (Table 2.2). According to these results, it can be suggested that chitin molecules with higher concentration of N-acetyl-glucosamine monomers on their structure are more difficult to solubilize and it was only possible after the second dissolution phase.

2.1.3.3.2. Fourier Transform Infrared Spectroscopy

The FTIR spectra of the CGC_0 and the co-polymers regenerated from the NaOH/urea solvent systems are presented in Fig. 2.4. Despite the structural differences related to the chitin deacetylation, no significant impact on the chemical structure was noticed. All spectra presented a broad and intense band around 3400 cm^{-1} (Fig. 2.4), characteristic of O–H stretching of hydroxyl groups, which is common to chitin/chitosan and glucan polymers [142,168,169]. As reported by Farinha et al. [154], this band overlaps the N–H (asymmetric) and N–H (symmetric) stretching peaks. Two peaks, corresponding to the C–H stretching of CH_3 and CH_2 groups, appear at 2916 and 2848 cm^{-1}, respectively. For CGC_0, the intensity of those peaks is higher, when comparing with the spectra of the regenerated polymers CGC1, CGC2 and CGC3. This difference was expected since these peaks are more evident in chitin than chitosan [170]. Additionally, it can be noticed that a decrease in the absorption at around 1650 cm^{-1} occurs for the regenerated polymers, which is associated with the frequency of the vibration modes of amide I (Fig. 2.4). This reduction in intensity is higher for the first soluble fractions, which is concomitant with the lower chitin content of $CGC_{1.1}$, $CGC_{2.1}$ and $CGC_{3.1}$ polymers (Table 2.2). Similarly, the N–H deformation of amide II and C–N stretching in amide III (1550 and 1311 cm^{-1}, respectively) [171] which are present in all the spectra but with low intensity in the $CGC_{1.1}$, $CGC_{2.1}$ and $CGC_{3.1}$.

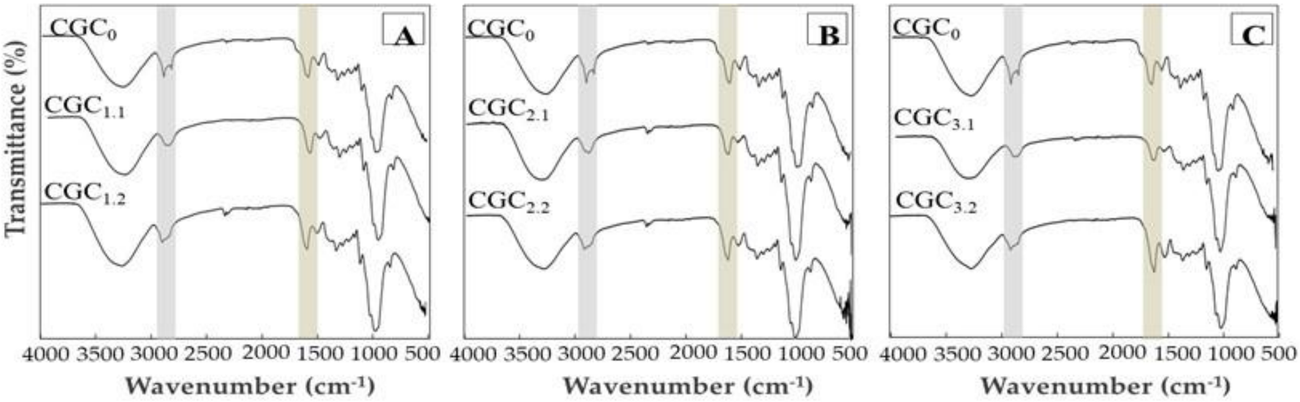

Figure 2.4 — FTIR spectra of CGC_0 and the polymer regenerated from the soluble fractions of CGC in: (**A**) solvent system 1 ($CGC_{1.1}$ and $CGC_{1.2}$), (**B**) solvent system 2 ($CGC_{2.1}$ and $CGC_{2.2}$) and (**C**) solvent system 3 ($CGC_{3.1}$ and $CGC_{3.2}$).

The nature of the linkages between β-glucan units can also be assessed by FTIR spectroscopy [169]. As described by Farinha et al. [154], β-1,3-glucan linkages are represented by small peaks at 890, 1156 and 1370 cm^{-1} and characteristic peaks of β-1,6-glucans linkage are noticed around 920, 1045 and 1730 cm^{-1}. Fig. 2.4 shows that all the polymers presented the small peaks assigned to β-1,3-glucans linkages. However, due to the low content of β-1,6-glucans in *K. pastoris* CGC, the peaks attributed to this linkage are vague and doubtful in all the spectra, including in CGC_0.

2.1.3.3.3. XRD Analysis

Similar XRD patterns were obtained for CGC_0 and the regenerated polymers (Fig. 2.5). The diffractograms of all the polymers presented a broad peak around $2\theta \sim 20°$, which is characteristic of amorphous polymers [172]. These results are in accordance with Farinha et al. [154] who reported a large peak in this region for *K. pastoris* CGC. The authors described the amorphous nature of chitin and glucan co-polymers mainly due to the presence of high β-glucan contents.

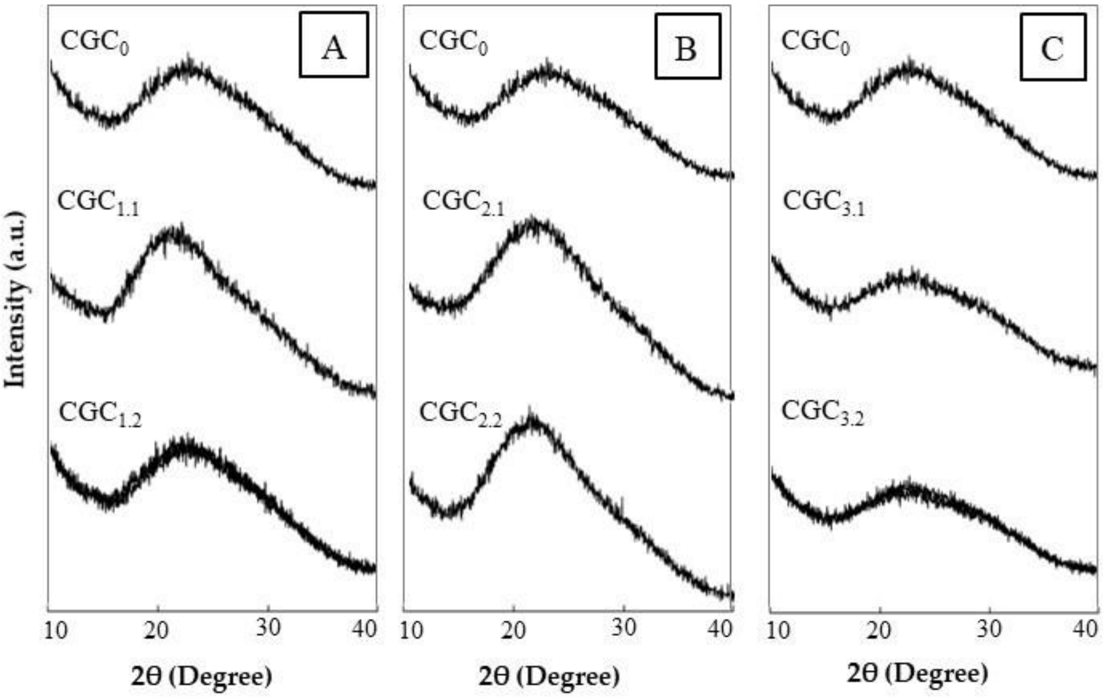

Figure 2.5 — X-ray diffraction profiles of CGC_0 and the polymer regenerated from the soluble fractions of CGC in: (**A**) solvent systems 1 ($CGC_{1.1}$ and $CGC_{1.2}$), (**B**) solvent systems 2 ($CGC_{2.1}$ and $CGC_{2.2}$) and (**C**) solvent systems 3 ($CGC_{3.1}$ and $CGC_{3.2}$).

Nevertheless, the peak intensity was different for CGC_0 and the regenerated polymers, reflecting differences in the polymers' crystallinity. The CI of CGC_0 determined based on the XRD data was 35%. This value is lower than the one reported in the literature for CGC from *K. pastoris* (50%) composed of 24.6mol% of chitin [154]. Despite this difference, the low crystallinity value was expected due to the presence of β-glucans within the co-polymer's structure. Considering the regenerated polymers, apparently, the exposure to the NaOH/urea solvent systems and the dissolution procedure led to a decrease in the CI to 23–32% (Table 2.3).

Table 2.3 — Degradation temperature (T_{deg}) and crystallinity index (CI) of the original. CGC (CGC_0) and polymer samples regenerated from the NaOH/urea solvent systems.

Sample	**CGC_0**	**$CGC_{1.1}$**	**$CGC_{1.2}$**	**$CGC_{2.1}$**	**$CGC_{2.2}$**	**$CGC_{3.1}$**	**$CGC_{3.2}$**
T_{deg} (°C)	302	250	293	256	300	267	302
CI (%)	35	28	30	32	32	23	25

These results may be related to the DA of the polymers. As suggested by Kumirska et al. [173], lower DA values lead to a decrease in the intensity of the peak and, consequently, to a decrease in crystallinity. Additionally, Seoudi and Nada [174] reported that the CI of chitin crab shells decreased after treatment with NaOH, which caused hydrolysis of acetamide groups.

Similar results were obtained for cellulose, where a decrease of around 8% in CI was verified after the dissolution with NaOH/urea aqueous solution [175].

2.1.3.3.4. Thermal Properties

The TGA demonstrates that CGC_0 and the regenerated polymers exhibited similar profiles, comprising three of thermal degradation steps. The main degradation ($\Delta m \approx 60\%$) proceeds in the second step that occurs between 220 and 320 °C, corresponding to the degradation of saccharide structure including dehydration of the saccharide rings, depolymerization of the branched part of the molecules, and decomposition of acetylated and deacetylated units of chitin [154]. The third degradation step occurring at temperatures above 320 °C might be related to the destruction of pyranose rings.

For CGC_0, the degradation temperature (T_{deg}) was 302 °C and there was a char yield of 26%, at 550 °C (Fig. 2.6). The results are in accordance with the ones reported by Farinha et al. [154] where the T_{deg} of CGC from *K. pastoris* was found to be 315 °C.

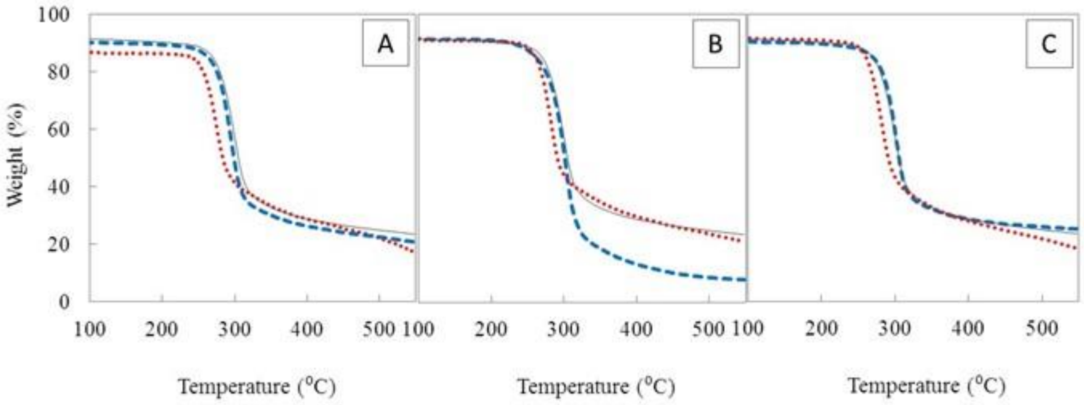

Figure 2.6 —Thermogravimetric analysis (TGA) of the polymers: CGC1 (**A**), CGC2 (**B**) and CGC3 (**C**). Continuous line represents CGC_0; Dotted and dashed lines correspond to first and second soluble fractions, respectively.

The polymers regenerated from the first soluble fractions ($CGC_{1.1}$, $CGC_{2.1}$ and $CGC_{3.1}$) had lower T_{deg} (250 °C, 256 °C and 267 °C, respectively). This result is probably due to the lower DA (33.9–41.6%) and CI (23–32%) of those polymers compared to CGC_0 (DA = 61.3% and CI = 35%). On the other hand, the polymers regenerated from the second soluble fractions ($CGC_{1.2}$, $CGC_{2.2}$ and $CGC_{3.2}$), owing to the higher DA (44.8–50.6%) and CI (25–32%), had higher T_{deg} (293–302 °C) similar to CGC_0 (302 °C). As expected, these results revealed the lower thermal stability of the regenerated polymers is a consequence of the decreased acetyl content since chitosan molecules are known for their lower thermal stability compared to chitin [176].

2.1.4. Conclusions

Three different water based solvent systems were designed to dissolve CGC, a biopolymer known for its intractability due to insolubility in water and most organic solvents. High polymer solubility (over 60%) was achieved for all the tested solvent systems. The solutions' rheological properties showed similar shear thinning behavior with Newtonian plateaus at shear rates between 13.3 and 21.5 s^{-1}, and liquid-like fluid behavior for all solutions. The characterization of the regenerated polymers obtained by freeze drying the solutions indicated that the original CGC co-polymer was deacetylated, yielding a chitosan-glucan complex (ChGC) that was characterized by lower crystallinity and lower T_{deg}. This study demonstrated the feasibility of using a water based green solvent to dissolve CGC, thus opening up the possibility of processing this biopolymer in different areas of application as a novel biomaterial.

2.2. Novel hydrogel based on yeast chitin-glucan complex: characterization and safety assessment

The results shown in this chapter were adapted from:

- **Araújo, D.,** Alves, V.D., Lima, S.A.C., Reis, S., Freitas, F., Reis, M.A.M. Novel hydrogels based on yeast chitin-glucan complex: Characterization and safety assessment. International Journal of Biological Macromolecules 2020, 156, 1104-111. https://doi.org/10.1016/j.ijbiomac.2019.11.141

Summary

Chitin-glucan complex (CGC) was used for the first time for the preparation of hydrogels. Alkali solvent systems, NaOH and KOH solutions, either at 1 or 5 mol/L, were used for CGC dissolution using a freeze-thaw procedure (freezing at −20 °C and thawing at room temperature; four cycles). The CGC solutions thus obtained were subjected to dialysis that induced the spontaneous gelation of the biopolymer, yielding translucid hydrogels with a yellowish coloration. Although all CGC hydrogels exhibited porous microstructures, high water content (above 97%), and good mechanical properties, their morphology, viscoelastic properties, and texture were influenced by the type of solvent system used for CGC dissolution, as well as by their ionic strength. The K-based hydrogels presented a less compact network with larger pores and exhibited lower elastic properties. The Na-based hydrogels, on the other hand, exhibited a denser structure with smaller pores and a stiffer gel structure. These results show that it is possible to prepare CGC hydrogels with differing characteristics that can be suitable for different applications. Furthermore, all hydrogels were non-cytotoxic towards L929 fibroblasts and HaCaT keratinocytes. This study demonstrates that CGC can be used to prepare biocompatible hydrogels with properties render them promising biomaterials.

2.2.1. Introduction

Hydrogels are three-dimensional macromolecular networks capable of adsorbing high amounts of water, saline and physiological media in their structure and swell [177–179]. These soft and pliable structures can be based on synthetic polymers (e.g. acrylic acid, acrylamide, poly(vinyl alcohol)) or biopolymers (e.g. gelatin, starch, alginate) [178–180]. The later have attracted considerable interest due to their biocompatibility, biodegradability, and tissue-mimicking consistency, and are used in applications that range from agriculture and water treatment to hygiene products and biomedicine [177,181]. Hydrogels can be divided into two types, namely, physical or chemical, depending on the type of procedure used to crosslink their polymer chains. Physical hydrogels are obtained by the establishment of physical interactions (e.g., chain entanglements, van der Waals forces, hydrogen bonds or ionic interactions), which are driven by exposing a polymer solution to specific temperatures, pH values and/or ionic strength. On the other hand, in chemical hydrogels, chemical crosslinkers (e.g., epichlorohydrin, succinic anhydride) are used to induce the formation of a hydrophilic network stabilized through covalent linkages [180,182].

Several natural polysaccharides have been used to obtain hydrogels, including starch, alginate, hyaluronic acid, cellulose, and chitin. These biopolymers hold great potential due to the high number of hydrophilic functional groups (e.g., hydroxyl groups) in their molecules. Most hydrogels are usually prepared using a procedure that involves polymer dissolution in a suitable solvent system, followed by gelation [177,180]. This constitutes a problem for biopolymers such as cellulose and chitin, whose solubility is limited to toxic and/or corrosive organic solvents (e.g., dimethylacetamide/lithium chloride, tetrabutylammonium chloride/dimethyl sulfoxide). ILs [182], DES [183], and alkali or alkali/urea aqueous solutions [165,180,184] have been proposed as alternative solvent systems for the dissolution of cellulose and chitin, and the production of hydrogels.

Similarly to cellulose and chitin, CGC is insoluble in water and aqueous solutions, and also in most organic solvents. Therefore, the development of CGC into commercial products has been hindered by its intractability. In this study, aqueous alkali systems based on NaOH or KOH were used for the first time for CGC dissolution by the freeze-thaw method, and the resulting solutions were subjected to dialysis to induce the biopolymer's gelation. The CGC hydrogels thus obtained were characterized in terms of morphology, rheology, mechanical properties, and biocompatibility.

2.2.2. Materials and Methods

2.2.2.1. Materials

Yeast biomass was obtained by cultivation of the yeast *Komagataella pastoris* (DSM 70877) using glycerol as the sole carbon source, as described by Farinha et al. [154]. CGC represented 20wt% of the cell dry mass. It was extracted from *K. pastoris* biomass by the hot alkaline procedure described by Araújo et al. [155].

2.2.2.2. Preparation of CGC hydrogels

Two aqueous alkali solvent systems, namely, NaOH and KOH, were tested at different concentrations (1 mol/L and 5 mol/L). CGC powder (0.5 g) was dispersed in the alkali solvent systems (25 g) and the suspensions were kept at −20 °C for 48 h. During this period, four freeze-thaw cycles were performed in which the thawed suspensions were extensively stirred (at 500 rpm, for 1 h), at room temperature. The insoluble fractions of the suspensions were separated from the soluble ones by centrifugation (20,000 ×g, 30 min, 4 °C). CGC hydrogels were prepared by dialysis of the soluble fractions with a 12,000 MWCO membrane (Nadir®, dialysis tubing, Carl Roth) against deionized water for 48 h, at 20 °C, until neutral pH and constant conductivity values (20 µS/cm) were achieved. The hydrogels prepared with NaOH or KOH, 1 mol/L and 5 mol/L, were labelled as Na1 and Na5, or K1 and K5, respectively.

2.2.2.3. Chemical characterization of CGC hydrogels

For quantification of sodium and potassium in the hydrogels, freeze dried CGC hydrogel samples (~5 mg) were hydrolyzed with nitric acid (5mL HNO_3 5%, v/v), at 120 °C, for 2 h, under constant stirring. Hydrolyzed samples were filtered (0.2 µm nylon, Whatman) and their content in sodium and potassium was determined by Inductively Coupled Plasma-Atomic Emission Spectrometry (ICP-AES) (Horiba Jobin-Yvon, France, Ultima, equipped with a 40.68 MHz RF generator, Czerny-Turner monochromator with 1.00 m (sequential) and autosampler AS500). Nitric acid solution (HNO_3 5%, v/v) was used as blank, being subjected to the same hydrolysis procedure as the samples.

The water content of the hydrogels was determined according to equation. (2.2.1) [185]:

$$Water\ content\ (\%) = \frac{(wet\ mass - dry\ mass)}{wet\ mass} \times 100 \tag{2.2.1}$$

where the dry mass (g) was determined by freeze drying a pre-weighed amount of the gels (wet mass, g).

The chemical composition of the hydrogels was analyzed by high performance liquid chromatography (HPLC) after two acid hydrolysis methods, as described by Araújo et al. [155].

2.2.2.4. Rheological properties

The rheological behavior of the CGC hydrogels was measured and analyzed using a controlled stress rheometer (HAAKEMARSIII, Thermo Scientific) equipped with a plate-plate serrated geometry (diameter 20 mm) with a gap of 1 mm. The hydrogels samples were equilibrated at 25 ± 0.03 °C for 5 min, after which the viscoelastic properties were evaluated by carrying out frequency sweeps at a constant tension within the linear viscoelastic region, for a frequency range from 0.01 to 1 Hz.

2.2.2.5. Texture profile analysis

The texture properties of the CGC hydrogels were determined with a texture analyzer TA-XT plus (Stable Micro Systems Ltd., Surrey, UK) equipped with a 50 N load cell. A double compression cycle was carried out up to 50% strain of the samples' original height at a speed rate of 1 mm/s using an aluminum plunger with a 60 mm diameter. A delay period of 5 seconds was allowed between the two compression cycles. The maximum tension of the first compression was defined as the hardness (Pa) and the ratio between the second and first compression distances until maximum forces was used to measure the springiness. Cohesiveness was defined as the ratio between the positive force area during the second cycle and that of the first compression cycle. All the measurements were performed in duplicate at room temperature (20 ± 0.2 °C).

2.2.2.6. Cryo-Scanning Electron Microscopy

The CGC hydrogels were characterized in terms of their structure and morphology by Scanning Electron Microscopy (SEM). The hydrogels were analyzed with a Tabletop Microscope TM3030 (Hitachi in High Technologies, America) equipped with a sample holder with refrigeration. Samples were observed at low temperature (−4 °C) using a magnification in the range of 150–500×.

2.2.2.7. Cytotoxicity tests

The cytocompatibility of the CGC hydrogels was evaluated according to the International Standard ISO 10993-5:2009(E) through assessment of metabolic activity (MTT (3-(4,5-dimethylthiazol-2-yl)-2,5-diphenyltetrazolium bromide) tetrazolium reduction assay) in two cell lines, human keratinocytes HaCaT and mouse L929 fibroblasts. The cells were grown in

Dulbecco's Modified Eagle Medium (DMEM) media supplemented with 10% (v/v) fetal bovine serum and 1% (v/v) streptomycin/penicillin and maintained at 37 °C in a humidified atmosphere of 5% (v/v) CO_2. For the cell viability assay, 5×10^4 cells per well were seeded in 96 well plates and cultured at the conditions above described. After 24 h, the medium was removed and 100 µL of fresh medium containing serial dilutions, up to 1000 µg/mL, of freeze dried CGC hydrogels dissolved in alkaline solvent (NaOH 1mol/L, at neutral pH) were added. Upon 24 h of exposure, the supernatant was replaced by the MTT solution (0.5 mg/mL) and incubated (37 °C, 5% (v/v) CO_2) for 2 h. During incubation, tetrazolium dye MTT is reduced by dehydrogenase enzymes to insoluble formazan. Following the incubation step, the medium was eliminated and replaced with dimethylsulfoxide to dissolve the formazan crystals accumulated inside living cells. For the quantification of formazan produced, the absorbance was measured at 590 nm using a Synergy™ HT Multi-mode microplate reader (BioTek Instruments Inc., Winooski, VT, USA), subtracting the background read at 630 nm. Cells grown in fresh medium without treatment and cells treated with Triton™X-100 (1% v/v) were used as positive and negative controls, respectively. Results were expressed as a percentage of metabolic activity relative to the values obtained at 2 h and considering the metabolic activity of non-treated cells as 100%.

2.2.3. Results and Discussion

2.2.3.1. Hydrogels formation

Four alkali solvent systems, NaOH and KOH solutions, either at 1 mol/L or 5 mol/L, were used for CGC dissolution using a freeze-thaw procedure (Fig. 2.7), proposed for dissolution of chitin and cellulose [165,177,180,184]. At temperatures below the freezing point, the hydrated alkali component disrupts the inter- and intramolecular hydrogen bonds between the polymeric chains. The hydrogels were obtained by dialyzing the CGC solutions, against deionized water until complete removal of the salt ions.

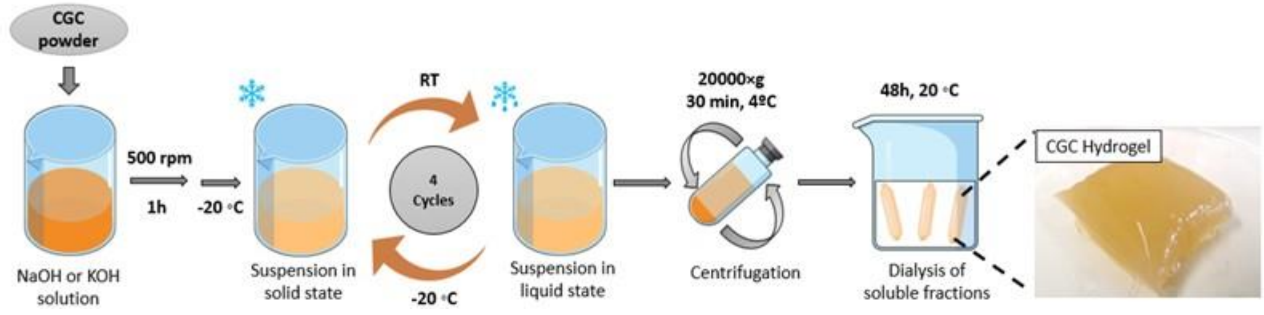

Figure 2.7 —Schematic illustration of CGC hydrogels preparation, comprising polymer suspension in the alkali systems, application of freeze-thaw cycles for polymer dissolution and dialysis for polymer gelation.

As shown in Fig. 2.8, the CGC hydrogels presented a yellow coloration and were translucid. The yellow color might be due to the presence of protein whose content in the gels was between 4.4 and 8.8wt%. The gels' shape was molded by the dialysis tubing, thus showing that the CGC hydrogels obtained by this methodology can be molded into other shapes by inducing gelation in appropriate molds.

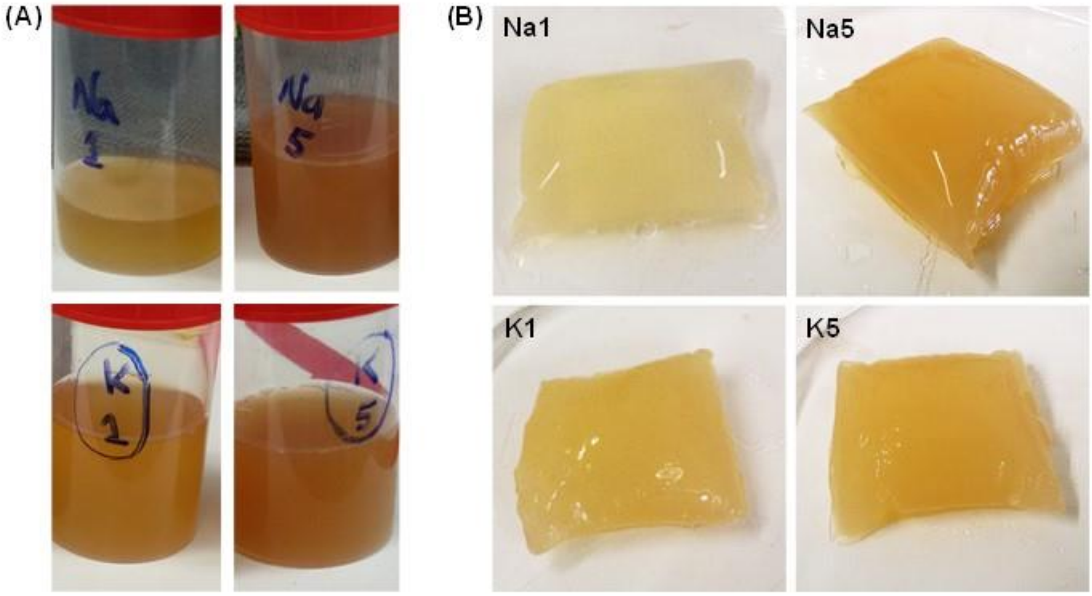

Figure 2.8 — Photographs of: (A) the CGC solutions obtained by the freeze-thaw procedure in the alkali solvent systems: NaOH 1 mol/L (Na1 hydrogel) and 5 mol/L (Na5 hydrogel) and in KOH 1 mol/L (K1 hydrogel) and 5 mol/L (K5 hydrogel); (B) the corresponding CGC hydrogels obtained by dialysis of the alkali solutions against deionized water.

As shown in Table 2.4, no sodium was detected in Na1 and Na5 samples, and only traces of potassium (0.14-0.17wt%) were detected in K1 and K5 hydrogels. In the alkali solutions, CGC molecules do not undergo gelation due to the strong ionic forces that promoted their solvation. During the dialysis procedure, the salt ions diffuse from the solutions into the dialysis water. The lack of ions available to promote CGC molecules' solvation results in the reduction of the ionic forces and allows more interaction among the CGC molecules, thus inducing gel formation.

Table 2.4 — Chemical characterization of CGC hydrogels (n.d. – not detected).

Sample	**Polymer Content (wt%)**	**Water content (wt%)**	**Na content (wt%)**	**K content (wt%)**	**Chitin:glucan ratio (%mol)**
CGC	-	-	n.d.	n.d.	29:71
Na1 gel	2.07	97.93	n.d.	-	27:73
Na5 gel	2.28	97.72	n.d.	-	25:75
K1 gel	1.42	98.58	-	0.14	24:76
K5 gel	1.70	98.30	-	0.17	22:78

The chitin:glucan molar ratios in all hydrogels ranged between 22:78 and 27:73 %mol (Table 2.4), which is similar to the composition of the original CGC sample (29:71 %mol) and also to that reported in previous studies (25:75 %mol) [154]. Although a slight reduction of the chitin fraction in the co-polymer hydrogels was noticed in comparison with the original sample, these results show that CGC was effectively dissolved in the alkali solvents used. All hydrogels presented a water content above 90% which is characteristic of this type of structures. Nevertheless, hydrogels prepared by dissolution of CGC in NaOH solutions had a slightly higher polymer content (2.07-2.28wt%) than the ones prepared with KOH (1.42-1.70wt%) (Table 2.4).

2.2.3.2. Morphological characterization

The morphological characteristics of the CGC hydrogels were assessed by cryo-SEM analysis (Fig. 2.9 and 2.10). Fig. 2.9 shows the K-based hydrogels microstructure, which consisted of a complex three-dimensional network made of CGC polymer chains, holding water inside. Both K-based hydrogels, K1 and K5, exhibited homogenous microstructures (Fig. 2.9a and 2.9c). Upon magnification (Fig. 2.9b and 2.9d), some differences of the pore sizes of K1 and K5 hydrogels can be noticed suggesting the influence of KOH concentration on the gels' network formation. Hydrogels prepared with KOH 1 mol/L presented a less compact network with larger pores (Fig. 2.9b) when compared to the hydrogels prepared with KOH 5 mol/L (Fig. 2.9d). A similar microstructure was reported by Nogueira et al. [186] for silk fibroin hydrogels prepared by dissolution in a ternary solvent of $CaCl_2$:CH_3CH_2OH:H_2O followed by dialysis for calcium removal and hydrogel formation.

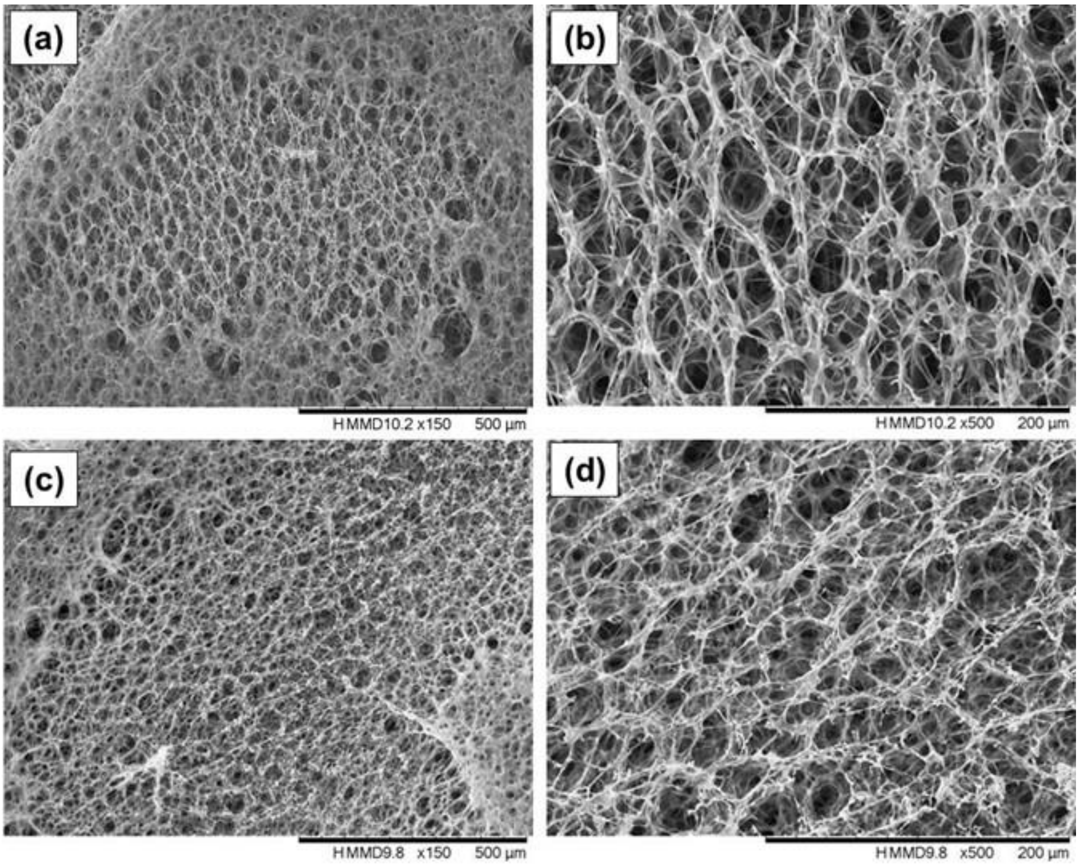

Figure 2.9 — SEM images of the K1 hydrogel prepared with KOH 1 mol/L (a, b) and of the K5 hydrogel prepared with 5 mol/L (c, d). Hydrogels' regions observed under magnification 500× (b, d) were expanded from images presented under magnification 150× (a, c).

The microstructure of the Na-based hydrogels exhibited a more compact and denser network than the ones prepared with KOH (Fig. 2.10a and 2.10c). In addition, they presented heterogeneous and irregular structures. This fact may be explained by the difference in the ionic radius of sodium and potassium atoms. During the hydrogelation process, the sodium atoms may have induced the formation of smaller pores within the hydrogel structure, while the bigger potassium atoms may have allowed the formation of larger pores in the polymeric structure. The NaOH concentration used for CGC dissolution and hydrogel preparation seems to have influenced the microstructure of the formed hydrogels. Na5 CGC hydrogels presented more regions of dense networks (Fig. 2.10c) than the Na1 CGC hydrogels (Fig. 2.10a). Upon magnification, small pores with thick pore walls are detected that explains the tighter microstructure of the hydrogels (Fig. 2.10b and 2.10d). The wide area of dense regions of Na5 CGC hydrogels has limited a clear observation of the pore size (Fig. 2.10d). The porous structure CGC hydrogels present renders them potentially suitable for use in applications such as drug delivery vectors and/or as matrices for cells in tissue engineering.

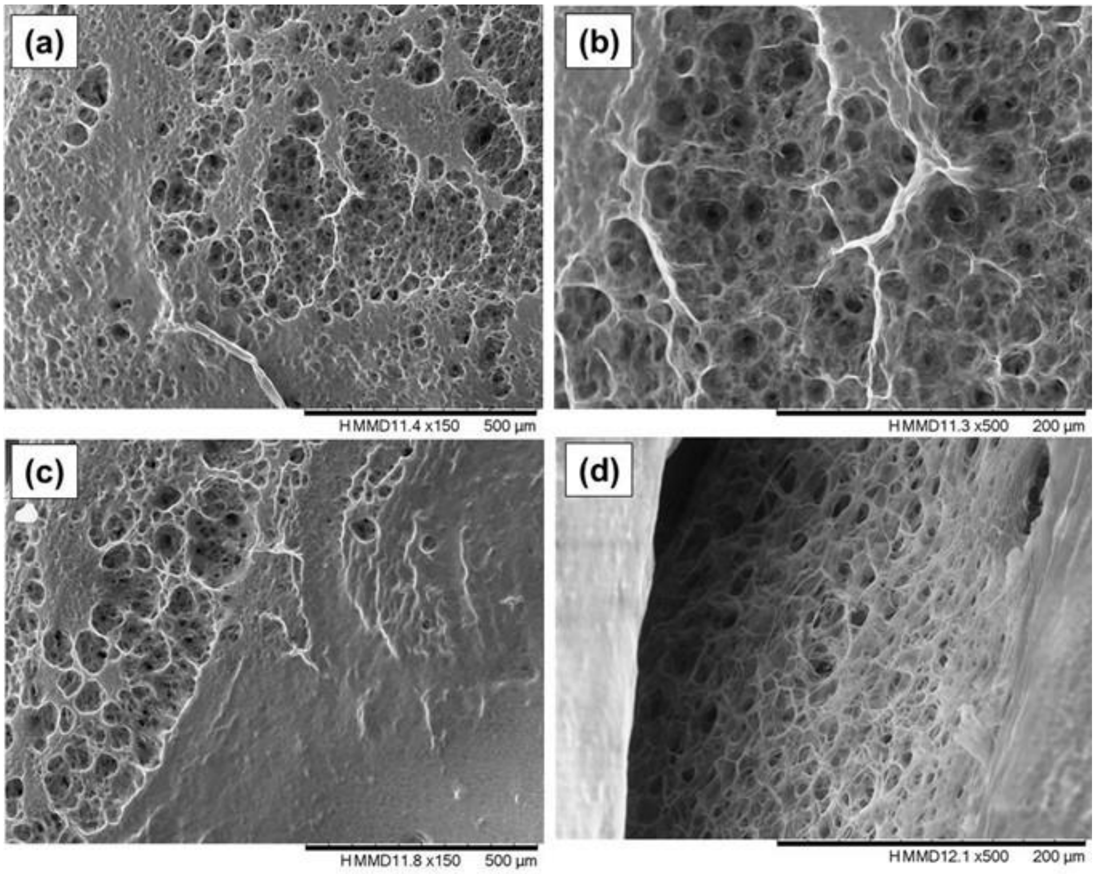

Figure 2.10 — SEM images of the Na1 hydrogels prepared with NaOH 1 mol/L (a, b), and of the Na5 hydrogels prepared 5 mol/L (c, d). Hydrogels' regions observed under magnification 500× (b, d) were expanded from images presented under magnification 150× (a, c).

2.2.3.3. Rheological properties

The mechanical properties of hydrogels are determinant to envisage the functional purposes of these biomaterials. In order to assess those parameters, the viscoelastic properties of CGC hydrogels were studied. As shown in Fig. 2.11, for the two types of CGC hydrogels prepared with either NaOH or KOH as solvent systems, it can be noticed that the storage moduli (G′) exhibited values one order of magnitude higher than the loss moduli (G′′) in the whole range of frequencies. This fact is consistent with the gel-like nature of the samples. Similar profiles were obtained for hydrogels developed using hyaluronic acid (HA) crosslinked with divinyl sulfone [181]. Despite the identical behavior, CGC hydrogels revealed to have improved mechanical properties compared to HA hydrogels. In particular, for the same frequency (0.1 Hz), Na-based CGC hydrogels presented storage moduli values of 389 Pa and 685 Pa (Na1 and Na5, respectively), while for the HA hydrogels G′ lower value was reported (304.30 Pa). On the other hand, lower storage moduli (218 and 270 Pa) were obtained with K1 and K5 CGC hydrogels, respectively. Lower values of G′ indicate that K-based CGC hydrogels exhibited lower elastic properties when stress was applied.

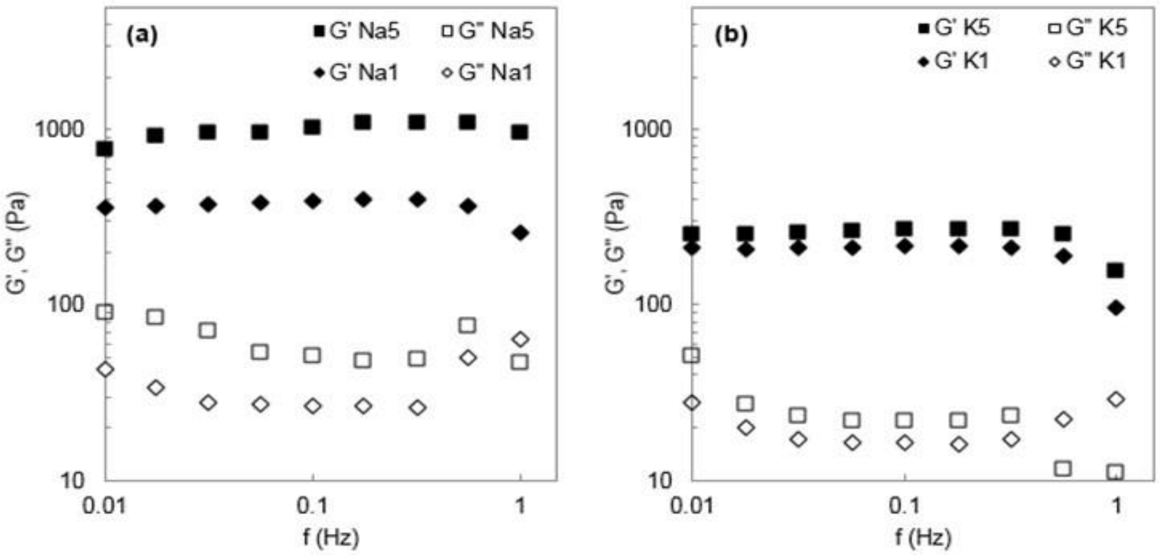

Figure 2.11 — Rheological properties of CGC hydrogels using (a) NaOH (Na1 and Na5 hydrogels) and (b) KOH (K1 and K5 hydrogels). Mechanical spectrum storage (G′, solid symbols) and loss moduli (G′′, open symbols).

As can be observed, CGC hydrogels prepared using NaOH (Fig. 2.11a) exhibited higher dynamic moduli than CGC hydrogels prepared with KOH (Fig. 2.11b), which is related to stronger mechanical properties. This result is in line with the morphology analysis, in which Na-based CGC hydrogels exhibited a denser structure with smaller pores with thicker pore walls (Fig. 2.9 and 2.10). As mentioned above, the characteristics of CGC hydrogels microstructure may be affected by the difference in ionic radius between sodium and potassium atoms.

Additionally, the mechanical spectra of CGC hydrogels shows that as the concentration of alkali solvents used increased, both dynamic moduli increased indicating a stronger structure (Fig. 2.11). In fact, higher values of both moduli, G′ and G′′, were observed for the hydrogels prepared with 5 mol/L when compared to those for 1 mol/L, this fact being more evident for Na-based CGC hydrogels. The observed changes may be related to the higher ionic strength present during the formation of the Na5 and K5 hydrogel structures. In fact, it was reported that ionic strength has a significant impact on hydrogelation and modulation of hydrogels' properties [187]. For example, Martínez-Ruvalcaba and co-workers [188] reported that for the same polymer content in chitosan-xanthan hydrogels (7%), the storage moduli increased around 6 times with the ionic strength of the different dispersion media used, namely distilled water and 0.05 mol/L potassium phosphate monobasic-sodium hydroxide buffer.

The differing properties displayed by the gels obtained under different ionic strength and cations render them potentially suitable for distinct applications: the stiffer structures of the Na-based gels may be used, for example, for the development of tissue scaffolds, while the more elastic K-based gels would be more appropriate for example as wound dressings.

2.2.3.4. Texture profile analysis

Texture profile analysis (TPA) parameters were obtained by applying a 50% strain of the hydrogels' original height in a double compression cycle. The results obtained, including hardness, springiness and cohesiveness, are represented in Fig. 2.12. It may be observed that the hardness, which is related to the maximum force required to cause the selected deformation of the gel [189], was affected by the type of alkali and by the ionic strength of the solvent used to prepare the hydrogels (Fig. 2.12A). Thus, a considerably higher hardness was obtained for the Na5 hydrogels (7229 ± 781 Pa) when compared to Na1 hydrogels (1647 ± 411 Pa), showing that a higher ionic strength favored the formation of a stronger gel in the presence of NaOH. On the other hand, for the K-based CGC hydrogels, the hardness values were similar for both ionic strength values tested (3169 ± 768 and 3423 ± 450 Pa, respectively). Moreover, the hardness of both K-based hydrogels was lower than that of the Na5 hydrogel (Fig. 2.12A).

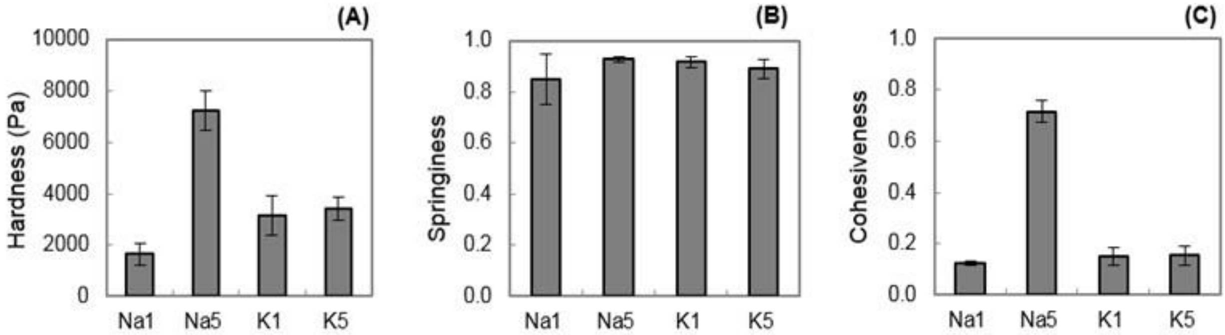

Figure 2.12 — Texture Profile Analysis parameters for hydrogels prepared with NaOH 1 mol/L (Na1) and 5 mol/L (Na5), and with KOH 1 mol/L (K1) and 5 mol/L (K5): (A) hardness, (B) springiness and (C) cohesiveness.

Springiness reflects how well the gel sample physically springs back after it has been deformed during the first compression and has been allowed to wait for a period between compressions [189]. It can be observed that similar values of springiness were obtained for all CGC hydrogels (Fig. 2.12B), which is indicative of elastic behavior, as the fraction of the sample's original height is quite high, in a range of 0.85 to 0.93. Cohesiveness is related to how well the product withstands compression, so that, if a hard product maintains its internal structure without failures when subjected to compression, it would also present a high cohesiveness [189].

This fact was only substantially observed for Na5 hydrogels, presenting a value of 0.716 ± 0.043 (Fig. 2.12C), while the other hydrogels, were much less cohesive. The results suggest that the energy required for the second compression was significantly lower than that for the first compression, indicating that the gel matrix of the Na1 and K-hydrogels was disrupted during the first compression. The low strength of polymer chain molecular interactions may have led to this hydrogel behavior [178].

Concomitantly with the mechanical spectra (Fig. 2.11), the TPA results demonstrate that the ionic strength of the solvent used has more impact on Na-based hydrogels than on K-based hydrogels (Fig. 2.12). Additionally, the Na5 hydrogels presented improved mechanical properties since significantly higher hardness and cohesiveness values were observed.

Several authors reported the improvement of the texture properties of hydrogels by increasing the concentration of the polymer [190,191]. The same strategy could be used to improve the mechanical properties of CGC hydrogels.

2.2.3.5. Cytotoxicity of the CGC hydrogels

The evaluation of CGC hydrogels' cytotoxicity was performed using L929 fibroblasts (International Standard ISO 10993-5:2009(E)). Fig. 2.13 shows the results of the cytotoxicity tests on the CGC hydrogels. The cell viability values on all tested hydrogels are greater than 90%, indicating nearly no cytotoxicity to the fibroblasts (Fig. 2.13). The non-cytotoxicity of the solvent used to prepare the CGC samples (NaOH 1 mol/L) was confirmed by exposing the cells solely to this solvent (Appendix A1). Chang and collaborators [180] have reported similar cytotoxicity results for chitin-based hydrogels towards 293T cells, most probably related to the biological nature of these macromolecules. Similarly, Abdel-Mohsen et al. [192] have demonstrated that chitin/chitosan-glucan complex (ChCsGC) revealed to be non-toxic for mouse fibroblasts cells (NIH-3T3) over all concentrations tested (100 – 1000 µg/mL).

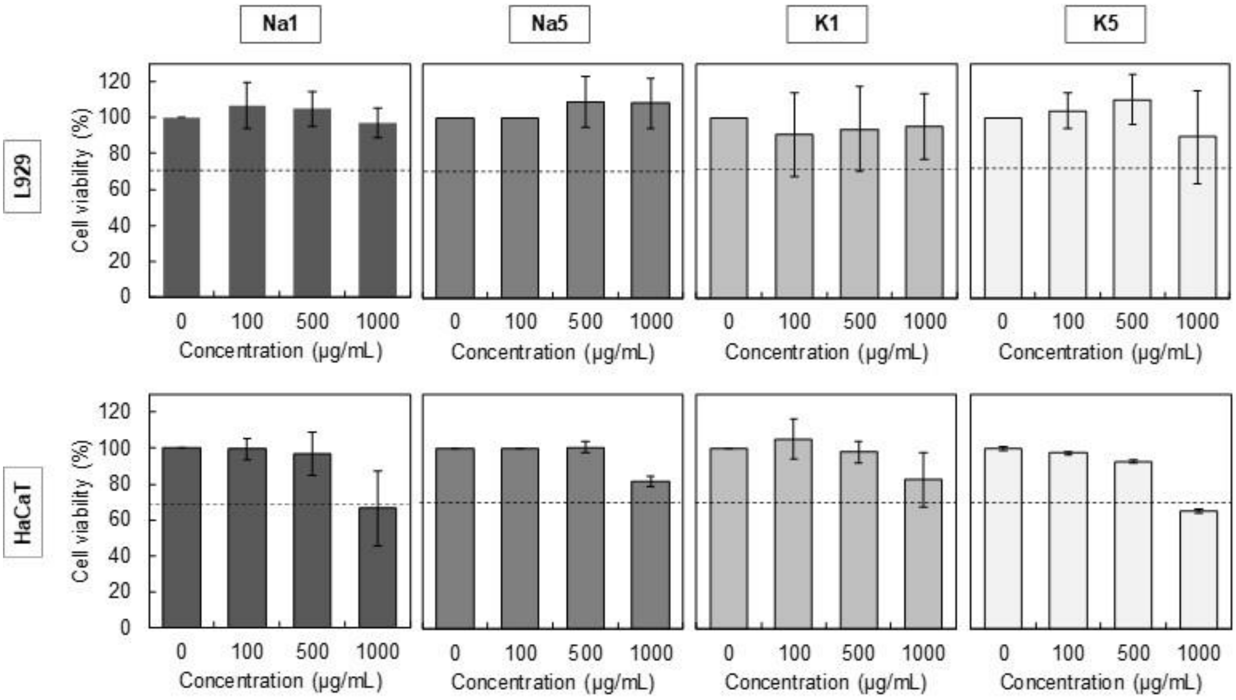

Figure 2.13 — L929 fibroblasts and HaCaT keratinocytes viability when exposed to different concentrations of freeze dried CGC hydrogels dissolved in NaOH 1mol/L, for 24 h. The dotted line at 70% represents the viability limits for non-toxic condition (ISO 10993-5, 2009).

To further evaluate the cytotoxicity of the CGC hydrogels for skin applications, HaCaT keratinocytes cells were used to assess the hydrogels for 24 h. Fig. 2.13 shows the viability of keratinocytes. Compared with the control group, the HaCaT cells exposed to the highest CGC hydrogel concentration (1000 µg/mL) exhibited reduced cellular viability to values around 70%. These results confirm that the CGC hydrogels could be used as an excellent matrix being non-cytotoxic, with potential applications in the field of skin wounds and skin therapies. Biocompatibility of chitin-based hydrogels obtained by various methods has been reported in the literature through *in vitro* cytotoxicity tests [193–195].

2.2.4. Conclusions

This study reported for the preparation of hydrogels based on the yeast biopolymer CGC. It was demonstrated that CGC gels form spontaneously during dialysis of CGC alkali solutions, obtained by the freeze-thaw procedure. The mechanical properties of the CGC hydrogels can be tailored according to the alkali solvent used for CGC dissolution, either NaOH or KOH, and also by changing the solution's ionic strength. Moreover, the best-performing hydrogels in terms of mechanical properties, namely, higher hardness and cohesiveness, were the ones obtained with NaOH 5 mol/L. Due to their non-cytotoxicity, CGC hydrogels are promising materials for use in several biomedical areas. Their characteristics, namely, their porous structure and mechanical properties, support their potential use as drug delivery vectors and/or as matrices for cells in tissue engineering.

2.3. Chitin-glucan complex hydrogels: optimization of gel formation and demonstration of drug loading and release ability

The results shown in this chapter were adapted from:

- **Araújo, D.**, Rodrigues, T., Alves, V.D., Freitas, F. Chitin-glucan complex hydrogels: Optimization of gel formation and demonstration of drug loading and release ability. Polymers 2022, 14, 785. https://doi.org/10.3390/polym14040785.

Summary

Chitin-glucan complex (CGC) hydrogels were fabricated through a freeze-thaw procedure for biopolymer dissolution in NaOH 5 mol/L, followed by a dialysis step to promote gelation. Compared to a previously reported methodology, reducing the number of freeze-thaw cycles from 4 to 1 had no significant impact on the hydrogels' formation, as well as reducing the total freezing time from 48 to 18 h. The optimized CGC hydrogels exhibited a high nearly spontaneous swelling ratio (2528 ± 68 %) and a water retention capacity of 55 ± 3 %, after 2 h incubation in water, at 37 ºC. The hydrogel was loaded with caffeine as a model drug and an enhancement in the mechanical and rheological properties of the hydrogels was achieved. In particular, compressive modulus was improved from 0.23 ± 0.004 to 1.2 ± 0.62 kPa and storage modulus was boosted from 149.9 ± 9.8 to 315.0 ± 76.7 Pa. Although the release profile of caffeine was similar in PBS and NaCl 0.9% solutions, the release rate was influenced by the solutions' pH and ionic strength, being faster in the NaCl solution. These results highlight the potential of CGC based hydrogels as promising structures to be used as drug delivery devices in biomedical applications.

2.3.1. Introduction

Hydrogels are three-dimensional network structures fabricated from synthetic or natural polymers capable of absorbing large amounts of water [177,196,197]. Biopolymer hydrogels have attracted increasing interest due to their biocompatibility, biodegradability, environmentally friendly features, and tissue-mimicking consistency. These interesting characteristics make them suitable materials to be used in a wide range of applications from food and agriculture [44] to cosmetics [45] and biomedicine [198].

Depending on the method used to crosslink the polymer chains, hydrogels can be classified as chemical or physical. Chemical hydrogels are mostly connected through a covalently crosslinked network, in which the addition of crosslinking agents allows the reaction between the functional groups of the polymer chains [43,199]. However, those chemical agents are often toxic compounds, and their presence may promote adverse effects, such as undesirable reactions with bioactive substances or affect hydrogels' biocompatibility [200]. On the other hand, physical hydrogels are synthesized by crosslinking among the polymer chains through non-covalent interactions such as ionic interaction, hydrogen bonds, chain entanglements, Van der Waals forces and hydrophobic interactions [43]. Therefore, physically crosslinked hydrogels, especially biopolymer-based ones, are promising materials to be used in the biomedical field due to the use of mild conditions during their fabrication, and the absence of organic solvents and toxic crosslinking agents [201,202].

Recently, alkali solvents based on NaOH or KOH have emerged as alternative solvents systems for CGC dissolution, through the freeze-thaw method [203]. In this process, the presence of a hydrated alkali component, below the freezing point, promotes the disruption of the polymer chain matrix by breaking inter and intramolecular hydrogen bonds, allowing for polymer dissolution [151]. CGC based physical hydrogels can be obtained by dialyzing the CGC dissolved in the alkali systems. During the dialysis process, gelation is induced by interactions between the CGC molecules that are promoted by the reduction of the ionic forces [150].

In this study, the impact of the number of freeze-thaw cycles and the freezing time on the hydrogel-forming capacity of CGC was evaluated in terms of hydrogels' chemical composition, morphology, and mechanical properties. The optimized CGC hydrogel was characterized according to its rheology, swelling properties, drug loading and drug release capacity.

2.3.2. Materials and Methods

2.3.2.1. Materials

Yeast biomass was obtained by cultivation of the yeast *Komagataella pastoris* (DSM 70877) using glycerol as the sole carbon source, as described by Farinha et al. [154]. CGC was extracted from *K. pastoris* biomass by the hot alkaline procedure described by Araújo et al. [155] and it represented 20wt% of the cell dry mass. CGC presented a chitin content of 35.6% and a DA of 63.4%.

2.3.2.2. Preparation of CGC hydrogels

The CGC hydrogels were prepared as described in section 2.2.2.2, with slight modifications. Briefly, the CGC powder (0.5 g) was dispersed in a NaOH 5 mol/L solution (25 g), and the suspensions were kept at -20 ºC, for either 18 or 48 h. During that period, different number of freeze-thaw cycles were performed, being the thawed suspensions extensively stirred (500 rpm, 1 h), at room temperature in each cycle. After centrifugation (20000 ×g, 30 min, 4 ºC) to eliminate the undissolved material, the hydrogels were prepared by dialyzing the soluble fractions, in deionized water, at room temperature, for 48 h. The obtained hydrogels were labelled according to the solvent system used (NaOH 5 mol/L) and the number of freeze-thaw cycles performed. The hydrogels prepared by freezing during 48 h using 0, 1, 2 or 3 freeze-thaw cycles were identified as $Na5_0$, $Na5_1$, $Na5_2$ and $Na5_3$ hydrogels, respectively, while the hydrogel prepared by 1 freezing cycle of 18 h was coded as $Na5_1$* hydrogel (Table 2.5).

2.3.2.3. CGC hydrogels characterization

2.3.2.3.1. Chemical characterization

The water content of the hydrogels was assessed gravimetrically by freeze drying using equation 2.2.1. The chitin content was determined by elemental analysis as described in equation 2.1.2.

2.3.2.3.2. Morphology, density and porosity

The morphology of the CGC hydrogels was characterized by SEM, as described in section 2.2.2.6, using a magnification of 500×.

The density (ϱ, g/cm^3) of the freeze-dried CGC hydrogels was determined by the following equation: (2.3.1)

$$\rho = \frac{W_{dry}}{V_{dry}} \tag{2.3.1}$$

where W_{dry} and V_{dry} represent the weight (g) and volume (cm^3) of the hydrogel, respectively.

The porosity of the CGC hydrogels was determined using the solvent replacement method [204]. Pre-weighed freeze-dried CGC hydrogels (W_0, g) were immersed in absolute ethanol, for 30 min, in sealed tubes. After 30 min, excess ethanol on the surface was blotted and the samples were weighed. The porosity (%) was calculated using the following equation (2.3.2):

$$Porosity = \frac{W_{30} - W_0}{\rho V_T} \tag{2.3.2}$$

where W_{30} and W_0 represent the hydrogel weight (g) at 30 min and 0 min, respectively, ϱ is the density of ethanol (0.790 g/cm^3) and V_T (cm^3) is the total volume of the hydrogel sample.

2.3.2.3.3. Compressive mechanical analysis

The compressive mechanical properties of the CGC hydrogels were assessed with a texture analyzer TMS-Pro (Food Technology Corporation, England) equipped with a 50 N load cell. Cylindrical hydrogels samples in the wet state (13.8 mm diameter, 0.7-1.1 cm height) were subjected to a compression of up to 80% strain of the samples' original height, at a speed rate of 60 mm/min, using an aluminum plunger with 60 mm diameter. The maximum tension of the compression corresponds to the hardness (kPa) and the toughness (kJ/m^3) was calculated by measuring the area underneath the stress-strain curve of each sample. Compressive modulus (kPa) was obtained as the slope of the initial linear region. All the experiments were performed at room temperature (20±0.2 °C).

2.3.2.3.4. Rheological properties

The rheological properties of the selected hydrogels ($Na5_1$* hydrogels) with a similar thickness (~ 3 mm) were analyzed as described in section 2.2.2.4, with a 1.5 mm gap.

2.3.2.3.5. Swelling and water retention behavior

To assess the swelling properties, pre-weighed cylindrical freeze-dried samples of $Na5_1$* hydrogel were immersed in deionized water, NaCl 0.9% or phosphate buffered saline (PBS), at 37 °C. At different time intervals, samples were carefully taken out from the solutions, blotted with filter paper, and weighed (W_{wet}, g). The swelling ratio (g/g) was determined using the equation (2.3.3):

$$Swelling\ ratio = \frac{W_{wet} - W_{dry}}{W_{dry}} \tag{2.3.3}$$

where W_{dry} (g) represents the initial mass of dry hydrogel.

To evaluate the water retention behavior of the structures, the equilibrated hydrogels were taken out from the solutions and weighed (W_e), after being blotted with a tissue paper. Swollen hydrogels were incubated at 37 °C and weighed (W_t) over time. Water retention (%) was calculated by the equation (2.3.4):

$$Water\ retention = \frac{W_t}{W_e} \times 100 \tag{2.3.4}$$

2.3.2.4. Drug loading

Caffeine (Alfa Aesar, 99%) was used as a model drug to assess the drug loading and drug release behavior of the $Na5_1$* hydrogels. For drug loading, pre-weighed cylindrical freeze-dried hydrogel samples were immersed in a caffeine solution (1.0wt%), for 24 h, at room temperature. After that period, the loaded hydrogels' samples were carefully taken out from the solution, blotted with filter paper, and weighed (W_L, g). Drug loading (DL, g) was determined by the equation (2.3.5):

$$DL = \left(W_L - W_{dry}\right) \times C_{caf} \tag{2.3.5}$$

where W_{dry} (g) represents the initial mass of dry hydrogel and C_{caf} (wt%) corresponds to the concentration of caffeine loading solution.

The entrapment efficiency (EE, %) of caffeine in hydrogels was calculated using the equation (2.3.6):

$$EE = \frac{DL}{W_{caf}} \times 100 \tag{2.3.6}$$

where W_{caf} (g) represents the mass of caffeine available.

2.3.2.5. Characterization of the loaded hydrogels

The $Na5_1$* hydrogels and the caffeine loaded $Na5_1$* hydrogels (coded as $Na5_1$* loaded hydrogels) were chemically characterized by FTIR. The analysis was conducted with a Spectrum II spectrometer (PerkinElmer, Llantrisant, UK), equipped with the attenuated total reflectance (ATR) accessory, and the spectra were obtained between 500 and 4000 cm^{-1} after 10 scans, at room temperature.

The mechanical and rheological properties of Na5$_1$* loaded hydrogels were assessed as described in sections 2.3.2.3.3 and 2.2.2.4, respectively.

2.3.2.6. *In vitro* drug release studies

The freeze-dried Na5$_1$* loaded hydrogels samples were immersed in 100 mL of different physiological media: PBS (pH 7.4) and NaCl 0.9% (pH 5.5), at 37 ºC, for 3 h, under constant stirring (100 rpm). Periodically, 2 mL of the release medium were withdrawn, and 2 mL of fresh medium, preheated at 37 ºC, were added to keep the volume of the solution constant. The caffeine concentration in the withdraw solution was determined by UV-Vis spectrophotometer (CamSpec M509T, Leeds, UK) at 273 nm [205], for a concentration range of 0.16 – 10 mg/L. Caffeine release (%) was obtained by the equation (2.3.7):

$$Caffeine\ release = \frac{C_w \times V}{DL} \times 100 \qquad (2.3.7)$$

where C_w (g/L) is the caffeine concentration in withdraw solution, V (L) represents the volume of the release media, and DL (g) is the amount of loaded drug. The caffeine cumulative release was fitted to the Korsmeyer-Peppas model [206].

2.3.2.7. Statistical analysis

The experimental data from all the studies were analyzed and the results were expressed as mean ± standard deviation (SD). Error bars represent the standard deviation (n ≥ 3).

2.3.3. Results and Discussion

2.3.3.1. Hydrogel formation

The freeze-thaw procedure followed by dialysis, recently reported by Araújo et al. [150], was used to dissolve CGC in NaOH 5 mol/L (freezing at -20 ºC, 4 freeze-thaw cycles, 48 h total freezing time) and prepare CGC hydrogels (labelled as Na5 hydrogels), which exhibited a dense and stiff gel structure. Following those results, the present study aimed at optimizing the procedure by assessing the impact of reducing the number of freeze-thaw cycles and of the freezing time on the hydrogels' properties.

Firstly, the effect of the number of cycles was studied by applying 1, 2, or 3 freeze–thaw cycles (samples $Na5_1$, $Na5_2$, and $Na5_3$, respectively). The procedures' performance was compared to that previously reported for four cycles. An experiment with no freeze–thaw cycles (sample $Na5_0$), in which CGC was simply contacted with the NaOH solution (at room temperature, for 48 h), was also performed for comparison. In this case, a viscous slurry was formed, with very low CGC dissolution, and no hydrogel formation upon dialyzing the supernatant recovered from the mixture. This outcome may be due to the non-deacetylation of chitin that the freeze–thaw procedure induces [203], and consequently, the low dissolution of CGC in the solvent system.

Except for $Na5_0$, all CGC solutions in NaOH 5 mol/L formed hydrogels upon coagulation by dialysis (Fig. 2.14). For the same freezing time (48 h), increasing the number of freeze–thaw cycles, from 1 to 3 cycles, led to a slight decrease in the polymer's content (from 1.68 ± 0.17 to 1.42 ± 0.02wt%, respectively). These results show that a single freeze–thaw cycle is sufficient for CGC gelling and the obtained hydrogels have a higher polymer content. Subsequently, the experiment was repeated for 1 freeze–thaw cycle, but the freezing time was reduced from 48 to 18 h (sample $Na5_1$*). The $Na5_1$ and $Na5_1$* hydrogels, both prepared with 1 freeze–thaw cycle, presented similar polymer content (1.68 ± 0.17 and 1.66 ±0.11wt %, respectively), indicating that freezing time had no significant impact on CGC dissolution in the NaOH solvent system.

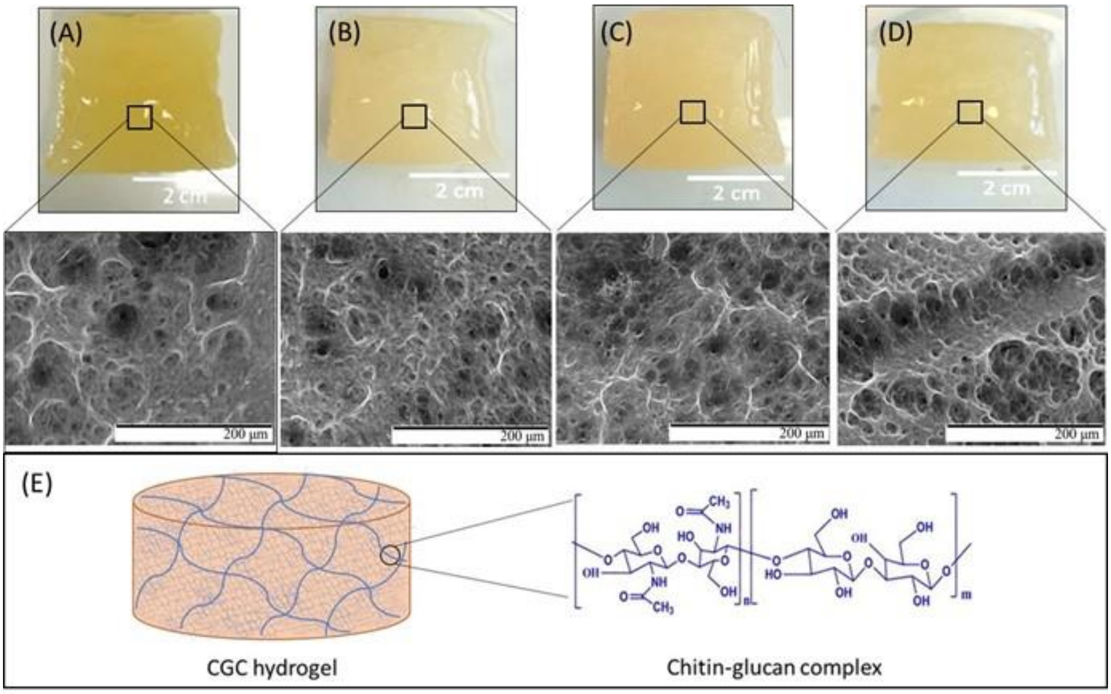

Figure 2.14 — Macroscopic aspect and SEM images of (A) $Na5_1$, (B) $Na5_2$, (C) $Na5_3$, and (D) $Na5_1$* hydrogels under magnification 500×; (E) chemical structure of CGC and schematic representation of the CGC hydrogel.

These results show that the procedure for CGC gelling can be simplified by reducing both the number of freeze–thaw cycles and the total freezing time. All the resulting hydrogels were characterized to evaluate their physicochemical properties and select the most suitable procedure for yielding structures with superior performance.

2.3.3.2. Chemical Characterization of the Hydrogels

Table 2.5 shows the chemical characterization of the CGC hydrogels. It can be observed that all hydrogels exhibited a water content above 98%, characteristic of these structures. No sodium was detected in the hydrogels, demonstrating the efficient removal of the ion from the structure during dialysis.

Table 2.5 — Chemical characterization of CGC hydrogels obtained by different number of freeze–thaw cycles: 1 cycle ($Na5_1$ hydrogel), 2 cycles ($Na5_2$ hydrogel), 3 cycles ($Na5_3$ hydrogel) and 1 cycle with reduced freezing time ($Na5_1$* hydrogel); n.a., data not available.

Samples	**$Na5_1$**	**$Na5_2$**	**$Na5_3$**	**$Na5_1$***	**Na5** [150]
No. of cycles	1	2	3	1	4
Freezing time (h)	48	48	48	18	48
Polymer content (wt %)	1.68 ± 0.17	1.58 ± 0.04	1.42 ± 0.02	1.66 ± 0.11	2.28
Water content (wt %)	98.32 ± 0.17	98.42 ± 0.04	98.58 ± 0.02	98.34 ± 0.11	97.72
Chitin content (%)	25.63 ± 0.78	24.71 ± 2.98	23.85 ± 0.14	21.51 ± 1.49	n.a.

As shown in Table 2.5, the chitin content was similar for all CGC hydrogels, however, a slight decrease was observed as the freezing cycles increased. In fact, the $Na5_1$ hydrogels presented a chitin content of 25.63 ± 0.78%, while the $Na5_3$ hydrogels showed 23.85 ± 0.14% of chitin. Moreover, the $Na5_1$* hydrogels exhibited the lowest chitin content (21.51 ± 1.49%), suggesting that extended freezing time might be required to dissolve the enriched chitin CGC macromolecules in the NaOH solution.

2.3.3.3. Morphological Characterization

As shown in Fig. 2.14, all CGC hydrogels were translucid, presented a yellow coloration and their shape was molded by the dialysis tubing. Furthermore, despite the different approaches applied for their preparation, all hydrogels exhibit similar macroscopic characteristics.

The morphological features of the CGC hydrogels were evaluated by SEM analysis (Fig. 2.14). Similarly to the Na5 hydrogels [150], all structures presented a heterogeneous, compact, and dense three-dimensional network microstructure made of polymeric chains. The porous structures of the obtained hydrogels seem to be slightly affected by the number of freeze–thaw cycles, with the pore size increasing as the number of cycles increases. As shown in Fig. 2.14, the $Na5_3$ hydrogels exhibited a microstructure composed of larger pores when compared to $Na5_1$ hydrogels. This fact might be explained by the lower polymer concentration present in the $Na5_3$ hydrogels (Table 2.5). It has been reported that pore volume and pore size distribution are affected by the polymer content present during hydrogel formation [207]. Indeed, the increasing intermolecular crosslinks and physical entanglements present in hydrogels with high polymer concentrations leads to the formation of smaller pore volumes and pore sizes. Similar results were reported for chitin hydrogels [180], where the average pore size decreased from 8 to 5 μm in diameter as the chitin concentration decreased from 1 to 2wt%.

Additionally, the SEM micrographs demonstrated that reducing the freezing time affected the hydrogels' microstructure (Fig. 2.14). Despite the similar polymer content of the $Na5_1$ and $Na5_1$* hydrogels (1.68 ± 0.17 and 1.66 ±0.11wt%, respectively), the lower freezing time (18 h) applied during preparation of the $Na5_1$* hydrogels induced the formation of microstructures with larger pores. Analogous results were reported by Figueroa-Pizano et al. [208] for chitosan-PVA hydrogels, where those produced with 4 h of freezing time presented larger pores than those formed with 12 h of freezing time.

2.3.3.4. Hydrogels' Porosity and Density

The porosity and density of the hydrogels are significantly dependent on their morphological characteristics and are important parameters for controlling the hydrogels' physicochemical properties and kinetics of drug release [204]. As shown in Fig. 2.15, the porosity values were similar for all CGC hydrogels, ranging from 53.8 ± 10.3 to 62.6 ± 3.9%. Even so, the $Na5_3$ hydrogels presented the highest porosity value (62.6 ± 3.9%) which suggests that the porosity might have increased with increasing number of freeze–thaw cycles. Porosity depends on the size and number of pores per unit of volume. From the SEM micrographs, the pore size is easier to observe, and the structure of the $Na5_3$ hydrogels comprised larger pores than $Na5_1$ and $Na5_2$ (Fig. 2.14), which is consistent with the higher porosity measured. On the other hand, the $Na5_1$* hydrogels exhibited the lowest porosity values (53.8 ± 10.3%), demonstrating that reducing the freezing time might have induced a decrease in the hydrogels' porosity. Overall, the prepared CGC hydrogels exhibited interesting porosity levels that render them suitable for application in areas such as drug delivery [209] and/or tissue engineering [210].

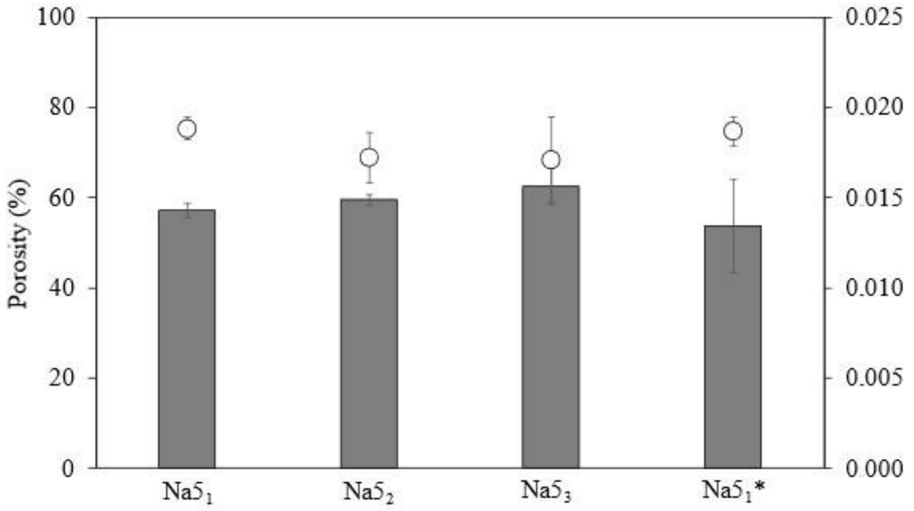

Figure 2.15 — Porosity (▬) and density (○) of the CGC hydrogels.

The density of the CGC hydrogels is shown in Fig. 2.15. It can be observed that the density of the hydrogels slightly decreased with the number of freeze–thaw cycles. Thus, the $Na5_1$ and $Na5_1$* hydrogels exhibited similar density values (0.019 ± 0.001 g/cm^3) and the highest ones. These results are consistent with the higher polymer content present in such hydrogels (Table 2.5), and the resulting increase in the degree of crosslinking observed in the SEM micrographs (Fig. 2.14). Hence, the denser CGC hydrogels ($Na5_1$ and $Na5_1$*) showed the lowest porosity, similar to the results reported for several polymer-based hydrogels, including chitosan [204] and collagen hydrogels [210].

2.3.3.5. Mechanical Properties

The mechanical properties of the CGC hydrogels (Fig. 2.16)—namely, their hardness, compressive modulus, and toughness—were obtained by applying a single compression (80% of the initial height) to wet CGC hydrogel samples. As shown in Fig. 2.16, the mechanical characteristics of the CGC hydrogels were not significantly influenced by the number of freeze–thaw cycles. The compressive stress–strain curves of the CGC hydrogels are represented in Fig. 2.16A. The maximum compressive stress obtained represents the force required to produce the deformation of the hydrogels and corresponds to the hardness value (Fig. 2.16B). It can be observed that similar stress–strain profiles were obtained for all hydrogels, with rupture strain occurring between 50% and 60% for compressive stress values of 80% (Fig. 2.16A). Additionally, identical hardness values were achieved for the $Na5_1$, $Na5_2$, and $Na5_3$ hydrogels (3.55 ± 0.23, 3.85 ±0.38 and 3.69 ± 0.21 kPa, respectively), while higher values were presented by the $Na5_1$* hydrogels (5.04 ± 0.14 kPa). The hardness values obtained were lower than those previously reported for the CGC Na5 hydrogels (7.23 ± 0.78 kPa) [150]. This difference is mainly related to the higher polymer content of those hydrogels (2.28wt%), which increased the crosslinking between the polymer chains and, consequently, improved the hydrogel's mechanical properties [191].

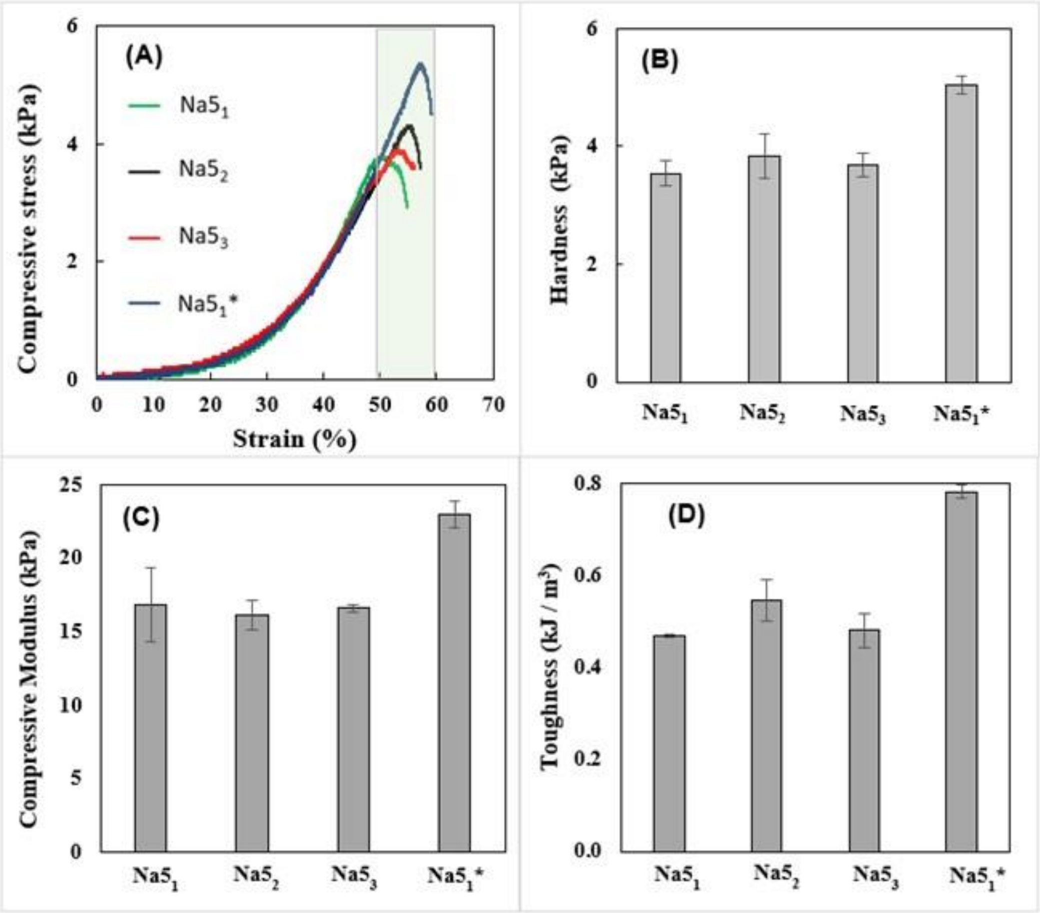

Figure 2.16 — Compressive mechanical properties of the CGC hydrogels compressive stress: (**A**) stress–strain curves, (**B**) hardness, (C) compressive modulus, and (**D**) toughness.

The compressive modulus and toughness of the CGC hydrogels, obtained from the stress–strain curves, are represented in Fig. 2.16C and 2.16D, respectively. As shown in Fig. 2.16C, similar compressive moduli were displayed by the $Na5_1$, $Na5_2$, and $Na5_3$ hydrogels (16.8 ± 2.6, 16.2 ± 1.0, and 16.6 ± 0.3 kPa, respectively), demonstrating that the number of freezing cycles had no significant impact on their stiffness. Nonetheless, the $Na5_1$* hydrogels were the stiffest material, characterized by a considerably higher compressive modulus (23.0 ± 0.89 kPa). As expected, analogous behavior was obtained for the hydrogels' toughness values. Fig. 2.16D shows that the $Na5_1$* hydrogels exhibited the highest toughness value (0.78 ± 0.015 kJ/m^3), while the remaining hydrogel samples displayed values between 0.47 ± 0.003 and 0.55 ± 0.045

kJ/m^3. Despite the similar polymer content, the wispy porous structure of the Na5$_1$* hydrogels might have resulted in higher strength, thus improving their compressive modulus.

Given these results, the Na5$_1$* CGC hydrogels were selected for further characterization, including rheological properties, swelling behavior, and drug delivery capability.

2.3.3.6. Rheological Properties

The viscoelastic properties of the Na5$_1$* hydrogels (Fig. 2.17A) show that the storage modulus (G′) displayed values one order of magnitude higher than the loss modulus (G′′) over the entire range of frequencies, characteristic of their solid-like nature [150]. This behavior also indicates that the hydrogels exhibited predominately elastic characteristics [211]. Analogous behavior and similar G′ and G′′ values (~100 and ~10 Pa, respectively) were obtained for hydrogels prepared with a chitin nanofiber content of 0.4wt%, in the same range of frequency [212]. Recently, Ferreira et al. [143] also described an identical profile for gels prepared with *Aspergillus niger* CGC dissolved in ILs. However, those gels presented higher values of both dynamic moduli which might be explained by the presence of ILs in the gel structure.

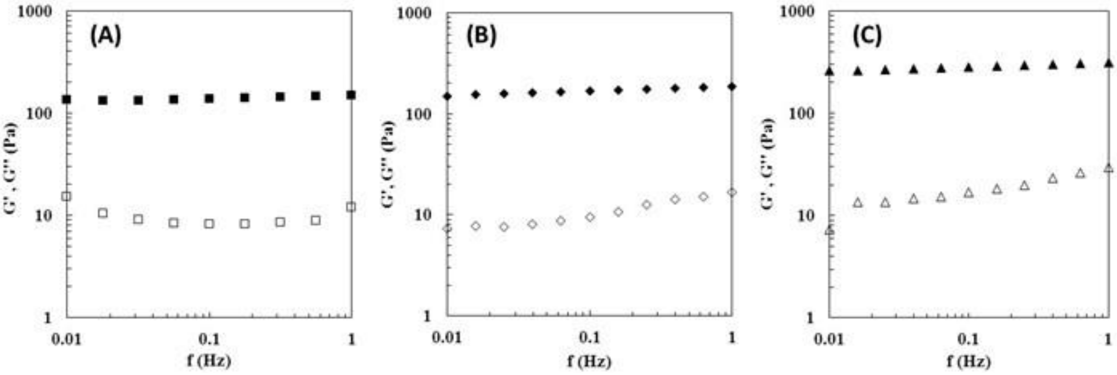

Figure 2.17 — Rheological properties of the (**A**) Na5$_1$* hydrogel, (**B**) Na5$_1$* rehydrated hydrogel, and (**C**) Na5$_1$* caffeine loaded hydrogel, at 25 °C. Mechanical spectrum storage (G′, solid symbols) and loss moduli (G′′, open symbols).

A similar profile was reported for the CGC Na5 hydrogels [150], however, this hydrogel presented significantly higher values for both G′ and G′′. In particular, for the same frequency (0.1 Hz), the Na5$_1$* hydrogel presented a G′ of 136.8 ± 11.1 Pa, while a higher value (685 Pa) was found for the Na5 hydrogel. This fact is explained by the increased polymer content of the Na5 hydrogels (2.28wt%) compared to the Na5$_1$* hydrogels (1.66wt%), which directly improve their rheological properties.

2.3.3.7. Swelling Behavior and Water Retention Kinetics

The hydrogels' water absorption capacity (swelling behavior) directly affects their drug loading and delivery capability [213]. The swelling ratio of the CGC hydrogels in the different tested media (PBS, NaCl 0.9%, and deionized water) at 37 °C is shown in Fig. 2.18A. For the three tested media, the $Na5_1$* hydrogels displayed excellent water absorption capacity, reaching the swelling equilibrium immediately (less than 1 min). This can be explained by the high hydrophilicity of CGC macromolecules that possess numerous hydrophilic groups, namely, hydroxyl and amino groups, capable of establishing hydrogen bonds with the water molecules [214].

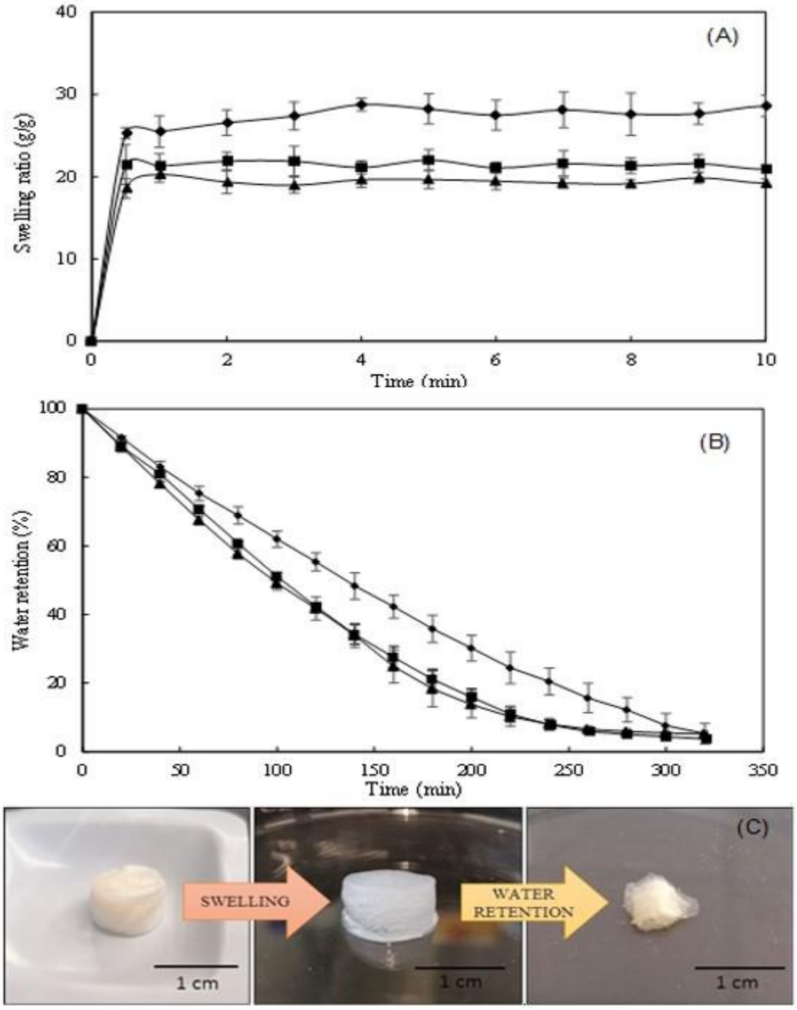

Figure 2.18 — Swelling behavior of (**A**) $Na5_1$* hydrogels in PBS (■), NaCl 0.9% (▲) and deionized water (◆), water retention kinetics of (**B**) water-swollen hydrogels, at 37 °C, and (**C**) macroscopic aspect of hydrogels after the two processes.

It can be noticed that the swelling capacity of the $Na5_1$* hydrogel was slightly higher in deionized water than in the other tested media (Fig. 2.18A). Indeed, after 30 s, the hydrogel placed in water reached a swelling ratio of 25.3 ± 0.28 g/g, while lower values were obtained in PBS and NaCl 0.9% (21.5 ± 2.42 and 18.6 ± 1.20 g/g, respectively), for the same period. This fact is probably related to the higher ionic strength of the PBS and NaCl 0.9% solutions, which decreases the swelling ability of polyelectrolyte hydrogels, due to the decreased osmotic pressure difference between the hydrogel structure and the solution [215].Significantly lower values were reported by Wu et al. [216] and Udeni Gunathilake et al. [217] for chitin-based hydrogels (~6 g/g) and chitosan-based hydrogels (4.1 g/g), respectively. In fact, the nearly spontaneous swelling of $Na5_1$* hydrogels renders them a sponge-like behavior which might enhance the drug loading capacity [218]. Interestingly, as shown in Fig. 2.18C, despite their high swelling ratio, the size of the hydrogels remained similar upon swelling in all the tested media.

The water retention kinetics of the $Na5_1$* hydrogels are shown in Fig. 2.18B. It can be observed that after placing at 37 °C for 320 min, over 95% of their water content was evaporated and the hydrogels considerably reduced their volume (Fig. 2.18C).

Additionally, the water-swollen hydrogels exhibited a lower water loss rate than those swollen in PBS or NaCl 0.9% (Fig. 2.18B). The largest difference was noticed after 160 min, where the water-swollen hydrogels still had retained 42% of their initial water content, while the PBS- and NaCl-swollen hydrogels had only kept 27% and 25%, respectively. The faster evaporation of water in these hydrogels may indicate the presence of higher levels of free water in their structures since free water has the highest mobility and is the first to evaporate [219].

The macroscopic aspect of water-swollen hydrogels is shown in Fig. 2.18C. It was observed that the visual characteristics of the hydrogel swollen in all three tested media were similar, with all hydrogels showing a white color.

2.3.3.8. Hydrogels Loading and Release Ability

2.3.3.8.1. Loading Na51* Hydrogels with Caffeine

The $Na5_1$* hydrogels were loaded with caffeine as a model drug (Fig. 2.19). The procedure involved soaking the freeze-dried structures with a caffeine solution (1.0wt%). The resulting loaded $Na5_1$* hydrogels were opaque with a whitish color and their dimensions remained similar to those before soaking.

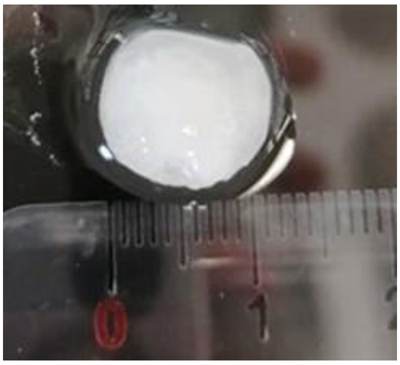

Figure 2.19 — Macroscopic aspect of $Na5_1$* hydrogels loaded with caffeine.

The entrapment efficiency of caffeine in the $Na5_1$* hydrogels was found to be 13.24 ± 1.03%, with caffeine representing 1.01 ± 0.03% of the total weight of the wet hydrogel. This result is lower than the values reported in the literature for caffeine entrapment in cellulose-based hydrogel membranes (100%) [205] and β-glucans microparticles (96.52 ±0.63%) [220]. This low EE% might be explained by the chemical structure of caffeine, which in water tends to protonate, and by the lower acetylation degree of the N-acetyl-glucosamine monomers of CGC. In fact, it was reported that the use of alkali solvent systems and freeze–thaw cycles promote the deacetylation of CGC chitin molecules [203]. The $Na5_1$* hydrogels presented a degree of acetylation of 27.93 ± 2.82%, which indicates that chitin was converted into chitosan. Thus, the interactions between protonated caffeine and positively charged deacetylated chitin groups lead to repulsion due to similar charges. Similar behavior was reported for nanocarriers of chitosan where a caffeine entrapment efficiency of 17.25 ± 1.48% was observed [221].

2.3.3.8.2. Characterization of the $Na5_1$* Loaded Hydrogels

The presence of caffeine in the $Na5_1$* hydrogel was detected by FTIR analysis. Fig. 2.20 shows the FTIR spectra of caffeine, the $Na5_1$* hydrogel, and the $Na5_1$* loaded hydrogel. The caffeine spectrum (Fig. 2.20A) displayed the typical bands of heterocyclic compounds, namely, at 3115 and 2952 cm^{-1} which depict the stretching of C-H bonds. The absorption peaks at 1697 and 1650 cm^{-1} are characteristic of the carbonyl group (C = O) of amide I and the additional adsorption peak at 1549 cm^{-1} can be attributed to amide II [222].

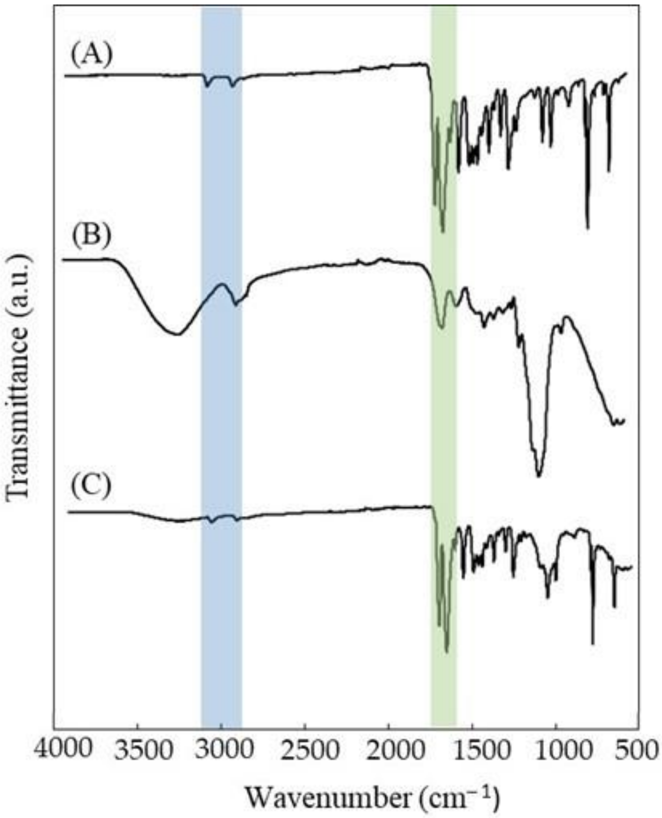

Figure 2.20 — FTIR spectra of (**A**) caffeine, (**B**) $Na5_1$* hydrogels, and (**C**) $Na5_1$* loaded hydrogels.

As expected, the $Na5_1$* hydrogel spectrum (Fig. 2.20B) is similar to the previously reported CGC spectrum [203], presenting a characteristic broad and intense band between 3000–3500 cm^{-1}, typical of the O-H stretching of hydroxyl groups, which overlaps the stretching peaks of N-H. The C-H stretching corresponding to CH_3 and CH_2 appeared at wavenumbers 2919 and 2852 cm^{-1} respectively. The small peaks characteristics of β-1,3-glucans are noticed at 890, 1156, and 1370 cm^{-1} while β-1,6-glucans are represented by peaks at 922, 1045, and 1730 cm^{-1}. The incorporation of caffeine in the hydrogel structure led to a general decrease in the intensity of $Na5_1$* hydrogel spectrum bands, namely the O-H band around 3400 cm^{-1} and the C-O stretching of the saccharide structure at 1020 cm^{-1} (Fig. 2.20C). This impact on the band's intensity might be explained by the high content of caffeine in the hydrogel structure (30.58 ± 4.28%, on a dry basis). Furthermore, peaks appearing at 3113 and 2955 cm^{-1} (heterocyclic compounds), 1697 and 1650 cm^{-1} (amide I) confirm the presence of caffeine, indicating a successful loading. Similar results were reported in several studies where caffeine was encapsulated in alginate beads [222] and chitosan nanoliposomes [223].

The effect of dehydration and the presence of caffeine on the mechanical and rheological properties of the $Na5_1$* hydrogels are presented in Table 2.6. Both the rehydration of the freeze-dried structure and its loading with caffeine apparently improved the mechanical parameters of the $Na5_1$* hydrogels, in particular the compressive modulus, which increased significantly from 23.0 ± 0.89 to 38.06 ± 4.46 and 120.0 ± 61.64 kPa, respectively, thus demonstrating that caffeine increased the structure's rigidity. Consequently, the rehydrated and the caffeine-loaded hydrogels presented higher toughness (1.67 ± 0.09 and 1.8 ± 0.33 kJ/m^3, respectively) and hardness (11.50 ± 0.58 and 15.6 ± 2.53 kPa, respectively) values than the original $Na5_1$* hydrogel (0.78 ± 0.01 kJ/m^3, 5.04 ± 0.14 kPa, respectively). These results suggest that the freeze-drying process reinforces the hydrogel structure, thus inducing a more rigid structure upon rehydration. It is attributed to an increase of interactions (hydrogen bonds) between macromolecules upon drying, forming pore walls made of a more tightly packed and ordered hydrogen-bonded network structure, similar to what is referred when producing polysaccharide films by solution casting and drying [224]. Loading caffeine into the same structures further strengthened the hydrogel's network and endows enhanced mechanical properties. According to the literature [225], caffeine molecules are able to bind to saccharide molecules (e.g., glucose), which may promote the observed reinforcement of the hydrogel pore walls. Though, the nature of caffeine interactions with the polymeric CGC is likely to be more complex than simple hydrophobic binding. Further studies (e.g., NMR) would be needed to fully characterize CGC-caffeine bonds.

Table 2.6 — Effect of caffeine on the mechanical and rheological properties of the $Na5_1$* hydrogel.

	Sample	**$Na5_1$* Hydrogel**	**$Na5_1$* Rehydrated Hydrogel**	**$Na5_1$* Loaded Hydrogel**
Mechanical properties	Compressive modulus (kPa)	23.0 ± 0.89	38.06 ± 4.46	120.0 ± 61.64
	Toughness (kJ/m^3)	0.78 ± 0.01	1.67 ± 0.09	1.8 ± 0.33
	Hardness (kPa)	5.04 ± 0.14	11.50 ± 0.58	15.6 ± 2.53
Rheological properties	Storage modulus$_{1\ Hz}$ (G', Pa)	149.9 ± 9.8	186.8 ± 22.0	315.0 ± 76.7
	Loss modulus$_{1\ Hz}$ (G'', Pa)	11.9 ± 0.5	16.8 ± 2.5	29.3 ± 8.4

In the same way, the rheological properties of hydrogels were also improved by the presence of caffeine within the structure (Table 2.6, Fig. 2.17C). The $Na5_1$* rehydrated and the loaded hydrogels presented a rheological profile similar to the original $Na5_1$* hydrogels, exhibiting a predominant elastic behavior (Fig. 2.17B and 2.17C). This fact shows that rehydration of the freeze-dried hydrogels and the incorporation of caffeine into their structure had no significant impact on the viscoelastic degree of the structure and the crosslinked network remained homogenous [211]. As a solid-like structures, the storage moduli values were one order of magnitude higher than the loss moduli values (Fig. 2.17). Nevertheless, both the rehydration process and caffeine loading increased the storage and the loss moduli, which is consistent with the observed enhanced mechanical properties. As demonstrated in Table 2.6, at a frequency of 1 Hz, G′ value was improved from 149.9 ± 9.8 to 186.6 ± 22.0 Pa and 315.0 ± 76.7 Pa and values of G′′ increased from 11.9 ± 0.5 to 16.8 ± 2.5 and 29.3 Pa, for rehydrated and loaded hydrogels, respectively. The strengthening of hydrogels network of polycapro-lactone-co-lactide (PCLA) by loading certain drugs into the structure was reported by Prince et al. [226]. Additional linkages promoted polymer-polymer interactions which increased G′ values and new polymer–drug interactions that raised G′′ values.

2.3.3.8.3. Release of Caffeine from the $Na5_1$* Hydrogels

The caffeine release profile of the $Na5_1$* loaded hydrogels was essayed in PBS (pH 7.4) and NaCl 0.9% (pH 5.5), at 37 °C (Fig. 2.21). It can be observed that a similar caffeine release profile was obtained for both media, comprising an initial phase where caffeine was rapidly released (burst phase) followed by a second phase where a steady slower release was achieved. The initial burst can be explained by the release of caffeine loaded close to the surface of the hydrogel [227,228]. Moreover, the maximum caffeine released achieved was similar in both PBS and NaCl 0.9% solutions (98.7 ± 1.6 and 96.3 ± 8.0%, respectively), which might be explained by the similar swelling behavior of $Na5_1$* hydrogels in each media (Fig. 2.18A).

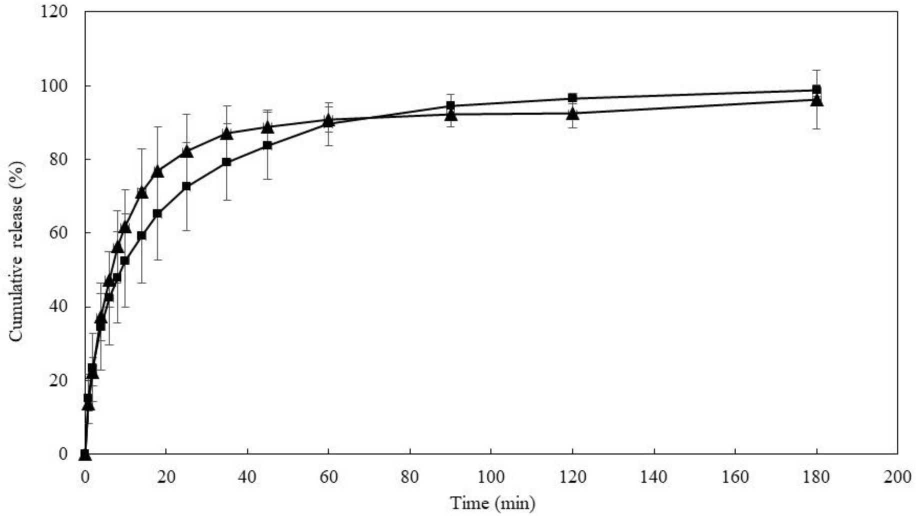

Figure 2.21 — Caffeine release profile of $Na5_1$* hydrogel in PBS (■) and NaCl 0.9% (▲), at 37 °C.

However, it can be noticed that the release of caffeine from the hydrogel was slightly faster in NaCl 0.9% solution than in PBS solution. In the NaCl 0.9% solution, 50% of the loaded caffeine was release in the first 6 min, whereas in PBS solution it took 10 min to reach the same release. This behavior might be related to the difference in pH of the solutions that might have affected the solubility of caffeine [229]. Due to its alkalinity, caffeine solubility is enhanced by low pH values, which explains its rapid release rate in NaCl solution (pH 5.5). Additionally, the slightly higher ionic strength of the NaCl 0.9% solution promoted a faster release of caffeine due to decreased osmotic pressure within the hydrogel structure and weakened interactions between caffeine and polymer [230].

The mechanism of caffeine release from hydrogels is predominantly controlled by diffusion [231]. To evaluate the caffeine release kinetics from $Na5_1$* loaded hydrogels, the first 60% of the released caffeine were analyzed using the Korsmeyer–Peppas model [206], according to the equation (2.3.8):

$$\frac{M_t}{M_\infty} = kt^n \tag{2.3.8}$$

where M_t and M_∞ represent the amount of caffeine (g) released at time t and infinite time, respectively, *k* is the kinetic constant and *n* is an empirical parameter for the release mechanism. According to this model, the diffusion mechanism can be classified as controlled diffusion (Fickian diffusion), anomalous transport (non-Fickian diffusion) and controlled swelling, as a function of the relationship between the diffusion rate and the polymer relaxation process [206,232]. For cylinder samples, a value of $n \leq 0.45$ indicates a Fickian diffusion, $0.45 \leq n \leq 0.89$ is a non-Fickian diffusion and $n \geq 0.89$ represents a relaxation-controlled diffusion. Plotting ln (Mt/M∞) vs. ln (t), the kinetic parameters *n* and *k* can be calculated from the slope and the interception, respectively.

As shown in Fig. 2.22, the kinetic parameters obtained in the PBS solution (*n*=0.52 and *k*=0.26) and in a NaCl 0.9% solution (*n*=0.69 and *k*=0.24) revealed that both release profiles followed a non-Fickian mechanism of diffusion, where the drug diffusion rate and the polymer relaxation process are relevant to the drug release rate [211,232]. The results obtained revealed that drug release from $Na5_1$* hydrogels is not only dependent on the physicochemical properties of the loaded drug but also on the properties of the medium used to release the drug.

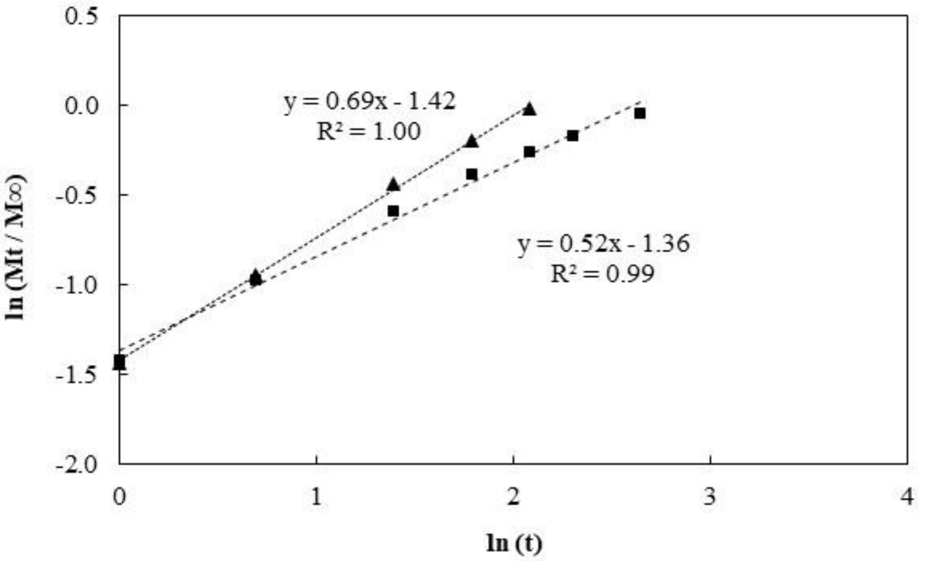

Figure 2.22 — Plot of ln (Mt/M∞) vs. ln (t) for the caffeine release from $Na5_1$* loaded hydrogels in PBS (■) and NaCl 0.9% (▲) solutions, following the Korsmeyer‑Peppas model.

2.3.4. Conclusions

The procedure for preparing CGC hydrogels comprising polymer dissolution in NaOH by the freeze–thaw method, followed by coagulation by dialysis of the obtained aqueous solution, was optimized by reducing the number of freeze–thaw cycles and the total freezing time. The optimized methodology resulted in CGC hydrogels with improved rheological, mechanical, and swelling properties, which were assayed for their ability for caffeine loading. The loaded hydrogels displayed improved mechanical and rheological properties, with caffeine release profiles following a non-Fickian diffusion mechanism in PBS and NaCl 0.9% solutions. Therefore, this study demonstrated that CGC can be processed into hydrogels by a simple procedure and the resulting structures possess suitable properties for their use as drug delivery systems.

2.4. Chitin-glucan complex hydrogels: physical-chemical characterization, stability *In vitro* drug permeation, and biological assessment in primary cells

The results shown in this chapter were adapted from:

- **Araújo, D.,** Rodrigues, T., Roma-Rodrigues, C., Alves, V.D., Fernandes, A.R., Freitas, F. Chitin-glucan complex hydrogels: Physical-chemical characterization, stability, *in vitro* drug permeation and biological assessment in primary cells. Polymers 2023, 15, 791. https://doi.org/10.3390/polym15040791.

Summary

Chitin-glucan complex (CGC) hydrogels were fabricated by coagulation of the biopolymer from an aqueous alkaline solution, and their morphology, swelling behavior, mechanical, rheological, and biological properties were studied. In addition, their *in vitro* drug loading/release ability and permeation through mimic-skin artificial membranes (Strat-M) were assessed. The CGC hydrogels prepared from 4 and 6wt% CGC suspensions ($Na5_1{}^{*4}$ and $Na5_1{}^{*6}$ hydrogels, respectively) had polymer contents of 2.40 ± 0.15 and 3.09 ± 0.22wt%, respectively, and displayed a highly porous microstructure, characterized by compressive modulus of 39.36 and 47.30 kPa and storage modulus of 523.20 and 7012.25 Pa, respectively. Both hydrogels had a spontaneous and almost immediate swelling in aqueous media, and a high-water retention capacity (>80%), after 30 min incubation, at 37 °C. Nevertheless, the $Na5_1{}^{*4}$ hydrogels had higher fatigue resistance and slightly higher-water retention capacity. These hydrogels were loaded with caffeine, ibuprofen, diclofenac, or salicylic acid, reaching entrapment efficiency values ranging between 13.11 ± 0.49% for caffeine, and 15.15 ± 1.54% for salicylic acid. Similar release profiles in PBS were observed for all tested APIs, comprising an initial fast release followed by a steady slower release. *In vitro* permeation experiments through Strat-M membranes using Franz diffusion cells showed considerably higher permeation fluxes for caffeine (33.09 $\mu g/cm^2/h$) and salicylic acid (19.53 $\mu g/cm^2/h$), compared to ibuprofen sodium and diclofenac sodium (4.26 and 0.44 $\mu g/cm^2/h$, respectively). Analysis in normal human dermal fibroblasts revealed that CGC hydrogels have no major effects on the viability, migration ability and morphology of the cells. Given their demonstrated features, CGC hydrogels are very promising

structures, displaying tunable physical properties, which support their future development into novel transdermal drug delivery platforms.

2.4.1. Introduction

Hydrogels are hydrophilic structures with the ability to absorb large amounts of water inside their three-dimensional polymeric network [196,233].

Polysaccharides emerged as very promising materials for the fabrication of hydrogels due to their nontoxicity, biocompatibility, biodegradability, and affordability [127,234]. Polysaccharide-based hydrogels have demonstrated great potential as delivery platforms for controlled drug delivery [235,236]. As drug delivery systems, polysaccharide-based hydrogels present improved functionalities such as stimuli-responsiveness, sustained drug release, target specificity, and therapeutic efficacy [237,238].

CGC hydrogels can be fabricated by polymer coagulation from an alkali solution [150,239]. The procedure involves CGC dissolution in alkali solvent systems based on NaOH, to which freeze-thaw cycles are applied. CGC-based physical hydrogels spontaneously form during dialysis of the CGC alkali solution in water. This methodology was optimized in terms of freeze-thaw cycles and total freezing time, thus reducing the overall hydrogel preparation procedure time without impacting on their physical properties. The resulting CGC-based hydrogels were evaluated as a drug delivery system, using caffeine as a model drug (Section 2.3).

In this study, the procedure was further optimized by increasing the CGC concentration used for hydrogel fabrication, whose morphology, mechanical and rheological properties were assessed. Furthermore, the hydrogels' drug loading and release were studied, and permeation studies were performed to evaluate the potential of CGC hydrogels to be used as topical or transdermal delivery platforms.

2.4.2. Materials and Methods

2.4.2.1. Materials

CGC with a chitin content of 35.6% was extracted from the yeast *Komagataella pastoris* (DSM 70877) produced as described by Araújo et al. [155]. Caffeine (99%), diclofenac sodium salt (98%), ibuprofen sodium salt (98%), and salicylic acid (99%) were purchased from Alfa Aesar, Tokyo Chemical Industry Co, Sigma-Aldrich, and BDH, respectively.

2.4.2.2. Preparation of the CGC hydrogels

The CGC hydrogels were prepared as described in section 2.3.2.2, with slight modifications. Briefly, the CGC powder was dispersed in a NaOH 5 mol/L solution, at two biopolymer concentrations (4 and 6wt%), and the suspensions were kept at -20 ºC. After that, the samples were thawed, extensively stirred (500 rpm, 1 h), at room temperature, and frozen again at -20 ºC until achieving a total freezing time of 18 h. The undissolved fraction was removed from the suspensions by centrifugation (at 40 000 or 60 000 ×*g* for the 4 and the 6wt% solutions, respectively), for 30 min, at 8 ºC. The hydrogels were obtained by coagulation of the biopolymer during dialysis (12–14 kDa MWCO membranes, Spectra/Por®, Spectrum Laboratories Inc., Piscataway, NJ, USA) of the alkali solutions, against deionized water, as described in section 2.2.2.2. The hydrogels prepared with 4 and 6wt% were labelled as $Na5_1{}^{*4}$ and $Na5_1{}^{*6}$ hydrogels, respectively.

2.4.2.3. CGC hydrogels characterization

2.4.2.3.1. Chemical characterization

The water content of the hydrogels was assessed gravimetrically by freeze drying using the equation 2.2.1. The chitin content was determined by elemental analysis following equation 2.1.2.

2.4.2.3.2. Morphology, density and porosity

The morphology of the $Na5_1{}^{*4}$ and $Na5_1{}^{*6}$ hydrogels were analyzed by SEM, as described in section 2.2.2.6, using magnifications of 500× and 1500×.

The hydrogels' density and porosity were assessed gravimetrically and by the solvent replacement method, respectively as described in section 2.3.2.3.2.

2.4.2.4. Compressive mechanical analysis

The compressive mechanical properties of the CGC hydrogels were evaluated with a texture analyzer TMS-Pro (Food Technology Corporation, Slinfold, West Sussex, UK) equipped with a 50 N load cell. The uniaxial compressive tests were performed as described in section 2.3.2.3.3. The hysteresis test was performed by compressing the cylindrical hydrogel samples in loading cycles to a maximum compression of 50% strain, with a speed rate of 60 mm/min and unloading at the same rate. The dissipation energy was calculated by measuring the area between the loading–unloading curves. To prevent water evaporation during the test, a thin layer of paraffin oil was applied to the hydrogel surface. All the experiments were performed at room temperature (20 ± 0.2 ºC).

2.4.2.5. Rheological properties

The rheological properties of the samples were analyzed as described in section 2.2.2.4.

2.4.2.6. Swelling and water retention behavior

The swelling ability and the water retention behavior of the $Na5_1{}^{*4}$ and $Na5_1{}^{*6}$ hydrogels were determined gravimetrically, as described in section 2.3.2.3.5.

2.4.2.7. Preparation of API-Loaded CGC Hydrogels

The $Na5_1{}^{*4}$ hydrogels were individually loaded with four different APIs, namely, caffeine, diclofenac, ibuprofen, and salicylic acid by diffusion method. Given the different water solubilities of the four APIs, solutions of 1.0wt% caffeine, 0.1wt% diclofenac, 1.0wt% ibuprofen, and 0.1wt% salicylic acid were prepared. For API loading, pre-weighed cylindrical freeze-dried hydrogel samples were immersed in the corresponding solution, for 24 h, at room temperature. After that period, API-loaded hydrogel samples were removed from the solutions, blotted with filter paper, and weighed (W_L, mg). Drug loading (DL, mg_{API}/cm^3) and entrapment efficiency (EE, %) were calculated with equations (2.4.1) and (2.4.2) [205,240] as follows:

$$DL = \frac{(W_L - W_{dry}) \times C_{API}}{V} \tag{2.4.1}$$

$$EE = \frac{W_{loaded}}{W_{API}} \times 100 \tag{2.4.2}$$

where W_{dry} (g) represents the initial mass of dry hydrogel, C_{API} (wt%) corresponds to the concentration of the API solution, W_{loaded} is the API-loaded weight, and W_{API} (g) represents the mass of API available.

2.4.2.8. *In Vitro* Drug Release Studies

Drug release studies were performed by immersion of cylindrical freeze-dried API loaded hydrogels in 100 mL of PBS (pH 7.4), at 37 ºC, for 4 h, under constant stirring (100 rpm). At predetermined time intervals, samples of 2 mL of the receptor medium were withdrawn and the same volume was replaced with a fresh and preheated medium. APIs concentrations in the withdrawn solution were determined by UV-Vis spectrophotometer (CamSpec M509T, Leeds, UK), at a wavelength of 273 nm for caffeine, 275 nm for diclofenac, 264 nm for ibuprofen, and 296 nm for salicylic acid. The APIs' cumulative release values were fitted to the Korsmeyer–Peppas model, according to equation 2.3.8.

2.4.2.9. *In Vitro* Drug Permeation Studies

The drug permeation studies were performed using a Franz diffusion cell (PermeGear Inc., Hellertown, PA, USA) with a 3.14 cm^2 diffusion area and a receptor volume of 10 mL. Strat-M membranes (Merck Millipore, Darmstadt, Germany) were used as skin-mimic artificial membranes. Prior to the diffusion experiments, the membranes were soaked in PBS (pH 7.4), at room temperature, for 12 h. After that period, the membranes were placed between the donor and the receptor compartments, and the latter was filled with PBS. The system was maintained under constant magnetic stirring (500 rpm), and the temperature was controlled at 37 ºC by a circulating water bath.

In each experiment, a cylindrical API-loaded hydrogel sample (1.7 cm diameter; 0.3–0.5 cm thickness) was applied to the membrane. To minimize evaporation, the donor compartment and sampling port were occluded with parafilm. Periodically, a 400 µL sample was collected from the receptor compartment, and the same volume was replaced with a fresh and preheated receptor solution. Ibuprofen, caffeine, and diclofenac concentrations in the withdrawn solution were determined by HPLC (Dionex Summit, Sunnyvale, CA, USA) using an Eclipse C18 column 4.6×250 mm (Agilent, Santa Clara, CA, USA) equipped with an amperometric detector. The analysis was performed at 25 ºC, with acetonitrile-dipotassium hydrogen phosphate (65:35 v/v) as eluent, at a flow rate of 0.7 mL/min. The salicylic acid concentration in the withdrawn solution was determined by HPLC, using a Luna C18 column 4.6×250 mm (Phenomenex, Torrance, CA, USA). The mobile phase was a mixture of acetonitrile and 0.1% of trifluoroacetic acid (TFA) used with the concentration of ACN varying from 12.5 to 100 to 12.5% in 0.1% TFA with the flow rate of 0.5 mL/min. The analysis was performed at 25 ºC.

2.4.2.10. CGC Hydrogels Effect on Fibroblasts

For the wound scratch assay, normal human dermal fibroblasts, acquired from ATCC (PCS-201-010, Manassas, VA, USA), were seeded on a 35 cm^2 tissue plate at a cell density of 4×10^5 cells/plate, in Dulbecco's modified Eagle medium (DMEM, Thermo Fisher Scientific, Waltham, MA, USA) supplemented with 10% (v/v) fetal bovine serum (ThermoFisher Scientific) and a mixture of 100 U/mL penicillin and 100 µg/mL streptomycin, and incubated at 37 C, 5% (v/v), and 99% (v/v) relative humidity, until confluence was reached. A scratch on the confluent monolayer was performed using a sterile micropipette tip, the medium was replaced by fresh medium and a sterilized CGC hydrogel freeze-dried sample with 5 mm diameter was placed over the scratch. For control purposes, a scratch was also done on another tissue plate that was not submitted to the presence of the CGC hydrogel. Regions of the scratch were imaged at 0 h and after 12 h with a Cytosmart Lux2 (Cytosmart technologies, Eindhoven, The Netherlands) and the size of the wound scratch was measured using ImageJ software.

The morphology of fibroblast cells after exposure to the hydrogel sample was evaluated by confocal microscopy. After measuring the scratch, the cells were fixed with 4% (w/v) formaldehyde, washed 3 times with PBS, and then permeabilized for 5 min with 0.1% (v/v) Triton X-100. Afterwards, the cells were incubated with 1% (w/v) bovine serum albumin, actin was stained with AlexaFluor 488 Phalloidin (Thermo Fisher Scientific) according to the manufacturer's procedure recommendations, and nuclei were stained with 7.5 µg/mL Hoechst 33258 (Thermo Fisher Scientific). Cells were visualized in a Zeiss LSM 710 confocal microscope, and five different images of cells exposed to CGC hydrogel were acquired using microscope software (Zen black edition, 2011).

Fibroblasts' viability was evaluated by preparing four wells in a 24-well plate, two with 7500 cells/well and two without cells. After 24 h for cell adherence, the CGC hydrogel sample (5 mm diameter) was added to a well with cells and to a well without cells. After 24 h, the medium was replaced by fresh medium supplemented with 3-(4,5-dimethylthiazol-2-yl)-5-(3-carboxymethoxyphenyl)-2-(4-sulfophenyl)-2H tetrazolium, inner salt (MTS, Promega, Madison, WI, USA), and the absorbance was measured at 490 nm, according to manufacturer's instructions. The percentage of fibroblasts' viability (%) exposed to CGC hydrogel was measured using equation (2.4.3) as follows:

$$Viability = \frac{Abs_{490}\ fibroblasts\ with\ CGC\ hydrogel - Abs_{490}\ medium\ with\ CGC\ hydrogel}{Abs_{490}\ fibroblasts - Abs_{490}\ medium} \times 100 \qquad (2.4.3)$$

2.4.2.11. Statistical Analysis

The experimental data from all the studies were expressed as mean ± standard deviation (SD). Error bars represent the standard deviation ($n \geq 3$).

2.4.3. Results and Discussion

2.4.3.1. Hydrogels Fabrication

The CGC hydrogels, named $Na5_1{}^{*4}$ and $Na5_1{}^{*6}$, prepared from 4 and 6wt% CGC suspensions, respectively, had polymer contents of 2.40 ± 0.15 and 3.09 ± 0.22wt% (Table 2.7), respectively, which shows that the CGC content of the suspensions was not completely solubilized in the NaOH solution. In fact, around 60% of the polymer in the 4wt% suspension was dissolved in

NaOH, while it decreased to 51.5% for the 6wt% suspension. Compared to previous work, where hydrogels with a polymer content of 1.66 ± 0.11wt% were obtained from a 2wt% CGC suspension in NaOH 5 M (named $Na5_1$* hydrogels) [239], corresponding to a dissolution of 83% of the biopolymer, it is clear that increasing the initial CGC content in the alkali suspension results in lower solubilization of the biopolymer. Nevertheless, the obtained hydrogels had higher polymer content (Table 2.7). As demonstrated in Table 2.7, all CGC hydrogels presented characteristic high water contents, above 96%, and had similar chitin contents (20.9 ± 0.78 and 21.4 ± 0.71%, for the $Na5_1{}^{*4}$ and $Na5_1{}^{*6}$ hydrogels, respectively).

Table 2.7 —Chemical characterization, compressive mechanical properties (under 80% strain), and dissipation energies (cycles under 50% strain) of $Na5_1{}^{*4}$ and $Na5_1{}^{*6}$ hydrogels.

Samples	**$Na5_1$***	**$Na5_1{}^{*4}$**	**$Na5_1{}^{*6}$**
$CGC_{initial}$ (wt%)	2	4	6
$CGC_{hydrogel}$ (wt%)	1.66 ± 0.11	2.40 ± 0.15	3.09 ± 0.22
Water content (wt%)	98.34 ± 0.11	97.60 ± 0.15	96.91 ± 0.22
Porosity (%)	53.8 ± 10.3	79.4 ± 0.60	72.0 ± 0.43
Density (g/cm^3)	0.019 ± 0.001	0.037 ± 0.005	0.052 ± 0.010
Hardness (kPa)	5.04 ± 0.14	10.08 ± 0.89	13.16 ± 0.15
Compressive modulus (kPa)	23.00 ± 0.89	39.36 ± 0.36	47.30 ± 2.04
Toughness (kJ/m^3)	0.78 ± 0.015	1.61 ± 0.33	2.14 ± 0.12
Dissipation energy (kJ/m^3)			
0 min	-	0.38 ± 0.09	2.38 ± 0.56
30 min	-	0.26 ± 0.02	0.70 ± 0.02
60 min	-	0.24 ±0.01	0.40 ± 0.04
120 min	-	0.19 ± 0.01	0.25 ± 0.06
References	[239]	This study	This study

The $Na5_1{}^{*6}$ hydrogels revealed a slightly lower porosity (72.0 ± 0.43%) than the $Na5_1{}^{*4}$ hydrogels (79.4 ± 0.60%) (Table 2.7), but considerably higher than the value reported for the $Na5_1$* hydrogels (53.8 ± 10.3%) [239]. The higher CGC concentration of the $Na5_1{}^{*6}$ hydrogels resulted in structures with a higher density (0.052 ± 0.010 g/cm^3) compared to the values found for the $Na5_1{}^{*4}$ (0.037 ± 0.005 g/cm^3) and the $Na5_1$* (0.019 ± 0.001 g/cm^3) hydrogels (Table 2.7). The porosity and density of hydrogels are essential parameters determined by their microstructure that significantly influence their physicochemical properties and their loading and release ability [241].

2.4.3.2. Morphological Characterization

Fig. 2.23 shows the macroscopic appearance of the $Na5_1^{*4}$ and $Na5_1^{*6}$ hydrogels immediately after the removal from the dialysis membrane (Fig. 2.23A) and after being cut into small samples (13.7 mm diameter, 0.7–1.1 cm height) (Fig. 2.23B), using a cylindrical mold to obtain samples with similar dimensions. Macroscopically, no significant differences were observed between the $Na5_1^{*4}$ and $Na5_1^{*6}$ hydrogels. The fresh hydrogels were translucid and exhibited a yellowish coloration (Fig. 2.23A and 2.23B). However, a more intense coloration was observed for the $Na5_1^{*6}$ hydrogels, which can be related to their higher polymer content.

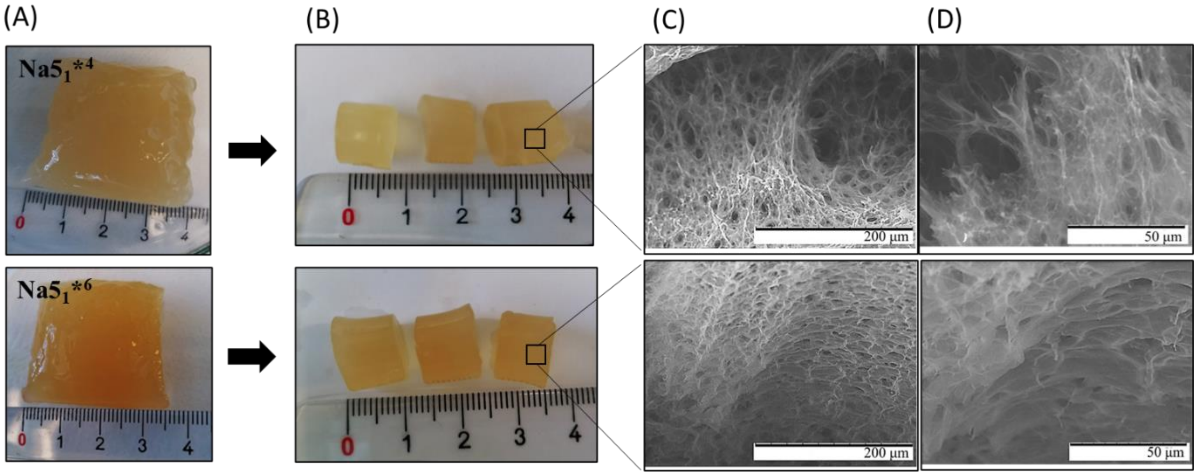

Figure 2.23 — $Na5_1^{*4}$ and $Na5_1^{*6}$ hydrogels: (A) immediately after dialysis, (B) after being cut with cylindrical mold and (C, D) SEM images of the hydrogels. Hydrogel regions observed under magnification 1500× (D) were expanded from images presented under magnification 500× (C).

SEM analysis (Fig. 2.23C and 2.23D) revealed that for both hydrogels the polymeric chains formed a heterogeneous and compact three-dimensional network, which is concomitant with the structures previously reported for CGC hydrogels [150,239]. However, the $Na5_1^{*4}$ hydrogels presented more irregular and open regions, while a regular and consistent microstructure was observed for the $Na5_1^{*6}$ hydrogels (Fig. 2.23C). Upon magnification, smaller pores were observed for the $Na5_1^{*6}$ hydrogels (Fig. 2.23D) which explains the denser and tighter microstructure of these structures. Similar observations were reported for chitosan [242] and cellulose hydrogels [243] upon increasing polymer concentration. The denser inner structure of the $Na5_1^{*6}$ sample can be explained by the higher physical crosslinking and chain entangling of CGC molecules displayed by those hydrogels. The observed lower pore size and denser structure of the $Na5_1^{*6}$ hydrogels are related to their higher polymer content [244]. These observations are in line with the increased density and lower porosity values obtained for the $Na5_1{}^{*6}$ hydrogels (Table 2.7).

2.4.3.3. Mechanical properties

The mechanical properties were evaluated by performing two types of experiments, namely, the application of a single 80% strain compression (Fig. 2.24) to determine the hydrogels' hardness, compressive modulus, and toughness (Table 2.7), and the application of cyclic compressive tests (Fig. 2.25A and 2.25B) to evaluate the dissipation energy (Table 2.7). As shown in Table 2.7, the highest hardness (13.16 ± 0.15 kPa), compressive modulus (47.30 ± 2.04 kPa), and toughness values (2.14 ± 0.12 kJ/m^3) were observed for the $Na5_1{}^{*6}$ hydrogels. This result is probably related to the higher polymer content of those hydrogels (3.09 ± 0.22wt%) compared to the $Na5_1{}^{*4}$ and $Na5_1{}^{*}$ hydrogels (2.40 ± 0.15 and 1.66 ± 0.11wt%, respectively) (Table 2.7). Liu et al. [245] reported higher hardness (2.0 kPa) for carboxymethyl chitin 2.0wt% hydrogels, compared to 0.5 kPa for hydrogels with 1.0wt% polymer content. Similar behavior was also demonstrated for gelatin methacrylate hydrogels, where the compressive modulus was significantly improved when the polymer concentration was increased from 5 to 10% [244]. In general, these results can be explained by the increase in multiple physical interaction sites and entrapped entanglements resulting from increased polymer concentration [246].

Despite this, all samples displayed similar compressive stress-strain curves (Fig. 2.24), characteristic of non-linear and viscoelastic solids [247], for which the rupture strain occurred between 50 and 60%. These results suggest that increasing the polymer concentration in the CGC hydrogels has no significant impact on their capacity to withstand deformation.

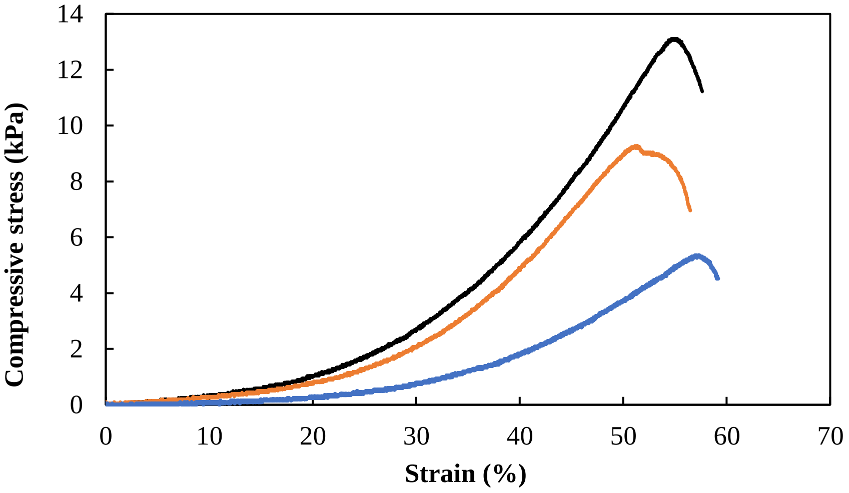

Figure 2.24 — Compression stress-strain curves of $Na5_1{}^{*}$ (blue line), $Na5_1{}^{*4}$ (orange line), and $Na5_1{}^{*6}$ (black line) hydrogels.

The cyclic compressive tests, in which the wet hydrogel samples were subjected to loading cycles at increasing periods of time (30, 60 and 120 min) at a maximum compression of 50% strain, revealed that the $Na5_1{*}^6$ hydrogels presented higher dissipation energy values than the $Na5_1{*}^4$ hydrogels (Table 2.7), for all tested loading times, despite decreasing with increasing loading cycles. In fact, the original $Na5_1{*}^6$ hydrogel sample presented a dissipation energy of 2.38 ± 0.56 kJ/m^3, while after 120 min the value decreased to 0.25 ± 0.06 kJ/m^3. The $Na5_1{*}^4$ hydrogels, on the other hand, although having a lower original dissipation energy (0.38 ± 0.09 kJ/m^3), was less impacted by the consecutive loading cycles, displaying a value of 0.19 ± 0.001 kJ/m^3 after 120 min (Table 2.7). These results indicate that increasing the polymer concentration led to a more efficient energy dissipation of the $Na5_1{*}^6$ hydrogels, but the efficiency decreased by applying more cycles.

The compression loading-unloading curves are shown in Fig. 2.25A and 2.25B. It can be observed that the loading curves differed from the unloading curves for all the tested periods of time. Moreover, the hysteresis loops or the area of loading and unloading closed curves, which reflected the dissipated energy, decreased as the number of cycles increased for all hydrogel samples. Nonetheless, the $Na5_1{*}^4$ hydrogels had a better recovery behavior as shown by the compressive stress values that decreased from 7.99 kPa for the first cycle to 5.56 kPa for the fourth cycles (Fig. 2.25A), compared to the $Na5_1{*}^6$ hydrogels for which a more significant decrease was observed (from 18.91 to 6.25 kPa, for the first and second cycles, respectively) (Fig. 2.25B). A similar behavior was reported by Shen et al. [248] for chitosan-gelatin hydrogels, for which a decrease in the hysteresis loop area was observed, followed by a plateau value, as compressive cycles increased. The authors attributed this behavior to the remarkable fatigue resistance of the hydrogels.

For the $Na5_1{*}^6$ hydrogels, there was a drastic decrease in the dissipated energy and compressive stress. As shown in Fig. 2.25B, a large hysteresis was obtained for the first cycle, corresponding to a compressive stress of 18.91 kPa, which decreased to 6.25, 3.83, and 3.36 kPa for the subsequent cycles. This significant reduction in dissipated energy concomitant with a decrease in strength might be attributed to a low recovery ability due to the internal fracture of the hydrogel structure during the first loading-unloading cycle [249]. These results show that, although the $Na5_1{*}^6$ hydrogels were tougher probably due to their higher polymer content, the $Na5_1{*}^4$ had higher fatigue resistance.

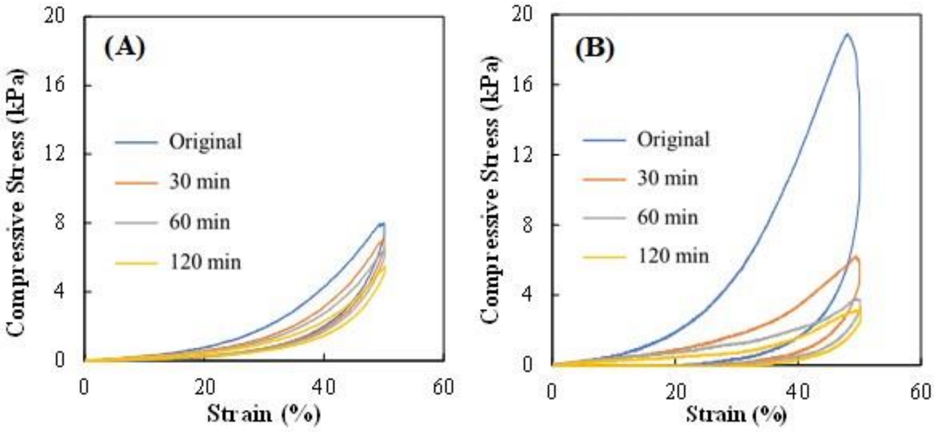

Figure 2.25 — Loading-unloading curves of (A) $Na5_1{}^{*4}$ and (B) $Na5_1{}^{*6}$ hydrogels, under 50% strain.

2.4.3.4. Rheological properties

As shown in Fig. 2.26A, both hydrogels exhibited predominantly elastic characteristics, with the elastic (storage) modulus G′ exceeding in one order of magnitude their corresponding viscous (loss) modulus G′′ over the whole range of frequencies. Both G′ and G′′ were mainly frequency-independent, suggesting the formation of a stable structure [250]. Similar elastic behavior has been previously reported for Na-based CGC hydrogels [150,239].

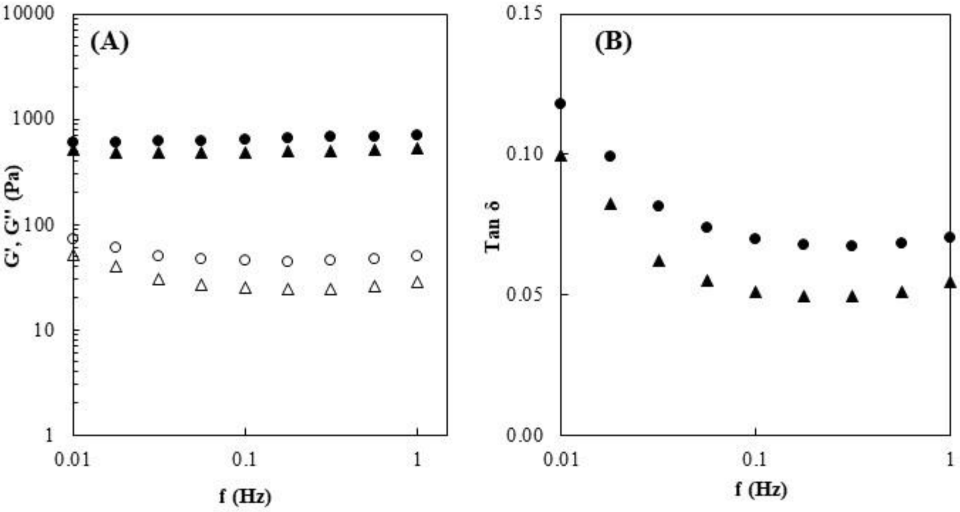

Figure 2.26 — Rheological properties of the $Na5_1{}^{*4}$ (▲) and $Na5_1{}^{*6}$ (●) hydrogels at 25 °C: (A) Mechanical spectrum storage (G′, solid symbols) and loss moduli (G′′, open symbols), (B) Loss tangent (Tan δ).

The $Na5_1{}^{*6}$ hydrogels exhibited higher values of both G′ and G′′ across the entire range of frequencies (Fig. 2.26A), which can be related to their higher polymer content. For a frequency of 1 Hz, the $Na5_1{}^{*6}$ hydrogels presented a G′ of 702.25 ± 28.65 Pa, while lower values were reached for the $Na5_1{}^{*4}$ hydrogels (523.20 ± 21.08 Pa), as well as for the $Na5_1{}^{*}$ hydrogels (149.9 ± 9.8 Pa) [239]. This behavior can be explained by the denser crosslinked structure of the $Na5_1{}^{*6}$ hydrogels formed (Fig. 2.23C) due to the higher polymer concentration and has been reported for other CGC-based hydrogels. An example is the hydrogel prepared with *Ganoderma lucidium* CGC dissolved in ILs [251], for which the authors reported a gel strength increase (from ~3500 to ~7000 Pa, at 1 Hz) by increasing the polymer concentration from 4 to 6wt%.

The viscoelastic behavior of CGC hydrogels was also determined by the value of the loss tangent of delta (tan δ) which represents the ratio of energy lost to energy stored during deformation [252]. As shown in Fig. 2.26B, both hydrogels exhibited tan δ values below 1, which confirms the elastic characteristics of CGC hydrogels [252]. Moreover, it can be observed that by increasing the frequency a decrease in the tan δ values was achieved, and for both hydrogels, a plateau was reached. This behavior is associated with the mostly frequency-independent performance of both moduli (Fig. 2.26A). Similar behavior was reported for chitosan-based hydrogels [253], however, those structures were weaker than CGC hydrogels since higher tan δ values (above 0.15) were obtained. Over the whole range of frequencies, the $Na5_1{}^{*4}$ hydrogels presented lower tan δ values (0.049 – 0.100) compared to $Na5_1{}^{*6}$ hydrogels (0.067 – 0.118). The results indicate that during deformation, $Na5_1{}^{*4}$ hydrogels have more elastic characteristics which give them a higher ability to store energy than to dissipate it. These findings are in accordance with the mechanical properties and revealed that increasing the polymer content led to the fabrication of more rigid hydrogels.

2.4.3.5. Swelling ratio and water retention behavior

The swelling ability of CGC hydrogels was assessed by immersing freeze-dried hydrogel samples in three different media (deionized water, PBS, and NaCl 0.9%) at 37 ºC, for 10 min. Macroscopically, after freeze-drying, the structures' dimensions were kept (Fig. 2.27A), showing that the polymer network was not significantly affected by water removal. Moreover, the structures presented a lighter yellowish coloration and were rigid. Upon rehydration, in spite of the similar dimensions, hydrogels exhibited a whitish color and became opaque (Fig. 2.27B).

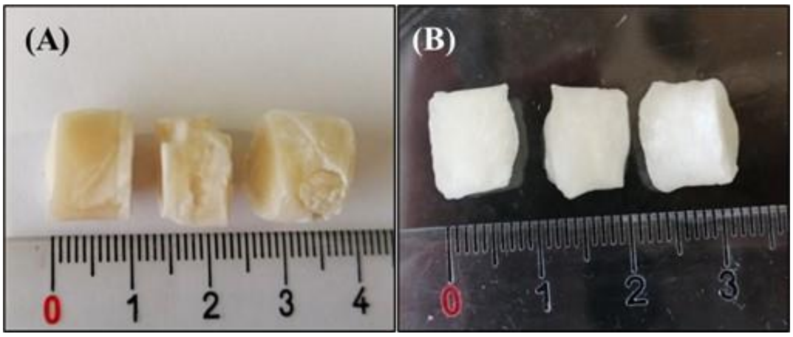

Figure 2.27 — Macroscopic appearance of (A) freeze-dried and (B) swollen CGC hydrogel samples.

As shown in Fig. 2.28A, upon immersion in the aqueous media for 10 min, the $Na5_1{}^{*4}$ hydrogels presented a high swelling ratio, achieving values of 20.3 ± 0.4, 19.4 ± 1.5, and 19.0 ± 1.1 g/g for deionized water, PBS, and NaCl 0.9%, respectively. Due to their lower polymer content, these structures presented a decreased crosslink density and, consequently, higher pore sizes for water absorption, as demonstrated by the SEM images (Figs. 2.23C and 2.23D). In contrast, for a similar time period, lower swelling ratio values (17.8 ± 0.3, 15.3 ± 1.5, and 15.5 ± 1.9 g/g, respectively) were obtained for the $Na5_1{}^{*6}$ hydrogels. In general, the obtained values for $Na5_1{}^{*4}$ and $Na5_1{}^{*6}$ hydrogels were lower than the ones reported for $Na5_1{}^{*}$ hydrogels (28.6 ± 1.3, 21.0 ± 0.5, and 19.2 ± 0.5 g/g, respectively) which is in line with the lower polymer content of the later (Table 2.7). Analogous performance was reported by Liu et al. [251] for the *Ganoderma lucidium* CGC hydrogels, whose swelling ratio also decreased (from 1181.0 to 1891.0%) as the polymer concentration increased from 2 to 7wt%. However, in deionized water, the hydrogels prepared with 4 and 6wt% of polymer exhibited lower swelling ratio values (~1400%, corresponding to 14 g/g) when compared to Na-based CGC hydrogels.

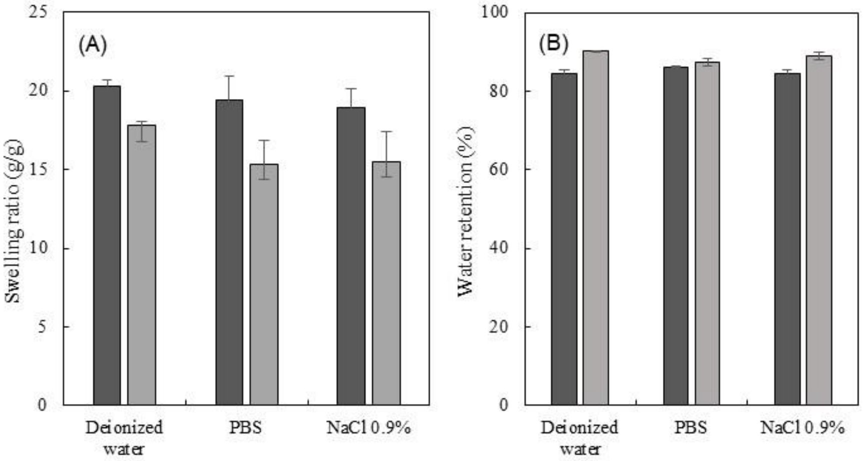

Figure 2.28 — Swelling ratio (A) after 10 min and water retention capacity (B) after 30 min incubation of the $Na5_1{}^{*4}$ (dark grey) and the $Na5_1{}^{*6}$ (light grey) hydrogels, in deionized water, PBS, and NaCl 0.9%, at 37 °C.

For all the tested media, both hydrogels exhibited exceptional water absorption ability (19.0-20.3 and 15.3-17.8 g/g, for the $Na5_1{}^{*4}$ and the $Na5_1{}^{*6}$ hydrogels, respectively), due to the presence of hydroxy and amino groups in the CGC macromolecules that provided it high hydrophilicity and surface polarity [214]. Moreover, it can be observed that for both hydrogels the swelling ratio was higher in deionized water than in either PBS or NaCl 0.9% (Fig. 2.28A). This behavior has been also reported for $Na5_1{}^{*}$ hydrogels and it can be related to the difference in osmotic pressure between the hydrogel's structure and the saline solutions [239]. Furthermore, the neutral pH of the PBS solution (7.4) might induce an increase in the swelling ratio of hydrogels due to the deprotonation of $-NH_3$ and the intra-chain hydrogen bonds in the hydrogel matrix [254]. Nonetheless, the slight difference between the swelling ratio in PBS and NaCl 0.9% suggested the absence of a pH-sensitive swelling behavior. Additionally, for both hydrogels, the swelling equilibrium was reached almost spontaneously (data not shown) in all the tested media, which demonstrates the sponge-like behavior of these structures (Fig. 2.27).

For the assessment of the water retention ability, swollen samples of the three different media were incubated at 37 ºC, for 30 min. At specific times, the water loss was evaluated by weighing the samples. Fig. 2.28B shows the water retention ability of the $Na5_1{}^{*4}$ and $Na5_1{}^{*6}$ hydrogels. As demonstrated, after 30 min at 37 ºC, both hydrogels were able to retain above 80% of their water content. Despite their lower swelling ratio, the $Na5_1{}^{*6}$ hydrogels had a higher water retention capacity (87.3 – 90.2%) than the $Na5_1{}^{*4}$ hydrogels (84.6 – 86.2%), which may be due to their more compact network structure. Nevertheless, for the tested period, no significant differences were observed between the hydrogels' water retention ability in the different media.

The swelling behavior defines the water absorption capacity of hydrogels, and it has a direct impact on their ability to load and deliver drugs [255]. In fact, a conventional method for loading hydrogel structures is performed by soaking a preformed hydrogel in a drug solution and allowing it to swell to equilibrium, avoiding adverse effects on drug properties caused by polymerization [213]. The subsequent drug release includes the simultaneous absorption of water into the hydrogel matrix and the desorption of drugs via diffusion. Several studies demonstrated that higher swelling ability leads to increased drug loading and drug release rates. For example, Suhail et al. [256] reported a decreased drug loading capacity of chondroitin sulfate-based hydrogels that presented lower swelling when compared to the ones with higher swelling.

Given their interesting mechanical and rheological properties, particularly their higher fatigue resistance, as well as their higher swelling ability, the $Na5_1{}^{*4}$ hydrogels were selected for the subsequent tests, namely APIs loading and *in vitro* release, and permeation tests.

2.4.3.6. Hydrogels loading and release ability

2.4.3.6.1. Loading of API

The drug loading capacity of the $Na5_1{}^{*4}$ was evaluated by soaking cylindrical freeze-dried hydrogel samples in four individual APIs solutions, namely caffeine, salicylic acid, diclofenac sodium, and ibuprofen sodium, at room temperature, for 24 h. Table 2.8 shows that the higher concentration of caffeine and ibuprofen sodium loading solutions (1.0wt%) led to a higher amount of those APIs within the hydrogel's matrix (11.98 and 11.25 mg/cm^3, respectively). On the other hand, due to the low water solubility of diclofenac sodium and salicylic acid, lower concentrations of those APIs (0.1wt%) were used and, consequently lower drug loading capacity values were obtained (1.30 and 1.49 mg/cm^3, respectively). In fact, the drug concentration of the loading solution has a direct effect on the hydrogels' drug loading since the increase in the concentration of the drug leads to a higher amount of drug available to be loaded in the hydrogels' structure. A similar effect has been reported for several drug delivery systems including calcium pectinate beads [257] and chitosan-silk fibroin films [258]. Indeed, the latter structures achieved an increase in diclofenac content from 1.075 to 4.564 µg/mm^3 using drug loading solutions of 62.5 and 250 µg/mL, respectively.

Table 2.8 —Concentration of loading solutions, drug loading (DL, mg/cm^3), entrapment efficiency (EE, %) and Korsmeyer-Peppas model parameters obtained from the *in vitro* release kinetics of $Na5_1{}^{*4}$ hydrogels; R^2, regression coefficient; *n*, release exponent.

API	Loading solution (wt%)	DL (mg/cm^3)	EE (%)	*n*	R^2
Caffeine	1.0	11.98 ± 1.29	13.11 ± 0.49	0.523	0.996
Sodium Diclofenac	0.1	1.30 ± 0.05	14.70 ± 0.60	0.520	0.996
Salicylic Acid	0.1	1.49 ± 0.15	15.15 ± 1.54	0.666	0.996
Sodium Ibuprofen	1.0	11.25 ± 2.04	14.43 ± 0.88	0.491	0.995

Additionally, the loading method also significantly affects the drug loading content. For example, Sriamornsak et al. [257] reported a decrease in the drug content on calcium pectinate beads when the drug loading process was based on gel swelling (0.97 – 4.37 mg/g), compared to mixing (27.97 – 29.15 mg/g). Despite the higher values of drug content achieved, the processes used for the formation of CGC hydrogels preclude the use of mixing methods.

Moreover, it was noticed that the entrapment efficiency was also affected by the physicochemical characteristics of the different tested APIs. As shown in Table 2.8, caffeine reached the lowest value of EE% (13.11 ± 0.49%), which can be explained by the API ionization and the lower acetylation degree of the N-acetyl-glucosamine monomers of CGC [239]. On contrary, the highest EE% values were obtained for salicylic acid, reaching values of 15.15 ± 1.54%, which might be justified by the low molecular weight (138.12 Da) of the API's molecules. In fact, with the loading swelling method, the drug's molecular weight has a significant impact on the drug loading process. For example, Caliceti et al. [259] reported a linear correlation between drug molecular weight and loading yield where a decrease in loaded drug amount was obtained as the drug molecular weight increased.

This behavior was also observed by Sethi et al. [260] that described a similar soaking method to load xanthan gum-starch hydrogels with paracetamol and aspirin, and higher EE% values were achieved (70.12 and 62.14%, respectively). Despite the low solubility of aspirin, its higher molecular weight might have a negative impact on the loading process. Wong et al. [211] reported a higher loading percentage of ibuprofen (59.08 ± 3.97%) compared to diclofenac (20.68 ± 0.47%) in poly(ethylene oxide) hydrogels using loading solutions with concentrations of 8.01 and 1.98% (w/v), respectively. In this case, the use of higher concentrations of loading solutions may contribute to the increased values achieved compared to CGC-based hydrogels.

2.4.3.6.2. *In vitro* release studies

The release studies were conducted by placing the API-loaded $Na5_1{}^{*4}$ hydrogels in PBS solution, at 37 ºC. The cumulative release profiles of the four APIs are shown in Fig. 2.29. It can be observed that hydrogels presented a release profile predominantly controlled by diffusion, characterized by an initial burst release [261]. For all the APIs tested, within 3 h of the experiment, the amount of API loaded in the structure of the hydrogel was totally released. An analogous drug release profile has been previously reported for caffeine-loaded CGC hydrogels [239]. However, due to their higher polymer content and consequent lower pore size, slightly lower release rates were displayed by the $Na5_1{}^{*4}$ hydrogels compared to the $Na5_1{}^{*}$ hydrogels. In particular, the latter achieved a caffeine release of around 50% after 10 min in the same release media, while values of 40% were reached for $Na5_1{}^{*4}$ hydrogels. A similar behavior was described for the polyacrylamide hydrogels that presented a 30% decrease in drug delivery rate when polymer concentration was increased from 2.5 to 10% [262].

Pore dimensions determine the diffusion of the drug through the hydrogel since it controls the steric interactions between the drug and the polymer network [261]. Moreover, when the drug molecules are smaller than the hydrogels´ pores, a fast diffusion occurs, and a short release duration is obtained. Fig. 2.29 shows that as the molecular weight of the API increased, a slight decrease in the drug release was observed. Indeed, salicylic acid, which was the API with the lower molecular weight, presented the highest release rate. On the other hand, the slowest release rate was obtained for diclofenac which has a higher molecular height. As shown in Fig. 2.29, within 1 h, a salicylic acid release percentage of 90.11 ± 3.11% was achieved, whereas a lower value (73.38 ± 1.02%) was reached for diclofenac sodium. For the same period and analogous released media, slower released rates were reported by Gull et al. [263] for the chitosan-based hydrogels, whose diclofenac release achieved values between 30 and 50%. However, a similar release percentage (>90%) was obtained after 130 min of the experiment. This difference might be attributed to the higher swelling ability of CGC-based hydrogels, at pH 7, which allows an increase in the drug release rate from the structure [256].

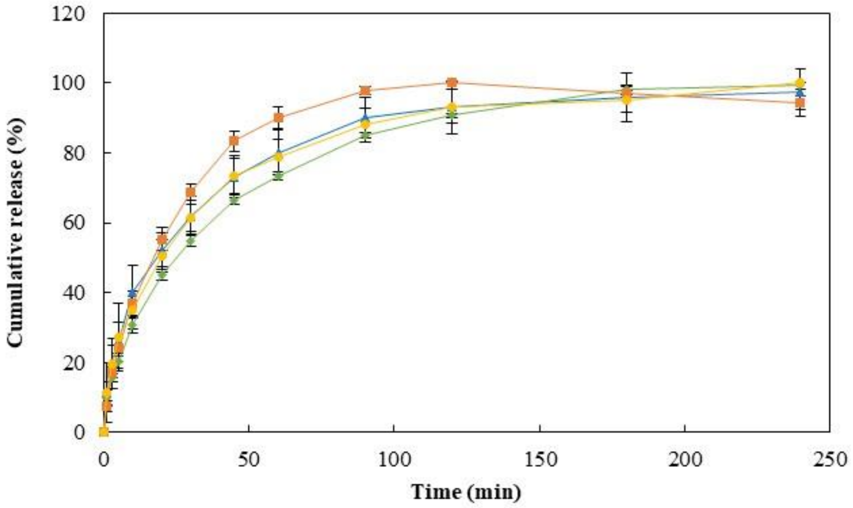

Figure 2.29 — Cumulative release profile of caffeine (▲, blue line), diclofenac sodium (◆, green line), salicylic acid (■, orange line), and ibuprofen sodium (●, yellow line) of $Na5_1{}^{*4}$ hydrogels in PBS, at 37 °C.

The drug release kinetics were evaluated by fitting the first initial 60% of the API released to the Korsmeyer-Peppas model [206]. Table 2.8 demonstrates that all the obtained release data fitted in the model since the regression coefficients (R^2) were around 0.99. Moreover, according to the kinetic parameters obtained, all the API releases followed a non-Fickian diffusion or anomalous transport, since the *n* values are between 0.45 and 0.89. These results indicate that drug diffusion and polymer chain relaxation contribute to the overall release rate [211].

It can be observed that the release profile of caffeine from $Na5_1{}^{*4}$ hydrogels presented an *n* value of 0.523 which is a similar value when compared to the one reported for $Na5_1{}^{*}$ hydrogels (0.52). A non-Fickian transport of caffeine and diclofenac molecules from bacterial nanocellulose membranes was also reported by Silva et al. [205]. In this case, *n* values obtained for those APIs were 0.52 and 0.55, respectively, which are similar to the ones obtained for $Na5_1{}^{*4}$ hydrogels (Table 2.8).

2.4.3.6.3. *In vitro* permeation studies

Fig. 2.30 shows the receptor cumulative amount profiles of the different tested APIs across mimic-skin artificial membranes (Strat-M), which are an effective alternative to human or animal skin to predict *in vivo* drug transdermal diffusion [264,265]. It can be noticed that all APIs were able to permeate the membrane, and this fact can be explained by their low molecular weights (138.12 – 318.13 Da). Indeed, for a drug to be passively delivered across the skin, the molecular weight should be below 500 Da [266,267]. As shown in Fig. 2.30, the maximum cumulative amount of 245.02 ± 11.17 $\mu g/cm^2$ was achieved for caffeine (Fig. 2.30A), while the lowest value was reached for diclofenac (3.45 ± 0.55 $\mu g/cm^2$) (Fig. 2.30B). Fig. 2.30C and 2.30D, shows that salicylic acid also achieved a high cumulative amount value (150.05 ± 14.24 $\mu g/cm^2$) and a low cumulative amount was obtained for ibuprofen (35.37 ± 2.77 $\mu g/cm^2$). This difference can be explained by the ionization properties of each API and the interaction between the API and the polymeric chains. Ionized drugs are poor candidates for transdermal delivery due to the lipophilic nature of the *stratum corneum* [267,268]. Among the APIs used, caffeine represents the only non-ionic molecule, which might have improved its permeation through the membrane, resulting in the highest cumulative amount achieved. For example, Uchida et al. [269] reported a permeability coefficient of unionized lidocaine 43-fold higher than the value obtained for the ionized form of the molecule. Besides their ionization, salicylic acid, ibuprofen, and diclofenac are negatively charged molecules which make them suitable for interactions with polymer chains and, consequently, decrease their permeation.

One important permeation parameter is the steady-state flux ($J_{ss,}$ $\mu g/cm^2/h$), corresponding to the amount of permeate crossing the membrane at a constant rate, that can be obtained from the slope of the linear region of the cumulative amount over time [270].

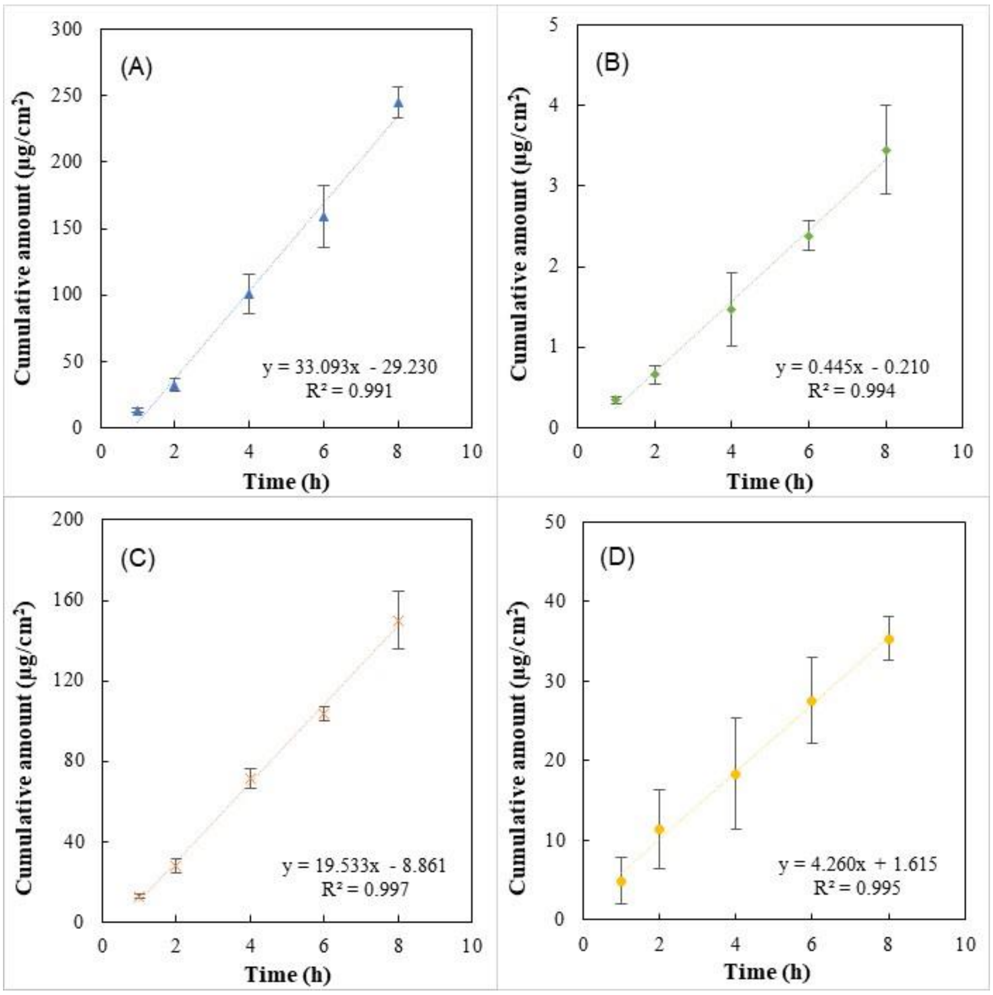

Figure 2.30 — Cumulative amount profiles of (A) caffeine, (B) diclofenac sodium, (C) salicylic acid and (D) ibuprofen sodium from $Na5_1{}^{*4}$ hydrogels.

As shown in Fig. 2.30, caffeine presented the highest permeation with a J_{ss} value of 33.09 µg/cm^2/h followed by salicylic acid and ibuprofen which were permeated with a flux of 19.53 and 4.26 µg/cm^2/h, respectively. On the other hand, the lowest permeation was achieved by diclofenac sodium with a J_{ss} value of 0.44 µg/cm^2/h. As explained above, these results can be attributed to the physicochemical nature of the API, namely the ionization, the molecular mass, and the partition coefficient. The partition coefficient is a key parameter for skin permeation since it determines which pathway a drug molecule would take after passing through the *stratum corneum* [267]. Moreover, the partitioning of a drug between the lipophilic *stratum corneum* and the hydrophilic living cells underlying the epidermis can be well represented by the n-octanol-water partition coefficient (log *P*) [267]. Among the ionized APIs used, salicylic acid exhibited a log *P* value of 2.26 which is within the ideal range (1< log *P* < 3) established for transdermal permeation [266]. This characteristic might explain the high cumulative amount achieved and the increased value of permeation flux (Fig. 2.30C). Additionally, the low molecular weight of salicylic acid also promotes its permeation. Uchida et al. [271] demonstrated a correlation between the permeated amount and molecular weight, where the permeated amount decreased with an increase in the molecule mass. This fact might explain the low cumulative amounts achieved for ibuprofen and diclofenac which are molecules with higher molecular weight (229.27 and 318.13 Da, respectively) when compared to the salicylic acid molecule (138.12 Da). In comparison with diclofenac, ibuprofen achieved higher permeation flux, and this might be attributed to the higher drug concentration used in loading solutions (Table 2.8, Fig. 2.30). Pradal et al. [272] also reported that increasing the drug content in the formulations, led to an enhancement of the permeation. These results demonstrated that CGC hydrogels can be used as a platform to deliver drugs with different physicochemical characteristics.

2.4.3.7. Effect of CGC hydrogels in fibroblasts

To assess the influence of the CGC hydrogels in tissue regeneration, a wound scratch assay was performed with human normal primary dermal fibroblasts in the presence and absence of the hydrogel, according to previously described procedures [273]. No major differences were observed in the remission percentage when the cells were exposed or not exposed to the hydrogel samples (Fig. 2.31A and 2.31B).

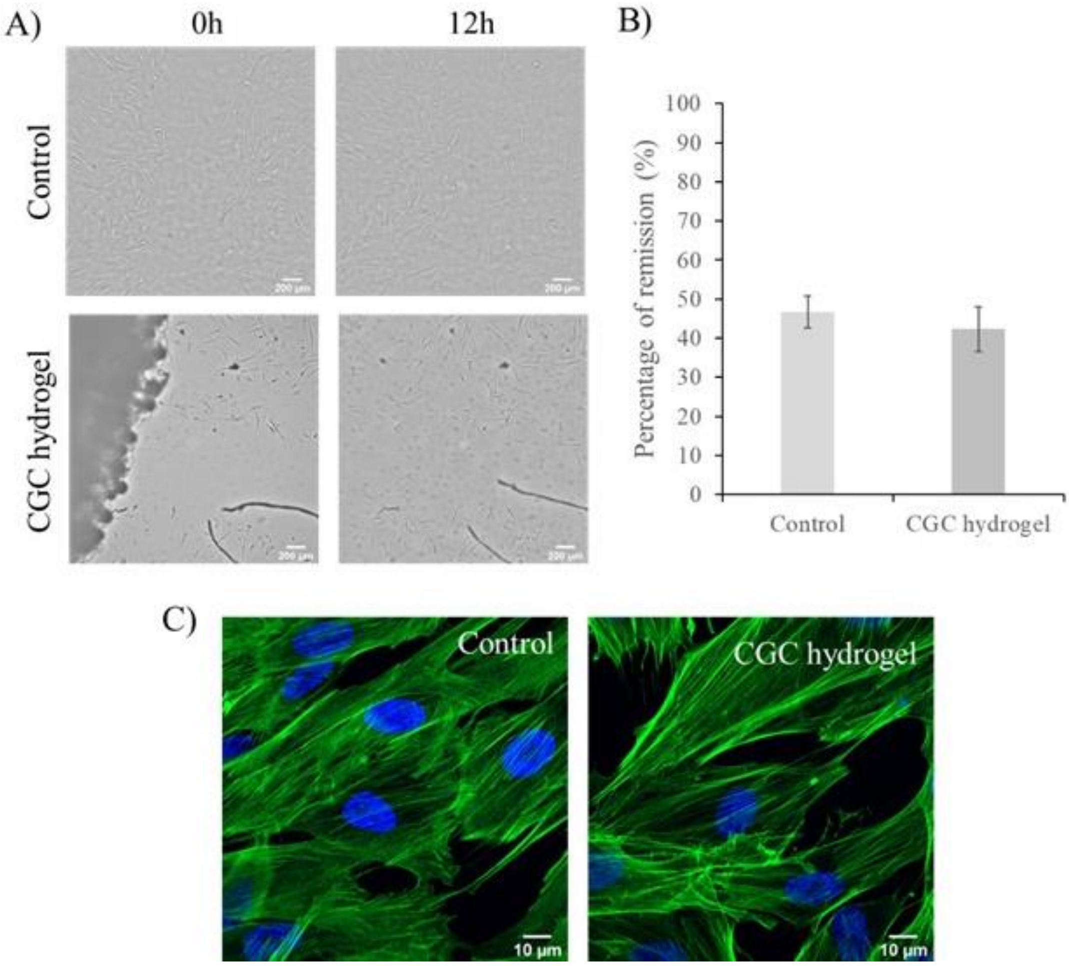

Figure 2.31 —Representative images of the wound healing assay (A) at 0 h and 12 h after performing a scratch in a Fibroblasts monolayer in the presence of a CGC hydrogel (CGC hydrogel) or absence (control); Percentage of remission (B) after 12 h exposure to CGC hydrogel, or untreated (control). Bars represent the mean ± SEM of two independent experiments. Aspect of fibroblasts (C) in the absence (control) or presence (CGC hydrogel) of the CGC hydrogel. Cells were exposed for 12h to the freeze-dried CGC hydrogel sample, fixed with 4% (w/v) formaldehyde, and then actin filaments were stained with Phalloidin conjugated with AlexaFluor 488 (green fluorescence) and nuclei stained with Hoechst 33258 (blue fluorescence). The presented images are representative of 5 images acquired with a Confocal microscope Zeiss LSM710.

A deeper look into the cells' appearance after actin and nuclei staining also revealed that no major differences were noticed in the morphology of the connective tissue cells after exposure to the CGC hydrogel (Fig. 2.31C), suggesting that it has no significant impact on these dermal cells. In line with these results, it was observed an 88.8 ± 3.5% viability for the fibroblasts exposed to the CGC hydrogel samples, compared to the unexposed cells.

2.4.4. Conclusions

This study demonstrated that increased CGC content led to the formation of denser hydrogels with improved mechanical and rheological properties. However, the more compact polymeric network of the $Na5_1{}^{*6}$ hydrogels was characterized by lower fatigue resistance and lower swelling ability compared to the $Na5_1{}^{*4}$ hydrogels. The latter revealed a high loading ability for several APIs, namely caffeine, salicylic acid, diclofenac sodium, and ibuprofen sodium, displaying a release profile following a non-Fickian diffusion. Drug loading and release were dependent on the APIs molecular weight and ionic character. Analysis in normal human dermal fibroblasts revealed that CGC hydrogels have no major effects on the viability, migration ability and morphology of cells, which is an indicator of their non cytotoxicity. This study highlights the use of CGC-based hydrogels as drug delivery systems and their potential as promising structures to be used in biomedical applications.

3. FucoPol Hydrogel Membranes

3.1. Novel hydrogel membranes based on the bacterial polysaccharide FucoPol: Design, characterization, and biological properties

The results shown in this chapter are part of the following published paper:

- **Araújo, D.**, Martins, M., Concórdio-Reis, P., Roma-Rodrigues, C., Alves, V.D., Fernandes, A. R.; Freitas, F. Novel hydrogel membranes based on the bacterial polysaccharide FucoPol: Design, characterization, and biological properties. Pharmaceuticals 2023, 16, 991. https://doi.org/10.3390/ph16070991.

Summary

FucoPol, a fucose-rich polyanionic polysaccharide, was used for the first time for the preparation of hydrogel membranes (HMs) using Fe^{3+} as a crosslinking agent. This study evaluated the impact of Fe^{3+} and FucoPol concentrations on the HMs' strength. The results show that, above 1.5 g/L, Fe^{3+} concentration had a limited influence on the HMs' strength, and varying the FucoPol concentration had a more significant effect. Three different FucoPol concentrations (1.0, 1.75 and 2.5 wt%) were combined with Fe^{3+} (1.5 g/L), resulting in HMs with a water content above 97wt% and Fe^{3+} content up to 0.16wt%. HMs with lower FucoPol content exhibited a porous microstructure that became denser as the polymer concentration increased. Moreover, the low polymer content HM presented the highest swelling ratio (22.3 ± 1.8 g/g) and a lower hardness value (32.4 ± 5.8 kPa). However, improved mechanical properties (221.9 ± 10.2 kPa) along with a decrease in the swelling ratio (11.9 ± 1.6 g/g) were obtained for HMs with a higher polymer content. Furthermore, all HMs were non-cytotoxic and revealed anti-inflammatory activity. The incorporation of FucoPol as a structuring agent and bioactive ingredient in the development of HMs opens up new possibilities for its use in tissue engineering, drug delivery and wound care management.

3.1.1. Introduction

Hydrogel membranes (HMs) are very interesting structures that combine the thin membranes' permeability and porous architecture with their water absorption ability and dynamic mechanical properties of hydrogels. This combination allows a controlled diffusion of the molecules since permeation is limited through the bulk hydrogel and the permeation rate depends on the size and hydrophobicity properties of the molecule, as well as an enhancement in gas permeation by the water uptake ability [274]. Thus, these unique features make HMs promising materials for various applications such as antifouling/antimicrobial coatings [275], transdermal delivery systems [70] and wound dressings [276]. Among the several methods used for their fabrication that include sintering [277], electrospinning [278], or molecular imprinting [279], casting solution has been the most commonly used technique due to its simplicity and low-cost [274]. In general, this method involves polymer dissolution followed by a crosslinking step [280,281], and pouring on the casting plate. Crosslinking can be established either physically or chemically by non-covalent or covalent interactions, respectively. Physical crosslinking might include hydrogen bonds, van der Walls forces, chain entanglements, and hydrophobic or ionic interactions, which lead to the formation of fragile and reversible hydrogels, due to the weakness of these interactions [43].

Ionic interactions, present in the so-called ionotropic gelation, occur through crosslinking of polymeric chains with ions, usually cation-mediated gelation of negatively charged polysaccharides [86,282]. Ionotropic hydrogels can be formed in the presence of divalent (e.g., Ca^{2+}, Pb^{2+}, Cu^{2+}) or trivalent (e.g., Fe^{3+}, Al^{3+}) cations under different types of binding mechanisms. For example, divalent cations typically adopt the so-called egg-box model characterized by two antiparallel polyuronate chains forming egg-box dimers with Ca^{2+} and aggregating laterally to form multimers [104]. Although the binding mechanism of trivalent cations, namely Fe^{3+}, remains under investigation, two gelation models have been proposed: (1) coordination of the metal cation by the polysaccharide, resulting in spatially separated Fe^{3+} centers along with polysaccharides, or (2) the colloidal model that suggests the production of oxyhydroxide colloids that are stabilized by polysaccharide chains, preventing their aggregation and keeping the colloids in the hydrogel matrix [283]. Although these models have been proposed for crosslinking by metal coordination in alginate hydrogels, other several polysaccharides such as xanthan gum [284], konjac glucomannan [285], carboxymethyl cellulose (CMC) [286] and succinoglycan [287] have been used to fabricate ionotropic hydrogels using Fe^{3+} as crosslinker. In fact, the use of polysaccharides in hydrogel fabrication presents several advantages due to their biocompatibility, biodegradability and non-toxicity which make them attractive biomaterials to be used in the biomedical field [41,49], particularly in topical applications [235,288].

FucoPol is a fucose containing polysaccharide, characterized by a high molecular weight (1.7–5.8 × 10^6 Da), that is synthesized by *Enterobacter* A47 (DSM 23139). It is composed of fucose (32–36 mol%), glucose (28–37 mol%) and galactose (25–26 mol%) as neutral sugars, glucuronic acid (9–10 mol%) as an acidic sugar and acetate (3.5–6.8wt%), pyruvate (3.7–14 wt%) and succinate (0.6–3wt%) as acyl groups [289]. Due to its intrinsic biological activity that includes antioxidant [290] and wound healing abilities [291], FucoPol is a promising biopolymer to be exploited for biomedical applications. Moreover, FucoPol possesses an anionic character given by the presence of glucuronic acid, succinyl and pyruvyl, which opens up the possibility to interact with ions and other charged macromolecules [289]. Recently, the interaction between FucoPol and several multivalent cations was studied, and the cation-mediated gelation ability of FucoPol was demonstrated [292]. In that procedure, trivalent Fe^{3+} cations were successfully used to crosslink polymeric functional groups, forming stable and non-cytotoxic hydrogel beads.

In this study, FucoPol was used for the first time to prepare HMs using Fe^{3+} as a crosslinker. The impact of FucoPol and Fe^{3+} concentration on the strength of the structures was evaluated, and the optimal conditions were selected to prepare the HMs. Furthermore, the HMs thus obtained were physically and chemically characterized in terms of their morphology and mechanical and swelling properties, and they were evaluated for their cytotoxicity and anti-inflammatory activity.

3.1.2. Materials and Methods

3.1.2.1. Materials

FucoPol was obtained via cultivation of the bacterium *Enterobacter* A47 (DSM 23139) in a 10 L bioreactor (BioStat B-plus, Sartorius, Germany) using glycerol as the sole carbon source, as described by Concórdio-Reis et al. [293]. FucoPol was recovered and purified from the cultivation broth via diafiltration and ultrafiltration, as previously described [291]. FucoPol was composed of fucose (36% mol), glucose (33% mol), galactose (26% mol) and glucuronic acid (5% mol), with a total acyl group content of 7.8wt%. The polymer presented a number (Mn) and molecular weight (Mw) of 1.68×10^6 Da and 3.19×10^6 Da, respectively, with a 1.90

polydispersity index. The sample had a protein and inorganic salt content of 14.3 and 1.4%, respectively.

3.1.2.2. Preparation of FucoPol HMs

FucoPol HMs were fabricated as shown in Fig. 3.1. Freeze-dried FucoPol (1wt%) was dissolved in deionized water under magnetic stirring (800 rpm) at room temperature until complete dissolution. The resulting FucoPol solution was cast into a cylindrical silicone mold (50 mm diameter, 3 mm height), and the height was leveled to the mold using a spatula. HMs were prepared via immersion of the silicone mold with the FucoPol solution into an aqueous $FeCl_3$ solution (250 mL) at room temperature for 2 h. Afterward, the HMs were washed with deionized water (250 mL) for the removal of the unreacted crosslinker. After 1 h, FucoPol HMs were removed from the mold, and their rheological properties were evaluated via oscillatory shear measurements. Different Fe^{3+} (0.05–9.95 g/L) and FucoPol (0.5–2.5 wt%) concentrations were tested to assess their impact on the strength of the HMs.

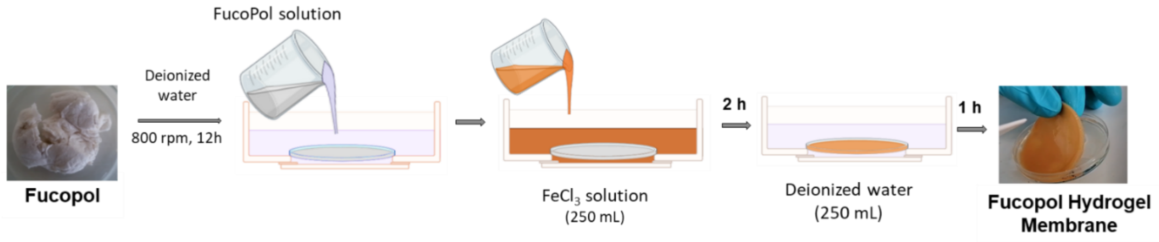

Figure 3.1 — Schematic illustration of Fucopol HMs preparation, comprising polymer dissolution in deionized water, immersion in $FeCl_3$ solution for polymer gelation and washing step.

3.1.2.3. Rheological Properties

The rheological behavior of FucoPol HMs was determined using a modular compact rheometer (MCR92, Anton Paar, Graz, Austria), equipped with a parallel plate geometry (diameter 20 mm) with a 1 mm gap. HMs samples with 25 mm of diameter and similar thickness (~2 mm) were equilibrated at 25 °C for 5 min. The viscoelastic properties were assessed by applying frequency sweeps at a constant tension within the linear viscoelastic region for a frequency range from 0.01 to 10 Hz.

3.1.2.4. FucoPol HMs Characterization

Based on the previous results, three different concentrations of FucoPol (1.0, 1.75 and 2.5 wt%) were selected to be combined with Fe^{3+} at a concentration of 1.5 g/L. The obtained membranes were labeled as HM1, HM2 and HM3, respectively. The prepared HMs were cut with a stainless-steel cylindrical mold (25 mm diameter) to promote better handling. Additionally, to remove all uncrosslinked Fe^{3+}, smaller HMs samples were washed with deionized water (250 mL) under continuous stirring (150 rpm) until constant conductivity (~1 μS/cm) was achieved.

3.1.2.4.1. Chemical Characterization

The water content of the hydrogels was assessed gravimetrically by freeze drying using the equation 2.2.1.

For the quantification of the HMs' iron content, freeze-dried FucoPol HM samples (~5 mg) were hydrolyzed with nitric acid (5 mL HNO_3 5% v/v) at 120 °C for 2 h. Hydrolyzed samples were filtered, and their iron content was determined via ICP-AES (Horiba Jobin-Yvon, France, Ultima model) equipped with a 40.68 MHz RF generator, Czerny–Turner monochromator with 1.00 m (sequential), autosampler AS500 and Concomitant Metals Analyzer. Nitric acid solution (HNO_3 5% v/v) was subjected to the same hydrolysis procedure and used as blank.

3.1.2.4.2. Morphology

The morphology of the FucoPol HMs were investigated by SEM equipped with a refrigerated sample holder. Wet HMs samples were placed in the sample holder, and small cuts were performed on its surface using a scalpel to promote better observation of the inner microstructures. The observations were performed at -4 °C using magnifications of 500× and 1000×.

3.1.2.4.3. Porosity

The porosity of the FucoPol HMs was evaluated via the solvent replacement method, as described in section 2.3.2.3.2, using freeze-dried HM samples with 13 mm diameter.

3.1.2.4.4. FT-IR Spectroscopy

FucoPol and FucoPol HMs were characterized via FT-IR spectroscopy as described in section 2.3.2.5.

3.1.2.4.5. XRD Analysis

The crystalline structure of FucoPol and the FucoPol HMs was studied/analyzed using a diffractometer (X'Pert Pro, PANalytical, Almelo, The Netherlands) with a monochromatic Cu Ka radiation source with a wavelength of 1.5406 Å. Measurements were carried out from 10 to 50° (2θ) with a scanning step size of 0.016° in the continuous scanning mode.

3.1.2.4.6. TGA Analysis

The TGA of FucoPol and FucoPol HMs was performed using thermogravimetric analyzer Setaram Labsys EVO (Setaram, Sophia Antipolis, France) in a temperature range from room temperature to 500 °C with a heating rate of 10 °C/min under an argon atmosphere. The 5% weight loss ($T_{5\%}$, °C) was attributed to the temperature at which the initial 5% of the mass was lost, and the thermal degradation temperature (T_{deg}, °C) was assigned to the temperature value obtained for the maximum decreasing peak of the sample mass.

3.1.2.4.7. Compressive Mechanical Analysis

The compressive mechanical properties of the FucoPol HMs were assessed with a texture analyzer TMS-Pro, equipped with a 250 N load cell. HMs samples with a thickness of 2–3 mm were cut into a cylindrical shape (25 mm diameter) and were compressed up to 50% strain of the original height at a speed rate of 60 mm/s using a plunger with a 37 mm diameter. Mechanical parameters including hardness, compressive modulus and toughness were calculated as described in section 2.3.2.3.3.

3.1.2.4.8. Water Retention Capacity

To determine the water retention capacity of FucoPol HMs, cylindrical samples (25 mm diameter, 2 mm thickness) were placed in a desiccator with two different saturated salt solutions, magnesium nitrate ($Mg(NO_3)_2$) and potassium sulfate (K_2SO_4), to provide relative humidity (RH) values of 55% and 99%, respectively. Samples were taken out from the desiccator at specific intervals and were weighed (W_t). The influence of temperature was also evaluated by performing the experiments at 20 and 30 °C. Water retention (%) was determined with the following equation (3.1.1):

$$Water\ retention = \frac{W_t}{W_{wet}} \times 100 \tag{3.1.1}$$

where W_{wet} represents the initial weight of the HMs.

3.1.2.4.9. Swelling Behavior

The swelling properties of the FucoPol HMs were assessed gravimetrically by immersing pre-weighed freeze-dried samples in deionized water and NaCl 0.9% (v/v) at room temperature for 96 h, as described in section 2.3.2.3.5.

3.1.2.4.10. Gel Fraction

For the determination of the gel fraction, which represents the crosslinking density in the hydrogel structure, freeze-dried samples of the HMs were immersed in deionized water at room temperature for 72 h. After that period, rehydrated HMs samples were freeze-dried again, and the gel fraction (%) was determined using the following equation (3.1.2):

$$Gel\,fraction = \frac{W_f}{W_{dry}} \times 100 \qquad (3.1.2)$$

where W_f and W_{dry} represent the dry weight (g) of HMs samples after and before immersion in deionized water, respectively.

3.1.2.5. Biological Assays

3.1.2.5.1. Cell Culture and Culture Media

Biological assays were performed with two cell lines acquired from American Type Culture Collection (ATCC, Manassas, VA, USA): human primary dermal fibroblasts (PCS-201-010) and human leukemia monocytic cell line THP1 (TIB-202). Fibroblasts cells were cultured in Dulbecco's modified Eagle medium (DMEM, Thermo Fisher Scientific, Waltham, MA, USA) supplemented with 10% (v/v) fetal bovine serum (FBS, Thermo Fisher Scientific) and a mixture of 100 U/mL of penicillin and 100 µg/mL of streptomycin (Thermo Fisher Scientific). THP1 cells were cultured in Roswell Park Memorial Institute medium (RPMI 1640, Thermo Fisher Scientific) supplemented with 10% (v/v) FBS, 1x MEM Non-Essential Amino Acids Solution (Thermo Fisher Scientific) and a mixture of 100 U/mL of penicillin and 100 µg/mL of streptomycin (Thermo Fisher Scientific).

3.1.2.5.2. Cytotoxicity Tests

For the cell viability experiments, fibroblasts cells were seeded in a 24-well plate at a concentration of 1×10^5 cells per well and were incubated at 37 °C, 5% (v/v) CO_2 and 99% (v/v) relative humidity. After 24 h for cell adherence, samples of FucoPol HMs (5 mm diameter) were added to a well with cells and to a well without cells, which were used as a control. Upon 24 h of exposure, the samples were removed, and the medium was replaced with a fresh medium (500 µL) supplemented with MTS, incubated (37 °C, 5% (v/v) CO_2) for 45 min. THP1 cells were cultured in a 24-well plate at a density of 1×10^5 cells per well, and samples of HMs (5 mm diameter) or 500 µg/mL Fucopol were added at the same time as cell seeding. Upon 24 h of exposure, the Cell Titer 96® Aqueous One solution cell proliferation assay (Promega, Madison, WI, USA) (200 µL) was added to the medium and incubated (37 °C, 5% (v/v) CO_2) for 60 min. Following incubation, the absorbance was measured at 490 nm according to the manufacturer's instructions. The cell viability of primary fibroblasts and THP1 exposed to FucoPol HMs was expressed in a percentage and was calculated using the equation described in section 2.4.2.10.

3.1.2.5.3. Anti-Inflammatory Activity

The analysis of the anti-inflammatory activity of the FucoPol HMs in THP1 cells proceeded as previously described with a few modifications [294]. Briefly, 1×10^6 THP1 cells were seeded in 6-well plates, incubated for 2 h with 7 µg/mL Lipopolysaccharide (LPS, Sigma Aldrich, St Louis, MO, USA) and were then incubated for 30 min or 3 h with the FucoPol HMs (13 mm diameter) or with 500 µg/mL of FucoPol. Identical samples without the addition of LPS were prepared (-LPS) for negative control purposes. In another approach, cells were simultaneously exposed for 2 h to both LPS and the FucoPol HMs or to 500 µg/mL of FucoPol. After the incubation time, cells were pelleted via centrifugation (500×*g*, 5 min) and solubilized in 300 µL of NZYol (NZYtech, Lisboa, Portugal), and RNA was extracted according to the manufacturer's instructions and reverse-transcribed with the NZY M-MulV First strand cDNA synthesis kit (NZYtech). The relative expression of the tumor necrosis factor α gene (*TNF-α*) and of the housekeeping gene *RNA18S* were determined using the Ct method ($2^{-\Delta\Delta Ct}$) [295] after real-time quantitative amplification using the NZYSupreme qPCR Green Master Mix (NZYtech) in a Corbett Rotor-Gene thermal cycler (Qiagen, Hilden, Germany).

3.1.2.6. Statistical Analysis

The experimental data from all the studies were analyzed, and the results are expressed as mean ± standard deviation (SD). Error bars represent the standard deviation ($n \geq 3$). Statistical analysis of biological studies was performed using one-way analysis of variance (ANOVA) followed by student's t-test (unpaired) using GraphPad Prism statistical software. Differences between results were considered statistically significant when the p-value was < 0.05.

3.1.3. Results and Discussion

3.1.3.1. Fabrication of FucoPol HMs

3.1.3.1.1. Effect of Fe^{3+} Concentration

The polyanionic character of FucoPol, given by the macromolecule's negatively charged groups, namely glucuronic acid and the acyl groups pyruvyl and succinyl, allowed the formation of physical crosslinking via electrostatic interaction with cations, leading to the formation of gel structures [296]. The cation-mediated gelation of FucoPol has been recently reported by Fialho et al. [292], who found that cations such as Fe^{3+} and Cu^{2+} promote the formation of FucoPol hydrogel beads. These structures were prepared by dropping a FucoPol solution (1wt%) into an $FeCl_3$ solution (1.5 g/L Fe^{3+}, 30 mL) through a needle (0.6 mm diameter). The resulting hydrogel beads revealed high stability in deionized water, NaCl 0.9% solution, and DMEM at 25 and 37 °C. After immersion for 24 h, no Fe^{3+} was detected in any of the media, which agrees with its revealed non-cytotoxicity properties.

Following such studies, the Fe^{3+}-mediated gelation of FucoPol was investigated to assess the impact of using different FucoPol and Fe^{3+} concentrations for HMs preparation. The effect of Fe^{3+} concentration on the rheological properties of FucoPol HMs was evaluated by combining the FucoPol concentration (1wt%) used for preparing hydrogel beads by Fialho et al. [292] with Fe^{3+} concentrations ranging from 0.05 to 9.95 g/L (Fig. 3.2). The selected range was demonstrated to be within the adequate values to promote FucoPol gelation. As shown in Fig. 3.2, for all the tested conditions, the G′ displayed higher values than the G″ over the entire frequency range, thus evidencing the structures' solid-like behavior and their predominant elastic character [297,298]. Furthermore, both moduli presented a low frequency-independent behavior, which indicates the formation of stable structures [250]. Analogous behavior has been reported for other cation-mediated hydrogels based on polysaccharides such as Ca^{2+}-gellan [299], Fe^{3+}-succinoglycan [287] and Fe^{3+}-xanthan gum [284].

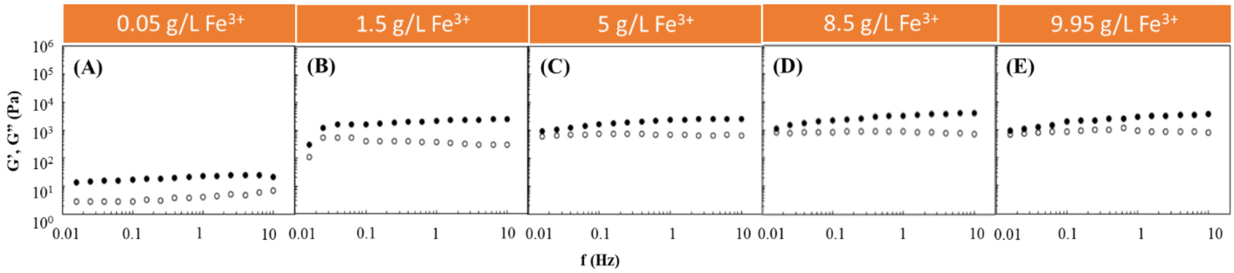

Figure 3.2 — Effect of Fe^{3+} concentration ((A) 0.05 g/L, (B) 1.5 g/L, (C) 5 g/L, (D) 8.5 g/L and (E) 9.95 g/L) on the storage (G', solid symbols) and loss (G", open symbols) moduli of FucoPol HMs prepared using 1wt% of FucoPol.

It can be observed that, for an angular frequency of 10 Hz, the lowest G' and G" values (0.020 and 0.007 kPa, respectively) were achieved for the lowest Fe^{3+} concentration (0.05 g/L) used (Fig. 3.2A). In this experiment, as the frequency increased, a slight increase in the G" value was observed that approached the G' value, indicating the hydrogel's lower resistance to deformation [300]. However, a significant increase in both moduli was noticed when the Fe^{3+} concentration was raised to 1.5 g/L (Fig. 3.2B). Interestingly, above this concentration, no significant impact on the rheological properties of the structures could be perceived because the G' and G" values remained within a range of 0.95–4.0 and 0.60–0.85 kPa (Fig. 3.2C–E), respectively, which are similar to the ones obtained using 1.5 g/L of Fe^{3+} (1.25–2.51 and 0.31–0.55 kPa, respectively) (Fig. 3.2B). The results suggest that a Fe^{3+} concentration of 1.5 g/L is likely enough for good crosslinking of the polymer's functional groups. Lu et al. [301] also described an improvement in the rheological properties of poly(ethylene glycol)-based hydrogels modified with dopamine by increasing the Fe^{3+} content in the dopamine:Fe^{3+} ratio from 1:07 to 1:1.

3.1.3.1.2. Effect of FucoPol Concentration

Based on the obtained results, an Fe^{3+} concentration of 1.5 g/L was chosen to study the effect of the FucoPol concentration on the HM's rheological properties. Therefore, Fucopol concentrations in the range of 0.5 to 2.5wt% were tested (Fig. 3.3). Higher FucoPol concentrations were not possible to test because of the polymer's high intrinsic viscosity that led to extremely viscous aqueous solutions. As shown in Fig. 3.3, all HMs exhibited a solid-like behavior similar to the ones obtained in the Fe^{3+} effect study (Fig 3.2). It can be observed that both moduli gradually increased as the polymer concentration rose. Increasing the FucoPol concentration from 0.5 to 2.5wt% resulted in an approximately 30-fold increase in the G' and G" values (Fig. 3.3A and 3.3D). Moreover, using 1.5 and 1.75wt% of FucoPol led to an increase in the G' (1.76–3.99 and 1.50–10.96 kPa, respectively) and G" (0.96–1.29 and 0.30–2.22 kPa, respectively) values' ranges (Fig. 3.3B and 3.3C). The results demonstrate that the maximum G' and G″ values (35.3 and 4.2 kPa, respectively) were obtained using the highest FucoPol concentrations (2.50wt%), for an angular frequency of 10 Hz (Fig. 3.3D). These values are lower than those reported for Fe^{3+}-succinoglycan hydrogel (~70 kPa) [287] and Fe^{3+}-xanthan gum (~60/70 kPa) [284] and are significantly higher than those described for Fe^{3+}-collagen hydrogels (~0.15 kPa) [302] for the same frequency value. This concentration dependence was also reported for Fe^{3+}-xylan hydrogels [303], where a considerable increase in the G′ value (~2.5 to ~10 kPa) was noticed using carboxymethyl xylan amounts of 0.02 and 0.08 g, respectively.

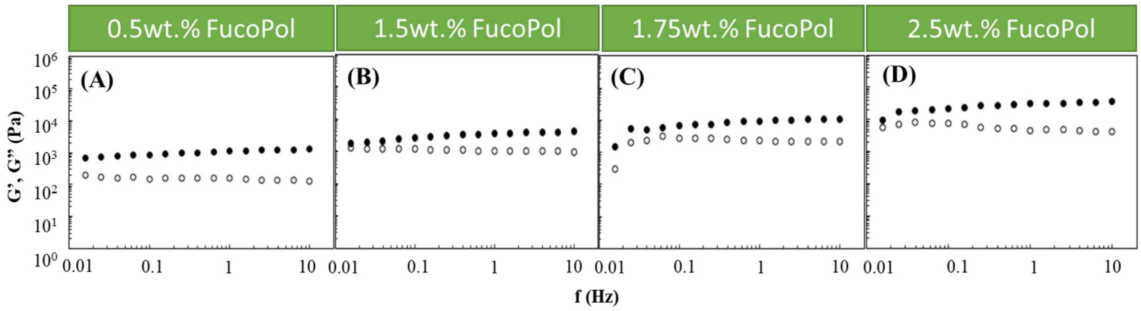

Figure 3.3 — Effect of FucoPol concentration ((A) 0.5wt%, (B) 1.5wt%, (C) 1.75wt% and (D) 2.5wt%) on the storage (G′, solid symbols) and loss (G″, open symbols) moduli of FucoPol HMs prepared using 1.5 g/L of Fe^{3+}.

In general, the obtained results demonstrate that both polymer and Fe^{3+} concentrations impact the hydrogel structure, and consequently, FucoPol HM strength can be tuned according to the desired application. Indeed, Fe^{3+} polysaccharide hydrogels comprising varied strengths and elastic properties have been reported as potential structures to be used in applications that include, for example, drug delivery and tissue engineering. For example, Fe^{3+}-succinoglycan hydrogels were used as a suitable platform for controlled drug delivery based on gel–sol conversion [287]. Moreover, a polyanionic hydrogel rich in carboxylates and sulphonates crosslinked with Fe^{3+} comprising G′ values between 102 and 104 Pa have been demonstrated to be a promising material in cartilage tissue engineering [304].

Based on the previous experiments, three different FucoPol concentrations (1.0, 1.75 and 2.5wt%) combined with 1.5 g/L of Fe^{3+} were selected to prepare FucoPol HMs with distinct rheological properties, which were named HM1, HM2 and HM3, respectively, and were characterized for their physical, chemical, and biological properties as described below.

3.1.3.2. Morphological Characterization

As shown in Fig. 3.4A, the three FucoPol HMs exhibited a similar macroscopic appearance, being translucid and displaying an orange coloration, given by the presence of Fe^{3+} cations.

However, color intensification and lower translucency were observed for the HM3 membranes, which might be related to their higher polymer and Fe^{3+} contents.

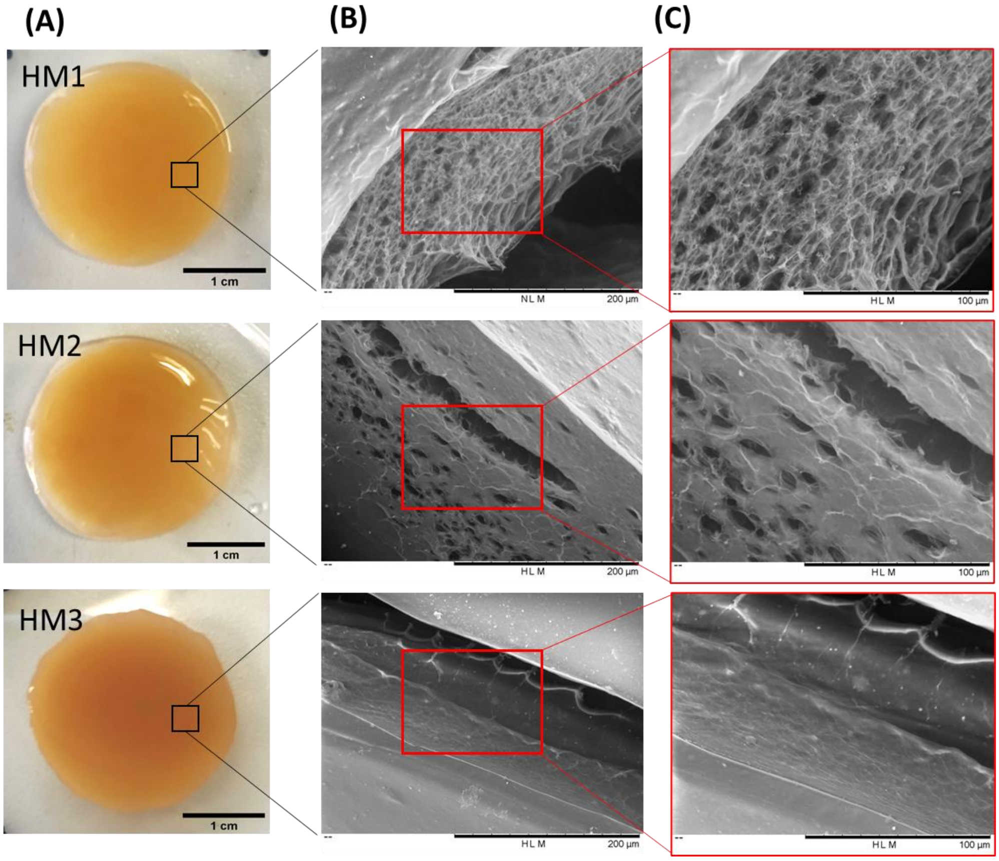

Figure 3.4 — FucoPol HMs: (**A**) macroscopic aspect and corresponding SEM images under (**B**) 500× and (**C**) 1000× magnifications.

To investigate the surfaces and inner morphology of the FucoPol HMs, SEM observations (Fig. 3.4B and 3.4C) were performed. The analysis revealed that all membranes presented a smooth surface, although some structural differences were noticed. The HM1 membranes showed a rather homogeneous three-dimensional network made of polymeric chains. Upon magnification (Fig. 3.4, top panel), it was possible to observe an irregular porous microstructure comprising pores of different sizes. A similar morphology was observed for Fe^{3+}-based FucoPol beads prepared with the same polymer concentration [292]. On the other hand, the HM2 membranes displayed a more heterogeneous and much less porous structure, containing several compact regions (Fig. 3.4, center panel). Additionally, for the HM3 membranes, an extremely consistent and dense microstructure could be observed (Fig. 3.4, bottom panel). These results suggest that polymer and Fe^{3+} content significantly impacted the HMs' microstructure. In fact, an increase in polymer and Fe^{3+} contents in the structures led to a gradual decrease in the porous regions, and the structures became more compact and tighter, likely promoted by higher crosslinking between the polymeric chains and the Fe^{3+} cations. A similar effect was reported for konjac glucomannan hydrogels, which showed a more stable structure and a compact morphology as the Fe^{3+} proportion increased [285].

The porosity of the HMs has an important role in several physicochemical properties of the structures, mainly those related to swelling behavior and drug loading ability [204,256]. As predicted by the SEM observations, the hydrogels' porosity decreased as the polymer content increased. Therefore, the highest porosity value was observed for the HM1 membranes (59.3 ± 8.3%), and the HM2 and HM3 membranes presented porosities of 22.1 ± 3.1 and 11.8 ± 0.6%, respectively (Table 3.1). A similar trend was reported for CGC-based [305], chitosan-PVA [256] and alginate-based [306] hydrogels, with the porosity of the hydrogels decreasing for higher polymer and/or crosslinker concentrations.

3.1.3.3. Chemical Characterization of FucoPol HMs

3.1.3.3.1. Composition

HM1, HM2 and HM3 presented polymer contents of 1.75 ± 0.001, 2.28 ± 0.163 and 2.83 ± 0.127wt% (Table 3.1), respectively, which demonstrates that increasing the initial polymer concentration led to the formation of membranes with higher polymer content. Moreover, the same trend was observed for the Fe^{3+} content of the membranes, with HM3 presenting the highest Fe^{3+} content (0.16 ± 0.010wt%), and lower values were obtained for the HM1 and HM2 membranes (0.06 ± 0.0002 and 0.10 ± 0.024wt%, respectively) (Table 3.1). These results can be explained by the higher number of anionic groups present in the HM3 hydrogels available to interact with Fe^{3+} cations, increasing their content in the structure.

Table 3.1 — Physical and chemical characterization and mechanical properties (under 90% strain) of FucoPol HMs prepared from the gelation of FucoPol with Fe^{3+} (1.5 g/L) using polymer concentrations of 1.0wt% (HM1), 1.75wt% (HM2) and 2.5wt% (HM3).

Sample ID	**HM1**	**HM2**	**HM3**
Polymer content (wt%)	1.75 ± 0.001	2.28 ± 0.163	2.83 ± 0.127
Fe^{3+} content (wt%)	0.06 ± 0.002	0.10 ± 0.024	0.16 ± 0.010
Water content (wt%)	98.19 ± 0.001	97.62 ± 0.187	97.02 ± 0.138
Mechanical properties			
Hardness (kPa)	32.4 ± 5.8	131.1 ± 6.5	221.9 ± 10.2
Compressive modulus (kPa)	56.3 ± 7.8	353.3 ± 24.9	523.3 ± 4.7
Toughness (kJ/m^3)	1.4 ± 0.1	34.5 ± 5.5	60.7 ± 2.7

As listed in Table 3.1, all FucoPol HMs presented a characteristic high water content [57,307] above 97wt%. These results are in accordance with previous work, in which FucoPol hydrogel beads prepared from an initial FucoPol concentration of 1.0wt% and gelled with 1.15 g/L Fe^{3+} displayed around 0.15wt% of Fe^{3+} and a water content of 98.60wt% [292]. The higher Fe^{3+} content obtained in the FucoPol Fe-P beads might be explained by the high content of FucoPol used in the pyruvyl (13–14wt%) and succinyl (3–5wt%) groups compared to those presented in this polymer (3.7 and 0.6wt%, respectively).

3.1.3.3.2. FT-IR Spectroscopy

The interaction between the functional groups of FucoPol and the Fe^{3+} cations was assessed via FT-IR analysis. As shown in Fig. 3.5, despite the similarity between the FucoPol and the HMs' FTIR spectra, the interaction with Fe^{3+} led to a shift in various absorption peaks, mainly those corresponding to the hydroxyl and carboxylate groups.

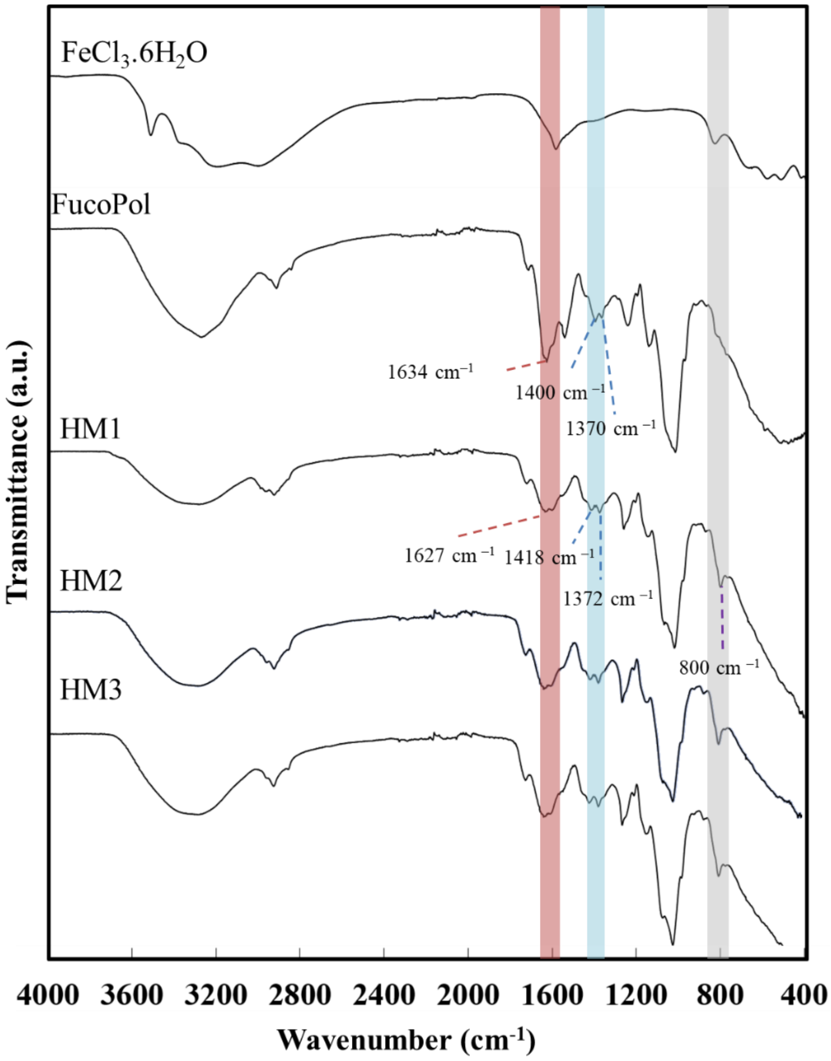

Figure 3.5 —FTIR spectra of $FeCl_3.6H_2O$, FucoPol, HM1, HM2 and HM3.

The intense broadband at 3277 cm^{-1}, characteristic of the O-H stretching of hydroxyl groups, and the weak vibration of the C-H stretching peak of CH_2 groups at 2924 cm^{-1} [308] were shifted to 3300 and 2927 cm^{-1}, respectively. Moreover, the absorption peaks at 1722 and 1020 cm^{-1}, corresponding to the acyl substituents of FucoPol, namely the C=O stretching of carbonyls and the C-O vibrations of the glycosidic bonds and C-C vibrations of the pyranoid ring [308], respectively, were also shifted to 1720 and 1016 cm^{-1}. The band of C–O–C vibrations of the acyls appearing at 1246 cm^{-1} in the FucoPol spectrum was also shifted to 1259 cm^{-1}. The peaks at 1634 and 1370–1400 cm^{-1}, attributed to the asymmetric and symmetric stretching of carboxylates from the glucuronic acid residue [308] were shifted to 1627 cm^{-1} and 1372–1418 cm^{-1}, respectively. The wavenumber separation between asymmetric and symmetric stretching vibrations could give information about the binding state of metal cations with -COO^{-} groups

[309]. For the HMs' spectra, wavenumber separations of 255 and 209 cm^{-1} were obtained, which suggest the presence of unidentate binding between Fe^{3+} and $-COO^{-}$ in the hydrogel's structure [310,311]. Additionally, compared to the FucoPol spectrum, a new peak at around 800 cm^{-1} was noticed in the HMs' spectra, which might be indicative of the bending of the Fe-O bond [312] from the interaction between the $-COO^{-}$ groups of FucoPol and Fe^{3+} cations.

3.1.3.3.3. XRD Analysis

The presence of Fe^{3+} in the structure of FucoPol HMs was also assessed via XRD. As shown in Fig. 3.6, FucoPol presents a diffractogram typical of an amorphous polysaccharide with no characteristic peaks, which is consistent with diffractograms previously reported for FucoPol and other polysaccharides [313]. On the other hand, the diffraction patterns of the HMs exhibited small peaks at around 28.2° and 35.5° (marked with * in Fig. 3.6), which correspond to the (−311) and (221) planes of iron chloride hydrate (ICDD card 033-0645), whose space group is C2/m. This observation confirms the presence of Fe^{3+} cations within the structures [314]. The low intensity of the peaks in the FucoPol HMs' patterns can be ascribed to the low amount of Fe^{3+} in the structures (Table 3.1) [314].

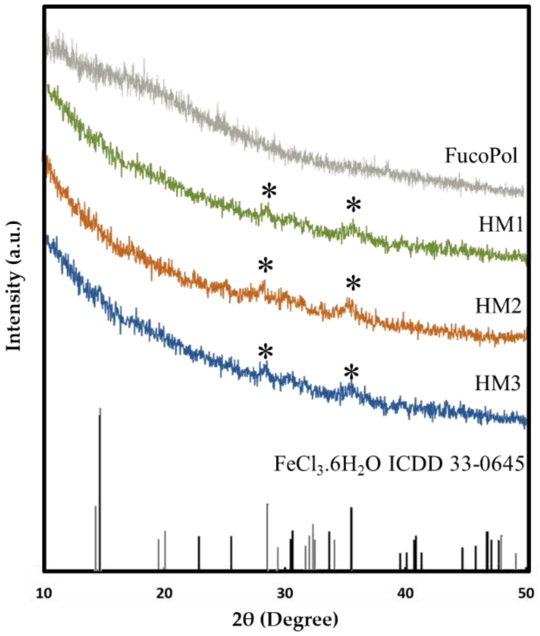

Figure 3.6 — X-ray diffraction patterns of FucoPol and HM1, HM2 and HM3 HMs.

3.1.3.3.4. Thermogravimetric Analysis

Similar TGA curves were observed for all samples, comprising three main thermal degradation steps (Fig. 3.7). In the first degradation step, an increase in temperature from 35–39 °C to 158–170 °C resulted in a weight loss between 6 and 13%, which can be related to the loss of adsorbed and structural water [315]. As shown in Fig. 3.7, up to temperatures of around 230 °C, the HM1 membranes displayed a degradation profile very similar to FucoPol, with similar weight losses (12.7 and 13.4%, respectively) (Table 3.2). The HM2 and HM3 samples, on the other hand, presented mass losses of 6.0 and 8.7%, respectively, and narrower temperature ranges indicative of a weak water binding capacity [291]. In fact, the higher temperature ranges and the higher weight loss observed for FucoPol and HM1 suggest that they strongly bind to water molecules due to the presence of more functional groups available to establish hydrogen bonds with water. In the HM2 and HM3 structures, those groups are involved in crosslinking with Fe^{3+} cations, which likely decreases the capacity for water binding. An analogous trend was reported by Concórdio-Reis et al. [291], who described a higher weight loss for FucoPol when compared to the biocomposite composed of FucoPol and silver nanoparticles. You et al. [316] also demonstrated that hydrogels of sodium alginate, gelatin and Ca^{2+} improve their thermal stability via the incorporation of copper/tannic acid nanosheets.

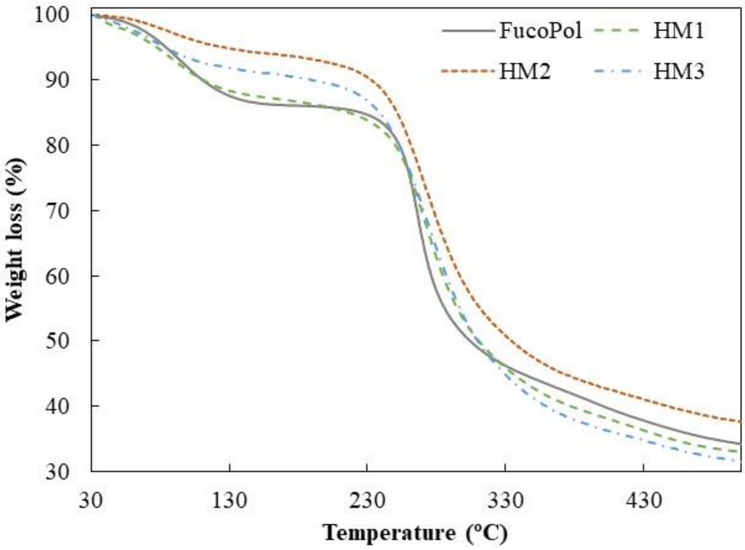

Figure 3.7 — Thermogravimetric curves of FucoPol and HM1, HM2 and HM3 HMs.

The second degradation step, attributed to the polysaccharide decomposition, begins at temperatures of around 164–194 °C, and a 5% mass loss was observed for a temperature range of 234.8–250.7 °C, with a maximum degradation rate from 266 to 272 °C (Table 3.2). For the FucoPol sample, the second and more significant weight loss (around 39%) occurred between 194 and 324 °C. The thermal degradation profile obtained was similar to that reported for FucoPol as well as for other structures based on FucoPol, such as silver nanocomposites [291] and Fe beads [292]. For the FucoPol HM samples, despite the degradation step starting at lower temperatures (164–186 °C) and higher weight losses being achieved (45.9–52.9%), the mass loss occurred more gradually when compared to the sharp profile obtained for FucoPol (Fig. 3.7). Moreover, those structures presented a T_{deg} of 271–272 °C, which is slightly higher than the value displayed by FucoPol (266 °C). These results suggest that the HMs had higher thermal stability, likely given by the crosslinking and coordinate interactions between Fe^{3+} and FucoPol [256]. Enhanced thermal stability was also reported for Fe^{3+}-konjac glucomannan hydrogels, which presented a higher T_{deg} (275 °C) than those of the other konjac glucomannan-based samples (235–265 °C) [285].

Table 3.2 — Thermal degradation steps and degradation temperature (T_{deg}) of FucoPol and FucoPol HMs.

Sample	1st Degradation Step		2nd Degradation Step				Char Yield (%)
	Temperature Range (°C)	**Weight Loss (%)**	**Temperature Range (°C)**	**Weight Loss (%)**	**T5% (°C)**	**Tdeg (°C)**	
FucoPol	37–166	13.4	194–324	39.2	250.7	266	34
HM1	36–170	12.7	186–370	45.9	244.8	271	33
HM2	39–162	5.9	174–374	49.0	240.0	272	38
HM3	35–158	8.5	164–378	52.9	234.8	272	31

As shown in Fig. 3.7, the gradual mass decrease observed after the second degradation step occurred due to the main-chain scission of the polysaccharide [291] and was identified as the third degradation step. Finally, all samples presented high char yields (31–38%), with the HM2 membranes exhibiting the highest value. Yang et al. [302] attributed this increase to a stronger crosslinking effect. In general, these results show that, although some differences were observed, the thermal properties of FucoPol were not significantly affected by the presence of Fe^{3+}.

3.1.3.3.5. Mechanical Properties

To assess the mechanical properties of the FucoPol HMs, a single compression (90% of the initial height) was applied to evaluate the membranes' hardness, compressive modulus, and toughness (Table 3.1). Fig. 3.8 shows the compressive stress–strain curves of HM1, HM2 and HM3, which demonstrated a linear elastic deformation under small strains (insert graph in Fig.

3.8), followed by a plateau attributed to the deformation of the porous structure via yielding or bending. After that, the denser structure due to the loss of pores resulted in significant strain hardening [317]. It can be noticed that the mechanical characteristics of HMs were significantly affected by their polymer and Fe^{3+} contents. Despite the similarities between the stress–strain profiles, HM1 and HM3 presented similar higher rupture strain values (88% and 86%, respectively), compared to that of the HM2 membrane (around 73%) for the same compressive stress value (90%) (Fig. 3.8).

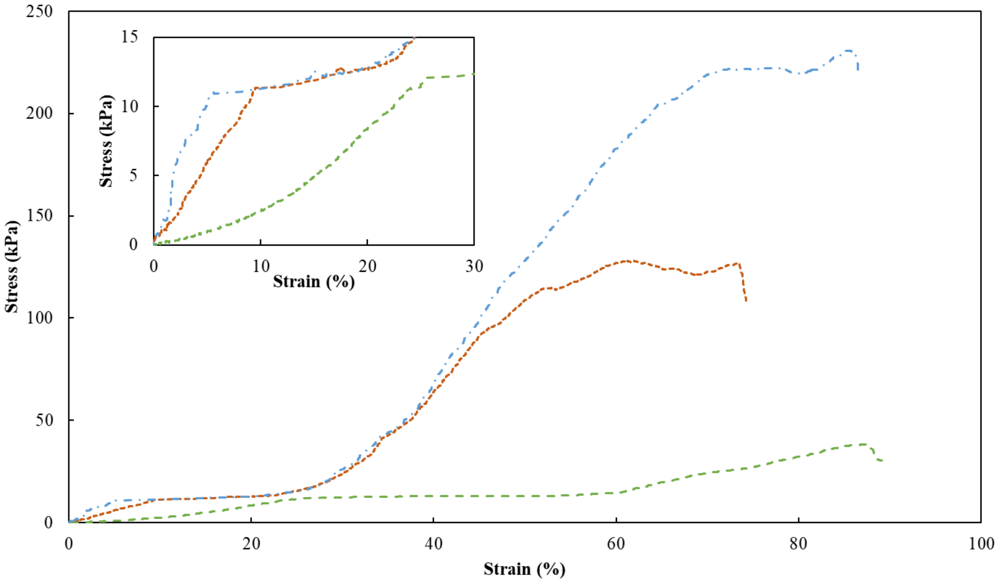

Figure 3.8 — Compression stress–strain curves of HM1 (dashed green line), HM2 (square dotted orange line) and HM3 (dash-dotted blue line) HMs. Insert graph highlights the initial linear deformation of the samples.

As presented in Table 3.1, the highest hardness (221.9 ± 10.2 kPa), compressive modulus (523.3 ± 4.7 kPa) and toughness values (60.7 ± 2.7 kJ/m^3) were achieved for the HM3 membranes. This result can be related to the higher polymer and Fe^{3+} contents of those membranes (2.83 ± 0.127 and 0.16 ± 0.010wt%, respectively) compared to the HM1 and HM2 membranes (1.75 ± 0.001 and 2.28 ± 0.163wt%, and 0.06 ± 0.002 and 0.10 ± 0.024wt%, respectively) (Table 3.1). Similar behavior was demonstrated for polyacrylamide/sodium alginate hydrogels, whose mechanical properties were improved by increasing the polymers' content [318]. Additionally, the introduction of Fe^{3+} in such structures led to the formation of a double crosslinked network, which significantly enhanced the mechanical features of the hydrogels, and as the Fe^{3+} increased from 4.76 to 13.04%, higher values of compressive strengths (495 and 820 kPa) were obtained. Popov et al. [319] also reported higher hardness and compressive modulus values for pectin hydrogels resulting from an increase in the crosslinking cation concentration. For instance, an increase of 24% in hardness was obtained when the Fe^{3+} concentration was increased from 21 to 42 mM. The improvement in the mechanical properties observed for the FucoPol hydrogels is in line and consistent with the SEM observations, which revealed a stronger, compacter and more stable morphology for the HM3 membranes when compared to the HM1 or HM2 membranes (Fig. 3.4).

3.1.3.3.6. Water Retention Capacity

The capacity of the FucoPol HMs to retain water inside their structures is determined by the van der Waals forces and hydrogen bonding established between the hydrogels and water molecules [320,321]. This feature plays an important role in several applications. The effect of temperature and relative humidity (RH) in the water retention behavior of the FucoPol HMs was evaluated by incubating samples under RH values of 55 and 99% at temperatures of 20 and 30 °C. The macroscopic appearance of all the membranes is shown in Fig. 3.9. It can be observed that, at the end of each experiment, the HM1 membranes presented a lighter coloration, whereas the HM2 and HM3 membranes intensified their color, and the membranes became brownish. Moreover, under high RH values (99%), all membranes remained flat regardless of the temperature used. On the other hand, under an RH ≈ 55%, likely due to faster water evaporation, wrinkling of the membranes was observed (Fig. 3.9).

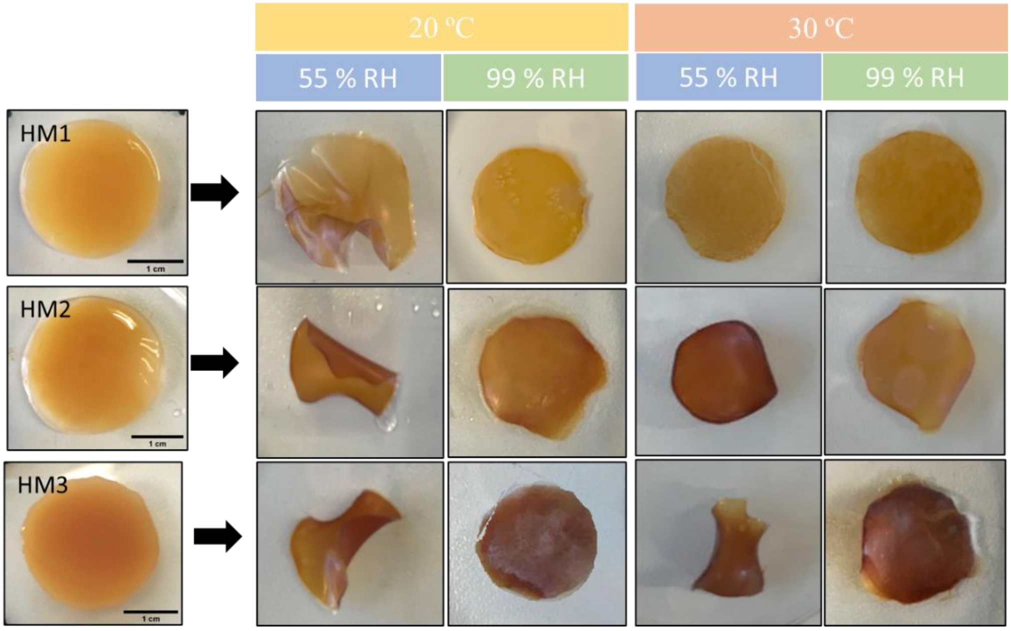

Figure 3.9 — Macroscopic appearance of HM1, HM2 and HM3 HMs samples after being subjected to all the conditions for the study of water retention ability.

As shown in Fig. 3.10, the RH strongly influenced the water retention ability of the membranes. In fact, under RH ≈ 55%, all membranes lost water sharply, and after 4 days of incubation, they were dry (water retention ~ 2%) (Fig. 3.10, dashed lines). In addition, 19 days were needed to achieve similar values for incubation carried out at RH ≈ 99% (Fig. 3.10, full lines). On the other hand, no significant differences were perceived for the incubation at 20 °C (Fig. 3.10A) or 30 °C, as similar profiles were observed at both temperatures for all membranes (Fig. 3.10B). However, for all membranes, the water loss rate was higher at 30 °C when compared to that obtained at 20 °C for the same RH value (99%). This behavior of a higher water release with an increase in temperature has also been reported for other polysaccharide hydrogels, such as those based on CMC [322] or chitosan [320].

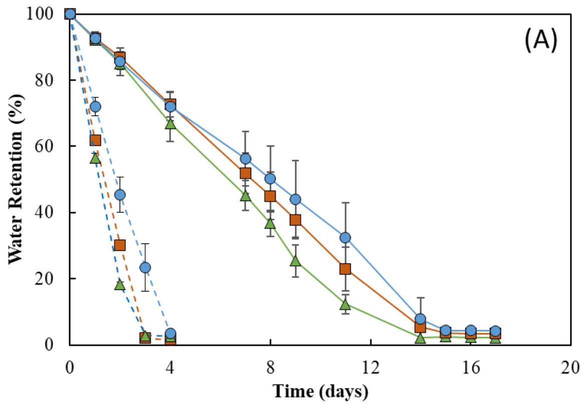

Figure 3.10 — Water retention behavior of HM1 (▲), HM2 (■) and HM3 (●) HMs at (**A**) 20 °C and (**B**) 30 °C under 55% (dashed lines) and 99% (full lines) relative humidity.

Fig. 3.10 shows that the water retention ability of the FucoPol HMs was influenced by their polymer and Fe^{3+} contents. For all tested conditions, the HM3 membranes revealed the highest capacity to retain water in their structure, whereas the lowest water retention ability was demonstrated by the HM1 membranes. This difference can be mostly noticed at 30 °C and 99% RH, where HM3 membranes retained approximately 15% more water than that of the HM1 membranes during the experiment. Under those conditions, after 13 days, the HM1 membranes presented a water retention value of 1.9 ± 0.9%, and a significantly higher value (23.5 ± 3.4%) was obtained for the HM3 membranes (Fig. 3.10B). This variation might be explained by the high degree of the crosslinking present in the HM3 membranes, which likely strengthened the physical structure of the hydrogel's network, promoting water retention inside the structure [323]. Several authors have reported a similar influence of polymer and crosslinker contents on the water retention ability of polysaccharide hydrogels. For example, Kang et al.

[320] demonstrated that increasing the concentration of 2,3-dialdehyde cellulose (DAC) from 2.5 to 10% (w/v) in DAC/chitosan hydrogels led to an increase in their water retention ability from ~30% to ~45% after 11 h, at 25 °C. Araújo et al. [305] reported a higher water retention capacity (87.3 to 90.2%) for CGC-based hydrogels with a polymer content of 3.09 ± 0.22wt%, compared to 84.6–86.2% for structures with lower polymer concentrations (2.40 ± 0.15wt%) after 30 min, at 37 °C. Similarly, polyethyleneimine/pectin hydrogels decreased their water retention capacity when the loaded polydopamine/copper nanoparticles were increased from a ratio of 8:0 to 8:2 [324].

3.1.3.3.7. Swelling Behavior and Gel Fraction

The water absorption capability (swelling behavior) of FucoPol HMs was evaluated by immersing previously freeze-dried samples in deionized water or NaCl 0.9% at room temperature for 96 h. Macroscopically, after freeze-drying, the membranes retained their dimensions (Fig. 3.11A), demonstrating that water removal had no significant impact on the polymer's network. However, the dried membranes presented a lighter brownish coloration, becoming extremely light and brittle. Upon rehydration, besides keeping their dimensions in either medium, all membranes also regained their original orange coloration and translucency. However, the rehydrated membranes were much more fragile (Fig. 3.11B and 3.11C).

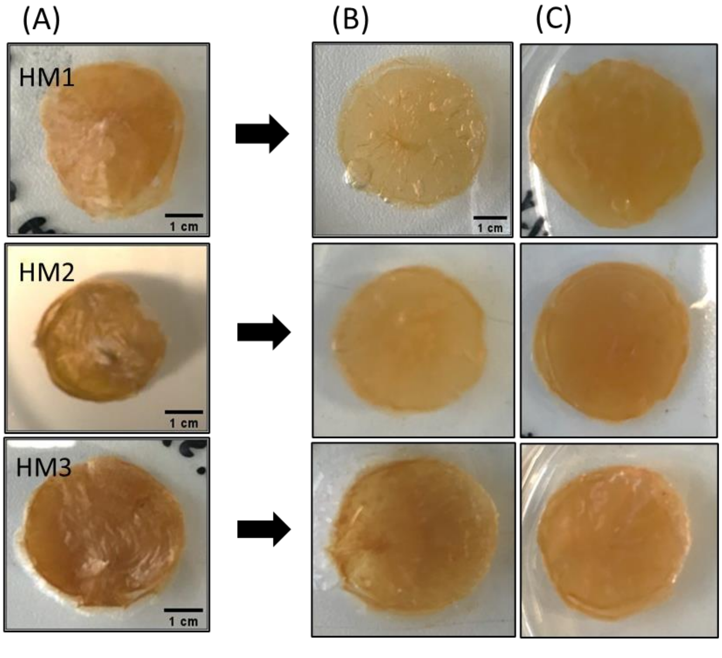

Figure 3.11 — Macroscopic appearance of (**A**) freeze-dried, (**B**) water-swollen and (**C**) NaCl 0.9% swollen HM samples.

As shown in Fig. 3.12 all the HMs revealed a good water absorption ability, explained by the high hydrophilicity of FucoPol given by the presence of -OH and -COOH groups on its structure [290,318]. It can be noticed that, for all the samples, the swelling equilibrium was achieved in the first 24 h in both media and remained constant thereafter (Fig. 3.12). Upon immersion in the aqueous media for 24 h, the HM1 membranes achieved swelling equilibrium and showed high swelling ratios, as follows: 22.3 ± 1.8 g/g for deionized water and 17.4 ± 1.3 g/g for NaCl. For a similar period, lower swelling ratio values were obtained for the HM2 (15.4 ± 0.3 and 15.0 ± 1.1 g/g) and HM3 (11.8 ± 2.8 and 11.9 ± 1.0 g/g) membranes. These differences can be attributed to an increase in the crosslinking density of those structures compared to the HM1 membranes, which led to a decrease in their ability to sustain water inside the structures [284,325].

Interestingly, the swelling ratio of the HM1 membranes was higher in deionized water (Fig. 3.12A) than in NaCl 0.9% (Fig. 3.12B). After 96 h, the membranes placed in water achieved a swelling ratio of 21.3 ± 1.7 g/g, whereas lower values were obtained in NaCl 0.9% (18.9 ± 0.7 g/g). The decrease in the swelling ability of NaCl 0.9% can be attributed to a lower osmotic pressure difference among the hydrogels and the medium, causing a decrease in the network volume and a shrinkage of the hydrogel. Analogous results were reported for CGC-based [305] and cellulose nanocrystal hydrogels [326].

This behavior was not noticed for the HM2 and HM3 membranes because similar swelling ratios were displayed in water (15.8 ± 0.3 and 11.9 ± 1.6 g/g, respectively) and in NaCl 0.9% (15.8 ± 0.5 and 12.7 ± 0.6 g/g, respectively). These results suggest that the swelling ratio of the HM2 and HM3 membranes is independent of the ionic strength of the solution, which might be explained by the lower size of the structure's mesh that prevents the shielding of Na^+ ions from the polymer's carboxylate groups [327].

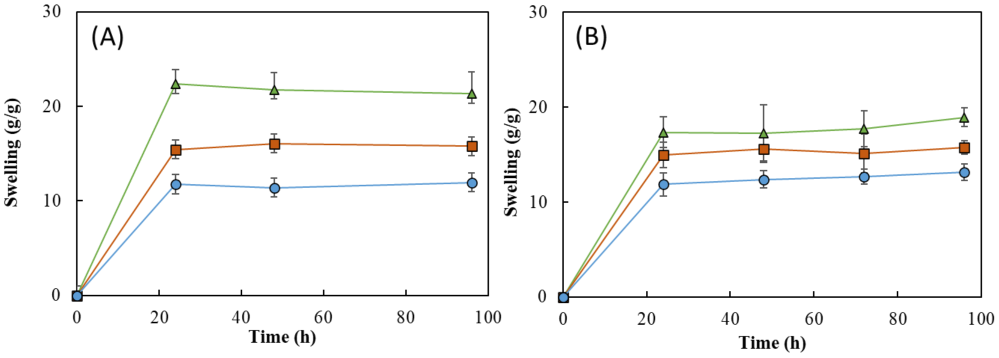

Figure 3.12 — Swelling behavior of HM1 (▲), HM2 (■), and HM3 (●) HMs in (**A**) deionized water and (**B**) NaCl 0.9%, at room temperature.

The ionic crosslinking density of HMs was assessed for the gel fraction study (Fig. 3.13). The gel fraction describes the degree of crosslinking present in the hydrogel polymer matrix, and its value is inversely proportional to the swelling capacity [328]. In fact, the HM3 membranes presented a slightly higher gel fraction (105.3 ± 2.0%) than that of either HM2 or HM1 (101.4 ± 1.9 and 98.3 ± 1.2%, respectively), which is consistent with the higher polymer and Fe^{3+} contents present in the HM3 membranes (Table 3.1). Moreover, increasing the crosslinker concentration induced a decrease in the polymer chain relaxation, causing low swelling of the hydrogel [329]. Similar behavior was demonstrated for the Fe^{3+}-xanthan gum hydrogels [284], for which the swelling ratio was lowered from 26.92 to 2.31 g/g when the polymer concentration increased from 0.01 to 0.07 g/mL.

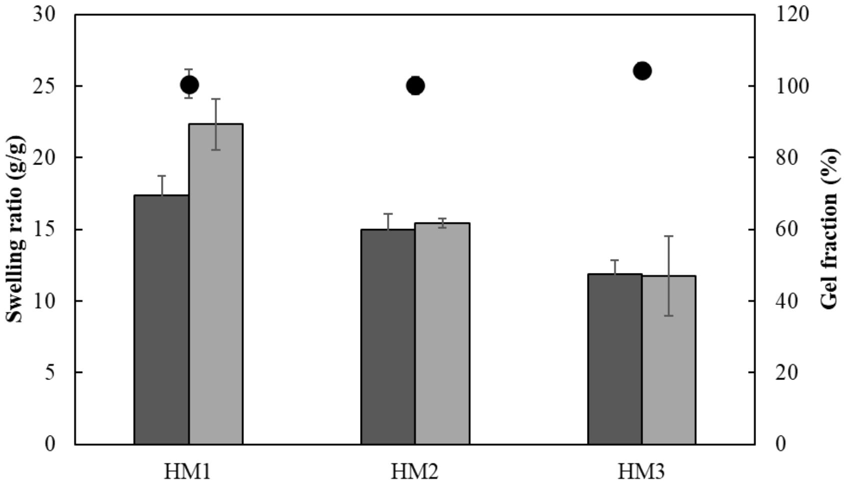

Figure 3.13 — Swelling ratio (columns) after 24 h and gel fraction (●) of HM1, HM2 and HM3 HMs in deionized water (light grey) and NaCl 0.9% (dark grey) determined at room temperature.

3.1.3.3.8. Cytotoxicity of FucoPol HMs

The cytotoxicity of the HMs was accessed in two human cell lines, an acute monocytic leukemia cell line, THP1, a suspension cell line and normal human dermal fibroblasts, an adherent type of cell line. After 24 h of exposure to each HM, the cells' viability was analyzed using MTS colorimetric assay, and the percentage of cell viability was calculated after normalization with control cells (untreated). The results show that no statistically significant alterations were detected in the cell viability after exposure to FucoPol HMs compared to the control (Fig. 3.14), demonstrating the non-cytotoxic potential of HMs as previously described by our group for FucoPol [292].

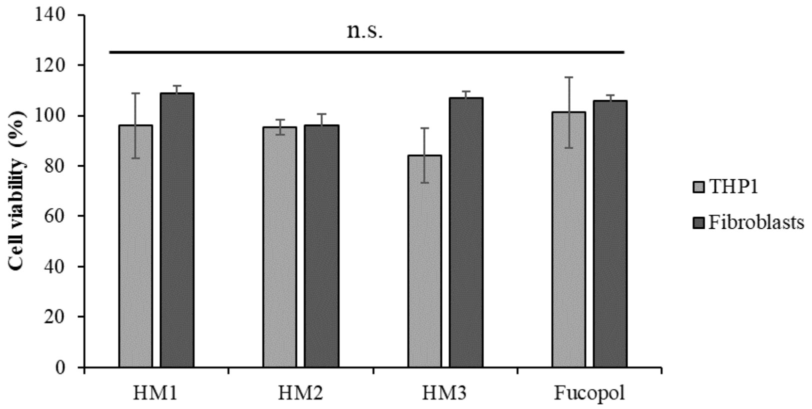

Figure 3.14 — Acute monocytic leukemia cell line, THP1 (light grey bars) and normal dermal fibroblasts (dark grey bars) cell viability (percentage) after 24 h of exposure to HM1, HM2 and HM3 HMs and 500 µg/mL of FucoPol. Bars represent the average ± SD of three independent experiments. ns—non-statistically significant.

3.1.3.3.9. Anti-Inflammatory Activity

The potential anti-inflammatory activity of the FucoPol HMs was examined in acute monocytic leukemia cells, THP1, after or simultaneously to their exposure to an inflammatory stimulus caused by a bacterial lipopolysaccharide (LPS) by analyzing the expression levels of the proinflammatory cytokine tumor necrosis factor alpha (*TNF-α*) (Fig. 3.15). As expected, TNF-α expression in samples incubated for 2 h with LPS showed a very high level (12x compared to the control) that reduced after 2h30 and 5 h of incubation, but it remained higher than that of the control (≅5.5×) (Fig. 3.15A). Interestingly, the addition of the FucoPol HMs to THP1 cells 2 h after the stimulus with LPS resulted in a decrease in *TNF-α* expression (Fig. 3.15B) of more than 80% for all membranes when compared to the control samples (incubated with LPS) (Fig. 3.15C). FucoPol was able to induce a reduction in *TNF- α* expression after 2h30 but not after 5 h of exposure (Fig. 3.15B). When samples were not previously stimulated with LPS, no statistically significant alterations were detected in the *TNF-α* expression of the cells exposed to the membranes, as opposed to a statistically significant increase in the TNF- *α* expression when cells were incubated with FucoPol (Fig. 3.15D). Moreover, the simultaneous exposure of THP1 cells to LPS and FucoPol HMs resulted in the decreased expression of *TNF-α* when compared to cells only incubated with LPS, with a higher reduction observed when cells were incubated with HM3 (Fig. 3.15D), indicating that the high level of iron content and mechanical characteristics of this membrane could indicate their more suitable application to avoid inflammatory processes. In general, these results show the anti-inflammatory potential of the HMs in cells previously stimulated with an inflammatory agent or during the inflammatory process, which might be a highly positive feature for the treatment of inflammatory diseases or to control inflammatory processes.

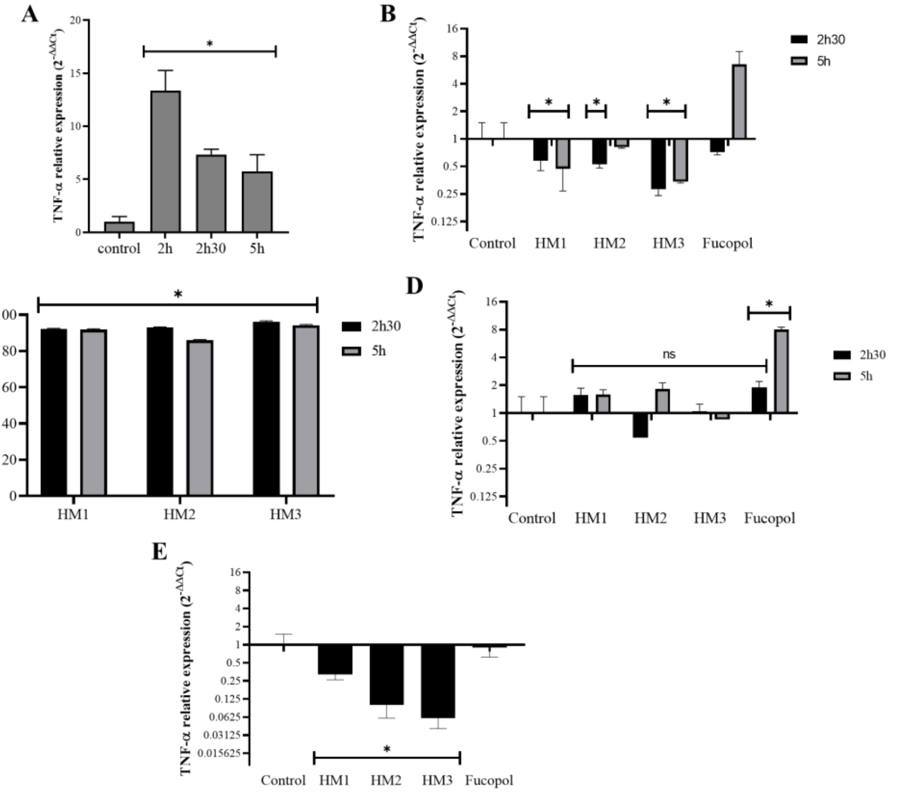

Figure 3.15 —Effect of HMs on *TNF-α* expression levels in THP1 cells. Inflammation in THP1 cells was stimulated for 2 h via the addition of 7 µg/mL lipopolysaccharides (LPS), and then the HMs or 500 µg/mL of FucoPol were added. In parallel, cells were submitted to the same treatment but without LPS. (**A**) *TNF-α* expression after 2 h, 2h30 and 5 h in LPS-treated samples calculated with $2^{-\Delta\Delta Ct}$ using the *RNA 18S* and corresponding LPS untreated samples as reference. (**B**) *TNF-α* expression after 2 h 30 and 5 h in LPS-treated samples that were exposed to the HMs and FucoPol for 30 min (2h30 samples) and 3 h (5 h samples), calculated with $2^{-\Delta\Delta Ct}$ using the *RNA 18S* and corresponding LPS control samples as reference. (**C**) Percentage of reduction in *TNF-α* expression in HM-treated samples relative to the respective control sample (treated with LPS and collected at the same time point). (**D**) *TNF-α* expression after 2h30 and 5 h in LPS untreated samples that were exposed to the HMs and FucoPol for 30 min (2h30 samples) and 3 h (5 h samples), calculated with $2^{-\Delta\Delta Ct}$ using the *RNA 18S* and corresponding control samples as reference. (**E**) *TNF-α* expression after 2 h in samples that were simultaneously submitted to LPS and to the HMs or FucoPol, calculated with $2^{-\Delta\Delta Ct}$ using the *RNA 18S* and corresponding LPS untreated samples as reference. Bars are the average ± SD of three independent experiments. **p*-value below 0.05 relative to control; ns—non-statistically significant.

3.1.4. Conclusions

This study demonstrates for the first time the preparation of hydrogel membranes based on the polysaccharide FucoPol, using Fe^{3+} as a crosslinking agent. From oscillatory shear measurements, it was shown that the FucoPol concentration had a significant impact on the HMs' strength. Regarding the effect of the Fe^{3+} concentration, for values above 1.5 g/L, a minimal effect was observed. Three FucoPol concentrations (1.0, 1.75 and 2.5wt%) were selected to be combined with Fe^{3+} (1.5 g/L), whose presence was confirmed via structural analysis. Despite the high water content of all the prepared HMs, their morphology and their mechanical, water retention and swelling properties were affected by their composition. Moreover, HMs did not show cytotoxic activity in two different human cell lines (leukemia cells line and normal primary human fibroblasts) but showed anti-inflammatory capability in cells previously stimulated with an inflammatory agent or during the inflammatory process, which might be a highly positive feature for the treatment of inflammatory diseases or to control the development of inflammatory processes. Overall, this study demonstrates the promising potential of FucoPol as a versatile material for HM fabrication, offering tunable properties, biocompatibility, and anti-inflammatory activity.

3.2. Exploring the drug loading and release ability of FucoPol hydrogel membranes

The results shown in this chapter are part of the following published paper:

- **Araújo, D.**, Martins, M., Freitas, F. Exploring the drug and release ability of FucoPol hydrogel membranes. International Journal of Molecular Science 2023, 24, 14591. https://doi.org/10.3390/ijms241914591

Summary

FucoPol hydrogel membranes (HMs), fabricated by ionic gelation using Fe^{3+} as a crosslinking agent, were tested for the first time as delivery systems. The HMs prepared with a FucoPol solution of 1wt% combined with 1.5 g/L Fe^{3+} (HM1 membranes) were successfully loaded with caffeine or diclofenac sodium as model drugs by either diffusion (HM1_D_{CAF} and HM1_D_{DS}, respectively) or mixing (HM1_M_{CAF} and HM1_M_{DS}, respectively) methods. However, the diffusion method led to a higher caffeine loading (101.9 ± 19.1 mg/g) within the HM structure, while the mixing method resulted in a higher diclofenac sodium loading (82.3 ± 5.1 mg/g). The HM1_D_{CAF} membranes were characterized by increased mechanical and rheological parameters such as their hardness (130.0 ± 5.3 kPa) and storage modulus (1014.9 ± 109.7 Pa), compared to the HM1_D_{DS} membranes that exhibited lower values (7.3 ± 1.2 kPa and 19.8 ± 3.8 Pa, respectively) probably due to a leaching phenomenon during the drug loading process. The release profiles revealed a fast release of both APIs from the HM1_D_{CAF} and HM1_D_{DS} membranes, while a prolonged and sustained release was obtained from the HM1_M_{CAF} and HM1_M_{DS} membranes. Moreover, for all API-loaded membranes, the release mechanism followed Fickian diffusion with the release rate being essentially governed by the diffusion process. These findings demonstrate FucoPol HMs' potential to be used as a platform for drug delivery.

3.2.1. Introduction

Polysaccharide HMs are hydrated porous media constructed by hydrophilic polymers that crosslink to form a three-dimensional network structure [70,274]. Their unique properties, including high water content, flexibility, and good mechanical strength, allow their use in several topical and transdermal applications such as drug delivery systems [70] and wound dressings [276]. Polysaccharide HMs have been described as promising structures for use as transdermal drug delivery systems since they provide the protection of the drugs from hostile environments (e.g., enzymes' degradation and low pH) and promote the release of the loaded drugs in a desired site [330,331].

Loading HMs with active pharmaceutical ingredients (APIs) is an important step in developing drug delivery systems. Several approaches have been used to incorporate APIs within the HMs structure, including permeation/diffusion, entrapment/mixing, and covalent bonding [257,332]. The permeation approach is a simple and easy method that involves the adsorption of the drug onto the membrane structure by soaking the pre-formed membrane in a drug-containing solution. Following this method, the drug diffuses slowly into the gel according to several factors such as structure porosity, drug size, and chemical properties. This approach is only suitable for loading small molecules that can easily migrate through the small pores of the hydrogel. It allows high loading efficiencies of hydrophilic drugs and decreases the possibility of drug deactivation [332,333]. The entrapment method consists of physically trapping the drug within the hydrogel's matrix by mixing it with the polymer solution prior to gelation. This method allows the loading of larger and hydrophobic drugs and increases the duration of release time. However, in addition to increasing the chance of drug deactivation, it can also lead to unnecessary crosslinking [334,335]. Drugs' release from hydrogels loaded by either method usually presents an initial burst release due to the drug concentration gradient between the hydrogel and the surrounding environment [332,334].

Diclofenac sodium is a nonsteroidal anti-inflammatory drug (NSAID) commonly used for the treatment of pain and inflammation. Its properties, such as small molecular weight, lipophilic nature, and ability to penetrate the skin barrier, make it a good candidate for transdermal drug delivery [336]. Diclofenac sodium is sparingly water-soluble, however has good solubility in various organic solvents (e.g., ethanol, dimethylsulfoxide), making it easy to incorporate into HMs using diverse loading methods, including permeation [333,337] and entrapment [263,335]. Caffeine is a stimulant of the central nervous system, and it is widely used as a model hydrophilic compound for skin toxicology studies. Its topical application prevents excessive fat accumulation in the skin, supports lymphatic drainage, and protects the skin from photo-damage [338,339]. Due to its properties, caffeine has been integrated into various topical or transdermal formulations for different applications, including scalp stimulation to promote hair growth [340] and antiaging and antioxidant agent in skincare creams [341].

Based on their properties, namely porous morphology, flexibility, and swelling behavior, the HM1 membranes prepared with 1wt% FucoPol (Chapter 3.1) were selected to investigate their ability as drug release systems. In this study, the HM1 FucoPol membranes were loaded with caffeine or diclofenac sodium as model drugs. The impact of the loading method used, diffusion or mixing, was evaluated, and the loaded HMs' mechanical and rheological properties were characterized. Finally, their drug loading and release capacity was evaluated envisaging their future use as drug delivery systems.

3.2.2. Materials and Methods

3.2.2.1. Materials

FucoPol composed of 36%mol of fucose, 33%mol of glucose, 26%mol of galactose, and 5%mol of glucuronic acid, with a total acyl group content of 7.8wt%, was obtained from the cultivation of the bacterium *Enterobacter* A47, as described by Concórdio-Reis et al. [293]. The polymer presented a protein content of 14.3% and an inorganic salt content of 1.4%. It has a molecular weight of 3.19×10^{6} Da, with a polydispersity index of 1.90. Caffeine (99%) and diclofenac sodium salt (98%) were purchased from Alfa Aesar and Tokyo Chemical Industry Co, respectively.

3.2.2.2. Preparation of HM1 membranes

The HM1 membranes were fabricated as described in section 3.1.2.2. Briefly, a FucoPol solution (1wt%) was cast into a cylindrical silicone (50 mm diameter, 3 mm height) mold and immersed into an aqueous $FeCl_3$ solution (1.5 g/L of Fe^{3+}, 250 mL), at room temperature, for 2 h. After a washing step with deionized water (250 mL, 1 h), the HMs were removed from the mold and cut with a stainless-steel cylindrical mold (25 mm diameter) to promote better handling. Then, an additional washing step with deionized water (250 mL) was performed under continuous stirring (150 rpm) until constant conductivity (~1 µS/cm) was achieved. Finally, the HM1 membranes were freeze-dried (-98 °C, 0.03 mbar) and the obtained structures were stored in a closed vessel, at room temperature, until further use.

3.2.2.3. Loading of the HM1 membranes with APIs

The HM1 membranes were individually loaded with each of the APIs, namely caffeine (99%, Alfa Aesar) or diclofenac sodium salt (98%, Tokyo Chemical Industry Co) through two different methods: diffusion and mixing. For the APIs loading by diffusion, the pre-weighed freeze-dried HM1 membranes were immersed in caffeine (1.0wt%) or diclofenac sodium (0.1wt%) solutions, at room temperature, for 24 h. After that period, the loaded HMs were removed from the API solutions, the excess solution was removed by blotting with filter paper, and the samples were freeze-dried. The obtained HM1 membranes loaded with caffeine and diclofenac sodium were labeled as HM1_D_{CAF} and HM1_D_{DS}, respectively. The APIs loading by the mixing method was performed by mixing 2.5 mg of the API powder with the freeze-dried FucoPol sample (100 mg) and dissolving the mixture in deionized water (10 mL), under continuous magnetic stirring (800 rpm), at room temperature. Then, the solution was cast into the silicone mold, and gelation was promoted by immersion in an aqueous $FeCl_3$ solution (1.5 g/L of Fe^{3+}), for 2 h. Afterwards, the API-loaded membranes were washed by replacing the $FeCl_3$ solution with deionized water. Then, the HMs were removed from the mold, cut with the cylindrical mold (25 mm diameter), and washed again with deionized water (250 mL, 150 rpm). Finally, the obtained API-loaded membranes were freeze-dried. The obtained HM1 membranes loaded with caffeine and diclofenac sodium were labeled as HM1_M_{CAF} and HM1_M_{DS}, respectively.

For quantification of the API content (mg), API-loaded membrane samples were suspended in PBS solution, pH 7.4, at room temperature, for 24 h, for hydrogel's disintegration [342]. After complete hydrogel dissolution and subsequent API extraction, the solution was filtered (0.2 µm filters, Whatman), and the concentration of caffeine and diclofenac was determined by measuring the solutions' absorbance (UV-Vis spectrophotometer CamSpec M509T, Leeds, UK), at 273 and 275 nm, respectively [263,343]. The drug loading (DL, mg/g) and the entrapment efficiency (EE, %) were calculated using the following equations (3.2.1) and (3.2.2) [263,335]:

$$DL = \frac{API\ content\ in\ the\ HMs}{W_L} \tag{3.2.1}$$

$$EE = \frac{API\ content\ in\ the\ HMs}{W_{API}} \times 100 \tag{3.2.2}$$

where W_L (g) represents the mass of the loaded freeze-dried HM, and W_{API} (mg) represents the initial mass of API available.

3.2.2.4. Characterization of the loaded hydrogel membranes

3.2.2.4.1. FT-IR Spectroscopy

The HM1 hydrogel membranes loaded with caffeine and diclofenac sodium were characterized by FT-IR spectroscopy as described in section 2.3.2.5.

3.2.2.4.2. Mechanical properties

The compressive mechanical properties of the loaded FucoPol HMs were evaluated as described in section 3.1.2.4.7.

3.2.2.4.3. Rheological properties

The rheological properties of loaded FucoPol HMs were assessed as described in section 3.1.2.3.

3.2.2.4.4. *In vitro* release studies

Drug release studies were carried out in deionized water (10 mL) as described in section 2.4.2.8. The APIs' cumulative release values were fitted to the Korsmeyer–Peppas model, according to equation 2.3.8.

3.2.3. Results and Discussion

3.2.3.1. Loading of APIs

The ability of the HM1 membranes to be loaded with APIs was evaluated by a diffusion method, in which freeze-dried membrane samples were soaked in two individual APIs solution, namely caffeine, a stimulant of the central nervous system with a well-known effect on adipocyte lipolytic activity [339], and diclofenac sodium, an NSAID widely used in pain management [336]. To study the impact of the loading method, HM1 membranes were also loaded with APIs individually, following a mixing method where a specific amount of each API was mixed with the freeze-dried FucoPol and API loading occurred through drug entrapment during the gelation process.

As shown in Fig. 3.16, macroscopically, all the freeze-dried loaded membranes retained their brownish coloration, lightness, and fragility, while keeping their dimensions. However, the HM1_D_{DS} presented a rectangular shape and a lighter coloration. These changes in shape are related to the loss of consistency of the freeze-dried HM1 membranes during immersion in the diclofenac loading solution caused by the possible interaction of the API's molecules with the Fe^{3+} ions.

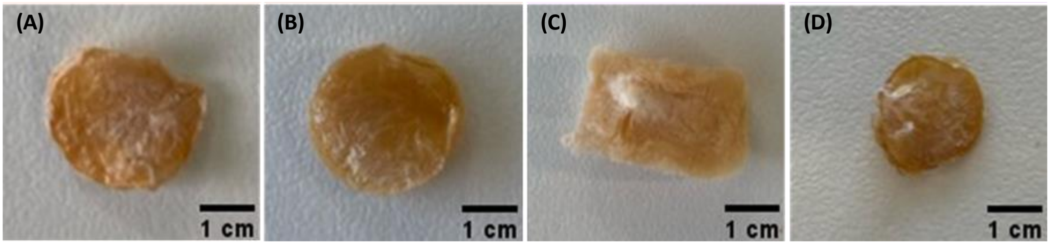

Figure 3.16 - Macroscopic aspect of the freeze-dried FucoPol hydrogel membranes loaded with caffeine (A and B) prepared by diffusion (HM1_D_{CAF}) or mixing (HM1_M_{CAF}) methods, respectively, and loaded with diclofenac sodium (C and D) prepared by diffusion (HM1_D_{DS}) or mixing (HM1_M_{DS}) methods, respectively.

The key parameters used to evaluate the loading ability of the HM1 membranes were the drug loading (DL) and the entrapment efficiency (EE), which represent the mass ratio of drug to drug-loaded HM and the efficacy of HM to retain the drug in its structure, respectively. As shown in Table 3.3, the diffusion method resulted in a higher DL capacity for caffeine (101.9 ± 19.1 mg/g) than for diclofenac sodium (53.9 ± 11.8 mg/g), which correlates with the APIs' concentration in the loading solutions. The higher concentration of caffeine in the loading solution (1.0wt%) resulted in a higher amount of caffeine being loaded into the membranes' matrix. On the other hand, owing to the lower water solubility of diclofenac sodium [344], a lower API concentration was used (0.1wt%), thus resulting in a lower DL. However, higher EE was noticed for diclofenac sodium (1.6 ± 0.2%) than for caffeine (0.6 ± 0.1%) (Table 3.3). Although these results might be significantly impacted by the API's concentration in the drug loading solution, the physicochemical characteristics of the APIs also contributed to this behavior. In fact, during the loading procedure, the negative ions of diclofenac might have interacted with the Fe^{3+} cations, probably promoting their leaching from the membrane's structure and, consequently, it became less consistent. Moreover, the leaching process might have promoted the accommodation of water molecules inside the membranes' structure, increasing their dimensions but decreasing their density. This is corroborated by the fact that after freeze-drying, the HM1_D_{DS} membranes were lighter and presented an altered shape, as observed in Fig. 3.16. The impact of the APIs' concentration in the loading solution on the drug loading amount was also reported for other structures including the CGC hydrogels [305] and chitosan/β-glycerophosphate hydrogels [333]. For the same concentration of diclofenac loading solution (0.1wt%), the latter structures presented a lower DL value (2.48 mg/g) which might be explained by the low swelling ability of those hydrogels [333].

Table 3.3 - APIs concentrations in the loading solutions, drug loading (DL) capacity, entrapment efficiency (EE), and API content in the HM1 membranes.

API	**Caffeine**		**Diclofenac Sodium**	
Loading method	**Diffusion**	**Mixing**	**Diffusion**	**Mixing**
Loading solution (wt%)	1.0	-	0.1	-
API concentration (wt%)	-	0.025	-	0.025
DL (mg API/g dry gel)	101.9 ± 19.1	78.6 ± 2.5	53.9 ± 11.8	82.3 ± 5.1
EE (%)	0.6 ± 0.1	25.8 ± 3.5	1.6 ± 0.2	25.4 ± 3.6

The low EE observed for loading both tested APIs by the diffusion method is correlated to the membranes' swelling capacity, which was limited by their low porosity and tight microstructure [345]. Following a similar loading methodology, CGC-based hydrogels obtained higher and similar EE values for caffeine and diclofenac sodium (13.11 ± 0.49% and 14.70 ± 0.60%, respectively) [305]. This difference can probably be justified by the high porosity of CGC hydrogels (79.4 ± 0.60%) when compared to HM1 membranes (59.3 ± 8.3%) [345]. Additionally, the loading might also be influenced by the low drug-polymer interactions resulting from repulsion between the anionic groups of FucoPol and APIs molecules [260].

Significantly higher EE was obtained with the mixing method for loading both tested APIs into HM1 compared to the diffusion method (Table 3.3). Moreover, the EE values were similar for caffeine and diclofenac sodium (25.8 ± 3.5% and 25.4 ± 3.6%, respectively). This result indicates that an identical API amount was entrapped within the membranes' structure and that the nature of the API had no significant impact. However, these values are low when compared to other structures and the explanation might be related to API leakage during the preparation process since the polymer solution containing the API was immersed in $FeCl_3$ solution for cross-linking. Tan et al. [335] reported EE values of 56 and 65% for diclofenac sodium loading in carboxymethyl sago pulp/chitosan hydrogels. In another study, chitosan/PVA hydrogels were loaded with caffeine, and an EE of around 99% was reported [343]. The same amount of API (0.025wt%) was used for both caffeine and diclofenac sodium loading, resulting in a similar DL for diclofenac (82.3 ± 5.1 mg/g) and caffeine (78.6 ± 2.5 mg/g). These results suggest that the physicochemical characteristics of the APIs had no effect on the loading process efficiency.

Overall, the results obtained showed that a higher DL for caffeine was achieved using the diffusion method while for diclofenac sodium the mixing method allowed reaching higher DL values. Furthermore, despite the lower concentration of API used, following the mixing method led to higher values of EE for both APIs. In general, it was demonstrated that drug loading can be affected by the methodology used to load the API as well as the physicochemical properties of the API used.

3.2.3.2. Characterization of the loaded HM1

3.2.3.2.1. FT-IR Spectroscopy

The structural characterization of the loaded HM1 was carried out by FT-IR analysis. As shown in Fig. 3.17, the loaded membranes exhibited a spectrum similar to that of FucoPol. However, the incorporation of the APIs within their structure led to some structural modifications. It can be observed that the spectra of the API-loaded membranes displayed the characteristic adsorption bands of FucoPol, along with specific vibrations of each API and the intensity of these vibrations is consistent with the API content. The spectrum of caffeine presents absorption peaks at 3115 and 2952 cm^{-1} (C-H stretching of methyl groups), 1697 and 1650 cm^{-1} (C=O stretching of amide I), and 1549 cm^{-1} (C=N stretching of amide II) [222] (Fig. 3.17A). The HM1_D$_{CAF}$ and HM1_M$_{CAF}$ membranes exhibited a decrease in the intensity of the broadband of O-H stretching of hydroxyl groups at 3300 cm^{-1} and the C-H stretching at 2927 cm^{-1}. Fig. 3.17A shows that the incorporation of caffeine can be confirmed by the increasing intensity of the peaks attributed to the C=O stretching at around 1700 and 1655 cm^{-1}, and increased C-N and C-C vibrations at 1019 cm^{-1}. Moreover, the presence of an additional peak at around 744 cm^{-1} confirms the presence of caffeine [346]. The low magnitude of these peaks in the spectra of the loaded membranes prepared by mixing corroborates the lower caffeine content in these structures (Table 3.3).

The diclofenac sodium spectrum comprised absorption peaks at 3387 cm^{-1} (N-H stretching), 1603 cm^{-1} (C=C ring skeletal vibration), 1573 cm^{-1} (COO^{-} anti-symmetrical vibration), 1350-1250 cm^{-1} (C-N stretching) and 730-745 cm^{-1} (C-H out of plane, di and tri substituted rings) [205] (Fig. 3.17B). Despite the low intensity of the peaks, the presence of diclofenac in the HM1_D$_{DS}$ and HM1_M$_{DS}$ membrane structures can be confirmed by the absorption peak at 1604 cm^{-1}, the increased intensity of the peak at 1256 cm^{-1} and the appearance of small peaks around 700 cm^{-1} (Fig. 3.17B).

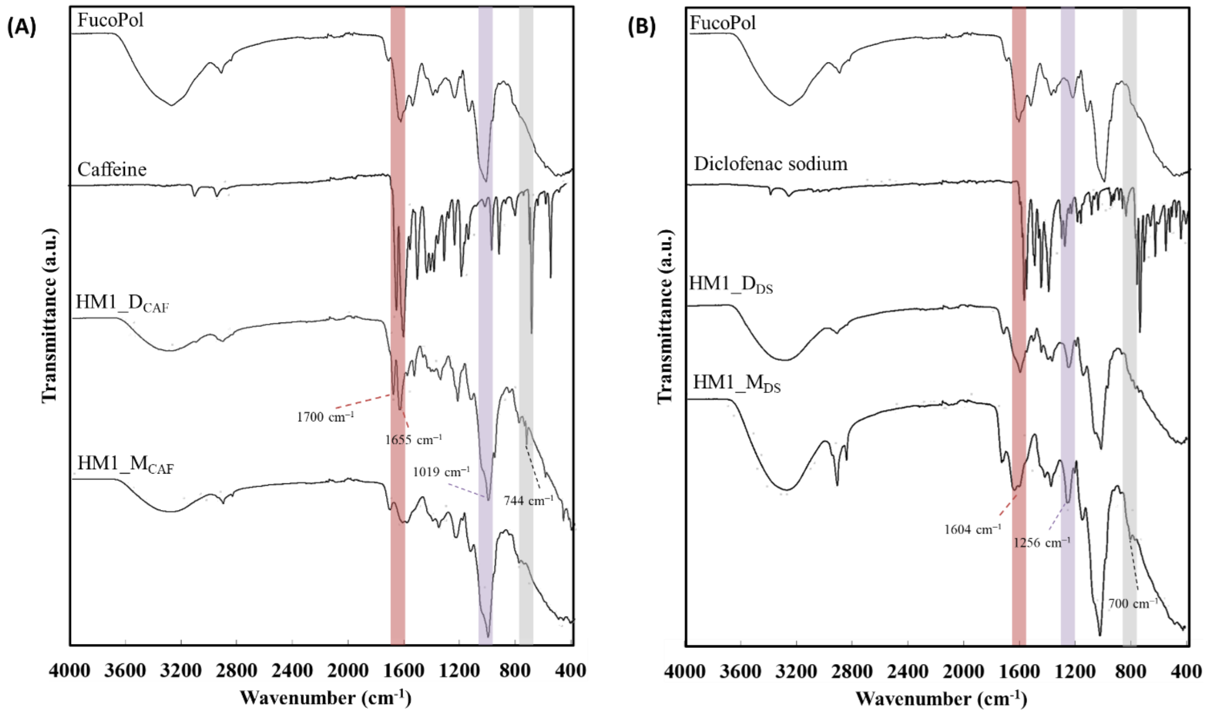

Figure 3.17 - FTIR spectra of HM1 loaded with (A) caffeine and (B) diclofenac sodium by diffusion (HM1_D) and mixing (HM1_M) methods.

When an API is loaded into a membrane structure, it may interact with the polymer matrix and affect several of its properties such as the mechanical strength and the viscoelastic properties.

3.2.3.2.2. Mechanical properties

The impact of dehydration/rehydration and the presence of the API on the mechanical properties of the HM1 membranes is shown in Fig. 3.18. It can be noticed that loading caffeine into the HM1 membranes either by diffusion or mixing methods, led to significant changes in the mechanical parameters. In fact, the hardness values of the caffeine-loaded membranes (130.0 ± 5.3 and 60.4 ± 7.2 kPa, respectively) were considerably higher than those displayed by the original HM1 membranes (32.4 ± 5.8 kPa) (Table 3.4). Moreover, the HM1_D$_{CAF}$ membranes presented a higher ability to withstand the deformation, since their rupture only occurred at 228.8% of strain (Fig. 3.18A). This result might be explained by the effect of the freeze-drying process and the incorporation of the caffeine that apparently reinforced the membranes' structure [347]. Consequently, the HM1_D$_{CAF}$ and HM1_M$_{CAF}$ membranes presented higher compressive modulus (34.1 ± 5.2 and 66.5 ± 8.5 kPa, respectively) and toughness (41.2 ± 0.6 and 16.3 ± 0.5 kJ/m^3, respectively). A similar trend was reported for CGC hydrogels, for which loading caffeine into the hydrogels resulted in higher hardness (15.6 ± 2.53 kPa), compressive modulus (120.0 ± 61.64 kPa), and toughness (120.0 ± 61.64 kJ/m^3) than the original ones (5.04 ± 0.14 kPa, 23.0 ± 0.89 kPa, and 0.78 ± 0.01 kJ/m^3, respectively) [239]. Chee et al. [347] also described changes in some mechanical parameters, such as a decrease in tensile strains and higher Young's modulus values of PVA hydrogels when loaded with caffeine. Although there are other factors to consider such as the number of freeze-thaw cycles and the polymer orientation, the authors assigned this effect to the caffeine crystallization during the drying process.

The HM1_M$_{CAF}$ membranes displayed lower values of hardness (60.4 ± 7.2 kPa), and toughness (16.3 ± 0.5 kJ/m^3) when compared to those loaded by the diffusion method (130.0 ± 5.3 kPa, 41.2 ± 0.6 kJ/m^3, respectively), which can be justified by the higher amount of caffeine present in the latter structures (Table 3.3). Similarly, Yang et al. [80] showed that increasing the methacrylamide dopamine content from 3 to 9% in chitosan-based hydrogels enhanced the compressive stress from 19 to 37 kPa and those values were higher than the ones displayed by the non-loaded hydrogel (18 kPa).

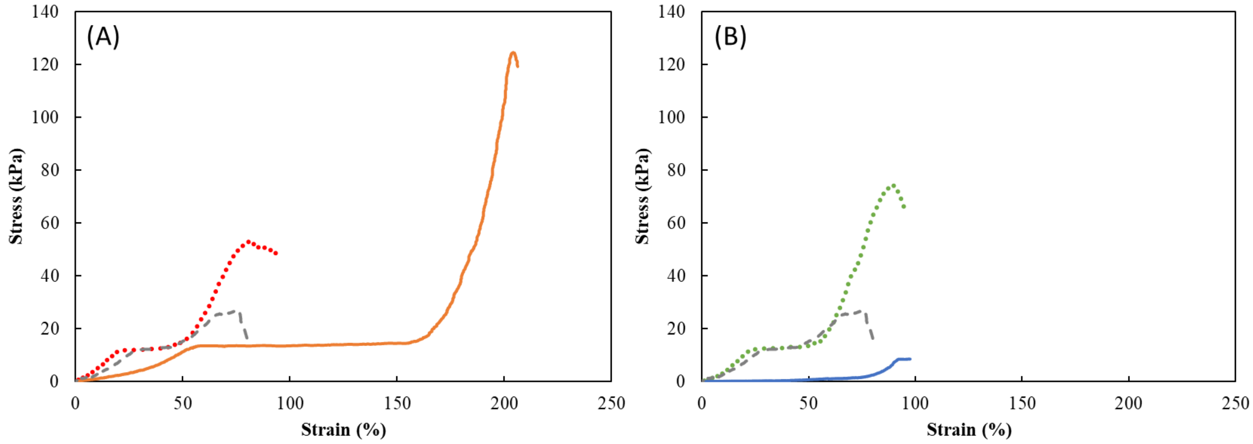

Figure 3.18 - Compression stress-strain curves of the HM1 membranes (light grey dashed line) and the HM1 membranes loaded with (A) caffeine and (B) diclofenac sodium by diffusion (full line) and mixing (dotted line) methods.

The results obtained for the HM1_D$_{DS}$ and HM1_M$_{DS}$ membranes are displayed in Fig. 3.18B. Contrary to that obtained for caffeine, the loading method used to incorporate diclofenac within the membrane structure had a very significant impact on their mechanical parameters. It can be observed that the HM1_M$_{DS}$ membranes exhibited higher hardness (81.8 ± 3.4 kPa), compressive modulus (67.7 ± 2.5 kPa), and toughness values (19.7 ± 0.6 kJ/m^3) than those loaded by the diffusion method (7.3 ± 1.2 kPa, 4.6 ± 1.3 kPa, and 1.7 ± 0.4 kJ/m^3, respectively) (Table 3.4). Despite the lower amount of diclofenac present in these later structures, the leaching phenomenon has probably contributed to the observed fragility of the membranes

(Fig. 3.16), and consequently, a decline in the mechanical properties. Wong et al. [211] evaluated the effect of loading polyethylene oxide (PEO) hydrogel films with diclofenac sodium via diffusion and mixing methods. The authors described a decrease in the mechanical properties of the hydrogel films and attributed it to a significant decrease in polymer crystallinity for the diffusion method and a low crosslinking density for the mixing method.

Table 3.4 - Mechanical properties (under 90% strain) and storage (G′) and loss (G′′) moduli (measured at 1 Hz) of the HM1 membranes loaded with caffeine (HM1_D_{CAF} and HM1_M_{CAF}) or diclofenac sodium (HM1_D_{DS} and HM1_M_{DS}), compared to the non-loaded membranes (HM1).

Sample ID	**Mechanical properties**			**Rheological properties**	
	Hardness (kPa)	Compressive modulus (kPa)	Toughness (kJ/m^3)	G′ (Pa)	G′′ (Pa)
HM1	32.4 ± 5.8	56.3 ± 7.8	1.4 ± 0.1	285.8 ± 36.1	36.7 ± 5.5
HM1_D_{CAF}	130.0 ± 5.3	34.1 ± 5.2	41.2 ± 0.6	1014.9 ± 109.7	113.2 ± 13.7
HM1_M_{CAF}	60.4 ± 7.2	66.5 ± 8.5	16.3 ± 0.5	609.7 ± 78.3	80.3 ± 2.7
HM1_D_{DS}	7.3 ± 1.2	4.6 ± 1.3	1.7 ± 0.4	19.8 ± 3.8	2.2 ± 0.1
HM1_M_{DS}	81.8 ± 3.4	67.7 ± 2.5	19.7 ± 0.6	421.0 ± 107.3	40.6 ± 10.2

3.2.3.2.3. Rheological properties

The effect of dehydration/rehydration and the presence of the API on the viscoelastic properties of the HM1 membranes is shown in Fig. 3.19. In general, all loaded membranes presented a rheological profile identical to the original HM1 membranes with a predominant elastic behavior, suggesting that the incorporation of APIs had no significant impact on the viscoelastic properties of the structure. As solid-like structures, the values of the storage modulus were one order of magnitude higher than the loss modulus values over almost the entire range of frequency. Similar behavior was reported for other ion-crosslinked hydrogels, namely hydrogels based on nanofibrillated cellulose [348], succinoglycan [287], and gellan [299]. As shown in Fig. 3.19A and 3.19C, the HM1_D_{CAF} and HM1_M_{CAF} membranes presented higher storage and loss moduli which is consistent with the observed enhancement of the structures' mechanical properties (Fig. 3.18A). As demonstrated in Table 3.4, at a frequency of 1 Hz, the G′ value was enhanced from 285.8 ± 36.1 Pa to 1014.9 ± 109.7 (Fig. 3.19A) and 609.7 ± 78.3 Pa (Fig. 3.19C), while the G′′ increased from 36.7 ± 5.5 to 113.2 ± 13.7 and 80.3 ± 2.7 Pa, for the HM1_D_{CAF} and HM1_M_{CAF} membranes, respectively. These results demonstrate that loading caffeine into the membranes can potentially impact the crosslinking density, affecting their ability to store and recover elastic energy. Moreover, the addition of caffeine to membranes may alter the molecular mobility and the relaxation behavior of the polymer chains which can affect internal friction and energy dissipation within the hydrogel's network [349]. A similar improvement of rheological parameters was reported for the CGC hydrogel loaded with caffeine by diffusion [239]. In that study, at a frequency of 1 Hz, the caffeine-loaded hydrogels presented G' and G'' values of 315.0 ± 76.7 Pa and 29.3 ± 8.4 Pa, respectively, while lower values were obtained for the original hydrogels (149.9 ± 9.8 and 11.9 ± 0.5 Pa, respectively).

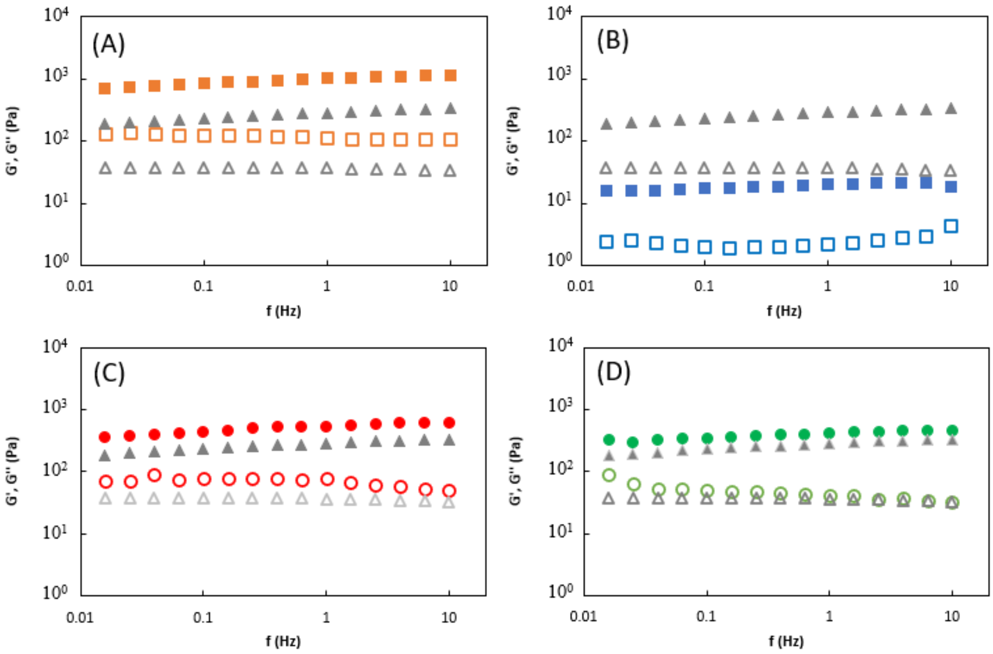

Figure 3.19 - Rheological properties of the HM1 membranes (grey symbols) and the HM1 membranes loaded with caffeine using (A) diffusion and (C) mixing method, and with diclofenac sodium using (B) diffusion and (D) mixing method, at 25 °C. Mechanical spectrum storage (G', solid symbols) and loss moduli (G'', open symbols).

The rheological properties of the HM1_D_{DS} and HM1_M_{DS} membranes showed that the loading method also had an impact on the storage and loss moduli values compared to the original HM1 membranes (Fig. 3.19B and 3.19D). The most relevant difference was obtained for the HM1_D_{DS} membranes on which, at a frequency of 1 Hz, the G' and G'' values were drastically reduced from 285.8 ± 36.1 Pa and 36.7 ± 5.5 Pa to 19.8 ± 3.8 Pa and 2.2 ± 0.1 Pa, respectively (Fig. 3.19B). Following a similar loading method, the incorporation of diclofenac sodium within the structure of starch/pectin hydrogels led to a decrease in the rheological parameters compared to the original hydrogels, namely for the G' values that decreased from 353.36 Pa to 72.74 Pa, suggesting that the interaction between the diclofenac and the carboxyl groups of the polymers prevent the original hydrogen bond formation among them [350]. On the other hand, performing the loading by mixing, an increase in the G' value from 285.8 ± 36.1 Pa to 421.0 ± 107.3 Pa was observed and a similar value of G'' was obtained (40.6 ± 10.2 Pa), at a frequency of 1 Hz (Table 3.4). The results suggest that mixing diclofenac with the polymer before gelation may promote the formation of additional crosslinking between the hydrogel matrix and the drug molecules. Russo et al. [351] also reported a slight increase in G′ values (21.61 ± 1.45 kPa) of diclofenac-loaded poloxamer gels when compared to non-loaded gels (18.58 ± 0.50 kPa).

Overall, these findings suggest that the addition of APIs to the membranes has an impact on their mechanical and rheological properties, which should be considered for designing drug delivery systems.

3.2.3.3. *In vitro* release studies

The release studies were performed by placing the API-loaded HM1 membranes in deionized water, at 37 °C, and evaluating the cumulative release profiles of the APIs from the membranes. As shown in Fig. 3.20 different release profiles could be identified for the HM1 membranes loaded by each method. The membranes loaded by diffusion presented an API release comprising an initial fast release (burst phase) followed by a lower release state. Fig. 3.20A shows that for both APIs, the burst period occurred within the first 4 min where around 75% was released. This initial burst is often attributed to the rapid release of surface-associated or weakly bound API molecules [352]. After that period, a slow release was observed, and the release rate reached 100% within 25 min, for both APIs. This indicates that the release mechanism for HM1_D_{CAF} and HM1_D_{DS} membranes is primarily controlled by diffusion. For the HM1_D_{DS} membranes, the release rate was further promoted by the disintegration of the membrane observed during the release experiment. Disintegration might be induced by ion exchange, leading to the leaching of Fe^{3+} cations from the membrane structure during immersion in a diclofenac solution. This exchange of ions can disrupt the crosslinking bonds within the membrane, leading to a loss of the structural integrity of the membrane. In the end, the loaded membrane showed a fragile structure that disintegrated when immersed in the release medium. Xylan/chitosan hydrogel films loaded following a diffusion mechanism presented a similar release profile of diclofenac in PBS solution [353]. The release profile demonstrated an initial burst phase with 43% of the drug being released within the first 5 min, and the total released after 60 min. Following similar loading conditions, the caffeine-loaded CGC hydrogels also demonstrated an analogous behavior, however, the maximum release was achieved within 3 h of the experiment [305]. Considering that a similar amount of caffeine per hydrogel volume was loaded through the same loading method in CGC hydrogels and HM1 membrane structures (11.98 ± 1.29 and 10.07 ± 1.89 mg/cm^3), the faster release in the membranes might be essentially explained by the larger surface area of membranes that promoted faster release by providing more sites for caffeine molecules to be released from the hydrogel's matrix [354]. Muchová et al. [338] also reported a burst release kinetics of caffeine from dialdehyde cellulose/PVA hydrogel films due to the low thickness of the structures which decreases the caffeine diffusion path. After 8 h, up to 90% of the caffeine was released which might be suitable for topical drug delivery.

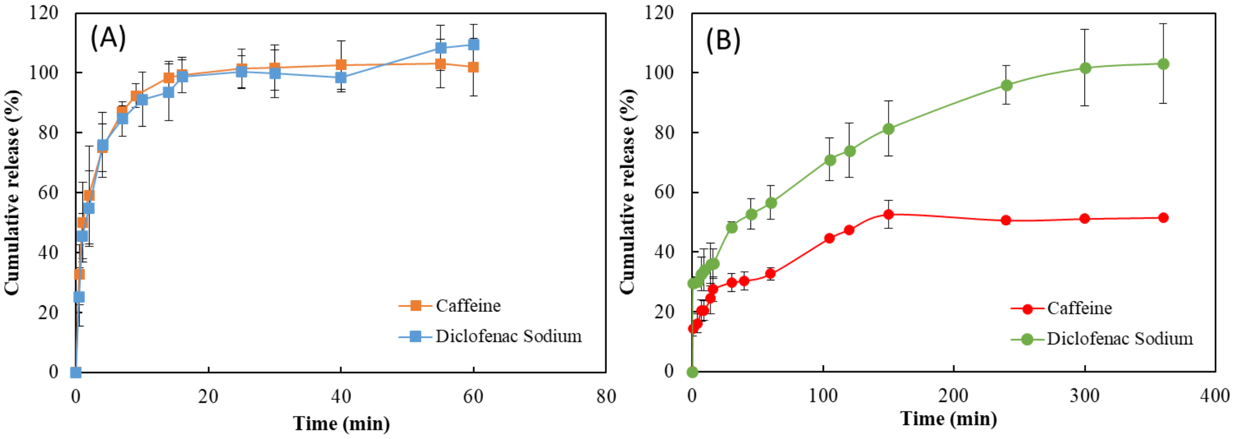

Figure 3.20 - Cumulative release profile of membranes (A) HM1_D_{CAF} (🟧) and HM1_D_{DS} (🟦) and (B) HM1_M_{CAF} (🔴) and HM1_M_{DS} (🟢), in deionized water, at 37 °C.

As shown in Fig. 3.20B, the release of caffeine and diclofenac sodium from the HM1_M_{CAF} and HM1_M_{DS} membranes, respectively, was extended when compared to HM1_D_{CAF} and HM1_D_{DS} membranes and revealed differences in release profiles. It can be observed that for HM1_M_{CAF} membranes the release occurred following two stages: an initial burst release during the first 16 min, where about 30% of the caffeine was released, followed by a second phase with a slow release of the caffeine. During the last phase, the maximum caffeine released (52.6 ± 4.7%) was achieved after 150 min of the experiment. Likewise, whey protein hydrogels enriched with $CaCl_2$ were loaded with caffeine through the mixing method, and an analogous maximum of caffeine was released (50-55%) within 4 h of the experiment [355].

The release profile of diclofenac from HM1_M_{DS} membranes also comprises an initial burst release where 36% of the diclofenac was released in the first 15 min (Fig. 3.20B). After that period, a decrease in the release rate was observed, reaching the maximum cumulative release (100%) after 300 min. This behavior was also obtained for the magnetic PVA/carrageenan nanocomposite hydrogels that exhibited a diclofenac release between 75% and 85% in PBS solution, after 7 h of the experiment [356].

The difference between both release profiles can be justified by the way that APIs were incorporated into the hydrogel's matrix, which affected their distribution and subsequent release behavior. In fact, in the diffusion method, the API can be easily deposited in microporous spaces of the hydrogel, and drug molecules adhere to the surface of the hydrogel, leading to faster release rates due to the immediate availability of the drug. When the API is loaded by mixing, their molecules are physically or chemically entrapped within the hydrogel matrix, providing a more controlled and sustained release since diffusion through the hydrogel network is needed [211].

Since the release of both APIs from the membranes is apparently controlled mainly by diffusion [231], the first 60% of the release data was modeled according to the Korsmeyer-Peppas model [206]. Based on the regression coefficients (R^2), all the release data fitted in the model since the R^2 values were higher than 0.97 (Table 3.5).

Table 3.5 - Korsmeyer–Peppas model parameters obtained from the *in vitro* release kinetics of HM1 membranes; R^2, regression coefficient; *n*, release exponent.

Sample ID	Loading method	*n*	R^2
HM1_D_{CAF}	Diffusion	0.392	0.994
HM1_D_{DS}	Diffusion	0.322	0.995
HM1_M_{CAF}	Mixing	0.246	0.978
HM1_M_{DS}	Mixing	0.233	0.971

As listed in Table 3.5, the kinetic parameters revealed that all the HM1 membranes follow a simple Fickian diffusion with *n* values below 0.45. These results indicate that until 60% of the release, the physicochemical properties of the API used had no significant impact on the release mechanism. Moreover, these *n* values suggest that the drug release mechanism is purely controlled by diffusion, with the drug being diffused faster through the membrane matrix than the process of polymeric chain relaxation [357]. It was demonstrated that following an identical loading method, both APIs presented similar *n* values. Using the diffusion method, HM1_D_{CAF} and HM1_D_{DS} membranes showed *n* values of 0.392 and 0.322, respectively, while using the mixing method HM1_M_{CAF} and HM1_M_{DS} obtained *n* values of 0.246 and 0.233, respectively. Several other structures have been reported to have similar release mechanisms for caffeine and diclofenac sodium. For example, starch-based hydrogels containing acrylamide and prepared by diffusion method also revealed a caffeine release rate dominated by Fickian diffusion (*n*=0.17), determined by the interactions between caffeine and the monomers [232]. Similar *n* values (0.3 – 0.35) and consequent release mechanism were obtained for caffeine release from

PVA/chitosan hydrogels prepared by mixing method [343]. Qiao et al. [358] also reported a mechanism controlled by Fickian diffusion (n=0.27) for diclofenac sodium release from gelatin-polyacrylamide hydrogels loaded by diffusion.

3.2.4. Conclusions

In this study, the FucoPol HMs were successfully loaded with caffeine and diclofenac sodium as model APIs, following two loading methods: diffusion and mixing. The membranes demonstrated the ability to be loaded with both APIs by either method, and the presence of the APIs in the membranes' structures was confirmed by FT-IR analysis. However, the incorporation of diclofenac sodium by diffusion led to the leaching of the crosslinking agent, and the membrane's structure suffered some physical alterations, including changes in the macroscopic appearance, and a decrease in the mechanical and rheological parameters. Except for this structure, all developed membranes displayed improved mechanical and rheological properties when compared to the non-loaded ones. For both APIs, a high release rate was obtained for the membranes loaded by diffusion, whereas sustained and extended release was observed for those prepared by the mixing method. Moreover, all loaded membranes displayed a release profile following a Fickian diffusion, suggesting that the initial release phase occurred independently of the API used. Despite future studies focused on exploring additional formulation parameters and optimization strategies that are needed to further enhance the entrapment efficiency and release performance of the hydrogel membranes, these findings highlight the potential of the FucoPol HMs to be used as drug delivery systems.

III. MICRONEEDLES ARRAYS

4. Microneedles Arrays based on natural polymers

Part of this chapter was adapted from the following published book chapter:

- **Araújo, D.**, Freitas, F. "Microneedles Arrays Based on Natural Polymers" in Encyclopedia of polymer applications Vol 2, 1st ed, Mishra M, Ed; CRC Press, Taylor & Francis Group: NW, USA, 2019, pp. 1800-1812.

Summary

Microneedle arrays (MNs) are minimally invasive devices that painlessly penetrate the skin's protective barrier, the *stratum corneum*, to enhance transdermal drug delivery. Recently, owing to their biocompatibility, biodegradability, and nontoxicity properties, several natural polymers have been proposed as materials for MNs fabrication. Polymeric MNs are promising substitutes for the more common solid MNs made of silicon, metals, and ceramics, due to fabrication simplicity, cost-effectiveness, and mass production capacity. This chapter describes the main methods available for the fabrication of polymeric MNs, the properties of the natural polymers proposed as materials for MNs fabrication, and based on that, the types of MNs that can be obtained. Depending on the polymers' properties, biodegradable, dissolving, and hydrogel-forming MNs can be fabricated with different shapes and geometries, to improve mechanical properties and performance. More importantly, drug release can be controlled by water solubility, degradation, and swelling properties of the polymers, which cannot be achieved by the inorganic materials. The advantages of MNs based on natural polymers are addressed, including the reduction of biohazardous sharp wastes and their safe disposal by biodegradation or dissolution as well as their limitations that are mainly associated with harsh fabrication methods and mechanical strength maintenance after drug loading. Finally, the prospects for MNs based on natural polymers are discussed, focusing on the development of the technology that

will allow it to overcome the disadvantages and/or limitations encountered so far and, thus, enable its progress in transdermal delivery therapies.

4.1.1. MNs arrays: Fabrication methods, materials and design

MNs arrays, minimally invasive devices that by-pass the *stratum corneum*, are applied to the skin and painlessly create microscopic aqueous pores that allow drug diffusion to the dermal microcirculation, avoiding contact with dermal nerves and blood vessels [21,359]. The concept of MNs appeared in the early 1970s when Gerstel and Place first proposed the creation of micropores in the skin [360]. Unfortunately, back then, the technology to produce micron-sized needles economically was not available. For over 40 years, research focused on MNs has been carried out, but only in the late 1990s it has evolved considerably with the emergence of microfabrication technology. The first paper on this topic was published by Henry et al. [361] describing the utilization of silicon MNs to enhance the delivery of calcein, across the human skin. Microfabrication allowed the mass production of MNs arrays and the development of this technology. Over the past decades, extensive research concerning MNs technology resulted in the development of different techniques that allow the fabrication of MNs in several three-dimensional designs from a wide variety of materials [21,362,363]. Conventionally, MNs can be fabricated in five different types: solid, coated, dissolving, hollow, and hydrogel-forming [21,364] (Fig. 4.1).

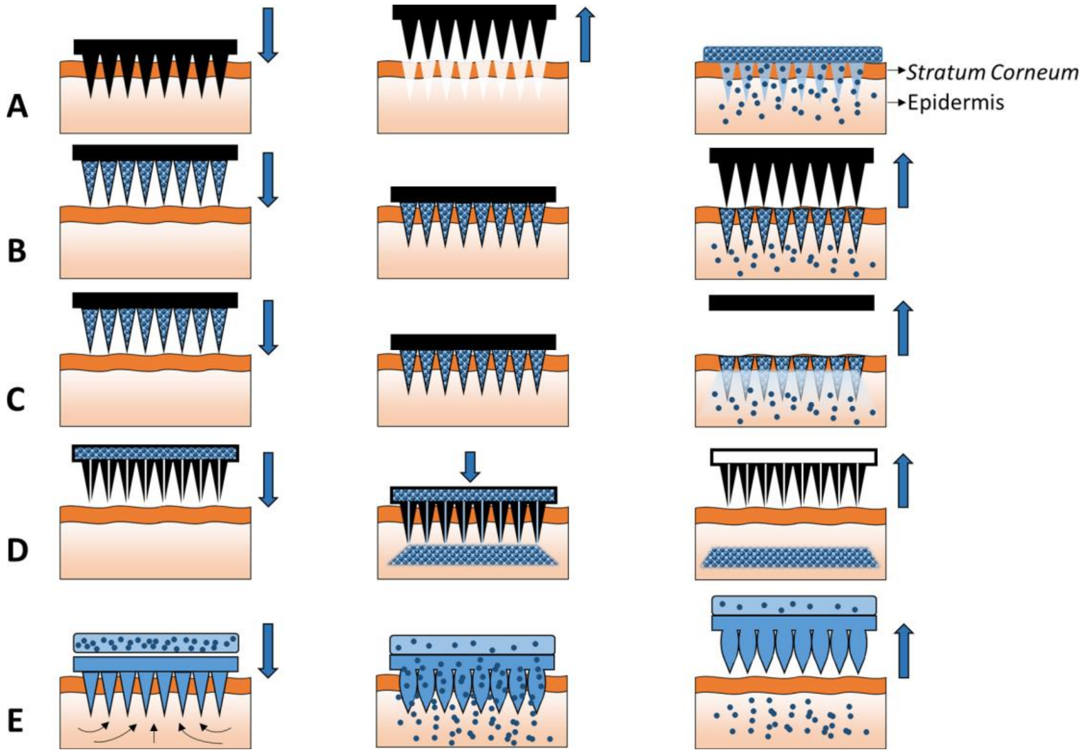

Figure 4.1 - A schematic representation of five different MN types used to facilitate transdermal drug delivery. (A) Solid MNs increase the permeability of a drug formulation by creating micro-holes across the skin. (B) Coated MNs for rapid dissolution of the coated drug into the skin. (C) Dissolvable MNs for rapid or controlled release of the drug incorporated within the microneedles. (D) Hollow MNs used to puncture the skin and enable the release of a liquid drug following active infusion or diffusion of the formulation through the needle bores. (E) Hydrogel-forming MNs take up interstitial fluids from the tissue, inducing diffusion of the drug located in a patch through the swollen microprojections (reproduced from [21]).

Solid MNs follow the approach "poke and patch" which involves the creation of transient aqueous micropores in the skin and, subsequently, the application of a drug-loaded patch or a drug formulation (gel, emulsion, cream, solution, etc.) that crosses the skin by passive diffusion (Fig. 4.1A). The requirement of a two-step application process is the main limitation of this MN type [4,21,364].

The "coat and poke" approach is used to produce coated MNs by coating solid MNs with a drug formulation prior to skin application (Fig. 4.1B). These MNs allow the deposition and dissolution of the coated drug within the skin, after insertion. Coated MNs enable the delivery of macromolecules, such as vaccines, peptides, virus, and DNA to the skin, and overcome the limitation of solid MNs by using a single-step application. Nevertheless, the main disadvantage is the limited amount of drugs that can be applied to the MNs surface.

Dissolving MNs are fabricated following the "poke and release" approach. When in contact with the skin interstitial fluid, these MNs rapidly dissolve, releasing the encapsulated drug over a period of time (Fig. 4.1C). This type of MNs avoids the biohazardous sharps waste in the skin, although it can suffer from the major limitation of drug mutations due to the high temperature required in the fabrication procedure [363].

Hollow MNs, also termed the "poke and flow" approach, are similar to hypodermic injection and allow the continuous flow of the drug into the skin through the hollow capillaries (Fig. 4.1D). Drug flow can be driven by diffusion, pressure, or electrical, allowing the infusion of large amounts of drugs and modulation of drug delivery by modifications in the infusion rate [363]. Moreover, this type of MNs enables the extraction of blood samples underneath the skin, allowing the monitoring of body fluids (e.g., glucose levels). Needle clogging during skin insertion and flow resistance are the main limitations of these MNs [21,364].

Recently, a new type of MNs, hydrogel-forming, has been developed. Hydrogel-forming MNs are characterized by the coupling of drug-free polymeric MNs projecting from a baseplate with an adhesive drug reservoir (Fig. 4.1E). Upon insertion into the skin, the MNs take up interstitial fluid and the drug can diffuse through the swollen microprojections [21,359,364].

Different methodologies using several types of materials have been developed to produce MNs. Techniques, mostly based on microelectromechanical systems (MEMS) technology, including micromolding, micromilling, atomized spray, 3D and 4D printing, laser cutting, lithography, and etching processes are used in MNs manufacture [365,366]. Materials such as silicon, metals (e.g., titanium and stainless steel), and ceramics have been extensively used to fabricate a wide variety of MNs, as summarized by several authors [364,366,367]. Although silicon and metals are the main materials used to fabricate MNs, disadvantages such as drug loading limitation, expensive fabrication, and non-biocompatibility are associated with the use of those structural materials [359].

Polymeric materials are promising alternatives for MNs preparation since some of them can present biocompatibility, biodegradability, low toxicity, and may have the strength/toughness required for skin penetration [21,367,368]. Among all the methodologies previously described, micromolding is one of the most widely used methodology in polymeric MNs fabrication due to the method's good reproducibility, facility to produce at a large scale, and cost-efficiency [369].

The micromolding fabrication process involves the replication of master structures using molds to define features. This technique is accomplished in several steps: production of the master MNs template, the introduction of the material to produce the female mold, curing or cooling of the material, coating the female mold with the desirable polymer to MNs fabrication, centrifugation, or application of vacuum to remove bubbles, application of drying or photocrosslinking process to promote solidification and peeling off the MNs from the female molds (Fig. 4.2) [369].

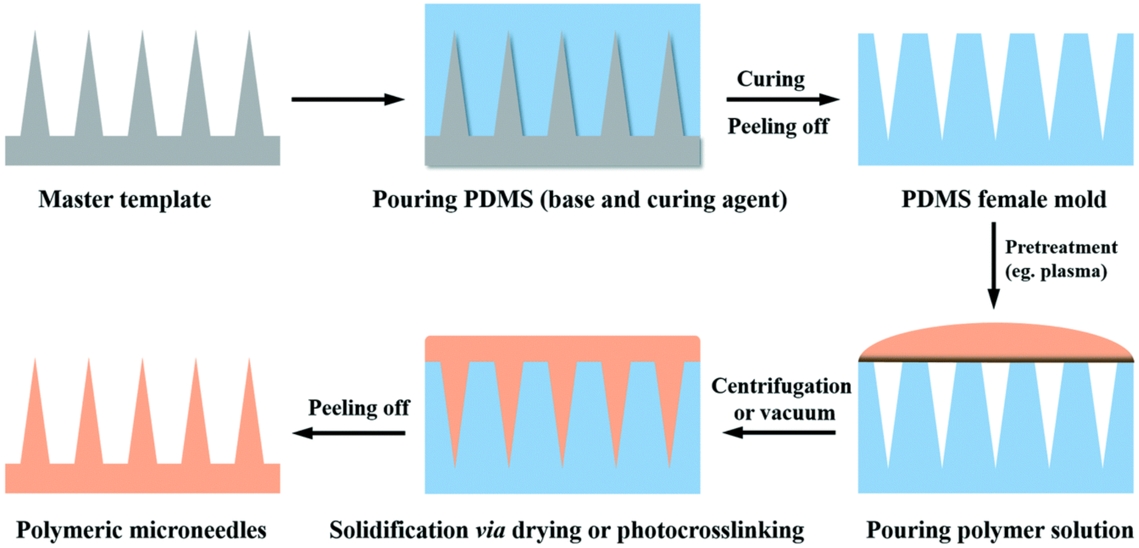
Master template
Pouring PDMS (base and curing agent)
Curing
Peeling off
PDMS female mold
Pretreatment
(eg. plasma)
Pouring polymer solution
Centrifugation
or vacuum
Solidification *via* drying or photocrosslinking
Peeling off
Polymeric microneedles

Figure 4.2 - Schematic illustration of polymeric MNs fabrication via PDMS micromolding (reproduced from [369]).

Several materials such as ceramics [370], PVA [371], and polydimethylsiloxane (PDMS) [368] have been used to transcribe the microstructures of the master MNs templates and produce female molds. Up to now, PDMS has been the main material used to fabricate molds for MNs production given its flexibility, thermo-stability, accurate reproducibility of master structures, and the ability to reproduce numerous molds by PDMS replica molding process [372]. Micromolding has been extensively used to fabricate several MNs based on natural polymers, such as chitosan [373], chitin [374], silk fibroin [375], and hyaluronic acid [376].

Polymeric materials are broadly classified as natural or synthetic polymers, according to their origin. While natural polymers occur in nature, synthetic polymers are mostly petrochemically derived [377]. Natural polymers, such as collagen, chitosan, hyaluronic acid, cellulose, alginate, and starch, can be obtained from animal, vegetable, algal, or microbial sources. Due to their properties, several polysaccharides, including CMC, amylopectin, alginate, and hyaluronic acid, were proposed as structural materials for the microfabrication of polymeric MNs [369].

Generally, according to their performance in contact with the dermal interstitial fluid, polymeric MNs can be classified into dissolving, biodegradable, or hydrogel-forming MNs (Fig. 4.3). Typically, drugs are embedded in the polymeric matrix (to avoid mechanical or biological disruption) and are released during MNs dissolution or degradation.

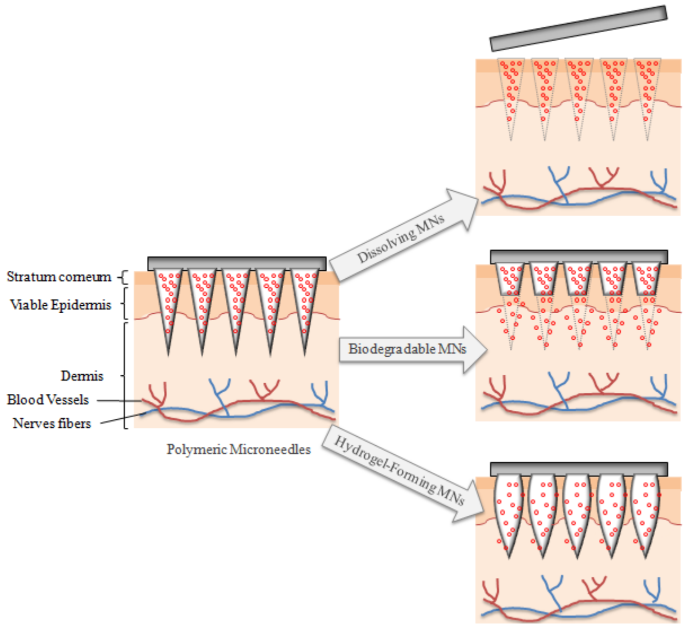

Figure 4.3 - Schematic illustration of polymeric MNs behavior in contact with the dermal interstitial fluid.

4.1.2. Biodegradable MNs

Biopolymers have received considerable attention due to their properties such as biocompatibility, biodegradability, flexibility, and minimal side effects that render them high potential to be used in biomedical applications. For the fabrication of biodegradable MNs, the polymers are required to degrade over time without dissolution or swelling, and their degradation must generate nontoxic compounds that are completely eliminated from the body by natural metabolic pathways with minimal side effects [378]. Controlling the degradation rate of the biodegradable MNs under physiological conditions regulates the drug delivery rate [369].

Biodegradable polymers such as PLA, PGA, and PLGA were used as materials to produce biodegradable MNs. Examples of natural biodegradable polymers proposed to fabricate MNs include chitosan, chitin, silk, and fish scale biopolymers.

Chitosan is a natural polymer derived from the chitin of crustacean shells via alkaline deacetylation [91]. Previous studies demonstrated the potential of chitosan as a polymeric matrix for MNs fabrication due to its non-cytotoxic properties and immune stimulating activity that can enhance both humoral and cellular responses. Castilla-Casadiego et al. [379] proposed the fabrication of biodegradable chitosan-based MNs using the micromolding method for the delivery of meloxicam for pain management in cattle. Results confirmed the time-sensitive nature of the chitosan solution, with reusing it after the fourth day leading to patch failure, while sterilization did not affect patch properties. The microneedle patches exhibited controlled drug release of meloxicam, full skin penetration at approximately 3.2 N, and dissolution capabilities with no observed adverse effects.

Another natural polymer proposed as material for MNs fabrication was chitin, which is one of the most abundant polysaccharides in nature. Jin et al. [374] investigated the fabrication of chitin MNs for tuberculosis diagnosis. Chitin MNs were fabricated by replica molding using a PDMS mold and coated with purified protein derivative, containing a mixture of tuberculosis antigens. These MNs were water-insoluble and demonstrated a mechanical strength of 0.2 N for a single microneedle when inserted into the skin. Moreover, the slow biodegradability of chitin ensured the long-term delivery of the drugs.

Biodegradable MNs fabricated from biopolymer extracted from fish scales were also developed by Olatunji et al. [380]. Each microneedle revealed sufficient mechanical strength (0.12 N) to penetrate the skin without fracture and its degradation occurred gradually after insertion. The results showed that MNs based on that material were promising for transdermal applications, and additionally, they provided health benefits due to the intrinsic bioactivity of the fish scale biopolymer. To improve MNs properties, Olatunji et al. [381] proposed the production of these MNs reinforced with nanocellulose using low temperature mechanical press microfabrication. Due to the swelling properties of nanocellulose, a slow dissolution rate of the MNs was achieved, which enabled prolonged drug delivery. The ability of those MNs to load and release drug by transdermal route was investigated by Medhi et al. [382] with the preparation of lidocaine loaded MNs. The MNs were loaded with different concentrations of lidocaine and the permeation rate was controlled using a Franz diffusion cell. After 36 h, the drug permeation rate increased from 2.5 to 7.5% (w/w), and a pseudo steady state profile was detected from 5 to 10% (w/w) lidocaine loaded MNs. Moreover, the dissolution of MNs was observed and, consequently, the loaded drug was released.

Silk fibroin protein, extracted from the *Bombyx mori* cocoons, is another example of a natural polymer that provide structural matrix to encapsulate drugs, maintaining their activity. Several silk MNs with different shapes and sizes were produced by Raja et al. [375]. Post-fabrication treatments, microparticle loading into the MNs structure, and drug coating were applied strategies to improve the mechanical stability and drug release kinetics. According to the design, treatment, and fabrication method used, the MNs demonstrated a mechanical strength in a range of 0.1 to 0.7 N, which allowed penetration into the skin. After 16 h, a minimum amount of drug was released from silk MNs loaded with drug (~0.4%), and most of the drug was still retained in the patch after two days. Recently, Lee and colleagues [383] developed a flexible and porous silk fibroin microneedle wrap (Silk MN wrap) for perivascular drug delivery, focusing on targeted and controlled drug release. The Silk MN wrap, which incorporates drug-embedded silk microneedles, effectively inhibited intimal hyperplasia, reducing neointimal formation by 62.1% over a 28-day period, making it a promising approach for post-treatment of vascular inflammatory responses.

As demonstrated, biodegradable polymers provide additional functionalities to the MNs themselves and enable their safe degradation in the body. These advantages make biopolymers highly suitable for use in MNs development.

4.1.3. Dissolving MNs

In contrast with biodegradable polymers, the main advantage of dissolving polymers is related to their structure since they are water-based polymers. MNs manufactured with these polymers presented rapid and complete dissolution in the skin without generating sharp biohazardous waste. Due to the fast dissolution of the polymers within the skin, an excessively rapid drug delivery is verified, and drug delivery rates are increased [369]. Similarly to biodegradable MNs, micromolding techniques are mainly used for the fabrication of dissolving MNs. Skin penetration capacity, drug release efficiency, and drug bioactivity and stability are directly related to the polymers' properties. Several water-based polysaccharides, including CMC, amylopectin, alginate, and hyaluronic acid, were proposed as structural materials for the preparation of dissolving MNs.

Numerous authors have described the utilization of CMC as a polymeric matrix for dissolving MNs fabrication. CMC is a hydrophilic polymer commonly used as an excipient in pharmaceutical products and as an aqueous gel base in transdermal patches [384]. Park et al. [385] fabricated a biocompatible and cost-effective dissolvable MNs array, made of CMC. The fabrication process involved using a laser writing process to create a PDMS mold, allowing rapid prototyping of various sizes with reasonable consistency. By controlling mechanical properties and dissolution rates through mixing with amylopectin at various ratios, improved skin permeability, with a three-fold enhancement observed using Rhodamine B as a model drug. Additionally, the antioxidant activity of ascorbic acid encapsulated in the microneedles exhibited a six-fold increase compared to direct topical application, demonstrating the potential of this biocompatible microneedle array for efficient drug and cosmetic compound delivery through the skin. Ono et al. [384] reported the fabrication of CMC-based MNs for vaccine delivery. After 2 min of application in rat skin, the MNs lengths reduced by 70% and complete dissolution was observed within 5 min after insertion. Clinical studies demonstrated that MNs had prolonged antigen deposition and no skin irritation was observed.

Sodium alginate is a natural polysaccharide extracted from brown seaweed. The use of alginate to fabricate MNs was suggested by Demir et al. [368] and the fabricated MNs were strong enough to create microholes in the skin without breaking. In that study, alginate MNs presented good deformation resistance and mechanical robustness, which enhanced protein delivery across the skin, following the "poke and release" approach. To increase the MNs performance, Yu et al. [386] proposed the use of an alginate and HA blend as polymeric matrix to encapsulate insulin. The as-prepared MNs exhibited a strong mechanical strength to pierce the skin and their biodegradability allowed the sustained release of over 90% of the loaded insulin within a period of 6 h. In addition, a relative insulin bioavailability of 92.9% was observed compared with subcutaneous injection, which demonstrated the potential of those MNs in diabetes treatment by transdermal delivery.

Natural sugars such as maltose and galactose were also tested as raw material for dissolving MNs microfabrication. The disaccharide maltose was used to fabricate MNs arrays for the first time by Miyano et al. [387]. In that work, powdered maltose was heated to form maltose candy and mixed with the powdered drug, ascorbate-2-glycoside. Afterward, the mixture was used to fill a casting MNs mold, and dissolving MNs were produced. Due to hydrolysis, when in an environment exceeding a humidity of 50%, the developed MNs dissolved within a few hours. To prevent the hydrolysis process, MNs were stored at a humidity below 40%, where they retained their shape for at least 3 months. Lee et al. [388] reported the manufacture of MNs based on maltose using the stepwise controlled drawing lithography method. By controlling the drawing time and maltose viscosity, MNs with 1200 μm length were fabricated which were able to administer ascorbic acid-2-glucoside and niacinamide into the skin by dissolving within 20 min in *in vivo* tests. Recently, composite microneedles made from Ca^{2+} crosslinked alginate/maltose were developed by Zhang et al. [389]. These microneedles demonstrated robust mechanical properties and excellent biocompatibility, allowing for the transdermal delivery of insulin in diabetic rat models. The released insulin exhibited a significant and effective hypoglycemic effect, with relative pharmacological availability and relative bioavailability of 94.1% and 93.7%, respectively, compared to subcutaneous injection, suggesting their potential for diabetes treatment via transdermal delivery. Besides maltose, galactose was also tested to produce dissolving MNs. However, this sugar was used as an example by Donnelly et al. [390] to describe the difficulties and limitations of sugars to be applied in MNs preparation using the micromolding technique. The high viscosity of molten galactose and its predisposition to solidify generated problems during MNs fabrication. Also, this process requires high temperatures that can cause loss of the loaded drugs, and the hygroscopic properties of the materials after cooling create storage and handling problems. Galactose MNs revealed high deformation when placed in ambient conditions at 43% relative humidity and completely dissolved after 1 h at 75% humidity. Drug delivery limitations were also observed since partially dissolved galactose sealed the holes induced by MNs and only 0.05% of the total drug was release across a silicon membrane.

4.1.4. Hydrogel-forming MNs

As previously described, hydrogels are polymeric materials with water-swollen ability, retaining a significant fraction of water within the structures without dissolving. Hydrophilic functional groups attached to the polymeric backbone provide the ability for water absorption, whereas cross-linking between network chains gives them resistance to dissolution. Some polysaccharides, including starch, alginate, and agarose, and proteins, such as collagen and gelatin, are hydrogel-forming natural polymers [43]. Compared with dissolving MNs, hydrogel-forming MNs presented advantages such as an increased amount of drug encapsulation due to the incorporation of the active pharmaceutical in a separate reservoir. Moreover, they allow the extraction of interstitial fluid from the skin [391]. In addition, hydrogel-forming MNs avoid the deposition of MNs tip materials in the skin and allow for treatment termination if adverse drug reactions occur.

An example of this type of MNs was reported by Zhou et al. [392] who developed novel swellable MNs made of Ca^{2+} crosslinked alginate, demonstrating good mechanical properties, biocompatibility, and improved transdermal drug delivery efficiency for both acidic and non-acidic drugs.

Wei et al. [393] fabricated hydrogel MNs based on carboxymethyl chitosan, silk fibroin peptide, and oxidized pullulan for effective and biocompatible transdermal drug delivery. The prepared hydrogels comprising excellent mechanical strength, water retention, and biocompatibility were selected to fabricate Salvia miltiorrhiza loaded hydrogel-based MNs. The authors reported that microneedles exhibited facile skin insertion due to their exceptional mechanical properties, including a high fracture force of 0.88 N and a tip diameter of approximately 20 µm. Moreover, MNs achieved a drug loading efficiency of 68.5%, comparable to the results obtained with the well-studied copolymer polyvinyl methyl ether/maleic acid (Gantrez™) MNs.

Although not commonly employed, silk has also been utilized in the fabrication of hydrogel-forming MNs. Yin et al. [394] reported the fabrication of swelling-modified silk fibroin MNs for transdermal delivery using several dextran’s tagged with fluorescein isothiocyanate isomer as a model drug. The authors combined silk fibroin with urea, N-dimethylformamide, glycine, and 2-ethoxytheanol to form silk-based hydrogel-forming MNs. The results indicate that these swelling modified MNs can efficiently penetrate porcine skin with a depth of ~200 μm *in vitro*, forming semi-solid hydrogels with varying porous networks. The enhanced swelling capacity of the MNs leads to the formation of larger pores, thereby increasing the kinetics of transdermal drug release compared to non-swelling MNs systems. Additionally, it ensures a relatively uniform drug release profile within the subcutaneous tissue when compared to dissolving silk fibroin microneedles.

Methacrylated hyaluronic acid (MeHA) is emerging as a promising material for hydrogel-forming microneedles. HA-based hydrogel MNs alone are water-soluble and cannot withstand the rigors of microneedle application, as their structure fails in the skin. Combining HA with methacrylic acid results in a more robust material, due to the formation of crosslinks during hydrogel fabrication. Chang et al. [395] designed a swellable MeHA MNs patch to extract skin interstitial fluid as biomarkers for disease diagnosis and prognosis. It was reported that within 10 min, 2.3±0.4 μL of interstitial fluid was extracted giving an extraction of 3.3 mg/mm^2. This represents a higher extraction volume within the same 1 h period compared to hydrogel-forming MNs based on Gantrez™ (0.84 ± 0.24 μL) which highlights the exceptional swelling rate of MeHA. The covalently crosslinked network ensures structural integrity during the swelling process, leaving no residue on the skin. Moreover, the extracted interstitial fluid metabolites, including glucose and cholesterol, can be easily recovered for subsequent offline analysis, offering a promising avenue for minimally invasive metabolic detection in point-of-care personal healthcare monitoring devices.

Transdermal delivery via MNs arrays is seen as one of the most promising drug delivery technologies. Natural polymers, due to their cost-effectiveness and ease of processing, are gaining attention in MNs manufacturing, although several challenges still require addressing to advance this technology further. Therefore, the future of microneedle arrays produced from natural polymers holds great promise for safer, more effective, and sustainable healthcare solutions across a wide range of applications. Continued research and technological advancements are expected to drive innovation in this field.

5. Development of PHA-based Microneedles Arrays

Summary

PHAs with different composition, namely PHB, PHBHV with varying HV content (14, 43, and 87wt%), and PHBVHx were used to fabricate polymeric MNs arrays through the micromolding process. Although it was demonstrated that most of the tested biopolymers were successfully used as structure materials for the fabrication of MNs, their different physicochemical properties resulted in MNs' with distinct characteristics. The results show that using the biopolymers PHB, PHBV with an HV content of 43%, and PHBVHx, sharp and well-defined MNs were fabricated comprising lengths of 678 ± 70, 538 ± 94, and 582 ± 47 μm, respectively, and a base diameter of 330 μm. The obtained MNs revealed appropriated mechanical properties with similar failure forces (~5.5 N), however, the PHBVHx MNs demonstrated higher resistance to deformation. Insertion tests in a parafilm multilayer system showed that PHBVHx MNs were able to reach the third layer, corresponding to an insertion capability of up to 396 μm, being inserted 68% of the MNs' total height. Following a drop coating method, diclofenac sodium was used as a model drug to fabricate coated PHBVHx MNs. The prepared coated MNs exhibited similar failure force (5.45 ± 0.11 N) and lower mechanical stiffness (0.42 ± 0.01 mm) compared to the original MNs. The release profile of DS in a PBS solution revealed a fast release with 73% of the drug being released within the first 10 min. These findings highlight the potential of PHAs to be used as structuring material for the development of MNs.

5.1.1. Introduction

Polymeric MNs made of biocompatible and biodegradable polymers, offer greater resilience to shear-induced fracture and provide improved drug-release patterns due to their viscoelasticity, biodegradation, and/or dissolving properties of the polymer, respectively [396]. Among all the processes developed to fabricate polymeric MNs, the micromolding technique has been the most applied since it represents good reproducibility and cost-effectiveness [369]. Generally, the use of biopolymers to fabricate MNs by micromolding involves first its dissolution to coat a female mold, followed by a drying process, and finally, the peeling off from the molds [397]. However, the dissolution of certain biopolymers (e.g., PLGA, PCL, and PHA) requires the use of organic solvents which should be avoided due to possible toxicity issues [398]. Since most of these materials have high thermal stability, the use of melted polymers emerges as a solvent-free alternative, being used for the fabrication of MNs based on PCL [398], PLA [399], and PLGA [400].

Coated MNs are fabricated by coating the surface of solid MNs with a drug formulation before skin application. Several methods including dip coating, drop coating, gas jet drying, spray coating, electrohydrodynamic atomization based processes and piezoelectric inkjet printing have been used to coat MNs [401,402]. Drop coating represents one of the numerous methods used to coat MNs. This method consists of dropping the drug coating liquid into the MNs array, preventing the coating of the base substrate backside which represents an advantage over dip coating [402]. After solvent evaporation, the dissolved drug coats the MNs as well as the base substrate. Several parameters such as surface tension and rheological properties of the coating formulation, MNs geometry, flatness of the array, and roughness of the MNs are crucial to guarantee the quality of the coating [403]. Despite the wastage of drugs located between MNs, this method has been used due to its simplicity and low cost [402].

PHAs are a class of biodegradable polyesters synthesized and accumulated intracellularly by several bacteria and plants as carbon and energy reserves [404]. Depending on the polymer chain length, PHAs can be classified as short-chain length (scl-PHA) when comprising 3 to 5 carbon atoms, or medium-chain length (mcl-PHA) when containing 6 to 14 carbon atoms. The type of PHA monomers and their distribution throughout the macromolecule, as well as the biopolymer's molecular mass distribution, determine the thermal, rheological, and mechanical properties of this material. Poly(3-hydroxybutyrate), (PHB), one of the most well-known and extensively studied PHA, is characterized by its high crystallinity and rigidity granted by stereoregularity [405]. However, due to the presence of large crystals, PHB presents poor physical and chemical properties that can be improved by the introduction of longer chain length monomers in the polymeric chain. A well-known example is the copolymer poly(3-hydroxybutyrate-co-3-hydroxyvalerate) (PHBV), in which the incorporation of 3-hydroxyvalerate (HV) monomers results in biopolymers with lower crystallinity, lower melting temperature, higher flexibility, and decreased stiffness, improving its processability comparing to PHB [405,406]. Another interesting example is the terpolymer poly(3-hydroxybutyrate-co-3-hydroxyvalerate-co-3-hydroxyhexanoate) (PHBVHx) in which the incorporation of the monomer 3-hydroxyhexanoate (HHx) confers the biopolymer the flexibility of mcl-PHAs while retaining the tensile and thermal properties of PHB and PHBV [407]. Therefore, alongside their biocompatibility and no cytotoxicity [408,409], tailoring the monomers' composition of PHAs allows the production of polymers with distinct mechanical properties and degradation rates, making them promising materials suitable for use in several biomedical purposes such as surgical sutures, implants, drug carriers, and scaffolds [409–411].

Recently, the use of PHAs for the fabrication of MNs arrays was reported for the first time [412]. In this process, PHBV with a 3HV content of 21% ($PHBV_{21}$) was used to produce biodegradable MNs by a thermosetting process. The obtained conical MNs with a length of 690 μm and a base diameter of 330 μm, revealed good mechanical properties and the ability to impregnate the fluorescent dye Rhodamine 6G.

In this study, following a similar methodology, several types of PHAs, such as the homopolymer PHB, the copolymer PHBV, and the terpolymer PHBVHx, were tested as structural biomaterials to fabricate MNs arrays. The resulting MNs were characterized in terms of morphology, and the most well-defined MNs were selected for evaluation of their mechanical properties. The drug loading and release ability of the obtained MNs were assessed using diclofenac sodium (DS) as a model drug.

5.1.2. Materials and Methods

5.1.2.1. PHAs Production, Extraction and Purification

The homopolymer PHB was obtained by the cultivation of *Cupriavidus necator* DSM 428 using cooking oil as a carbon source, as described by Cruz et al. [413]. The same strain was used to produce the copolymer PHBV with an HV content of 87wt%, using glucose as the main carbon source and levulinic acid as a co-substrate, as described by Esmail et al. [414]. PHBV with different HV contents (14 and 43wt%) and the terpolymer PHBVHx were produced by mixed microbial cultures (MMC), using fermented fruit pulp as feedstock, as described by

Matos et al. [76] and Silva et al. [415], respectively. For simplicity, the PHBV copolymers were labeled according to their HV contents, i.e., $PHBV_{14}$, $PHBV_{43}$, and $PHBV_{87}$.

To recover the biopolymers from the biomass, the cultivation broth was centrifuged (10,350 ×*g*, 20 min, 4 ºC) and the obtained cell pellets were freeze-dried and milled (Fig. 5.1A-D). The biopolymers were extracted from the freeze-dried biomass (~10 g) by Soxhlet extraction with chloroform (~250 mL), at 80 ºC for 48 h. Cell debris was removed from the biopolymer solution by syringe filtration (0.45 µm, Whatman) and the biopolymers were purified by precipitation in ice-cold ethanol (1:10, v/v), under vigorous stirring [416]. The biopolymer was recovered, dried at room temperature in a fume hood, and stored until further use (Fig. 5.1E).

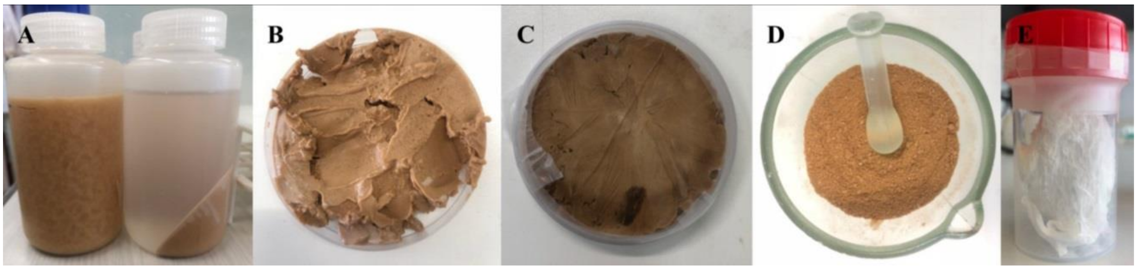

Figure 5.1 - Images of the (A) cultivation broth, before and after centrifuging, (B) the cell pellet, (C) the freeze-dried cell pellet, (D) the milled biomass, and (E) the dried biopolymer, following Soxhlet extraction with chloroform, precipitation in ice-cold ethanol and freeze-drying.

5.1.2.2. PHA Characterization

5.1.2.2.1. Monomer composition

The biopolymers monomer composition was determined by gas chromatography (GC) as described by Pereira et al. [407]. Briefly, dried biopolymer samples (1–2 mg) were subjected to acidic methanolysis using 2 mL 20% (v/v) sulphuric acid in methanol and 2 mL of benzoic acid in chloroform (1 g/L), at 100 ºC, for 4 h. Then, 1 mL of water was added, and the organic phase was recovered and analyzed by GC using a Restek column (Crossbond, Stabilwax), at constant pressure (100 kPa) with helium as carrier gas. The analysis was performed using a splitless injection mode and the heating ramp comprised three stages: 20 ºC/min until 100 ºC, 3 ºC/min until 155 ºC, and 20 ºC/min until 220 ºC. 3-hydroxybutyric acid, 3-hydroxyvaleric acid, and 3-hydroxyhexanoic acid (97%, Sigma-Aldrich, Darmstadt, Germany) were used as standards at concentrations between 0.05 and 1.0 g/L. The standards were prepared following the same protocol used for samples' preparation.

5.1.2.2.2. Molecular mass distribution

The average molecular weight (Mw) and the polydispersity index (PDI) of the biopolymers were determined by gel permeation and size exclusion chromatography (GPC/SEC) system (KNAUER Smartline, Berlin, Germany) using a Phenomenex Phenogel Linear Liquid Chromatography Column (300×7.8 mm) (Phenomenex, Torrance, CA, USA) coupled to a refractive index detector (Waters2414, Waters, Milford, CT, USA). The samples were dissolved in chloroform in a concentration range of 0.3-0.4% (w/v), and monodisperse polystyrene was used as standards (0.37 -2520 kDa). The analysis was performed at 30 ºC and a flow rate of 1mL/min of chloroform was used as the mobile phase.

5.1.2.2.3. Thermal Properties

The thermal properties were determined by Differential Scanning Calorimetry (DSC) and Thermogravimetric Analysis (TGA). DSC was carried out with a DSC Q2000 instrument (TA Instruments, New Castle, FL, USA). Hermetic aluminum pans were used to place the samples and analysis was performed with a heating and cooling rate of 10 ºC/min over a temperature range of -90 ºC to 200 ºC, through three heating cycles. The glass transition temperature (T_g) was determined by the endothermic slope of the last heating ramp, while the endotherm peak's temperature and area of the first heating cycle were used to determine melting temperatures (T_m) and melting enthalpies (ΔHm), respectively. The crystallinity (X_C) was estimated as the ratio between the obtained melting enthalpy and the melting enthalpy of 100% crystalline PHB, estimated as 146 J/g [417]. TGA was performed as described in section 3.1.2.4.6.

5.1.2.3. Fabrication of MNs Arrays Molds

For the fabrication of MNs molds, polydimethylsiloxane (PDMS) sheets were prepared by mixing PDMS with a curing agent (Silicone Elastomer, Sylgard 184, Dow Corning) at a ratio of 10:1 (v/v). The mixture was cast into a Petri dish until it filled up to about 3–4 mm in height and degassed under a vacuum to remove air bubbles. Afterward, the mixture was subjected to a curing process (70 ºC, 1 h) and the PDMS sheet was peeled off. A pulsed CO_2 infrared laser cutting system (Universal Laser System, VLS3.5, Vienna, Austria) was used for molds' fabrication by engraving controlled microstructures on the PDMS sheets (Fig. 5.2). Laser engraving was performed as described by Silvestre et al. [412] using a 2.0'' lens with a laser power of 30 W and a speed of 0.15 m/s to produce a spiral pattern. Each microcavity was engraved with 0.6 mm of tip-to-tip distance. After engraving, the molds were treated with isopropyl alcohol under ultrasounds for 10 min, washed with deionized water to remove residual residues, and dried with a nitrogen jet. Finally, the hydrophilicity of the mold surface was improved by heat treatment (220 ºC, 2 h). The final PDMS molds comprised an array of 15×15 MNs, in an area of 1 cm^2, where each conical spiral microcavity has a length of approximately 0.69 mm and a base diameter of 0.33 mm.

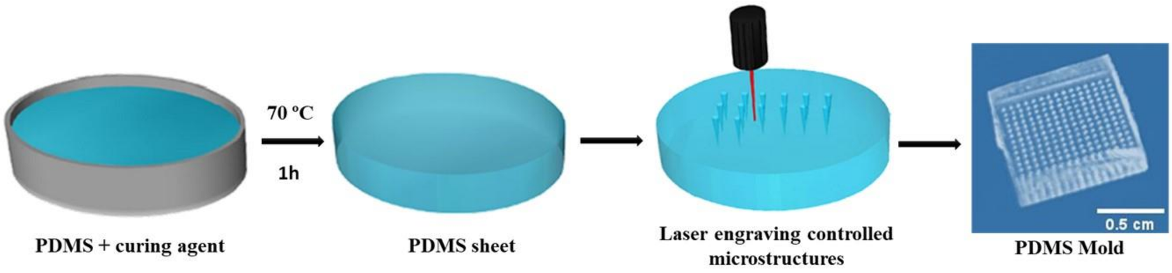
70 ºC
1h
PDMS + curing agent
PDMS sheet
Laser engraving controlled microstructures
0.5 cm
PDMS Mold

Figure 5.2 - Schematic illustration of the PDMS mold preparation (adapted from [412]).

5.1.2.4. Preparation of PHA MNs Arrays

The PHA MNs arrays were prepared as described in Fig. 5.3. The biopolymer (~ 0.1 g) was placed over the PDMS mold and subjected to a heat treatment (Nabertherm Furnace, Germany) comprising three main steps: first, the temperature was gradually increased from room temperature to 200 ºC, along 20 min (Fig. 5.3A); second, the temperature was maintained at 200 ºC for 20 min (Fig. 5.3B); then, a weight (~ 40 g) was placed on top of the melted biopolymer to promote the filling of the microcavities as the temperature decreased until room temperature (Fig. 5.3C). Finally, the sample was removed from the oven, the demolding process was performed and the PHA MNs array was obtained (Fig. 5.3D). The molds were washed twice with chloroform after each use to guarantee complete removal of any biopolymer left on it and dried with compressed air.

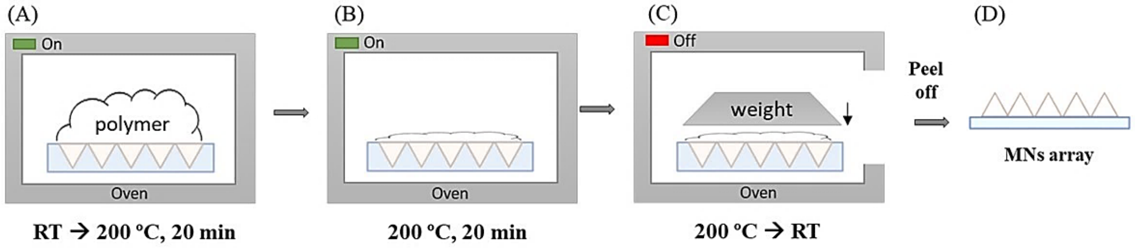
(A)
On
polymer
Oven
RT → 200 ºC, 20 min
(B)
On
Oven
200 ºC, 20 min
(C)
Off
weight
Oven
200 ºC → RT
Peel off
(D)
MNs array

Figure 5.3 - Schematic illustration of the fabrication process used for the preparation of PHA MNs arrays (adapted from [412]).

5.1.2.5. PHA MNs Arrays Characterization

5.1.2.5.1. Morphology

The morphology of the PHA MNs was observed with a stereo microscope (Leica M80, Leica Microsystems, Germany) using a magnification of 1.25×. For the observation of the detailed morphology, MNs samples were coated with iridium (20 nm) and analyzed by SEM (Table Microscope TM3030Plus, Hitachi High Technologies, Tokyo, Japan) using magnifications of 80×, 200× and 250×. MNs dimensions were determined by the SEM observations using ImageJ version 1.53k (National Institutes of Health, MD, USA).

5.1.2.5.2. Compressive axial mechanical analysis

The mechanical axial compressive properties of the PHA MNs were assessed using a texture analyzer TMS-Pro (Food Technology Corporation, England) equipped with a 10 N load cell, as described by Silvestre et al. [412]. Briefly, the MNs arrays were placed on the base plate and an axial force at a constant speed of 0.05 mm/s was applied, using a plunger with a 13 mm diameter. The test was performed with a trigger force of 0.01 N.

5.1.2.5.3. Insertion studies

For insertion studies, a commercial polymeric film (Parafilm®, Bemis Company Inc., Soignies, Belgium) was used as a model membrane. To simulate the thickness of excised skin (~1 mm), a sheet of Parafilm was folded into eight layers, as described by Larrañeta et al. [418]. The MNs arrays were inserted into the Parafilm surface using a texture analyzer in compression mode, by applying a force of 40 N, for 30 s. Then, each Parafilm layer was examined under the stereo microscope, and the number of holes was counted.

5.1.2.6. Preparation of loaded MNs

5.1.2.6.1. Loading of the PHBVHx MNs

The PHA MNs were loaded with DS (98%, Tokyo Chemical Industry Co) following a coating method. For fabricating the coated MNs, 200 µl of an aqueous solution of FucoPol (1.0%, w/v) and DS (1.0, w/v) were dropped on the surface of the PHBVHx MNs using a micropipette (Fig. 5.4). FucoPol was used as a thickener agent to increase the viscosity of the solution and, hence, facilitate its deposition onto the needles' surface. The arrays were placed in an oven at 30 ºC, until completely dry. The amount of DS coated on each MNs array was evaluated gravimetrically as 50% of the difference between the weight of coated and uncoated MNs.

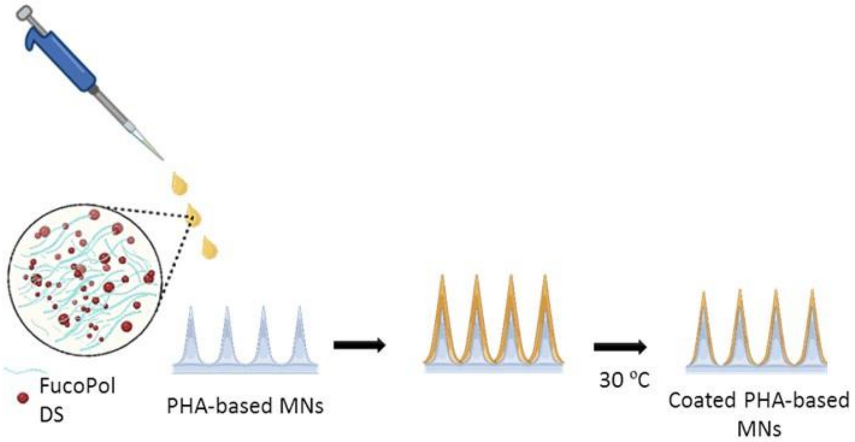

Figure 5.4 - Schematic illustration of the preparation of DS-coated PHA MNs.

5.1.2.6.2. Characterization of the coated PHBVHx MNs

The morphology of the PHBVHx MNs arrays coated with DS were characterized by SEM as previously described in section 5.1.2.5.1 and their mechanical properties were assessed as described in section 5.1.2.5.2.

5.1.2.6.3. *In vitro* drug release studies

Drug release studies were performed by immersing the DS-coated PHBVHx MNs arrays in 10 mL of PBS at 37 °C, under constant magnetic stirring (50 rpm). At predetermined time intervals, 1 mL samples of the release medium were withdrawn, and the same volume of fresh PBS preheated at 37 °C, was replaced. The DS concentration in the withdrawn samples was determined by UV-Vis spectrophotometer (CamSpec M509T, Leeds, UK), at a wavelength value of 275 nm [419].

5.1.3. Results and Discussion

5.1.3.1. Biopolymers' Physical and Chemical Properties

The biopolymers chosen to be tested for their suitability for the fabrication of MNs arrays were characterized by distinct physical and chemical properties, namely, in terms of their composition, molecular mass distribution, and thermal properties (Table 5.1). The homopolymer PHB had an average M_w of 5.2×10^5 Da and a PDI of 1.8. This biopolymer presented a glass transition (T_g) at 2.85 °C, melting (T_m), and degradation temperatures (T_{deg}) of 176 °C and 293 °C, respectively, and a crystallinity degree (X_c) of 52.4% [414].

The PHBV copolymers with HV contents of 14, 43, and 87wt% presented M_w values of 2.2, 0.6, and 4.0×10^5 Da, respectively, and similar PDI values (1.7, 1.8, and 1.8, respectively). These values are within the range of those reported for PHBV (0.6×10^5 – 28×10^5 Da) [420–422]. Regarding the polymers' thermal properties, their T_m values were significantly lower (90 – 117 °C) than that of the homopolymer (176 °C). Moreover, a decrease in the polymers' T_m was observed for increasing HV contents (Table 5.1), in accordance with previous reports [406,423]. On the other hand, PHBV14 showed an isomorphism phenomenon characterized by the presence of two melting peaks: the first (T_{m1}), occurring at 117 °C, corresponds to melting of the amorphous 3HV-rich fractions of the polymeric chain, and the second (T_{m2}) that occurred at 142 °C, corresponds to the most thermodynamically stable 3HB-rich fractions [422,424]. The semi-crystalline behavior of the copolymers was demonstrated by lower T_g values that ranged between -3.9 °C, for $PHBV_{43}$, and -14.4 °C for $PHBV_{87}$, compared to the homopolymer (2.85 °C) (Table 5.1). The lower Tg values correlate with the presence of longer side chain monomers in the macromolecule, demonstrating that biopolymer flexibility can be controlled by its composition [425]. The polymers' 3HV content also had an impact on their crystallinity degree. Compared to PHB (Xc=52.4%), $PHBV_{14}$ was characterized by a significantly lower Xc (28.5%), which was further reduced for $PHBV_{43}$ (3.8%). This reduction is ascribed to a limitation of crystallization of 3HB by the 3HV repetitive units introduced in the polymer chain [424,425]. On the other hand, $PHBV_{87}$ had an Xc of 24.0% which is similar to the value obtained for the copolymer $PHBV_{14}$ (28.5%), demonstrating that copolymers mainly composed of HV units recover the crystallinity fraction [409,426]. As shown in Table 5.1, the T_{deg} values for the copolymers were lower (255 – 281 °C) than that reported for PHB (293 °C) which can be also explained by the presence of the 3HV units [422,427].

The terpolymer PHBVHx was composed of 55wt% 3HB, 21wt% HV, and 24wt% HHx, and had an Mw of 0.9×10^5 Da with a PDI of 2.2 (Table 5.1). This biopolymer also showed an isomorphism phenomenon, presenting two melting temperatures, at 144 °C (T_{m1}) and at 159 °C (T_{m2}), which can be related to the high contents of monomers 3HV and 3HHx [407]. Similar thermal behavior was reported for a terpolymer composed of 68wt% 3HB, 17wt% 3HV, and 15wt% 3HHx, however, a lower value of T_{m1} was observed (111 °C) while a higher value of T_{m2} was achieved (173 °C), probably due to decreased content in 3HV and increased content in 3HB [424]. In general, the obtained T_m values were higher compared to those reported for other similar terpolymers. Typically, T_{m1} ranges from 91 °C to 129 °C, whereas T_{m2} presents values within a range of 139 °C to 148 °C [428,429]. The terpolymer's T_g was -3.8 °C with a $T_{5\%}$ of 275 °C. Its melting enthalpy was 7.9 J/g with an Xc of 5.4% (Table 5.1).

Table 5.1 - Composition, molecular mass distribution, and thermal properties of different PHA used (3HB, 3-hydroxybutyrate; 3HV, 3-hydroxyvalerate; 3HHx, 3-hydroxyhexanoate; M_w, molecular weight; PDI, polydispersity index; T_g, glass transition temperature; Tm, melting temperature; $T_{5\%}$, the temperature at which 5% weight loss occurs; ΔHm, melting enthalpy, Xc, degree of crystallinity; n.d., not detected).

Biopolymer ID	PHB	$PHBV_{14}$	$PHBV_{43}$	$PHBV_{87}$	PHBVHx
Composition (wt%)					
3HB	100	86	57	13	55
3HV	n.d.	14	43	87	21
3HHx	n.d.	n.d.	n.d.	n.d.	24
Molecular mass					
M_w ($\times 10^5$ Da)	5.2	2.2	0.6	4.0	0.9
PDI	1.8	1.7	1.8	1.8	2.2
Thermal properties					
T_g	n.d.	-5.3	-3.9	-14.4	-3.8
T_{m1} (ºC)	176	117	110	90	144
T_{m2} (ºC)	n.d.	142	n.d.	n.d.	159
$T_{5\%}$ (ºC)	277	255	281	277	275
ΔHm (J/g)	76.5	41.6	5.1	35.1	7.9
Xc (%)	52.4	28.5	3.5	24.0	5.4
Reference	[414]	This study	This study	This study	[407]

5.1.3.2. Fabrication of the PHA MNs arrays

In a previous study, a micromolding procedure was used, in which PHBV-based MNs were prepared by placing a dried $PHBV_{21}$ sample on the PDMS mold. The set was subjected to a gradual temperature increase from room temperature up to 220 °C, during a 30 min period, and then maintaining the temperature at 220 °C for 40 min. Subsequently, the melted $PHBV_{21}$ was pressed to make a flat backing surface and, afterwards, the temperature was gradually decreased until polymer solidification occurred [412]. In this study, a similar methodology was followed to fabricate the PHA MNs arrays. First, to verify the most appropriate temperature for melting each of the biopolymers used, their thermal stability was evaluated. As shown by Fig. 5.5, the TGA curves demonstrated that all biopolymers were thermal stable until around 230 °C, suffering a fast degradation, in a single-step process. For PHB, the copolymers $PHBV_{43}$ and $PHBV_{87}$, and the terpolymer PHBVHx a similar weight loss of 5% (275-281 °C) was observed, while for the copolymer $PHBV_{14}$, the same weight loss was achieved at a temperature of around 255 °C (Table 5.1). The maximum degradation rate for all biopolymers was observed between 240 °C and 310 °C where a major weight loss occurred (96.7-99.2%). The results suggested that all biopolymers could be subject to temperatures up to 200 ºC to fabricate MNs with no significant degradation.

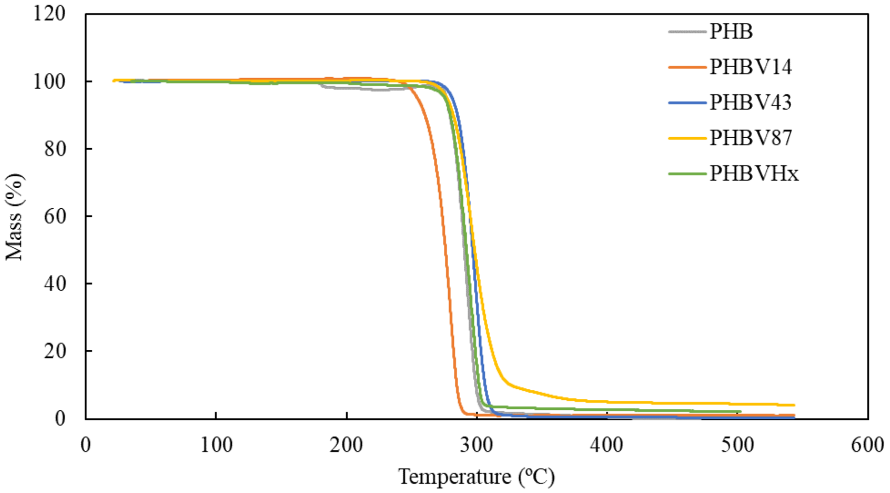

Figure 5.5 - Thermogravimetric curves of PHB, copolymers $PHBV_{14}$, $PHBV_{43}$, and PHBV87, and terpolymer PHBVHx.

The DSC analysis was performed with a heating rate of 10 ºC/min to investigate the melting behavior of the biopolymers (Appendix A2). As shown in Fig. 5.6, the thermogram obtained for one of the copolymers ($PHBV_{43}$), revealed that although for the copolymers the melting point was significantly below 200 ºC (110 ºC, for this biopolymer), for this process, it was not possible to use lower temperatures because polymer melting occurred in a wide range of temperatures (80-180 ºC). This phenomenon probably can be justified by the heterogeneity of the polymeric chains due to the presence of the HV and HHx monomers. Chan et al. [406] also reported a broader melting peak ranging from 49 ºC to 171 ºC and 47 ºC to 177 ºC for PHBV copolymers composed of 24mol% and 63mol%, respectively. The authors suggest a possible correlation between the broad melting peaks with a wide chemical composition distribution of the copolymers [406].

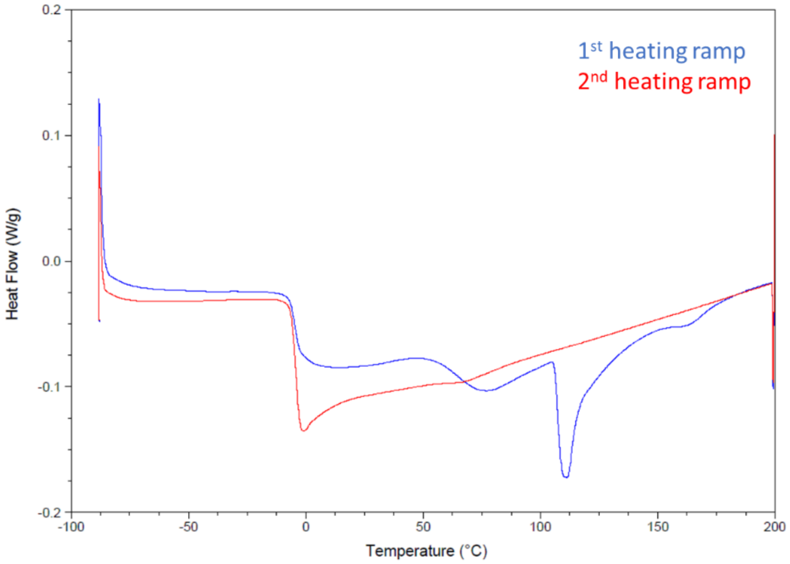

Figure 5.6 - Differential scanning calorimetry (DSC) thermogram of PHBV$_{43}$ comprising the first (blue line) and the second (red line) heating scan.

Fig. 5.7 shows the main steps of the preparation of the PHA MNs arrays. In the first step, a dried sample of the biopolymer was placed on the surface of the PDMS mold (Fig. 5.7A), and the set was submitted to a heat treatment at 200 °C. In the second step of the process, after the uniform melting of the entire sample, the melted polymer was homogeneously pressed to promote the filling of the microcavities (Fig. 5.7B). Finally, the set was cooled to room temperature, and the final MNs array was obtained by detachment from the mold (Fig. 5.7C).

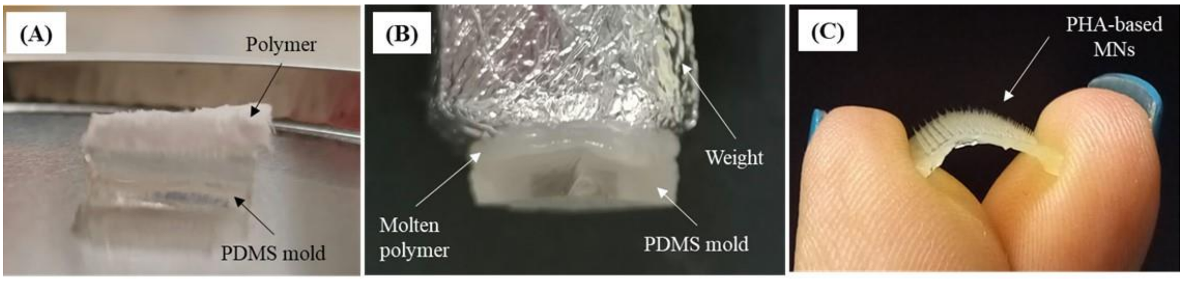

Figure 5.7 - Three-step process for the MNs array fabrication: (A) PHBV$_{43}$ sample over the PDMS mold, (B) filling the mold microcavities with molten polymer, and (C) demolding process and obtaining MNs array.

The obtained arrays prepared from the biopolymers listed in Table 5.1 are shown in Fig. 5.8. Although all tested biopolymers could be used for the MNs arrays fabrication, via the melting method, upon melting, the biopolymer PHBV$_{87}$ revealed high viscosity, hindered its uniform spreading over the mold and resulted in an incomplete array being formed. The arrays presented a white coloration, similar to the starting materials. In line with the intrinsic properties of the biopolymers, the PHB-based arrays were more rigid and opaque, while the arrays produced from the copolymers and the terpolymer were more flexible and translucid.

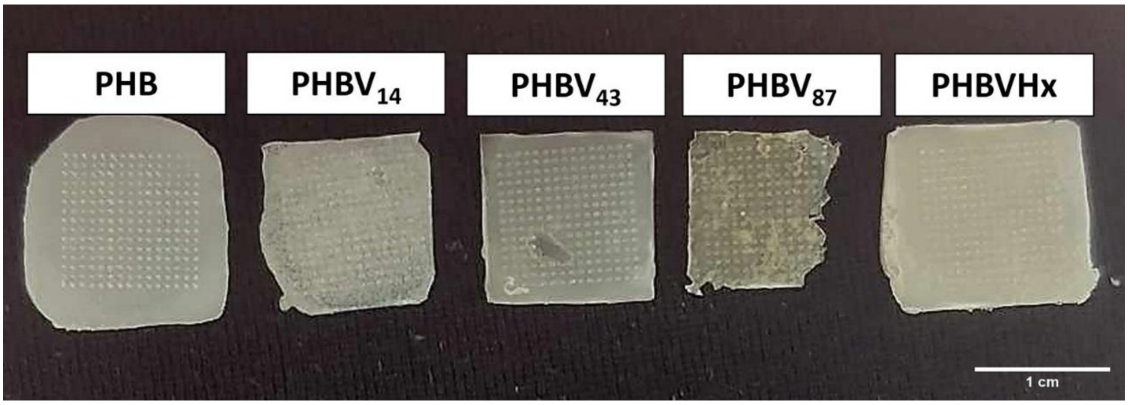

Figure 5.8 - Macroscopically appearance of MNs arrays fabricated using different types of PHAs.

5.1.3.3. Morphological characterization

The morphology of the fabricated MNs arrays was assessed with a stereo microscope (Fig. 5.9). Except for biopolymer $PHBV_{14}$, all tested biopolymers successfully filled the molds' microcavities, producing MNs with a three-dimensional (3D) conical structure and sharp tips, following the pattern and design of the PDMS mold.

The arrays produced from PHB, $PHBV_{43}$, and PHBVHx presented the sharp and well-defined MNs, with lengths of 678 ± 70, 538 ± 94, and 582 ± 47 µm, respectively, and a diameter of around 330 µm, concomitant with the PDMS mold dimensions (Fig. 5.7). On the other hand, the poorest result was obtained for the $PHBV_{14}$ MNs, in which only the base of the MNs was formed. This outcome might be explained by the need for a higher amount of biopolymer. The $PHBV_{87}$ array, although presenting shorter MNs (300 ± 36 µm), still resulted in well-defined and sharp needles. The results demonstrate that the size of all fabricated MNs agrees with the dimensions and design of the mold's microcavities (690 µm length, 330 µm base diameter). Typically, MNs can have lengths between 150 and 1500 µm [396], however, lengths above 600 µm demonstrated high efficiency in creating pathways across the skin [430]. These results show that the biopolymers' intrinsic properties impact their suitability for fabricating MNs, as well as the resulting array characteristics. Concerning the copolymers, the high molecular weight of biopolymers $PHBV_{14}$ and $PHBV_{87}$ compared to $PHBV_{43}$ might contribute to the decrease in the size of the MNs, since in the molten state their higher viscosity makes it difficult to fill the mold [431,432]. Additionally, the heterogeneity of the polymeric chain and the sample used might also conduce to difficulties in fulfilling the mold's cavities.

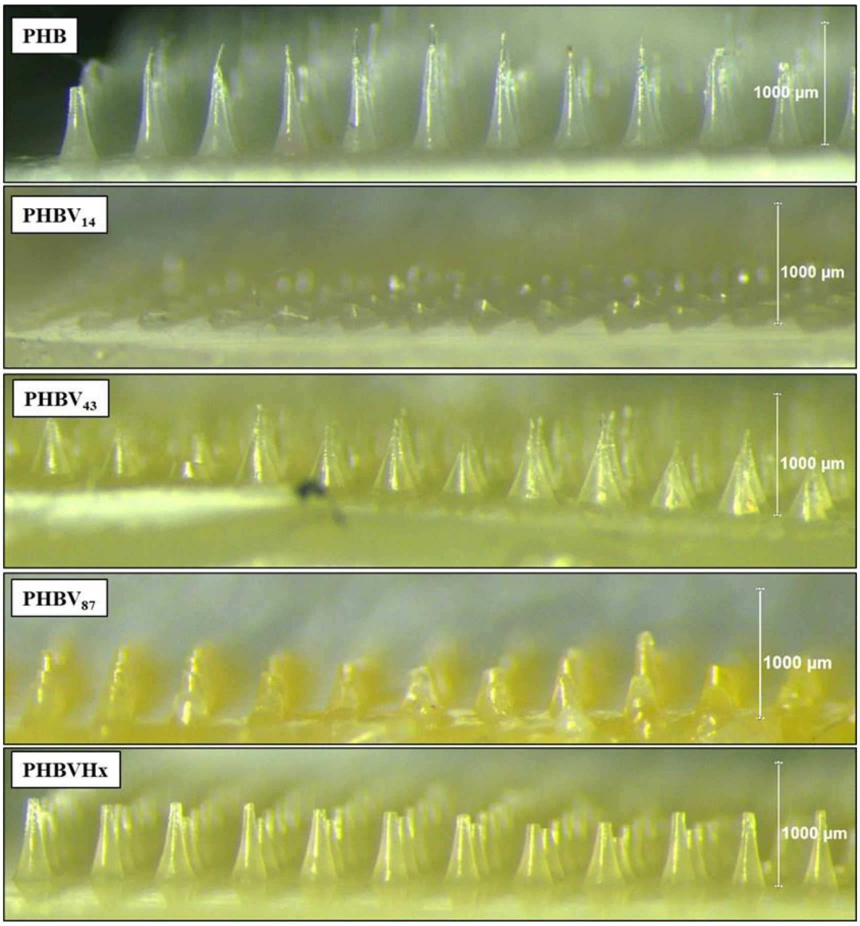

Figure 5.9 - Optical images of MNs arrays fabricated using PHB, copolymers $PHBV_{14}$, $PHBV_{43}$, and $PHBV_{87}$, and terpolymer PHBVHx, in a side view.

Based on these results, MNs fabricated from biopolymers PHB, $PHBV_{43}$, and PHBVHx were further characterized for their mechanical properties, aiming to select the best performing MNs arrays.

5.1.3.4. Mechanical Characteristics of the MNs

The mechanical properties of the materials play a crucial role in the development of MNs since they represent their ability to overcome the skin barrier and realize efficient transdermal drug delivery [35,433]. The mechanical characteristics of the MNs arrays fabricated from the three types of PHA were evaluated by a compression test, where the axial force loaded vs the displacement behavior was assessed using a texture analyzer. As shown in Fig. 5.10A, a similar mechanical behavior was obtained for the three MNs arrays, comprising a progressive initial deformation until achieving the yield point, that represents the end of the elastic deformation, followed by the beginning of plastic deformation [35]. Moreover, an identical force was required to bend PHB, $PHBV_{43}$, and PHBVHx MNs (5.65 ± 0.18, 5.56 ± 0.32, and 5.49 ± 0.04 N, respectively). These values are significantly lower than the ones (30 N) reported for the MNs arrays prepared with PHBV with a 21wt% 3HV content [412]. This difference might be explained by the variation of several parameters in the measurement methodology, namely the fixed maximum displacement. Silvestre et al. [412] defined a maximum displacement of 1 mm, for which the force was applied, while in the present study, the test was performed until the yield point, which usually marks the failure force, was achieved (Fig. 5.10A). Nevertheless, all MNs exhibited failure forces higher than the required minimum force (4 N) to penetrate the skin [434], confirming that the fabricated MNs arrays are suitable for human skin penetration. Shah et al. [435] reported a similar failure force (~5 N and ~6 N) for polymeric MNs (~500 µm length and ~200 µm base diameter) produced using dextran and HA. On the other hand, higher failure forces were observed for MNs prepared with PLA (10.5 ± 1.3 N) [436], PLGA (106 ± 2 N), and SA (18 ± 5 N) [368]. However, it should be noted that in addition to the intrinsic properties of each material, other factors such as geometry and dimensions of the MNs as well as the number of MNs per array [437].

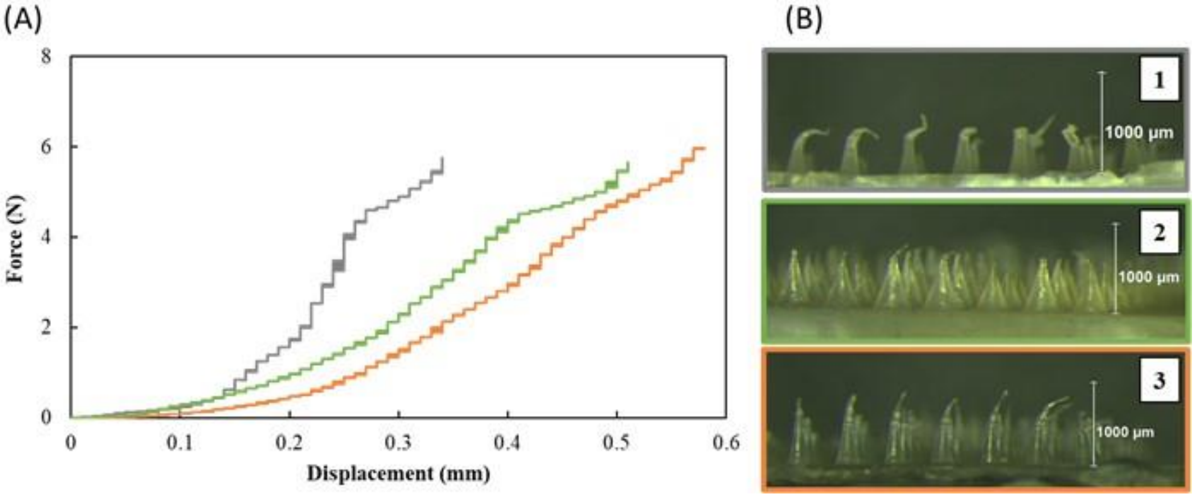

Figure 5.10 - (A) Compression stress-strain curves of the MNs arrays fabricated from PHB (grey line), PHBV$_{43}$ (green line), and PHBVHx (orange line), and (B) optical images of MNs based on PHB (1), PHBV$_{43}$ (2) and PHBVHx (3) after the compression test.

At the failure point, PHBV$_{43}$ and PHBVHx MNs revealed displacement values of 0.48 ± 0.09 and 0.61 ± 0.04 mm, respectively, while a lower value was obtained for PHB-based MNs (0.35 ± 0.05 mm). These results demonstrate that the biopolymer used to fabricate the MNs arrays influences their resistance to deformation. The lower value obtained for the PHB-based MNs can be explained by the stiffness characteristics of PHB compared to the copolymers and the terpolymer. In fact, PHB exhibits a high Young's modulus value (218 ± 8 MPa) due to its rigid and stiff nature [414]. On the other hand, the incorporation of 3HV and 3HHx units into the polymeric chain led to a significant decrease in Young's modulus value of copolymers and terpolymers. For example, Lemechko et al. [421] reported a decrease in Young's modulus value of a copolymer from 531 MPa to 45 MPa when 3HV content increased from 15 to 45%. In another study, Abassi et al. [422] also described a higher Young's modulus value (1120 MPa) for a copolymer composed of 17% of HV and when the HV content increased to 25%, the value decreased to 570 MPa. Regarding the terpolymers, PHBVHx presented a Young's modulus value of 78.3 ± 6.9 MPa [407]. Zhang et al. [438] showed that increasing the 3HV and 3HHx content from 10.9 and 10.3% to 25.7 and 19.1%, respectively led to a decrease in Young's modulus value from 234.9 to 2.08 MPa.

The same behavior was reported for MNs arrays based on other biopolymers, such as HA [439] and PLA/poly(p-dioxanone) (PPDO) [440]. For example, MNs based on PLA with a Young's modulus of 3000 MPa presented a failure force of 3.23 N at a displacement of 0.066 mm, however when PLA was blended with PPDO, the Young's modulus of the material slightly decreased, and the obtained MNs exhibited failure at a displacement of 0.124 mm. The authors attributed this behavior to the higher elongation at the break of PLA/PPDO blends compared to PLA alone [440].

To investigate the morphology of the MNs after the compression tests, the arrays were recovered and analyzed by a stereo microscope (Fig. 5.10B). It can be observed that the MNs suffer deformations with more visible damage at the tips. Due to their higher lengths, the structures of the PHB and the PHVHX MNs were more affected by the compression. However, the nature of the biopolymers led to different behaviour. In addition to deformation, several PHB MNs revealed brittle tips with loss of structure, whereas PHBVHx MNs exhibited only deformation without breaking. These observations suggest that PHBVHx MNs might be more appropriate, as one of the concerns about MNs fabrication is their insertion into the skin without fracturing [32,34]. A similar bending behaviour was observed for MNs prepared with copolymer PHBV [412] and with CMC [419].

Considering the MNs arrays higher ability to withstand deformation, the PHBVHx-based arrays were selected to perform preliminary insertion studies and evaluate their loading and release ability.

5.1.3.5. Insertion studies

The skin insertion ability of the PHBVHx MNs arrays was assessed using an eight-layer Parafilm model system as a skin simulant, presenting the thickness of excised skin (~1 mm) [418]

(Fig. 5.11). The experiment was carried out by placing the arrays over the Parafilm multilayer and applying an axial force of 40 N for 30 s (Fig. 5.11A). Fig. 5.11B shows the number of holes created in each Parafilm layer according to the insertion ability of the MNs. The first layer of parafilm, corresponding to a depth of 132 µm was almost fully pierced (95.3 ± 0.8%), while only a small number of MNs reached the second (28.9 ± 4.9%) and the third layers (16.9 ± 5.8%). Moreover, none of the MNs were able to penetrate the fourth layer of the parafilm model. An identical result was obtained for HA MNs that fully pierced the first layer of parafilm but only 72% and 19% of the MNs were able to pierce the second and third layer, respectively [441]. Silva et al. [419] also demonstrated the ability of CMC MNs to penetrate the first layer completely, decreasing the percentage of puncture to 90% for the second layer and to 29% for the third layer. The commercial MNs systems Dermapen® and Dermastamp™ comprising MNs fabricated with stainless steel revealed the ability to pierce approximately 100% of the first three layers of parafilm, with the fifth and sixth layers being pierced less than 50% [442].

Thus, it was demonstrated that the MNs could easily penetrate the first parafilm layer and it could reach the third layer which corresponds to a thickness of around 396 µm (Fig. 5.11C). This suggests that PHBVHx MNs would pierce through the *stratum corneum* (~10 to 30 µm of thickness), allowing insertion into the epidermis [35,443]. Considering that each layer has a mean thickness of 132 µm, this suggests that the PHBVHx MNs were inserted to approximately 68% of their total height (582 µm).

After tests on the parafilm system, several studies reported the ability of MNs to pierce the skin. Fonseca et al. [441] developed a patch of rutin-loaded HA/BC MNs able to pierce 81% of the third parafilm layer, and insertion tests into porcine ear skin revealed their capacity to create cavities with 47.3-99.3 µm of depth which corresponds to ~22% of the height of the MNs. A patch of DS-loaded CMC MNs that pierced 99%, 86%, and 18% of the first, second, and third parafilm layers, respectively, demonstrated the ability to puncture ex vivo human skin with depths of 133-401 µm, equivalent to 29% and 88% of the MNs' height [419]. The similarities of the results obtained for the parafilm multilayer system suggest that PHBVHx MNs would be able to penetrate the skin and create microchannels allowing the delivery of molecules through the skin.

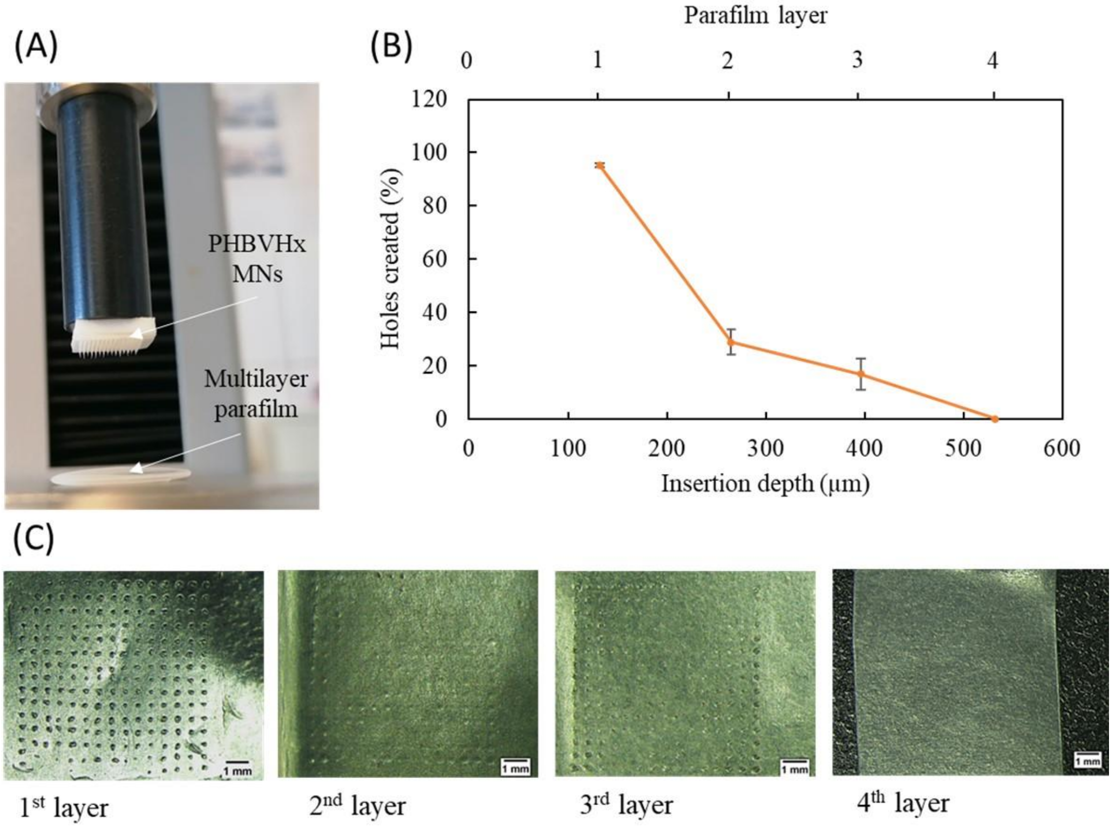

Figure 5.11 - Parafilm insertion studies: (A) Optical image of the set-up (B) Percentage of holes created in each Parafilm layer using PHBVHx MNs, and (C) optical images of parafilm layers after insertion.

Fig. 5.12 shows the SEM images of the PHBVHx MNs before and after insertion in the Parafilm multilayer system. Before the insertion, the MNs presented a conical structure with sharp tips (Fig. 5.12A), as previously described. Upon magnification, it is possible to see in detail the surface roughness of MNs. These rougher surfaces might be advantageous for the process of coating the MNs with the drug, as they allow the distribution of higher amounts of the drug in the MN instead, of accumulating it in the MN's tip [444]. As expected, given their mechanical behavior, the MNs remained unbroken after the insertion in the Parafilm, exhibiting a slight bending of the tip without any damage to the MN's structure (Fig. 5.12B). This result demonstrates their capacity to withstand the required force for skin penetration without breaking. Similar behavior was demonstrated in CMC-based MNs that exhibited a deformation upon force loading application without breaking [419]. An MNs array prepared with sodium alginate was also subjected to parafilm insertion studies, and an identical curvature of the structure was observed [445]. On the other hand, the morphologies of MNs fabricated from polyether ether ketone (PEEK) [446] and a copolymer of methyl vinyl ether/maleic acid (Gantrez®) [447] remained unchanged with similar heights before and after insertion into parafilm.

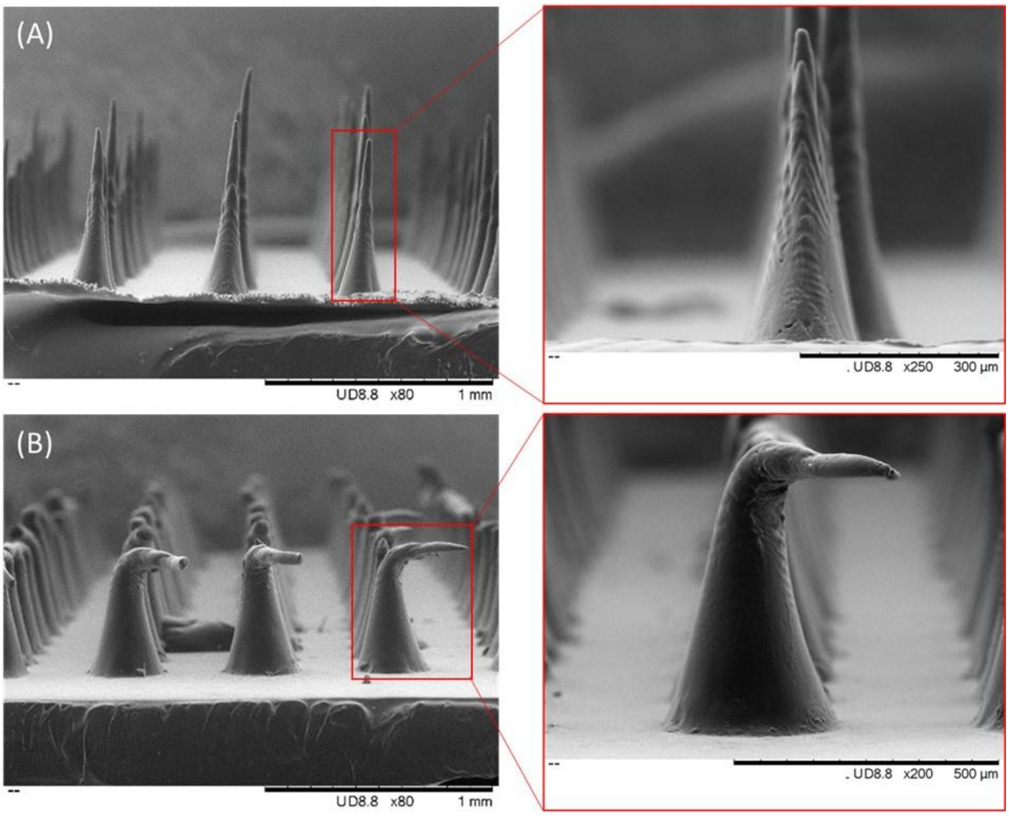

Figure 5.12 - SEM images of PHBVHx based MNs: (A) before and (B) after insertion in Parafilm.

5.1.3.6. Preparation of loaded PHBVHx MNs

PHBVHx MNs arrays were loaded using a coating method and DS as a model drug. FucoPol was used as a thickener agent to improve the coating solution's viscosity [289]. Thus, a solution of FucoPol and DS was dropped on the arrays, and the samples were left to dry. A similar approach was used for PLA-based MNs, where PVA was used as a thickener to control the viscosity of the sulforhodamine B coating solution [448]. In that study, increasing the viscosity of the coating solution from 150 to 20100 mPa/s led to an increase in the drug loading from 2.5 ng/needle to 33.4 ng/needle. Wu et al. [431] also reported the preparation of identical rhodamine B coated PLA MNs, using CMC as a thickener agent. The obtained DS-coated PHBVHx MNs were characterized in terms of morphology and their mechanical properties were investigated.

5.1.3.7. Characterization of the DS-coated PHBVHx MNs

5.1.3.7.1. Morphology

The morphological characterization of the DS-coated PHBVHx MNs was assessed by SEM analysis. Fig. 5.13 shows that the drop coating method led to an accumulation of the coating solution on the base substrate between MNs. Moreover, the coating was not uniform, as some tips of the MNs were not coated. The irregular and non-uniform pattern was also described for silicon MNs coated following a similar methodology [449]. The authors attribute this to a surface tension effect and overcome it by adding trehalose to the coating formulation. However, a high improvement was achieved when the methodology was changed to spray-coating. Chen et al. [448] avoided this type of drawback by using an adjustable apparatus that allowed only the structure of the MNs to be immersed in the coating solution.

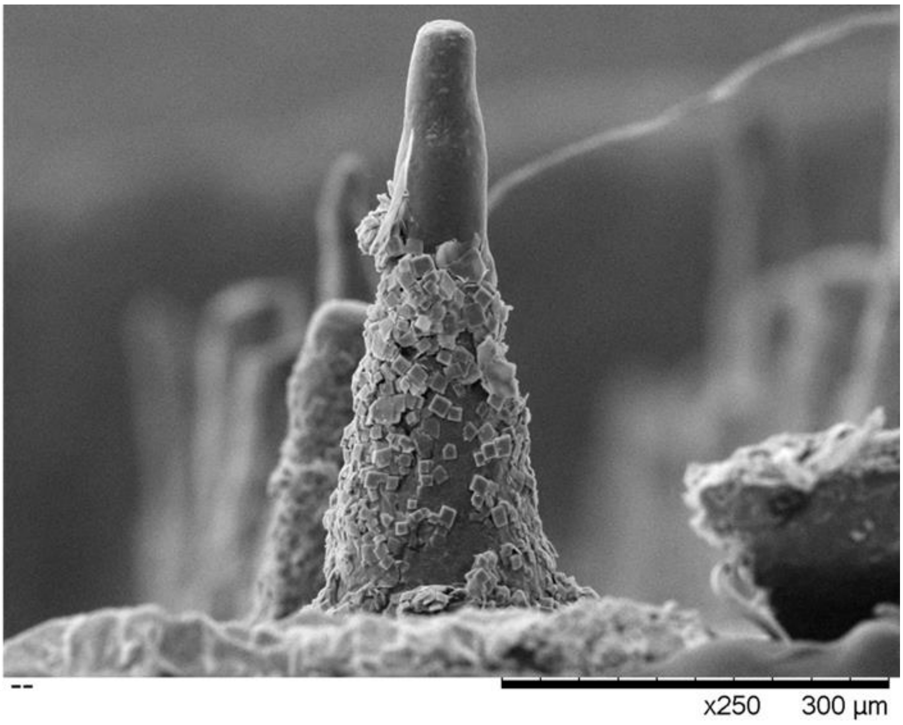

Figure 5.13 - SEM image of DS-coated PHBVHx MNs.

5.1.3.7.2. Mechanical properties

The effect of the coating solution deposited on the PHBVHx MNs on their mechanical properties is shown in Fig. 5.14. The compressive stress-strain curves demonstrate that no significant impact on the MNs' strength was observed since a similar force was required to bend the DS-coated MNs (5.45 ± 0.11 N) and the non-coated MNs (5.49 ± 0.04 N). This result shows that the required minimum force to pierce the skin (4 N) was achieved by the DS-coated MNs, evidencing their possible use as transdermal delivery systems. Identical mechanical properties were also reported for the PLA MNs (~2.5 N/needle) and PLA coated MNs (~2.75 N/needle) [448]. On the other hand, compared to non-coated MNs, it was noticed a decrease in the displacement value from 0.61 ± 0.04 to 0.42 ± 0.01 mm, at the failure point. This result suggests that the elastic properties of the PHBVHx MNs were affected by the coating. An increase in mechanical stiffness was also observed for acrylic based MNs when coated with polypyrrole [450]. In fact, for a force of 0.08 N/needle, the non-coated MNs achieved a displacement of 48.1 ± 8.79 µm while a lower displacement value (33.7 ± 4.09 µm) was obtained for the polypyrrole-coated MNs. Despite this difference, *in vitro* skin insertion tests revealed that the latter structures achieved 100% penetration in porcine skin without damage to the surrounding skin and MNs, suggesting a possible use of these MNs as a painless minimally invasive platform.

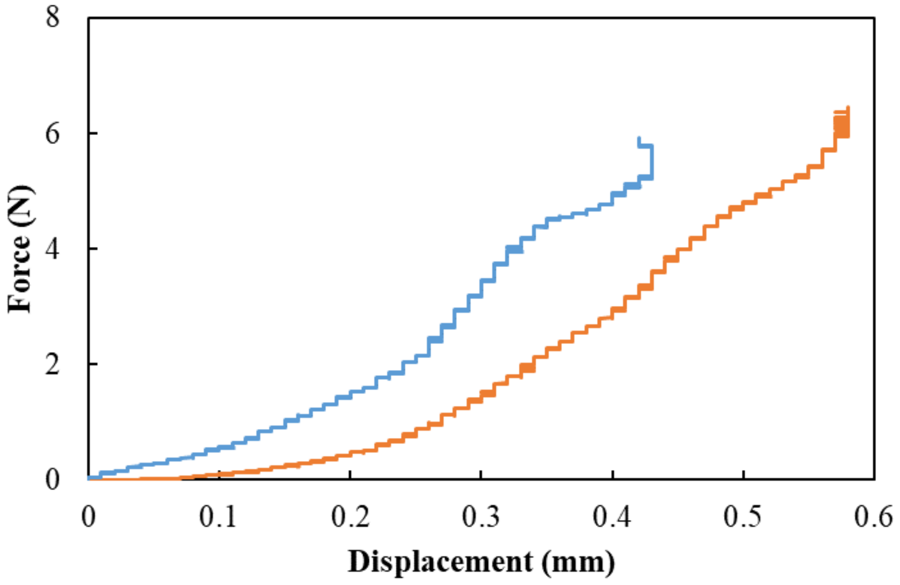

Figure 5.14 - Compression stress-strain curves of the DS-coated PHBVHx MNs (blue line) and non-coated PHBVHx MNs (orange line).

5.1.3.7.3. *In vitro* drug release studies

The release profile of DS from the PHBVHx MNs arrays was performed in PBS, at 37 ºC. As shown in Fig. 5.15, the release profile of DS was characterized by an initial fast release phase followed by a slower release state. An initial fast release phase (10 min) was noticed, during which 73% of the DS was released, followed by a slower release phase (10-40 min), after which a plateau was reached. After 300 min, an overall release of 80% was achieved.

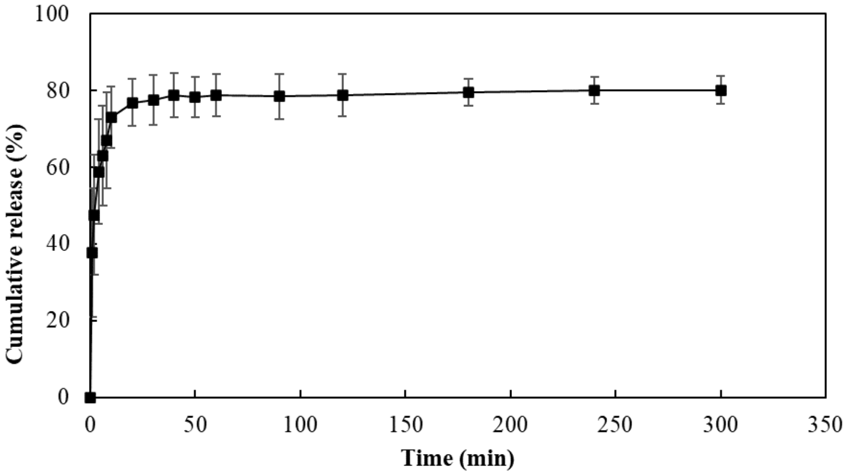

Figure 5.15 - Cumulative release profile of DS from coated PHBVHx MNs.

As shown in the morphological characterization (Fig. 5.13), after loading a layer of DS adhered to the surface of the DS-coated MNs, and when in contact with the released medium, rapid dissolution of the DS occurs, leading to a high percentage of release within the initial burst phase. Following a similar approach, bioceramics-based MNs were coated with ovalbumin, and it was demonstrated that in PBS, at room temperature, 43% of the drug was released within the first 10 min, and a percentage of 90% was achieved after 60 min [451]. Zhou and coworkers [452] prepared PLA MNs coated with BSA, and under similar *in vitro* release conditions, around 40% of BSA was released within the first 24 hours.

Despite the differences in the loading methodology, a similar release profile of DS was obtained from CMC-based MNs [419]. In that case, around 58% of the loaded DS was released in the first 10 min, reaching the maximum cumulative release (98%) after 40 min. Considering the therapeutical use of DS, this rapid-release profile is appropriate as it can provide immediate local analgesic and anti-inflammatory action [453].

The mechanism of DS release from the coated PHBVHx MNs was investigated by adjusting the first 60% of the obtained release profile to the Korsmeyer-Peppas model [206]. The results demonstrated that the release data fit the model since the regression coefficient value was 0.99. Moreover, the *n* value obtained (0.32) suggests that the release mechanism follows a Fickian diffusion.

5.1.4. Conclusions

The present study demonstrates for the first time the preparation of MNs arrays with different types of PHAs, namely, the homopolymer PHB, PHBV copolymers with different 3HV contents (14, 43, and 87wt%), and the terpolymer PHBVHx. Most of the biopolymers tested were suitable as structural materials for MNs arrays' fabrication via the melting micromolding process. Most of the obtained MNs presented a conical geometry with sharp tips and revealed appropriate mechanical properties to penetrate the skin. PHBVHx MNs were selected to prepare coated MNs, using DS as a model drug, following the drop coating method. The coating layer was observed by SEM images that revealed a layer of DS adhered to the MNs surface. Although the failure forces were similar, coated PHBVHx MNs demonstrated lower mechanical stiffness when compared to unloaded PHBVHx MNs. Furthermore, a high release rate of DS was obtained. Despite several studies focused on the optimization of loading methodology and skin permeation are essential to further improve the efficacy and efficiency of the PHA-based MNs, this study demonstrated that PHAs are very interesting biomaterials with great potential to be used as structuring materials for MNs.

IV. CONCLUSIONS AND FUTURE WORK

IV.1. Conclusions

In contemporary society, the importance of drug delivery in healthcare is immeasurable. Its extensive application in modern medicine is seamlessly integrated into our daily lives, shaping the way we receive and benefit from therapeutic agents. This thesis embarked on a comprehensive exploration and development of novel TDDS, focusing on hydrogels and MNs based on natural polymeric biomaterials for their fabrication.

The journey began by addressing the challenge of dissolving the typically intractable biopolymer CGC, which culminated in using environmentally friendly solvent systems that achieved high polymer solubility, paving the way for diverse biopolymer applications. The subsequent work unveiled the innovative preparation of hydrogels based on CGC, highlighting their versatility and customization potential, particularly through the choice of alkali solvent and ionic strength. Moreover, optimization of the CGC hydrogel preparation process further enhanced their mechanical and swelling properties, with successful loading of different APIs, opening up possibilities for tailored drug delivery. Importantly, CGC hydrogels exhibited biocompatibility for different cell lines, bolstering their potential in biomedical applications as drug delivery platforms and/or scaffolds for tissue engineering.

The journey continued with the exploration of FucoPol, another promising natural polymer, as material for HMs using Fe^{3+} as a crosslinker. This novel development showed the versatility of FucoPol, offering tunable properties, biocompatibility, and anti-inflammatory activity, making it a promising biomaterial for HMs in various applications. Furthermore, the drug loading experiments with caffeine and diclofenac sodium into FucoPol HMs demonstrated their potential as efficient drug delivery systems, with release profiles suited for different applications.

The study also included the fabrication of MNs using various types of PHA. The success in fabricating conical-shaped MNs with different PHAs through a melt micromolding process demonstrated their potential as structuring materials for these innovative drug delivery devices. Moreover, PHBVHx MNs, chosen for drug coating, exhibited non-uniform coverage of MNs, comparable mechanical strength, and lower stiffness post-coating. *In vitro* drug release experiments showed that maximum cumulative release was achieved within 20 min.

Overall, this thesis has illuminated new pathways in the development of transdermal delivery systems, emphasizing the potential of natural polymers in creating effective and biocompatible hydrogels, HMs, and MNs arrays. These contributions hold promise for the advancement of drug delivery technologies, ultimately benefiting healthcare and biomedical applications.

IV.2. Future Work

During this thesis, significant advances were performed in the development of hydrogels and MNs for transdermal drug delivery using different natural polymeric biomaterials, but it also drove interest into exciting new opportunities for further research and future improvements.

Considering the hydrogels, it is crucial to perform permeation studies using skin models (e.g., SkinEthic, EpiDerm) that will provide a more physiologically relevant environment, mimicking the complexities of human skin, to evaluate the effectiveness of these biomaterials for transdermal drug delivery. Moreover, it is of interest to study several alternative strategies, including polymer blending and surface modifications, to achieve a sustained drug release which is crucial in several cases. It is also relevant to explore the stability of the structures through accelerated and long-term studies to better understand their optimal storage conditions, extending their shelf life. Additionally, scaling-up the procedures for hydrogels' production is crucial for their implementation as commercial products, which could involve refining the manufacturing methods to ensure consistency and quality on a larger scale. Furthermore, taking advantage of the gelling ability of CGC and FucoPol, it could be very interesting to evaluate their ability for the fabrication of stimulus responsive hydrogels, or even their ability to fabricate injectable hydrogels.

Regarding the MNs, the methodology used in MNs fabrication should be optimized to obtain identical MNs over the array. Moreover, to optimize MN performance, enhancing the mechanical properties of PHA-based MNs strategies including different designs and dimensions might be useful to improve their strength, and insertion characteristics. It is also crucial to follow an optimal coating technique that can proficiently apply drug coatings, with special emphasis on the MN tips. This aspect is pivotal in ensuring consistent and reliable drug delivery via this type of MNs. Furthermore, to validate the effectiveness of MNs for transdermal drug delivery, *in vitro* penetration studies using *ex vivo* animal or human skin should be performed. These experiments are essential to understanding the actual insertion capacity and drug permeation capabilities of the MNs. Also, scaling up the production of PHA-based MNs while maintaining their quality and consistency will be crucial for practical use.

Overall, this Thesis, not only demonstrated the great potential of the different tested natural polymers for use as drug delivery systems, but it also paved the way for further exploring the novel developed biomaterials. The future perspectives outlined, which include fine tuning the biomaterials' properties, evaluation of their performance under physiological conditions, and scaling up the procedures, among others, will further enhance the potential of the developed structures as platforms for improved transdermal drug delivery application.

REFERENCES

1. Tiwari, G.; Tiwari, R.; Bannerjee, S.; Bhati, L.; Pandey, S.; Pandey, P.; Sriwastawa, B. Drug Delivery Systems: An Updated Review. *Int J Pharma Investig* **2012**, *2*, 2, doi:10.4103/2230-973X.96920.
2. Nunes, D.; Andrade, S.; Ramalho, M.J.; Loureiro, J.A.; Pereira, M.C. Polymeric Nanoparticles-Loaded Hydrogels for Biomedical Applications: A Systematic Review on In Vivo Findings. *Polymers* **2022**, *14*, 1010, doi:10.3390/polym14051010.
3. Anselmo, A.C.; Mitragotri, S. An Overview of Clinical and Commercial Impact of Drug Delivery Systems. *J. Control Release* **2014**, *190*, 15–28, doi:10.1016/j.jconrel.2014.03.053.
4. Prausnitz, M.R.; Langer, R. Transdermal Drug Delivery. *Nat Biotechnol* **2008**, *26*, 1261–1268, doi:10.1038/nbt.1504.
5. Langer, R. Drug Delivery and Targeting. *Nature* **1998**, *392*, 5–10.
6. Kim, J.; De Jesus, O. Medication Routes of Administration. In *StatPearls*; StatPearls Publishing: Treasure Island (FL), 2021.
7. Alkilani, A.; McCrudden, M.T.; Donnelly, R. Transdermal Drug Delivery: Innovative Pharmaceutical Developments Based on Disruption of the Barrier Properties of the Stratum Corneum. *Pharmaceutics* **2015**, *7*, 438–470, doi:10.3390/pharmaceutics7040438.
8. Sullivan, S.P.; Murthy, N.; Prausnitz, M.R. Minimally Invasive Protein Delivery with Rapidly Dissolving Polymer Microneedles. *Adv. Mater.* **2008**, *20*, 933–938, doi:10.1002/adma.200701205.
9. Park, J.-H.; Allen, M.G.; Prausnitz, M.R. Biodegradable Polymer Microneedles: Fabrication, Mechanics and Transdermal Drug Delivery. *J. Control. Release* **2005**, *104*, 51–66, doi:10.1016/j.jconrel.2005.02.002.
10. Jeong, W.Y.; Kwon, M.; Choi, H.E.; Kim, K.S. Recent Advances in Transdermal Drug Delivery Systems: A Review. *Biomater. Res.* **2021**, *25*, 24, doi:10.1186/s40824-021-00226-6.
11. Lai-Cheong, J.E.; McGrath, J.A. Structure and Function of Skin, Hair and Nails. *Medicine* **2013**, *41*, 317–320, doi:10.1016/j.mpmed.2013.04.017.
12. Byrd, A.L.; Belkaid, Y.; Segre, J.A. The Human Skin Microbiome. *Nat. Rev. Microbiol.* **2018**, *16*, 143–155, doi:10.1038/nrmicro.2017.157.
13. Cañedo-Dorantes, L.; Cañedo-Ayala, M. Skin Acute Wound Healing: A Comprehensive Review. *Int. J. Inflam.* **2019**, *2019*, 1–15, doi:10.1155/2019/3706315.

14. Tottoli, E.M.; Dorati, R.; Genta, I.; Chiesa, E.; Pisani, S.; Conti, B. Skin Wound Healing Process and New Emerging Technologies for Skin Wound Care and Regeneration. *Pharmaceutics* **2020**, *12*, 735, doi:10.3390/pharmaceutics12080735.
15. Dijkhoff, I.M.; Drasler, B.; Karakocak, B.B.; Petri-Fink, A.; Valacchi, G.; Eeman, M.; Rothen-Rutishauser, B. Impact of Airborne Particulate Matter on Skin: A Systematic Review from Epidemiology to in Vitro Studies. *Part Fibre Toxicol* **2020**, *17*, 35, doi:10.1186/s12989-020-00366-y.
16. Yousef, H.; Alhajj, M.; Sharma, S. Anatomy, Skin (Integument), Epidermis. In *StatPearls*; StatPearls Publishing: Treasure Island (FL), 2023.
17. Mohamed, S.A.; Hargest, R. Surgical Anatomy of the Skin. *Surgery (Oxford)* **2022**, *40*, 1–7, doi:10.1016/j.mpsur.2021.11.021.
18. Marwah, H.; Garg, T.; Goyal, A.K.; Rath, G. Permeation Enhancer Strategies in Transdermal Drug Delivery. *Drug Delivery* **2016**, *23*, 564–578, doi:10.3109/10717544.2014.935532.
19. Zoabi, A.; Touitou, E.; Margulis, K. Recent Advances in Nanomaterials for Dermal and Transdermal Applications. *Colloids and Interfaces* **2021**, *5*, 18, doi:10.3390/colloids5010018.
20. Barnes, T.M.; Mijaljica, D.; Townley, J.P.; Spada, F.; Harrison, I.P. Vehicles for Drug Delivery and Cosmetic Moisturizers: Review and Comparison. *Pharmaceutics* **2021**, *13*, 2012, doi:10.3390/pharmaceutics13122012.
21. Larrañeta, E.; Lutton, R.E.M.; Woolfson, A.D.; Donnelly, R.F. Microneedle Arrays as Transdermal and Intradermal Drug Delivery Systems: Materials Science, Manufacture and Commercial Development. *Mater. Sci. Eng. R Rep.* **2016**, *104*, 1–32, doi:10.1016/j.mser.2016.03.001.
22. Watkinson, A.C.; Kearney, M.-C.; Quinn, H.L.; Courtenay, A.J.; Donnelly, R.F. Future of the Transdermal Drug Delivery Market – Have We Barely Touched the Surface? *Expert Opinion on Drug Delivery* **2016**, *13*, 523–532, doi:10.1517/17425247.2016.1130034.
23. Jijie, R.; Barras, A.; Boukherroub, R.; Szunerits, S. Nanomaterials for Transdermal Drug Delivery: Beyond the State of the Art of Liposomal Structures. *J. Mater. Chem. B* **2017**, *5*, 8653–8675, doi:10.1039/C7TB02529G.
24. Rehman, K.; Zulfakar, M.H. Recent Advances in Gel Technologies for Topical and Transdermal Drug Delivery. *Drug Dev. Ind. Pharm.* **2014**, *40*, 433–440, doi:10.3109/03639045.2013.828219.
25. Almoshari, Y. Novel Hydrogels for Topical Applications: An Updated Comprehensive Review Based on Source. *Gels* **2022**, *8*, 174, doi:10.3390/gels8030174.
26. Labie, H.; Blanzat, M. Hydrogels for Dermal and Transdermal Drug Delivery. *Biomater. Sci.* **2023**, *11*, 4073–4093, doi:10.1039/D2BM02070J.
27. Jacob, S.; Nair, A.B.; Shah, J.; Sreeharsha, N.; Gupta, S.; Shinu, P. Emerging Role of Hydrogels in Drug Delivery Systems, Tissue Engineering and Wound Management. *Pharmaceutics* **2021**, *13*, 357, doi:10.3390/pharmaceutics13030357.
28. Gudin, J.; Nalamachu, S. Utility of Lidocaine as a Topical Analgesic and Improvements in Patch Delivery Systems. *Postgraduate Medicine* **2020**, *132*, 28–36, doi:10.1080/00325481.2019.1702296.
29. Huang, D.; Sun, M.; Bu, Y.; Luo, F.; Lin, C.; Lin, Z.; Weng, Z.; Yang, F.; Wu, D. Microcapsule-Embedded Hydrogel Patches for Ultrasound Responsive and Enhanced Transdermal

Delivery of Diclofenac Sodium. *J. Mater. Chem. B* **2019**, *7*, 2330–2337, doi:10.1039/C8TB02928H.

30. Brumberg, V.; Astrelina, T.; Malivanova, T.; Samoilov, A. Modern Wound Dressings: Hydrogel Dressings. *Biomedicines* **2021**, *9*, 1235, doi:10.3390/biomedicines9091235.
31. Aliakbar Ahovan, Z.; Esmaeili, Z.; Eftekhari, B.S.; Khosravimelal, S.; Alehosseini, M.; Orive, G.; Dolatshahi-Pirouz, A.; Pal Singh Chauhan, N.; Janmey, P.A.; Hashemi, A.; et al. Antibacterial Smart Hydrogels: New Hope for Infectious Wound Management. *Materials Today Bio* **2022**, *17*, 100499, doi:10.1016/j.mtbio.2022.100499.
32. Halder, J.; Gupta, S.; Kumari, R.; Gupta, G.D.; Rai, V.K. Microneedle Array: Applications, Recent Advances, and Clinical Pertinence in Transdermal Drug Delivery. *J Pharm. Innov.* **2021**, *16*, 558–565, doi:10.1007/s12247-020-09460-2.
33. Avcil, M.; Çelik, A. Microneedles in Drug Delivery: Progress and Challenges. *Micromachines* **2021**, *12*, 1321, doi:10.3390/mi12111321.
34. Dugam, S.; Tade, R.; Dhole, R.; Nangare, S. Emerging Era of Microneedle Array for Pharmaceutical and Biomedical Applications: Recent Advances and Toxicological Perspectives. *Futur. J. Pharm. Sci.* **2021**, *7*, 19, doi:10.1186/s43094-020-00176-1.
35. Makvandi, P.; Josic, U.; Delfi, M.; Pinelli, F.; Jahed, V.; Kaya, E.; Ashrafizadeh, M.; Zarepour, A.; Rossi, F.; Zarrabi, A.; et al. Drug Delivery (Nano)Platforms for Oral and Dental Applications: Tissue Regeneration, Infection Control, and Cancer Management. *Advanced Science* **2021**, *8*, 2004014, doi:10.1002/advs.202004014.
36. He, X.; Sun, J.; Zhuang, J.; Xu, H.; Liu, Y.; Wu, D. Microneedle System for Transdermal Drug and Vaccine Delivery: Devices, Safety, and Prospects. *Dose-Response* **2019**, *17*, 155932581987858, doi:10.1177/1559325819878585.
37. Menon, I.; Bagwe, P.; Gomes, K.B.; Bajaj, L.; Gala, R.; Uddin, M.N.; D'Souza, M.J.; Zughaier, S.M. Microneedles: A New Generation Vaccine Delivery System. *Micromachines* **2021**, *12*, 435, doi:10.3390/mi12040435.
38. Mansoor, I.; Eassa, H.A.; Mohammed, K.H.A.; Abd El-Fattah, M.A.; Abdo, M.H.; Rashad, E.; Eassa, H.A.; Saleh, A.; Amin, O.M.; Nounou, M.I.; et al. Microneedle-Based Vaccine Delivery: Review of an Emerging Technology. *AAPS PharmSciTech* **2022**, *23*, 103, doi:10.1208/s12249-022-02250-8.
39. Cai, L.; Xu, J.; Yang, Z.; Tong, R.; Dong, Z.; Wang, C.; Leong, K.W. Engineered Biomaterials for Cancer Immunotherapy. *MedComm.* **2020**, *1*, 35–46, doi:10.1002/mco2.8.
40. Saha, I.; Rai, V.K. Hyaluronic Acid Based Microneedle Array: Recent Applications in Drug Delivery and Cosmetology. *Carbohydr. Polym.* **2021**, *267*, 118168, doi:10.1016/j.carbpol.2021.118168.
41. Kesharwani, P.; Bisht, A.; Alexander, A.; Dave, V.; Sharma, S. Biomedical Applications of Hydrogels in Drug Delivery System: An Update. *J. Drug Deliv. Sci. Technol.* **2021**, *66*, 102914, doi:10.1016/j.jddst.2021.102914.
42. Zhu, T.; Mao, J.; Cheng, Y.; Liu, H.; Lv, L.; Ge, M.; Li, S.; Huang, J.; Chen, Z.; Li, H.; et al. Recent Progress of Polysaccharide-Based Hydrogel Interfaces for Wound Healing and Tissue Engineering. *Adv. Materials Inter.* **2019**, *6*, 1900761, doi:10.1002/admi.201900761.
43. Bashir, S.; Hina, M.; Iqbal, J.; Rajpar, A.H.; Mujtaba, M.A.; Alghamdi, N.A.; Wageh, S.; Ramesh, K.; Ramesh, S. Fundamental Concepts of Hydrogels: Synthesis, Properties, and Their Applications. *Polymers* **2020**, *12*, 2702, doi:10.3390/polym12112702.

44. Klein, M.; Poverenov, E. Natural Biopolymer-based Hydrogels for Use in Food and Agriculture. *J. Sci. Food Agric.* **2020**, *100*, 2337–2347, doi:10.1002/jsfa.10274.
45. Mitura, S.; Sionkowska, A.; Jaiswal, A. Biopolymers for Hydrogels in Cosmetics: Review. *J. Mater. Sci.: Mater. Med.* **2020**, *31*, 50, doi:10.1007/s10856-020-06390-w.
46. Chai, Q.; Jiao, Y.; Yu, X. Hydrogels for Biomedical Applications: Their Characteristics and the Mechanisms behind Them. *Gels* **2017**, *3*, 6, doi:10.3390/gels3010006.
47. Lee, Y.; Song, W.J.; Sun, J.-Y. Hydrogel Soft Robotics. *Mater. Today Phys.* **2020**, *15*, 100258, doi:10.1016/j.mtphys.2020.100258.
48. Chang, H.; Zhao, H.; Qu, F.; Yan, Z.; Liu, N.; Lu, M.; Liang, Y.; Lai, B.; Liang, H. State-of-the-Art Insights on Applications of Hydrogel Membranes in Water and Wastewater Treatment. *Sep. Purif. Technol.* **2023**, *308*, 122948, doi:10.1016/j.seppur.2022.122948.
49. Radulescu, D.-M.; Neacsu, I.A.; Grumezescu, A.-M.; Andronescu, E. New Insights of Scaffolds Based on Hydrogels in Tissue Engineering. *Polymers* **2022**, *14*, 799, doi:10.3390/polym14040799.
50. Ishihara, K.; Fukazawa, K.; Sharma, V.; Liang, S.; Shows, A.; Dunbar, D.C.; Zheng, Y.; Ge, J.; Zhang, S.; Hong, Y.; et al. Antifouling Silicone Hydrogel Contact Lenses with a Bioinspired 2-Methacryloyloxyethyl Phosphorylcholine Polymer Surface. *ACS Omega* **2021**, *6*, 7058–7067, doi:10.1021/acsomega.0c06327.
51. Zhao, W.; Lin, Z.; Wang, X.; Wang, Z.; Sun, Z. Mechanically Interlocked Hydrogel–Elastomer Strain Sensor with Robust Interface and Enhanced Water—Retention Capacity. *Gels* **2022**, *8*, 625, doi:10.3390/gels8100625.
52. Bustamante-Torres, M.; Romero-Fierro, D.; Arcentales-Vera, B.; Palomino, K.; Magaña, H.; Bucio, E. Hydrogels Classification According to the Physical or Chemical Interactions and as Stimuli-Sensitive Materials. *Gels* **2021**, *7*, 182, doi:10.3390/gels7040182.
53. Barbucci, R. *Hydrogels: Biological Properties and Applications*; Springer Milan: Milano, 2009; ISBN 978-88-470-1103-8.
54. Bhatia, J.K.; Kaith, B.S.; Kalia, S. Polysaccharide Hydrogels: Synthesis, Characterization, and Applications. In *Polysaccharide Based Graft Copolymers*; Kalia, S., Sabaa, M.W., Eds.; Springer Berlin Heidelberg: Berlin, Heidelberg, 2013; pp. 271–290 ISBN 978-3-642-36565-2.
55. Siqueira, E.C.D.; França, J.A.A.D.; Souza, R.F.M.D.; Leoterio, D.M.D.S.; Cordeiro, J.N.; Doboszewski, B. Mecanisms of the Chemical Crosslinking to Obtain the Hydrogels: Synthesis, Conditions of Crosslinking and Biopharmaceutical Applications. *RSD* **2023**, *12*, e18312943072, doi:10.33448/rsd-v12i8.43072.
56. Thang, N.H.; Chien, T.B.; Cuong, D.X. Polymer-Based Hydrogels Applied in Drug Delivery: An Overview. *Gels* **2023**, *9*, 523, doi:10.3390/gels9070523.
57. Ahmad, Z.; Salman, S.; Khan, S.A.; Amin, A.; Rahman, Z.U.; Al-Ghamdi, Y.O.; Akhtar, K.; Bakhsh, E.M.; Khan, S.B. Versatility of Hydrogels: From Synthetic Strategies, Classification, and Properties to Biomedical Applications. *Gels* **2022**, *8*, 167, doi:10.3390/gels8030167.
58. Oliveira, J.T.; Reis, R.L. Hydrogels from Polysaccharide-Based Materials: Fundamentals and Applications in Regenerative Medicine. In *Natural-Based Polymers for Biomedical Applications*; Elsevier, 2008; pp. 485–514 ISBN 978-1-84569-264-3.
59. Ahmed, E.M. Hydrogel: Preparation, Characterization, and Applications: A Review. *J. Adv. Res.* **2015**, *6*, 105–121, doi:10.1016/j.jare.2013.07.006.

60. Usta, A.; Asmatulu, R. Synthesis and Analysis of Electrically Sensitive Hydrogels for Advanced Drug Delivery Systems. In Proceedings of the Volume 3: Biomedical and Biotechnology Engineering; American Society of Mechanical Engineers: Houston, Texas, USA, November 13 2015; p. V003T03A001.
61. Soppimath, K.S.; Aminabhavi, T.M.; Dave, A.M.; Kumbar, S.G.; Rudzinski, W.E. Stimulus-Responsive "Smart" Hydrogels as Novel Drug Delivery Systems. *Drug Dev. Ind. Pharm.* **2002**, *28*, 957–974, doi:10.1081/DDC-120006428.
62. Deen, G.; Loh, X. Stimuli-Responsive Cationic Hydrogels in Drug Delivery Applications. *Gels* **2018**, *4*, 13, doi:10.3390/gels4010013.
63. Rudzinski, W.E.; Dave, A.M.; Vaishnav, U.H.; Kumbar, S.G.; Kulkarni, A.R.; Aminabhavi, T.M. Hydrogels as Controlled Release Devices in Agriculture. *Des. Monomers Polym.***2002**, *5*, 39–65, doi:10.1163/156855502760151580.
64. El Sayed, M.M. Production of Polymer Hydrogel Composites and Their Applications. *J. Polym. Environ.* **2023**, *31*, 2855–2879, doi:10.1007/s10924-023-02796-z.
65. Ho, T.-C.; Chang, C.-C.; Chan, H.-P.; Chung, T.-W.; Shu, C.-W.; Chuang, K.-P.; Duh, T.-H.; Yang, M.-H.; Tyan, Y.-C. Hydrogels: Properties and Applications in Biomedicine. *Molecules* **2022**, *27*, 2902, doi:10.3390/molecules27092902.
66. Madduma-Bandarage, U.S.K.; Madihally, S.V. Synthetic Hydrogels: Synthesis, Novel Trends, and Applications. *J. Applied Polymer Sci.* **2021**, *138*, 50376, doi:10.1002/app.50376.
67. Mohammed, A.S.A.; Naveed, M.; Jost, N. Polysaccharides; Classification, Chemical Properties, and Future Perspective Applications in Fields of Pharmacology and Biological Medicine (A Review of Current Applications and Upcoming Potentialities). *J. Polym. Environ.* **2021**, *29*, 2359–2371, doi:10.1007/s10924-021-02052-2.
68. Malaka, R. Bacterial Exopolysaccharides Production and Their Roles for Human Life. *IOP Conf. Ser.: Earth Environ. Sci.* **2021**, *788*, 012109, doi:10.1088/1755-1315/788/1/012109.
69. Zhou, Y.; Petrova, S.P.; Edgar, K.J. Chemical Synthesis of Polysaccharide–Protein and Polysaccharide–Peptide Conjugates: A Review. *Carbohydr. Polym.* **2021**, *274*, 118662, doi:10.1016/j.carbpol.2021.118662.
70. Shariatinia, Z.; Barzegari, A. Polysaccharide Hydrogel Films/Membranes for Transdermal Delivery of Therapeutics. In *Polysaccharide Carriers for Drug Delivery*; Elsevier, 2019; pp. 639–684 ISBN 978-0-08-102553-6.
71. Dedhia, N.; Marathe, S.J.; Singhal, R.S. Food Polysaccharides: A Review on Emerging Microbial Sources, Bioactivities, Nanoformulations and Safety Considerations. *Carbohydr. Polym.* **2022**, *287*, 119355, doi:10.1016/j.carbpol.2022.119355.
72. Massironi, A.; Morelli, A.; Puppi, D.; Chiellini, F. Renewable Polysaccharides Micro/Nanostructures for Food and Cosmetic Applications. *Molecules* **2020**, *25*, 4886, doi:10.3390/molecules25214886.
73. Khan, R.; Shah, M.D.; Shah, L.; Lee, P.-C.; Khan, I. Bacterial Polysaccharides—A Big Source for Prebiotics and Therapeutics. *Front. Nutr.* **2022**, *9*, 1031935, doi:10.3389/fnut.2022.1031935.
74. Antunes, S.; Freitas, F.; Sevrin, C.; Grandfils, C.; Reis, M.A.M. Production of FucoPol by *Enterobacter* A47 Using Waste Tomato Paste By-Product as Sole Carbon Source. *Bioresour. Technol.* **2017**, *227*, 66–73, doi:10.1016/j.biortech.2016.12.018.

75. Roca, C.; Chagas, B.; Farinha, I.; Freitas, F.; Mafra, L.; Aguiar, F.; Oliveira, R.; Reis, M.A.M. Production of Yeast Chitin–Glucan Complex from Biodiesel Industry Byproduct. *Process Biochemistry* **2012**, *47*, 1670–1675, doi:10.1016/j.procbio.2012.04.004.
76. Matos, M.; Cruz, R.A.P.; Cardoso, P.; Silva, F.; Freitas, E.B.; Carvalho, G.; Reis, M.A.M. Combined Strategies to Boost Polyhydroxyalkanoate Production from Fruit Waste in a Three-Stage Pilot Plant. *ACS Sustainable Chem. Eng.* **2021**, *9*, 8270–8279, doi:10.1021/acssuschemeng.1c02432.
77. Schmid, J.; Sieber, V.; Rehm, B. Bacterial Exopolysaccharides: Biosynthesis Pathways and Engineering Strategies. *Front. Microbiol.* **2015**, *6*, doi:10.3389/fmicb.2015.00496.
78. Cress, B.F.; Englaender, J.A.; He, W.; Kasper, D.; Linhardt, R.J.; Koffas, M.A.G. Masquerading Microbial Pathogens: Capsular Polysaccharides Mimic Host-Tissue Molecules. *FEMS Microbiol. Rev.* **2014**, *38*, 660–697, doi:10.1111/1574-6976.12056.
79. Freitas, F.; Torres, C.A.V.; Reis, M.A.M. Engineering Aspects of Microbial Exopolysaccharide Production. *Bioresour. Technol.* **2017**, *245*, 1674–1683, doi:10.1016/j.biortech.2017.05.092.
80. Yang, Y.; Liang, Y.; Chen, J.; Duan, X.; Guo, B. Mussel-Inspired Adhesive Antioxidant Antibacterial Hemostatic Composite Hydrogel Wound Dressing via Photo-Polymerization for Infected Skin Wound Healing. *Bioact. Mater.* **2022**, *8*, 341–354, doi:10.1016/j.bioactmat.2021.06.014.
81. Yildiz, H.; Karatas, N. Microbial Exopolysaccharides: Resources and Bioactive Properties. *Process Biochem.* **2018**, *72*, 41–46, doi:10.1016/j.procbio.2018.06.009.
82. Yu, Y.; Shen, M.; Song, Q.; Xie, J. Biological Activities and Pharmaceutical Applications of Polysaccharide from Natural Resources: A Review. *Carbohydr. Polym.* **2018**, *183*, 91–101, doi:10.1016/j.carbpol.2017.12.009.
83. Shariatinia, Z.; Jalali, A.M. Chitosan-Based Hydrogels: Preparation, Properties and Applications. *Int. J. Biol. Macromol.* **2018**, *115*, 194–220, doi:10.1016/j.ijbiomac.2018.04.034.
84. Abasalizadeh, F.; Moghaddam, S.V.; Alizadeh, E.; Akbari, E.; Kashani, E.; Fazljou, S.M.B.; Torbati, M.; Akbarzadeh, A. Alginate-Based Hydrogels as Drug Delivery Vehicles in Cancer Treatment and Their Applications in Wound Dressing and 3D Bioprinting. *J. Biol. Eng.* **2020**, *14*, 8, doi:10.1186/s13036-020-0227-7.
85. Tomić, S.Lj.; Babić Radić, M.M.; Vuković, J.S.; Filipović, V.V.; Nikodinovic-Runic, J.; Vukomanović, M. Alginate-Based Hydrogels and Scaffolds for Biomedical Applications. *Mar. Drugs* **2023**, *21*, 177, doi:10.3390/md21030177.
86. Auriemma, G.; Russo, P.; Del Gaudio, P.; García-González, C.A.; Landín, M.; Aquino, R.P. Technologies and Formulation Design of Polysaccharide-Based Hydrogels for Drug Delivery. *Molecules* **2020**, *25*, 3156, doi:10.3390/molecules25143156.
87. Pacheco-Quito, E.-M.; Ruiz-Caro, R.; Veiga, M.-D. Carrageenan: Drug Delivery Systems and Other Biomedical Applications. *Mar. Drugs* **2020**, *18*, 583, doi:10.3390/md18110583.
88. Dong, Y.; Wei, Z.; Xue, C. Recent Advances in Carrageenan-Based Delivery Systems for Bioactive Ingredients: A Review. *Trends Food Sci. Technol.* **2021**, *112*, 348–361, doi:10.1016/j.tifs.2021.04.012.
89. Lahiri, D.; Nag, M.; Dutta, B.; Dey, A.; Sarkar, T.; Pati, S.; Edinur, H.A.; Abdul Kari, Z.; Mohd Noor, N.H.; Ray, R.R. Bacterial Cellulose: Production, Characterization, and Application as Antimicrobial Agent. *IJMS* **2021**, *22*, 12984, doi:10.3390/ijms222312984.

90. Swingler, S.; Gupta, A.; Gibson, H.; Kowalczuk, M.; Heaselgrave, W.; Radecka, I. Recent Advances and Applications of Bacterial Cellulose in Biomedicine. *Polymers* **2021**, *13*, 412, doi:10.3390/polym13030412.
91. Aranaz, I.; Alcántara, A.R.; Civera, M.C.; Arias, C.; Elorza, B.; Heras Caballero, A.; Acosta, N. Chitosan: An Overview of Its Properties and Applications. *Polymers* **2021**, *13*, 3256, doi:10.3390/polym13193256.
92. Azuma, K.; Osaki, T.; Minami, S.; Okamoto, Y. Anticancer and Anti-Inflammatory Properties of Chitin and Chitosan Oligosaccharides. *JFB* **2015**, *6*, 33–49, doi:10.3390/jfb6010033.
93. Avelelas, F.; Horta, A.; Pinto, L.F.V.; Cotrim Marques, S.; Marques Nunes, P.; Pedrosa, R.; Leandro, S.M. Antifungal and Antioxidant Properties of Chitosan Polymers Obtained from Nontraditional Polybius Henslowii Sources. *Mar. Drugs* **2019**, *17*, 239, doi:10.3390/md17040239.
94. Díaz-Montes, E. Dextran: Sources, Structures, and Properties. *Polysaccharides* **2021**, *2*, 554–565, doi:10.3390/polysaccharides2030033.
95. Luanda, A.; Badalamoole, V. Past, Present and Future of Biomedical Applications of Dextran-Based Hydrogels: A Review. *Int. J. Biol. Macromol.* **2023**, *228*, 794–807, doi:10.1016/j.ijbiomac.2022.12.129.
96. Della Sala, F.; Longobardo, G.; Fabozzi, A.; Di Gennaro, M.; Borzacchiello, A. Hyaluronic Acid-Based Wound Dressing with Antimicrobial Properties for Wound Healing Application. *Applied Sciences* **2022**, *12*, 3091, doi:10.3390/app12063091.
97. Gupta, R.C.; Lall, R.; Srivastava, A.; Sinha, A. Hyaluronic Acid: Molecular Mechanisms and Therapeutic Trajectory. *Front. Vet. Sci.* **2019**, *6*, 192, doi:10.3389/fvets.2019.00192.
98. Hwang, H.S.; Lee, C.-S. Recent Progress in Hyaluronic-Acid-Based Hydrogels for Bone Tissue Engineering. *Gels* **2023**, *9*, 588, doi:10.3390/gels9070588.
99. Agrawal, S.; Budhwani, D.; Gurjar, P.; Telange, D.; Lambole, V. Pullulan Based Derivatives: Synthesis, Enhanced Physicochemical Properties, and Applications. *Drug Delivery* **2022**, *29*, 3328–3339, doi:10.1080/10717544.2022.2144544.
100. Raychaudhuri, R.; Naik, S.; Shreya, A.B.; Kandpal, N.; Pandey, A.; Kalthur, G.; Mutalik, S. Pullulan Based Stimuli Responsive and Sub Cellular Targeted Nanoplatforms for Biomedical Application: Synthesis, Nanoformulations and Toxicological Perspective. *Int. J. Biol. Macromol.* **2020**, *161*, 1189–1205, doi:10.1016/j.ijbiomac.2020.05.262.
101. Bhat, I.M.; Wani, S.M.; Mir, S.A.; Masoodi, F.A. Advances in Xanthan Gum Production, Modifications and Its Applications. *Biocatal. Agric. Biotechnol.* **2022**, *42*, 102328, doi:10.1016/j.bcab.2022.102328.
102. Kumar, A.; Rao, K.M.; Han, S.S. Application of Xanthan Gum as Polysaccharide in Tissue Engineering: A Review. *Carbohydr. Polym.* **2018**, *180*, 128–144, doi:10.1016/j.carbpol.2017.10.009.
103. Abka-khajouei, R.; Tounsi, L.; Shahabi, N.; Patel, A.K.; Abdelkafi, S.; Michaud, P. Structures, Properties and Applications of Alginates. *Mar. Drugs* **2022**, *20*, 364, doi:10.3390/md20060364.
104. Cao, L.; Lu, W.; Mata, A.; Nishinari, K.; Fang, Y. Egg-Box Model-Based Gelation of Alginate and Pectin: A Review. *Carbohydr. Polym.* **2020**, *242*, 116389, doi:10.1016/j.carbpol.2020.116389.
105. Fleten, K.G.; Hyldbakk, A.; Einen, C.; Benjakul, S.; Strand, B.L.; Davies, C.D.L.; Mørch, Ý.; Flatmark, K. Alginate Microsphere Encapsulation of Drug-Loaded Nanoparticles: A Novel

Strategy for Intraperitoneal Drug Delivery. *Mar. Drugs* **2022**, *20*, 744, doi:10.3390/md20120744.

106. Dodero, A.; Alberti, S.; Gaggero, G.; Ferretti, M.; Botter, R.; Vicini, S.; Castellano, M. An Up-to-Date Review on Alginate Nanoparticles and Nanofibers for Biomedical and Pharmaceutical Applications. *Adv. Materials Inter.* **2021**, *8*, 2100809, doi:10.1002/admi.202100809.
107. Huang, C.-H.; Chuang, T.-J.; Ke, C.-J.; Yao, C.-H. Doxorubicin–Gelatin/Fe3O4–Alginate Dual-Layer Magnetic Nanoparticles as Targeted Anticancer Drug Delivery Vehicles. *Polymers* **2020**, *12*, 1747, doi:10.3390/polym12081747.
108. Aluani, D.; Tzankova, V.; Kondeva-Burdina, M.; Yordanov, Y.; Nikolova, E.; Odzhakov, F.; Apostolov, A.; Markova, T.; Yoncheva, K. Evaluation of Biocompatibility and Antioxidant Efficiency of Chitosan-Alginate Nanoparticles Loaded with Quercetin. *Int. J. Biol. Macromol.* **2017**, *103*, 771–782, doi:10.1016/j.ijbiomac.2017.05.062.
109. Spadari, C.D.C.; De Bastiani, F.W.M.D.S.; Lopes, L.B.; Ishida, K. Alginate Nanoparticles as Non-Toxic Delivery System for Miltefosine in the Treatment of Candidiasis and Cryptococcosis. *Int. J. Nanosci.* **2019**, *Volume 14*, 5187–5199, doi:10.2147/IJN.S205350.
110. Varaprasad, K.; Jayaramudu, T.; Kanikireddy, V.; Toro, C.; Sadiku, E.R. Alginate-Based Composite Materials for Wound Dressing Application:A Mini Review. *Carbohydr. Polym.* **2020**, *236*, 116025, doi:10.1016/j.carbpol.2020.116025.
111. Thirupathi, K.; Raorane, C.J.; Ramkumar, V.; Ulagesan, S.; Santhamoorthy, M.; Raj, V.; Krishnakumar, G.S.; Phan, T.T.V.; Kim, S.-C. Update on Chitosan-Based Hydrogels: Preparation, Characterization, and Its Antimicrobial and Antibiofilm Applications. *Gels* **2022**, *9*, 35, doi:10.3390/gels9010035.
112. Tian, B.; Liu, J. Smart Stimuli-Responsive Chitosan Hydrogel for Drug Delivery: A Review. *Int. J. Biol. Macromol.***2023**, *235*, 123902, doi:10.1016/j.ijbiomac.2023.123902.
113. G.Tahrir, F.; Ganji, F.; Ahooyi, T. Injectable Thermosensitive Chitosan/Glycerophosphate-Based Hydrogels for Tissue Engineering and Drug Delivery Applications: A Review. *Defect Diffus. Forum.* **2015**, *9*, 107–120, doi:10.2174/1872211308666141028145651.
114. Rizwan, M.; Yahya, R.; Hassan, A.; Yar, M.; Azzahari, A.; Selvanathan, V.; Sonsudin, F.; Abouloula, C. pH Sensitive Hydrogels in Drug Delivery: Brief History, Properties, Swelling, and Release Mechanism, Material Selection and Applications. *Polymers* **2017**, *9*, 137, doi:10.3390/polym9040137.
115. Rohindra, D.R.; Nand, A.V.; Khurma, J.R. Swelling Properties of Chitosan Hydrogels. *S. Pac. J. Nat. App. Sci.* **2004**, *22*, 32, doi:10.1071/SP04005.
116. Abd El-Hady, M.M.; Saeed, S.E.-S. Antibacterial Properties and pH Sensitive Swelling of Insitu Formed Silver-Curcumin Nanocomposite Based Chitosan Hydrogel. *Polymers* **2020**, *12*, 2451, doi:10.3390/polym12112451.
117. Jing, H.; Huang, X.; Du, X.; Mo, L.; Ma, C.; Wang, H. Facile Synthesis of pH-Responsive Sodium Alginate/Carboxymethyl Chitosan Hydrogel Beads Promoted by Hydrogen Bond. *Carbohydr. Polym.* **2022**, *278*, 118993, doi:10.1016/j.carbpol.2021.118993.
118. Chowdhury, F.; Ahmed, S.; Rahman, M.; Ahmed, Md.A.; Hossain, Md.D.; Reza, H.M.; Park, S.Y.; Sharker, S.Md. Chronic Wound-Dressing Chitosan-Polyphenolic Patch for pH Responsive Local Antibacterial Activity. *Mater. Today Commun.* **2022**, *31*, 103310, doi:10.1016/j.mtcomm.2022.103310.

119. Taokaew, S.; Kaewkong, W.; Kriangkrai, W. Recent Development of Functional Chitosan-Based Hydrogels for Pharmaceutical and Biomedical Applications. *Gels* **2023**, *9*, 277, doi:10.3390/gels9040277.
120. Fan, R.; Cheng, Y.; Wang, R.; Zhang, T.; Zhang, H.; Li, J.; Song, S.; Zheng, A. Thermosensitive Hydrogels and Advances in Their Application in Disease Therapy. *Polymers* **2022**, *14*, 2379, doi:10.3390/polym14122379.
121. Ahsan, A.; Farooq, M.A.; Parveen, A. Thermosensitive Chitosan-Based Injectable Hydrogel as an Efficient Anticancer Drug Carrier. *ACS Omega* **2020**, *5*, 20450–20460, doi:10.1021/acsomega.0c02548.
122. Trombino, S.; Servidio, C.; Curcio, F.; Cassano, R. Strategies for Hyaluronic Acid-Based Hydrogel Design in Drug Delivery. *Pharmaceutics* **2019**, *11*, 407, doi:10.3390/pharmaceutics11080407.
123. Pérez, L.A.; Hernández, R.; Alonso, J.M.; Pérez-González, R.; Sáez-Martínez, V. Hyaluronic Acid Hydrogels Crosslinked in Physiological Conditions: Synthesis and Biomedical Applications. *Biomedicines* **2021**, *9*, 1113, doi:10.3390/biomedicines9091113.
124. Kwon, S.S.; Kong, B.J.; Park, S.N. Physicochemical Properties of pH-Sensitive Hydrogels Based on Hydroxyethyl Cellulose–Hyaluronic Acid and for Applications as Transdermal Delivery Systems for Skin Lesions. *Eur. J. Pharm. Biopharm.* **2015**, *92*, 146–154, doi:10.1016/j.ejpb.2015.02.025.
125. Jung, Y.; Park, W.; Park, H.; Lee, D.-K.; Na, K. Thermo-Sensitive Injectable Hydrogel Based on the Physical Mixing of Hyaluronic Acid and Pluronic F-127 for Sustained NSAID Delivery. *Carbohydr. Polym.* **2017**, *156*, 403–408, doi:10.1016/j.carbpol.2016.08.068.
126. Park, S.H.; Seo, J.Y.; Park, J.Y.; Ji, Y.B.; Kim, K.; Choi, H.S.; Choi, S.; Kim, J.H.; Min, B.H.; Kim, M.S. An Injectable, Click-Crosslinked, Cytomodulin-Modified Hyaluronic Acid Hydrogel for Cartilage Tissue Engineering. *NPG Asia Mater* **2019**, *11*, 30, doi:10.1038/s41427-019-0130-1.
127. Safarzadeh Kozani, P.; Safarzadeh Kozani, P.; Hamidi, M.; Valentine Okoro, O.; Eskandani, M.; Jaymand, M. Polysaccharide-Based Hydrogels: Properties, Advantages, Challenges, and Optimization Methods for Applications in Regenerative Medicine. *Int. J. Polym. Mater. Polym. Biomater.* **2022**, *71*, 1319–1333, doi:10.1080/00914037.2021.1962876.
128. Meĭchik, N.R.; Vorob'ev, D.V. Chitin-glucan complex in cell walls of the Peltigera aphthosa lichen. *Prikl Biokhim Mikrobiol* **2012**, *48*, 340–345.
129. Gautier, S.; Xhauflaire-Uhoda, E.; Gonry, P.; Piérard, G.E. Chitin-Glucan, a Natural Cell Scaffold for Skin Moisturization and Rejuvenation. *Int. J. Cosmet. Sci.* **2008**, *30*, 459–469, doi:10.1111/j.1468-2494.2008.00470.x.
130. Wu, T.; Zivanovic, S.; Draughon, F.A.; Conway, W.S.; Sams, C.E. Physicochemical Properties and Bioactivity of Fungal Chitin and Chitosan. *J. Agric. Food Chem.* **2005**, *53*, 3888–3894, doi:10.1021/jf048202s.
131. Berecochea-Lopez, A.; Decordé, K.; Ventura, E.; Godard, M.; Bornet, A.; Teissèdre, P.-L.; Cristol, J.-P.; Rouanet, J.-M. Fungal Chitin−Glucan from *Aspergillus Niger* Efficiently Reduces Aortic Fatty Streak Accumulation in the High-Fat Fed Hamster, an Animal Model of Nutritionally Induced Atherosclerosis. *J. Agric. Food Chem.* **2009**, *57*, 1093–1098, doi:10.1021/jf803063v.
132. Feofilova, E.P. The Fungal Cell Wall: Modern Concepts of Its Composition and Biological Function. *Microbiology* **2010**, *79*, 711–720, doi:10.1134/S0026261710060019.

133. Kulev, D.; Negrutsa, I. Chitin-Glucan Complex - Food Additive with Sorbent Properties. *J. Hyg. Eng. Des.* **2015**, 11, 53–56.
134. Mogoşanu, G.D.; Grumezescu, A.M. Natural and Synthetic Polymers for Wounds and Burns Dressing. *Int. J. Pharm.* **2014**, *463*, 127–136, doi:10.1016/j.ijpharm.2013.12.015.
135. Neyrinck, A.M.; Possemiers, S.; Verstraete, W.; De Backer, F.; Cani, P.D.; Delzenne, N.M. Dietary Modulation of Clostridial Cluster XIVa Gut Bacteria (*Roseburia* Spp.) by Chitin–Glucan Fiber Improves Host Metabolic Alterations Induced by High-Fat Diet in Mice. *J. Nutr. Biochem.* **2012**, *23*, 51–59, doi:10.1016/j.jnutbio.2010.10.008.
136. Mislovičová, D.; Masárová, J.; Bendžálová, K.; Šoltés, L.; Machová, E. Sonication of Chitin–Glucan, Preparation of Water-Soluble Fractions and Characterization by HPLC. *Ultrasonics Sonochemistry* **2000**, *7*, 63–68, doi:10.1016/S1350-4177(99)00030-9.
137. Cabib, E.; Blanco, N.; Arroyo, J. Presence of a Large β(1-3)Glucan Linked to Chitin at the *Saccharomyces Cerevisiae* Mother-Bud Neck Suggests Involvement in Localized Growth Control. *Eukaryot. Cell* **2012**, *11*, 388–400, doi:10.1128/EC.05328-11.
138. Reis, M.A.M.; Oliveira, R.; Freitas, F.; Chagas, B.; Cruz, A.L.; Cunha, A.E.; Clemente, J.J. Process for the Co-Production of Chitin, Its Derivates and Polymers Containing Glucose, Mannose and/or Galactose by the Fermentation of the Yeast *Pichia Pastoris*. International Patent WO2010/013174, February, 2010.
139. Tarabukina, E.B.; Kalinina, N.A.; Adamov, A.V.; Petrova, V.A.; Nud'ga, L.A.; Klenin, S.I. Molecular Characteristics and Supermolecular Organization of Chitin-Glucan Complexes in Solutions. *Polym. Sci. Ser. A* **2005**, *47*, 462–468.
140. Sietsma, J.H.; Wessels, J.G.H. Solubility of (1-3)-β-D/(1-6)-β-D-Glucan in Fungal Walls: Importance of Presumed Linkage between Glucan and Chitin. *Microbiology* **1981**, *125*, 209–212, doi:10.1099/00221287-125-1-209.
141. Gamayurova, V.S.; Kotlyar, M.N.; Shabrukova, N.V.; Khalitov, F.G. Synthesis of Soluble Derivatives of Chitin-Glucan Complex. *Part I Chem.Comut. Simul. Commun.* **1998**, 73–76.
142. Skorik, Y.A.; Pestov, A.V.; Yatluk, Y.G. Evaluation of Various Chitin-Glucan Derivatives from Aspergillus Niger as Transition Metal Adsorbents. *Bioresour. Technol.y* **2010**, *101*, 1769–1775, doi:10.1016/j.biortech.2009.10.033.
143. Ferreira, I.C.; Araújo, D.; Voisin, P.; Alves, V.D.; Rosatella, A.A.; Afonso, C.A.M.; Freitas, F.; Neves, L.A. Chitin-Glucan Complex – Based Biopolymeric Structures Using Biocompatible Ionic Liquids. *Carbohydr. Polym.* **2020**, *247*, 116679, doi:10.1016/j.carbpol.2020.116679.
144. Hu, X.; Du, Y.; Tang, Y.; Wang, Q.; Feng, T.; Yang, J.; Kennedy, J.F. Solubility and Property of Chitin in NaOH/Urea Aqueous Solution. *Carbohydr. Polym.* **2007**, *70*, 451–458, doi:10.1016/j.carbpol.2007.05.002.
145. Gong, P.; Wang, J.; Liu, B.; Ru, G.; Feng, J. Dissolution of Chitin in Aqueous KOH. *Cellulose* **2016**, *23*, 1705–1711, doi:10.1007/s10570-016-0932-z.
146. Chen, X.; Xu, X.; Zhang, L.; Kennedy, J.F. Flexible Chain Conformation of (1→3)-β-d-Glucan from Poria Cocos Sclerotium in NaOH/Urea Aqueous Solution. *Carbohydr. Polym.* **2009**, *75*, 586–591, doi:10.1016/j.carbpol.2008.08.027.
147. Yoshida, T.; Honda, Y.; Tujimoto, T.; Uyama, H.; Azuma, J. Freeze-Thaw Treatment in 2% w/w NaOH-6 M Urea Enhanced Extraction of ʙ-(1,3;1,4)-Glucan from Corn Pericarp. *Macromol. Symp.* **2015**, *353*, 205–211, doi:10.1002/masy.201550328.

148. Chen, X.; Chen, J.; You, T.; Wang, K.; Xu, F. Effects of Polymorphs on Dissolution of Cellulose in NaOH/Urea Aqueous Solution. *Carbohydr. Polym.* **2015**, *125*, 85–91, doi:10.1016/j.carbpol.2015.02.054.
149. Mense, A.L.; Shi, Y.-C. Dissolution of Wheat Bran by NaOH/Urea Solutions and Structure of Soluble Materials. *ACS Sustainable Chem. Eng.* **2018**, *6*, 4264–4271, doi:10.1021/acssuschemeng.7b04707.
150. Araújo, D.; Alves, V.D.; Lima, S.A.C.; Reis, S.; Freitas, F.; Reis, M.A.M. Novel Hydrogels Based on Yeast Chitin-Glucan Complex: Characterization and Safety Assessment. *Int. J. Biol. Macromol.***2020**, *156*, 1104–1111, doi:10.1016/j.ijbiomac.2019.11.141.
151. Roy, J.C.; Salaün, F.; Giraud, S.; Ferri, A.; Chen, G.; Guan, J. Solubility of Chitin: Solvents, Solution Behaviors and Their Related Mechanisms. In *Solubility of Polysaccharides*; Xu, Z., Ed.; InTech, 2017 ISBN 978-953-51-3649-1.
152. Zhou, J.; Zhang, L. Solubility of Cellulose in NaOH/Urea Aqueous Solution. *Polym J* **2000**, *32*, 866–870, doi:10.1295/polymj.32.866.
153. Cai, J.; Zhang, L.; Chang, C.; Cheng, G.; Chen, X.; Chu, B. Hydrogen-Bond-Induced Inclusion Complex in Aqueous Cellulose/LiOH/Urea Solution at Low Temperature. *ChemPhysChem* **2007**, *8*, 1572–1579, doi:10.1002/cphc.200700229.
154. Farinha, I.; Duarte, P.; Pimentel, A.; Plotnikova, E.; Chagas, B.; Mafra, L.; Grandfils, C.; Freitas, F.; Fortunato, E.; Reis, M.A.M. Chitin–Glucan Complex Production by Komagataella Pastoris : Downstream Optimization and Product Characterization. *Carbohydr. Polym.* **2015**, *130*, 455–464, doi:10.1016/j.carbpol.2015.05.034.
155. Araújo, D.; Freitas, F.; Sevrin, C.; Grandfils, C.; Reis, M.A.M. Co-Production of Chitin-Glucan Complex and Xylitol by Komagataella Pastoris Using Glucose and Xylose Mixtures as Carbon Source. *Carbohydr. Polym.* **2017**, *166*, 24–30, doi:10.1016/j.carbpol.2017.02.088.
156. Wang, Y.; Li, Y.; Liu, S.; Li, B. Fabrication of Chitin Microspheres and Their Multipurpose Application as Catalyst Support and Adsorbent. *Carbohydr. Polym.* **2015**, *120*, 53–59, doi:10.1016/j.carbpol.2014.12.005.
157. Shang, Y.; Ding, F.; Xiao, L.; Deng, H.; Du, Y.; Shi, X. Chitin-Based Fast Responsive pH Sensitive Microspheres for Controlled Drug Release. *Carbohydr. Polym.* **2014**, *102*, 413–418, doi:10.1016/j.carbpol.2013.11.039.
158. Alves, L.; Medronho, B.; Filipe, A.; E. Antunes, F.; Lindman, B.; Topgaard, D.; Davidovich, I.; Talmon, Y. New Insights on the Role of Urea on the Dissolution and Thermally-Induced Gelation of Cellulose in Aqueous Alkali. *Gels* **2018**, *4*, 87, doi:10.3390/gels4040087.
159. Barrera, G.E.; Beltran, L.M.; Diosa, J.A. Chitin-Glucan Complexes and Method for the Preparation Thereof from Chitin-Rich Biomaterials 2016.
160. Xiong, B.; Zhao, P.; Hu, K.; Zhang, L.; Cheng, G. Dissolution of Cellulose in Aqueous NaOH/Urea Solution: Role of Urea. *Cellulose* **2014**, *21*, 1183–1192, doi:10.1007/s10570-014-0221-7.
161. Terbojevich, M.; Carraro, C.; Cosani, A.; Marsano, E. Solution Studies of the Chitin-Lithium Chloride-N,N-Di-Methylacetamide System. *Carbohydrate Research* **1988**, *180*, 73–86, doi:10.1016/0008-6215(88)80065-X.
162. Sharma, M.; Mukesh, C.; Mondal, D.; Prasad, K. Dissolution of α-Chitin in Deep Eutectic Solvents. *RSC Adv.* **2013**, *3*, 18149, doi:10.1039/c3ra43404d.

163. Jaworska, M.M.; Górak, A.; Zdunek, J. Modification of Chitin Particles with Ionic Liquids Containing Ethyl Substituent in a Cation. *Advances in Materials Science and Engineering* **2017**, *2017*, 1–9, doi:10.1155/2017/3961318.
164. Huber, T.; Starling, K.; Cen, W. (Samantha); Fee, C.; Dimartino, S. Effect of Urea Concentration on the Viscosity and Thermal Stability of Aqueous NaOH/Urea Cellulose Solutions. *Journal of Polymers* **2016**, *2016*, 1–9, doi:10.1155/2016/2658747.
165. Hu, X.; Tang, Y.; Wang, Q.; Li, Y.; Yang, J.; Du, Y.; Kennedy, J.F. Rheological Behaviour of Chitin in NaOH/Urea Aqueous Solution. *Carbohydr. Polym.* **2011**, *83*, 1128–1133, doi:10.1016/j.carbpol.2010.09.014.
166. Pillai, C.K.S.; Paul, W.; Sharma, C.P. Chitin and Chitosan Polymers: Chemistry, Solubility and Fiber Formation. *Progress in Polymer Science* **2009**, *34*, 641–678, doi:10.1016/j.progpolymsci.2009.04.001.
167. Zargar, V.; Asghari, M.; Dashti, A. A Review on Chitin and Chitosan Polymers: Structure, Chemistry, Solubility, Derivatives, and Applications. *ChemBioEng Reviews* **2015**, *2*, 204–226, doi:10.1002/cben.201400025.
168. Cárdenas, G.; Cabrera, G.; Taboada, E.; Miranda, S.P. Chitin Characterization by SEM, FTIR, XRD, and ^{13} C Cross Polarization/Mass Angle Spinning NMR: Chitin Characterization. *J. Appl. Polym. Sci.* **2004**, *93*, 1876–1885, doi:10.1002/app.20647.
169. Synytsya, A.; Novak, M. Structural Analysis of Glucans. *Annals of Translational Medicine* **2014**, *2*, 17.
170. Kumari, S.; Rath, P.; Sri Hari Kumar, A.; Tiwari, T.N. Extraction and Characterization of Chitin and Chitosan from Fishery Waste by Chemical Method. *Environmental Technology & Innovation* **2015**, *3*, 77–85, doi:10.1016/j.eti.2015.01.002.
171. Jalal, A.F. Optimization of Chitin Extraction from Chicken Feet. *J Anal Bioanal Techniques* **2012**, *03*, doi:10.4172/2155-9872.1000145.
172. Young, A.L. Powder X-Ray Diffraction and Its Application to Biotherapeutic Formulation Development. *American Pharmaceutical Review* **2012**, *15*, 74.
173. Kumirska, J.; Czerwicka, M.; Kaczyński, Z.; Bychowska, A.; Brzozowski, K.; Thöming, J.; Stepnowski, P. Application of Spectroscopic Methods for Structural Analysis of Chitin and Chitosan. *Mar. Drugs* **2010**, *8*, 1567–1636, doi:10.3390/md8051567.
174. Seoudi, R.; Nada, A.M.A. Molecular Structure and Dielectric Properties Studies of Chitin and Its Treated by Acid, Base and Hypochlorite. *Carbohydr. Polym.* **2007**, *68*, 728–733, doi:10.1016/j.carbpol.2006.08.009.
175. Tang, Z.; Li, W.; Lin, X.; Xiao, H.; Miao, Q.; Huang, L.; Chen, L.; Wu, H. TEMPO-Oxidized Cellulose with High Degree of Oxidation. *Polymers* **2017**, *9*, 421, doi:10.3390/polym9090421.
176. Wanjun, T.; Cunxin, W.; Donghua, C. Kinetic Studies on the Pyrolysis of Chitin and Chitosan. *Polymer Degradation and Stability* **2005**, *87*, 389–394, doi:10.1016/j.polymdegradstab.2004.08.006.
177. Shen, X.; Shamshina, J.L.; Berton, P.; Gurau, G.; Rogers, R.D. Hydrogels Based on Cellulose and Chitin: Fabrication, Properties, and Applications. *Green Chem.* **2016**, *18*, 53–75, doi:10.1039/C5GC02396C.
178. Calixto, G.; Yoshii, A.C.; Rocha E Silva, H.; Stringhetti Ferreira Cury, B.; Chorilli, M. Polyacrylic Acid Polymers Hydrogels Intended to Topical Drug Delivery: Preparation and

Characterization. *Pharmaceutical Development and Technology* **2015**, *20*, 490–496, doi:10.3109/10837450.2014.882941.

179. Tang, H.; Chen, H.; Duan, B.; Lu, A.; Zhang, L. Swelling Behaviors of Superabsorbent Chitin/Carboxymethylcellulose Hydrogels. *J Mater Sci* **2014**, *49*, 2235–2242, doi:10.1007/s10853-013-7918-0.
180. Chang, C.; Chen, S.; Zhang, L. Novel Hydrogels Prepared via Direct Dissolution of Chitin at Low Temperature: Structure and Biocompatibility. *J. Mater. Chem.* **2011**, *21*, 3865–3871, doi:10.1039/c0jm03075a.
181. Borzacchiello, A.; Russo, L.; Malle, B.M.; Schwach-Abdellaoui, K.; Ambrosio, L. Hyaluronic Acid Based Hydrogels for Regenerative Medicine Applications. *BioMed Research International* **2015**, *2015*, 1–12, doi:10.1155/2015/871218.
182. Shen, X.; Shamshina, J.L.; Berton, P.; Bandomir, J.; Wang, H.; Gurau, G.; Rogers, R.D. Comparison of Hydrogels Prepared with Ionic-Liquid-Isolated vs Commercial Chitin and Cellulose. *ACS Sustainable Chem. Eng.* **2016**, *4*, 471–480, doi:10.1021/acssuschemeng.5b01400.
183. Mukesh, C.; Mondal, D.; Sharma, M.; Prasad, K. Choline Chloride–Thiourea, a Deep Eutectic Solvent for the Production of Chitin Nanofibers. *Carbohydr. Polym.* **2014**, *103*, 466–471, doi:10.1016/j.carbpol.2013.12.082.
184. Fang, Y.; Duan, B.; Lu, A.; Liu, M.; Liu, H.; Xu, X.; Zhang, L. Intermolecular Interaction and the Extended Wormlike Chain Conformation of Chitin in NaOH/Urea Aqueous Solution. *Biomacromolecules* **2015**, *16*, 1410–1417, doi:10.1021/acs.biomac.5b00195.
185. Raia, N.R.; Partlow, B.P.; McGill, M.; Kimmerling, E.P.; Ghezzi, C.E.; Kaplan, D.L. Enzymatically Crosslinked Silk-Hyaluronic Acid Hydrogels. *Biomaterials* **2017**, *131*, 58–67, doi:10.1016/j.biomaterials.2017.03.046.
186. Nogueira, G.M.; De Moraes, M.A.; Rodas, A.C.D.; Higa, O.Z.; Beppu, M.M. Hydrogels from Silk Fibroin Metastable Solution: Formation and Characterization from a Biomaterial Perspective. *Materials Science and Engineering: C* **2011**, *31*, 997–1001, doi:10.1016/j.msec.2011.02.019.
187. Feng, Y.; Taraban, M.; Yu, Y.B. The Effect of Ionic Strength on the Mechanical, Structural and Transport Properties of Peptide Hydrogels. *Soft Matter* **2012**, *8*, 11723, doi:10.1039/c2sm26572a.
188. Martínez-Ruvalcaba, A.; Chornet, E.; Rodrigue, D. Viscoelastic Properties of Dispersed Chitosan/Xanthan Hydrogels. *Carbohydr. Polym.* **2007**, *67*, 586–595, doi:10.1016/j.carbpol.2006.06.033.
189. Sanderson, G.R. Gellan Gum. In *Food Gels*; Harris, P., Ed.; Springer Netherlands: Dordrecht, 1990; pp. 201–232 ISBN 978-94-010-6825-3.
190. Lau, M.H.; Tang, J.; Paulson, A.T. Texture Profile and Turbidity of Gellan/Gelatin Mixed Gels. *Food Research International* **2000**, *33*, 665–671, doi:10.1016/S0963-9969(00)00111-3.
191. Hurler, J.; Engesland, A.; Poorahmary Kermany, B.; Škalko-Basnet, N. Improved Texture Analysis for Hydrogel Characterization: Gel Cohesiveness, Adhesiveness, and Hardness. *J. Appl. Polym. Sci.* **2012**, *125*, 180–188, doi:10.1002/app.35414.
192. Abdel-Mohsen, A.M.; Jancar, J.; Massoud, D.; Fohlerova, Z.; Elhadidy, H.; Spotz, Z.; Hebeish, A. Novel Chitin/Chitosan-Glucan Wound Dressing: Isolation, Characterization,

Antibacterial Activity and Wound Healing Properties. *International Journal of Pharmaceutics* **2016**, *510*, 86–99, doi:10.1016/j.ijpharm.2016.06.003.

193. Duan, J.; Liang, X.; Cao, Y.; Wang, S.; Zhang, L. High Strength Chitosan Hydrogels with Biocompatibility via New Avenue Based on Constructing Nanofibrous Architecture. *Macromolecules* **2015**, *48*, 2706–2714, doi:10.1021/acs.macromol.5b00117.
194. Tyliszczak, B.; Drabczyk, A.; Kudłacik, S. Comparison of Hydrogels Based on Commercial Chitosan and Beetosan® Containing Nanosilver. *Molecules* **2016**, *22*, 61, doi:10.3390/molecules22010061.
195. Zhao, L.; Niu, L.; Liang, H.; Tan, H.; Liu, C.; Zhu, F. pH and Glucose Dual-Responsive Injectable Hydrogels with Insulin and Fibroblasts as Bioactive Dressings for Diabetic Wound Healing. *ACS Appl. Mater. Interfaces* **2017**, *9*, 37563–37574, doi:10.1021/acsami.7b09395.
196. Ahsan, A.; Tian, W.-X.; Farooq, M.A.; Khan, D.H. An Overview of Hydrogels and Their Role in Transdermal Drug Delivery. *Int. J. Polym. Mater. Polym. Biomater.* **2021**, *70*, 574–584, doi:10.1080/00914037.2020.1740989.
197. Hoffman, A.S. Hydrogels for Biomedical Applications. *Advanced Drug Delivery Reviews* **2012**, *64*, 18–23, doi:10.1016/j.addr.2012.09.010.
198. Chen; Tang; Wang; Zhao; Chen; Zhu Applications of Hydrogels with Special Physical Properties in Biomedicine. *Polymers* **2019**, *11*, 1420, doi:10.3390/polym11091420.
199. Xiang, J.; Shen, L.; Hong, Y. Status and Future Scope of Hydrogels in Wound Healing: Synthesis, Materials and Evaluation. *European Polymer Journal* **2020**, *130*, 109609, doi:10.1016/j.eurpolymj.2020.109609.
200. Zhang, H.; Zhang, F.; Wu, J. Physically Crosslinked Hydrogels from Polysaccharides Prepared by Freeze–Thaw Technique. *Reactive and Functional Polymers* **2013**, *73*, 923–928, doi:10.1016/j.reactfunctpolym.2012.12.014.
201. Coviello, T.; Matricardi, P.; Marianecci, C.; Alhaique, F. Polysaccharide Hydrogels for Modified Release Formulations. *J. Control. Release* **2007**, *119*, 5–24, doi:10.1016/j.jconrel.2007.01.004.
202. Tang, S.; Zhao, L.; Yuan, J.; Chen, Y.; Leng, Y. Physical Hydrogels Based on Natural Polymers. In *Hydrogels Based on Natural Polymers*; Elsevier, 2020; pp. 51–89 ISBN 978-0-12-816421-1.
203. Araújo, D.; Alves, V.D.; Marques, A.C.; Fortunato, E.; Reis, M.A.M.; Freitas, F. Low Temperature Dissolution of Yeast Chitin-Glucan Complex and Characterization of the Regenerated Polymer. *Bioengineering* **2020**, *7*, 28, doi:10.3390/bioengineering7010028.
204. Pawar, V.; Dhanka, M.; Srivastava, R. Cefuroxime Conjugated Chitosan Hydrogel for Treatment of Wound Infections. *Colloids and Surfaces B: Biointerfaces* **2019**, *173*, 776–787, doi:10.1016/j.colsurfb.2018.10.034.
205. Silva, N.H.C.S.; Mota, J.P.; Santos de Almeida, T.; Carvalho, J.P.F.; Silvestre, A.J.D.; Vilela, C.; Rosado, C.; Freire, C.S.R. Topical Drug Delivery Systems Based on Bacterial Nanocellulose: Accelerated Stability Testing. *IJMS* **2020**, *21*, 1262, doi:10.3390/ijms21041262.
206. Zarzycki, R.; Modrzejewska, Z.; Nawrotek, K. Drug Release from Hydrogel Matrices. **2010**, *17*, 117–136.
207. Ferreira, L.; Figueiredo, M.M.; Gil, M.H.; Ramos, M.A. Structural Analysis of Dextran-Based Hydrogels Obtained Chemoenzymatically. *J. Biomed. Mater. Res.* **2006**, *77B*, 55–64, doi:10.1002/jbm.b.30394.

208. Figueroa-Pizano, M.D.; Vélaz, I.; Peñas, F.J.; Zavala-Rivera, P.; Rosas-Durazo, A.J.; Maldonado-Arce, A.D.; Martínez-Barbosa, M.E. Effect of Freeze-Thawing Conditions for Preparation of Chitosan-Poly (Vinyl Alcohol) Hydrogels and Drug Release Studies. *Carbohydr. Polym.* **2018**, *195*, 476–485, doi:10.1016/j.carbpol.2018.05.004.
209. Hoare, T.R.; Kohane, D.S. Hydrogels in Drug Delivery: Progress and Challenges. *Polymer* **2008**, *49*, 1993–2007, doi:10.1016/j.polymer.2008.01.027.
210. Song, X.; Zhu, C.; Fan, D.; Mi, Y.; Li, X.; Fu, R.; Duan, Z.; Wang, Y.; Feng, R. A Novel Human-Like Collagen Hydrogel Scaffold with Porous Structure and Sponge-Like Properties. *Polymers* **2017**, *9*, 638, doi:10.3390/polym9120638.
211. Wong, R.S.H.; Dodou, K. Effect of Drug Loading Method and Drug Physicochemical Properties on the Material and Drug Release Properties of Poly (Ethylene Oxide) Hydrogels for Transdermal Delivery. *Polymers* **2017**, *9*, 286, doi:10.3390/polym9070286.
212. Mushi, N.E.; Kochumalayil, J.; Cervin, N.T.; Zhou, Q.; Berglund, L.A. Nanostructurally Controlled Hydrogel Based on Small-Diameter Native Chitin Nanofibers: Preparation, Structure, and Properties. *ChemSusChem* **2016**, *9*, 989–995, doi:10.1002/cssc.201501697.
213. Kim, S.W.; Bae, Y.H.; Okano, T. Hydrogels: Swelling, Drug Loading and Release. *Pharmaceutical Research* **1992**, *09*, 283–290, doi:10.1023/A:1015887213431.
214. Araújo, D.; Ferreira, I.C.; Torres, C.A.; Neves, L.; Freitas, F. Chitinous Polymers: Extraction from Fungal Sources, Characterization and Processing towards Value-added Applications. *J Chem Technol Biotechnol* **2020**, *95*, 1277–1289, doi:10.1002/jctb.6325.
215. Kong, B.J.; Kim, A.; Park, S.N. Properties and in Vitro Drug Release of Hyaluronic Acid-Hydroxyethyl Cellulose Hydrogels for Transdermal Delivery of Isoliquiritigenin. *Carbohydr. Polym.* **2016**, *147*, 473–481, doi:10.1016/j.carbpol.2016.04.021.
216. Wu, S.; Duan, B.; Lu, A.; Wang, Y.; Ye, Q.; Zhang, L. Biocompatible Chitin/Carbon Nanotubes Composite Hydrogels as Neuronal Growth Substrates. *Carbohydr. Polym.* **2017**, *174*, 830–840, doi:10.1016/j.carbpol.2017.06.101.
217. Udeni Gunathilake, T.; Ching, Y.; Chuah, C. Enhancement of Curcumin Bioavailability Using Nanocellulose Reinforced Chitosan Hydrogel. *Polymers* **2017**, *9*, 64, doi:10.3390/polym9020064.
218. Raza, H.; Ranjha, N.M.; Razzaq, R.; Ansari, M.; Mahmood, A.; Rashid, Z. Fabrication and in Vitro Evaluation of 5-Florouracil Loaded Chondroitin Sulfate-Sodium Alginate Microspheres for Colon Specific Delivery. *Acta Poloniae Pharmaceutica* **2016**, *73*, 495–507.
219. Zhang, S.; Guan, Y.; Fu, G.-Q.; Chen, B.-Y.; Peng, F.; Yao, C.-L.; Sun, R.-C. Organic/Inorganic Superabsorbent Hydrogels Based on Xylan and Montmorillonite. *Journal of Nanomaterials* **2014**, *2014*, 1–11, doi:10.1155/2014/675035.
220. Noor, N.; Shah, A.; Gani, A.; Gani, A.; Masoodi, F.A. Microencapsulation of Caffeine Loaded in Polysaccharide Based Delivery Systems. *Food Hydrocolloids* **2018**, *82*, 312–321, doi:10.1016/j.foodhyd.2018.04.001.
221. Abosabaa, S.A.; ElMeshad, A.N.; Arafa, M.G. Chitosan Nanocarrier Entrapping Hydrophilic Drugs as Advanced Polymeric System for Dual Pharmaceutical and Cosmeceutical Application: A Comprehensive Analysis Using Box-Behnken Design. *Polymers* **2021**, *13*, 677, doi:10.3390/polym13050677.
222. Belščak-Cvitanović, A.; Komes, D.; Karlović, S.; Djaković, S.; Špoljarić, I.; Mršić, G.; Ježek, D. Improving the Controlled Delivery Formulations of Caffeine in Alginate Hydrogel Beads

Combined with Pectin, Carrageenan, Chitosan and Psyllium. *Food Chemistry* **2015**, *167*, 378–386, doi:10.1016/j.foodchem.2014.07.011.

223. Seyedabadi, M.M.; Rostami, H.; Jafari, S.M.; Fathi, M. Development and Characterization of Chitosan-Coated Nanoliposomes for Encapsulation of Caffeine. *Food Bioscience* **2021**, *40*, 100857, doi:10.1016/j.fbio.2020.100857.
224. Alves, V.D.; Costa, N.; Coelhoso, I.M. Barrier Properties of Biodegradable Composite Films Based on Kappa-Carrageenan/Pectin Blends and Mica Flakes. *Carbohydr. Polym.* **2010**, *79*, 269–276, doi:10.1016/j.carbpol.2009.08.002.
225. Tavagnacco, L.; Engström, O.; Schnupf, U.; Saboungi, M.-L.; Himmel, M.; Widmalm, G.; Cesàro, A.; Brady, J.W. Caffeine and Sugars Interact in Aqueous Solutions: A Simulation and NMR Study. *J. Phys. Chem. B* **2012**, *116*, 11701–11711, doi:10.1021/jp303910u.
226. Prince, D.A.; Villamagna, I.J.; Hopkins, C.C.; De Bruyn, J.R.; Gillies, E.R. Effect of Drug Loading on the Properties of Temperature-responsive Polyester–Poly(Ethylene Glycol)–Polyester Hydrogels. *Polymer International* **2019**, *68*, 1074–1083, doi:10.1002/pi.5797.
227. Moradi, S.; Barati, A.; Salehi, E.; Tonelli, A.E.; Hamedi, H. Preparation and Characterization of Chitosan Based Hydrogels Containing Cyclodextrin Inclusion Compounds or Nanoemulsions of Thyme Oil. *Polymer International* **2019**, *68*, 1891–1902, doi:10.1002/pi.5899.
228. Damiri, F.; Bachra, Y.; Bounacir, C.; Laaraibi, A.; Berrada, M. Synthesis and Characterization of Lyophilized Chitosan-Based Hydrogels Cross-Linked with Benzaldehyde for Controlled Drug Release. *Journal of Chemistry* **2020**, *2020*, 1–10, doi:10.1155/2020/8747639.
229. Lim, L.-Y.; Go, M.-L. Caffeine and Nicotinamide Enhances the Aqueous Solubility of the Antimalarial Agent Halofantrine. *European Journal of Pharmaceutical Sciences* **2000**, *10*, 17–28, doi:10.1016/S0928-0987(99)00084-6.
230. Wang, Q.; Dong, Z.; Du, Y.; Kennedy, J.F. Controlled Release of Ciprofloxacin Hydrochloride from Chitosan/Polyethylene Glycol Blend Films. *Carbohydr. Polym.* **2007**, *69*, 336–343, doi:10.1016/j.carbpol.2006.10.014.
231. Hu, Y.; Wu, X.Y.; Xu, J.R.; Guo, J. Study on the Preparation and Drug Release Property of Soybean Selenoprotein/Carboxymethyl Chitosan Composite Hydrogel. *Journal of Polymer Engineering* **2018**, *38*, 963–970, doi:10.1515/polyeng-2017-0222.
232. Quintanilla De Stéfano, J.C.; Abundis-Correa, V.; Herrera-Flores, S.D.; Alvarez, A.J. pH-Sensitive Starch-Based Hydrogels: Synthesis and Effect of Molecular Components on Drug Release Behavior. *Polymers* **2020**, *12*, 1974, doi:10.3390/polym12091974.
233. Aswathy, S.H.; Narendrakumar, U.; Manjubala, I. Commercial Hydrogels for Biomedical Applications. *Heliyon* **2020**, *6*, e03719, doi:10.1016/j.heliyon.2020.e03719.
234. Manzoor, A.; Dar, A.H.; Pandey, V.K.; Shams, R.; Khan, S.; Panesar, P.S.; Kennedy, J.F.; Fayaz, U.; Khan, S.A. Recent Insights into Polysaccharide-Based Hydrogels and Their Potential Applications in Food Sector: A Review. *Int. J. Biol. Macromol.* **2022**, *213*, 987–1006, doi:10.1016/j.ijbiomac.2022.06.044.
235. Cui, R.; Zhang, L.; Ou, R.; Xu, Y.; Xu, L.; Zhan, X.-Y.; Li, D. Polysaccharide-Based Hydrogels for Wound Dressing: Design Considerations and Clinical Applications. *Front. Bioeng. Biotechnol.* **2022**, *10*, 845735, doi:10.3389/fbioe.2022.845735.
236. Rial-Hermida, M.I.; Rey-Rico, A.; Blanco-Fernandez, B.; Carballo-Pedrares, N.; Byrne, E.M.; Mano, J.F. Recent Progress on Polysaccharide-Based Hydrogels for Controlled Delivery

of Therapeutic Biomolecules. *ACS Biomater. Sci. Eng.* **2021**, *7*, 4102–4127, doi:10.1021/acsbiomaterials.0c01784.

237. Pushpamalar, J.; Meganathan, P.; Tan, H.L.; Dahlan, N.A.; Ooi, L.-T.; Neerooa, B.N.H.M.; Essa, R.Z.; Shameli, K.; Teow, S.-Y. Development of a Polysaccharide-Based Hydrogel Drug Delivery System (DDS): An Update. *Gels* **2021**, *7*, 153, doi:10.3390/gels7040153.
238. Liao, J.; Hou, B.; Huang, H. Preparation, Properties and Drug Controlled Release of Chitin-Based Hydrogels: An Updated Review. *Carbohydr. Polym.* **2022**, *283*, 119177, doi:10.1016/j.carbpol.2022.119177.
239. Araújo, D.; Rodrigues, T.; Alves, V.D.; Freitas, F. Chitin-Glucan Complex Hydrogels: Optimization of Gel Formation and Demonstration of Drug Loading and Release Ability. *Polymers* **2022**, *14*, 785, doi:10.3390/polym14040785.
240. Don, T.-M.; Huang, M.-L.; Chiu, A.-C.; Kuo, K.-H.; Chiu, W.-Y.; Chiu, L.-H. Preparation of Thermo-Responsive Acrylic Hydrogels Useful for the Application in Transdermal Drug Delivery Systems. *Materials Chemistry and Physics* **2008**, *107*, 266–273, doi:10.1016/j.matchemphys.2007.07.009.
241. Ahumada, M.; Jacques, E.; Calderon, C.; Martínez-Gómez, F. Porosity in Biomaterials: A Key Factor in the Development of Applied Materials in Biomedicine. In *Handbook of Ecomaterials*; Martínez, L.M.T., Kharissova, O.V., Kharisov, B.I., Eds.; Springer International Publishing: Cham, 2019; pp. 3503–3522 ISBN 978-3-319-68254-9.
242. Park, J.; Kim, D. Effect of Polymer Solution Concentration on the Swelling and Mechanical Properties of Glycol Chitosan Superporous Hydrogels. *J. Appl. Polym. Sci.* **2010**, *115*, 3434–3441, doi:10.1002/app.30632.
243. Akalin, G.O.; Pulat, M. Preparation and Characterization of Nanoporous Sodium Carboxymethyl Cellulose Hydrogel Beads. *Journal of Nanomaterials* **2018**, *2018*, 1–12, doi:10.1155/2018/9676949.
244. Celikkin, N.; Mastrogiacomo, S.; Jaroszewicz, J.; Walboomers, X.F.; Swieszkowski, W. Gelatin Methacrylate Scaffold for Bone Tissue Engineering: The Influence of Polymer Concentration: GELATIN METHACRYLATE SCAFFOLD FOR BONE TISSUE ENGINEERING. *J. Biomed. Mater. Res.* **2018**, *106*, 201–209, doi:10.1002/jbm.a.36226.
245. Liu, H.; Liu, J.; Qi, C.; Fang, Y.; Zhang, L.; Zhuo, R.; Jiang, X. Thermosensitive Injectable In-Situ Forming Carboxymethyl Chitin Hydrogel for Three-Dimensional Cell Culture. *Acta Biomaterialia* **2016**, *35*, 228–237, doi:10.1016/j.actbio.2016.02.028.
246. Ben Bouali, A.; Montembault, A.; David, L.; Von Boxberg, Y.; Viallon, M.; Hamdi, B.; Nothias, F.; Fodil, R.; Féréol, S. Nanoscale Mechanical Properties of Chitosan Hydrogels as Revealed by AFM. *Prog Biomater* **2020**, *9*, 187–201, doi:10.1007/s40204-020-00141-4.
247. Kumar, B.Y.S.; Isloor, A.M.; Kumar, C.M.; Asiri, A.M. Nanohydroxyapatite Reinforced Chitosan Composite Hydrogel with Tunable Mechanical and Biological Properties for Cartilage Regeneration. *Scientific Reports* **2019**, *9*.
248. Shen, Z.-S.; Cui, X.; Hou, R.-X.; Li, Q.; Deng, H.-X.; Fu, J. Tough Biodegradable Chitosan–Gelatin Hydrogels via in Situ Precipitation for Potential Cartilage Tissue Engineering. *RSC Adv.* **2015**, *5*, 55640–55647, doi:10.1039/C5RA06835E.
249. Zhao, D.; Huang, J.; Zhong, Y.; Li, K.; Zhang, L.; Cai, J. High-Strength and High-Toughness Double-Cross-Linked Cellulose Hydrogels: A New Strategy Using Sequential Chemical and Physical Cross-Linking. *Adv. Funct. Mater.* **2016**, *26*, 6279–6287, doi:10.1002/adfm.201601645.

250. Baby, D.K. Rheology of Hydrogels. In *Rheology of Polymer Blends and Nanocomposites*; Elsevier, 2020; pp. 193–204 ISBN 978-0-12-816957-5.
251. Liu, Y.; Zhang, C.; Liu, L.; Zhang, X.; Hou, Y.; Zhao, L. Characterization of Chitin-Glucan Complex of Ganoderma Lucidum Extract and Its Application as Hemostatic Hydrogel. *Waste Biomass Valor* **2022**, *13*, 3297–3308, doi:10.1007/s12649-022-01711-2.
252. Murata, H. Rheology - Theory and Application to Biomaterials. In *Polymerization*; De Souza Gomes, A., Ed.; InTech, 2012 ISBN 978-953-51-0745-3.
253. Yang, J.; Shen, M.; Luo, Y.; Wu, T.; Wen, H.; Xie, J. Construction and Characterization of Mesona Chinensis Polysaccharide-Chitosan Hydrogels, Role of Chitosan Deacetylation Degree. *Carbohydr. Polym.* **2021**, *257*, 117608, doi:10.1016/j.carbpol.2020.117608.
254. Dalei, G.; Das, S.; Das, S.P. Non-Thermal Plasma Assisted Surface Nano-Textured Carboxymethyl Guar Gum/Chitosan Hydrogels for Biomedical Applications. *RSC Adv.* **2019**, *9*, 1705–1716, doi:10.1039/C8RA09161G.
255. Ganji, F.; Vasheghani-Farahani, S.; Vasheghani-Farahani, E. Theoretical Description of Hydrogel Swelling: A Review. **2010**, *19*, 375–398.
256. Suhail, M.; Liu, J.-Y.; Hung, M.-C.; Chiu, I.-H.; Minhas, M.U.; Wu, P.-C. Preparation, In Vitro Characterization, and Cytotoxicity Evaluation of Polymeric pH-Responsive Hydrogels for Controlled Drug Release. *Pharmaceutics* **2022**, *14*, 1864, doi:10.3390/pharmaceutics14091864.
257. Sriamornsak, P.; Nunthanid, J.; Cheewatanakornkool, K.; Manchun, S. Effect of Drug Loading Method on Drug Content and Drug Release from Calcium Pectinate Gel Beads. *AAPS PharmSciTech* **2010**, *11*, 1315–1319, doi:10.1208/s12249-010-9513-x.
258. Jeencham, R.; Sutheerawattananonda, M.; Rungchang, S.; Tiyaboonchai, W. Novel Daily Disposable Therapeutic Contact Lenses Based on Chitosan and Regenerated Silk Fibroin for the Ophthalmic Delivery of Diclofenac Sodium. *Drug Delivery* **2020**, *27*, 782–790, doi:10.1080/10717544.2020.1765432.
259. Caliceti, P.; Salmaso, S.; Lante, A.; Yoshida, M.; Katakai, R.; Martellini, F.; Mei, L.H.I.; Carenza, M. Controlled Release of Biomolecules from Temperature-Sensitive Hydrogels Prepared by Radiation Polymerization. *J. Control. Release* **2001**, *75*, 173–181, doi:10.1016/S0168-3659(01)00380-7.
260. Sethi, S.; Saruchi; Kaith, B.S.; Kaur, M.; Sharma, N.; Kumar, V. Cross-Linked Xanthan Gum–Starch Hydrogels as Promising Materials for Controlled Drug Delivery. *Cellulose* **2020**, *27*, 4565–4589, doi:10.1007/s10570-020-03082-0.
261. Li, J.; Mooney, D.J. Designing Hydrogels for Controlled Drug Delivery. *Nat Rev Mater* **2016**, *1*, 16071, doi:10.1038/natrevmats.2016.71.
262. Briggs, F.; Browne, D.; Asuri, P. Role of Polymer Concentration and Crosslinking Density on Release Rates of Small Molecule Drugs. *IJMS* **2022**, *23*, 4118, doi:10.3390/ijms23084118.
263. Gull, N.; Khan, S.M.; Butt, O.M.; Islam, A.; Shah, A.; Jabeen, S.; Khan, S.U.; Khan, A.; Khan, R.U.; Butt, M.T.Z. Inflammation Targeted Chitosan-Based Hydrogel for Controlled Release of Diclofenac Sodium. *Int. J. Biol. Macromol.* **2020**, *162*, 175–187, doi:10.1016/j.ijbiomac.2020.06.133.
264. Haq, A.; Goodyear, B.; Ameen, D.; Joshi, V.; Michniak-Kohn, B. Strat-M® Synthetic Membrane: Permeability Comparison to Human Cadaver Skin. *International Journal of Pharmaceutics* **2018**, *547*, 432–437, doi:10.1016/j.ijpharm.2018.06.012.

265. Simon, A.; Amaro, M.I.; Healy, A.M.; Cabral, L.M.; de Sousa, V.P. Comparative Evaluation of Rivastigmine Permeation from a Transdermal System in the Franz Cell Using Synthetic Membranes and Pig Ear Skin with in Vivo-in Vitro Correlation. *International Journal of Pharmaceutics* **2016**, *512*, 234–241, doi:10.1016/j.ijpharm.2016.08.052.
266. Neupane, R.; Boddu, S.H.S.; Renukuntla, J.; Babu, R.J.; Tiwari, A.K. Alternatives to Biological Skin in Permeation Studies: Current Trends and Possibilities. *Pharmaceutics* **2020**, *12*, 152, doi:10.3390/pharmaceutics12020152.
267. N'Da, D. Prodrug Strategies for Enhancing the Percutaneous Absorption of Drugs. *Molecules* **2014**, *19*, 20780–20807, doi:10.3390/molecules191220780.
268. Knudsen, N.; Pedersen, G. pH and Drug Delivery. In *pH of the Skin: Issues and Challenges*; Surber, C., Abels, C., Maibach, H., Eds.; Current Problems in Dermatology; S. Karger AG, 2018; Vol. 54, pp. 143–151 ISBN 978-3-318-06384-4.
269. Uchida, T.; Kadhum, W.R.; Kanai, S.; Todo, H.; Oshizaka, T.; Sugibayashi, K. Prediction of Skin Permeation by Chemical Compounds Using the Artificial Membrane, Strat-M^{TM}. *European Journal of Pharmaceutical Sciences* **2015**, *67*, 113–118, doi:10.1016/j.ejps.2014.11.002.
270. Klebeko, J.; Ossowicz-Rupniewska, P.; Nowak, A.; Janus, E.; Duchnik, W.; Adamiak-Giera, U.; Kucharski, Ł.; Prowans, P.; Petriczko, J.; Czapla, N.; et al. Permeability of Ibuprofen in the Form of Free Acid and Salts of L-Valine Alkyl Esters from a Hydrogel Formulation through Strat-M^{TM} Membrane and Human Skin. *Materials* **2021**, *14*, 6678, doi:10.3390/ma14216678.
271. Uchida, T.; Nishioka, K.; Motoki, A.; Yakumaru, M.; Sano, T.; Todo, H.; Sugibayashi, K. Through Synthetic Artificial Membranes Using a High-Throughput. *Chem. Pharm. Bull.* **2016**, *64*, 1597–1606.
272. Pradal, J. Comparison of Skin Permeation and Putative Anti-Inflammatory Activity of Commercially Available Topical Products Containing Ibuprofen and Diclofenac. *JPR* **2020**, *Volume 13*, 2805–2814, doi:10.2147/JPR.S262390.
273. Lenis-Rojas, O.A.; Roma-Rodrigues, C.; Carvalho, B.; Cabezas-Sainz, P.; Fernández Vila, S.; Sánchez, L.; Baptista, P.V.; Fernandes, A.R.; Royo, B. In Vitro and In Vivo Biological Activity of Ruthenium 1,10-Phenanthroline-5,6-Dione Arene Complexes. *IJMS* **2022**, *23*, 13594, doi:10.3390/ijms232113594.
274. Yazdi, M.K.; Vatanpour, V.; Taghizadeh, A.; Taghizadeh, M.; Ganjali, M.R.; Munir, M.T.; Habibzadeh, S.; Saeb, M.R.; Ghaedi, M. Hydrogel Membranes: A Review. *Materials Science and Engineering: C* **2020**, *114*, 111023, doi:10.1016/j.msec.2020.111023.
275. Pan, F.; Zhang, S.; Altenried, S.; Zuber, F.; Chen, Q.; Ren, Q. Advanced Antifouling and Antibacterial Hydrogels Enabled by Controlled Thermo-Responses of a Biocompatible Polymer Composite. *Biomater. Sci.* **2022**, *10*, 6146–6159, doi:10.1039/D2BM01244H.
276. Kamoun, E.A.; Kenawy, E.-R.S.; Chen, X. A Review on Polymeric Hydrogel Membranes for Wound Dressing Applications: PVA-Based Hydrogel Dressings. *J. Adv. Res.***2017**, *8*, 217–233, doi:10.1016/j.jare.2017.01.005.
277. Cam, C.; Segura, T. Chemical Sintering Generates Uniform Porous Hyaluronic Acid Hydrogels. *Acta Biomaterialia* **2014**, *10*, 205–213, doi:10.1016/j.actbio.2013.10.002.
278. Zang, L.; Ma, J.; Dongwei, L.; Liu, Q.; Jiao, W.; Wang, P. Core-Shell Fibers Constructed pH-Responsive Nanofibrous Hydrogel Membrane for Efficient Oil/Water Separation. *J. Mater. Chem. A* **2017**, *5*, 19398–19405, doi:10.1039/C7TA05148D.

279. Qi, M.; Zhao, K.; Bao, Q.; Pan, P.; Zhao, Y.; Yang, Z.; Wang, H.; Wei, J. Adsorption and Electrochemical Detection of Bovine Serum Albumin Imprinted Calcium Alginate Hydrogel Membrane. *Polymers* **2019**, *11*, 622, doi:10.3390/polym11040622.
280. Ahmad, S.; Minhas, M.U.; Ahmad, M.; Sohail, M.; Khalid, Q.; Abdullah, O. Synthesis and Evaluation of Topical Hydrogel Membranes; a Novel Approach to Treat Skin Disorders. *J Mater Sci: Mater Med* **2018**, *29*, 191, doi:10.1007/s10856-018-6191-9.
281. Altaf, F.; Niazi, M.B.K.; Jahan, Z.; Ahmad, T.; Akram, M.A.; safdar, A.; Butt, M.S.; Noor, T.; Sher, F. Synthesis and Characterization of PVA/Starch Hydrogel Membranes Incorporating Essential Oils Aimed to Be Used in Wound Dressing Applications. *J Polym Environ* **2021**, *29*, 156–174, doi:10.1007/s10924-020-01866-w.
282. Gadziński, P.; Froelich, A.; Jadach, B.; Wojtyłko, M.; Tatarek, A.; Białek, A.; Krysztofiak, J.; Gackowski, M.; Otto, F.; Osmałek, T. Ionotropic Gelation and Chemical Crosslinking as Methods for Fabrication of Modified-Release Gellan Gum-Based Drug Delivery Systems. *Pharmaceutics* **2022**, *15*, 108, doi:10.3390/pharmaceutics15010108.
283. Massana Roquero, D.; Othman, A.; Melman, A.; Katz, E. Iron(III)-Cross-Linked Alginate Hydrogels: A Critical Review. *Mater. Adv.* **2022**, *3*, 1849–1873, doi:10.1039/D1MA00959A.
284. Kang, M.; Oderinde, O.; Liu, S.; Huang, Q.; Ma, W.; Yao, F.; Fu, G. Characterization of Xanthan Gum-Based Hydrogel with Fe3+ Ions Coordination and Its Reversible Sol-Gel Conversion. *Carbohydr. Polym.* **2019**, *203*, 139–147, doi:10.1016/j.carbpol.2018.09.044.
285. Wang, L.; Li, Y.; Lin, L.; Mu, R.; Pang, J. Novel Synthesis of Mussel Inspired and Fe3+ Induced pH-Sensitive Hydrogels: Adhesion, Injectable, Shapeable, Temperature Properties, Release Behavior and Rheological Characterization. *Carbohydr. Polym.* **2020**, *236*, 116045, doi:10.1016/j.carbpol.2020.116045.
286. Kumar, B.; Priyadarshi, R.; Sauraj; Deeba, F.; Kulshreshtha, A.; Gaikwad, K.K.; Kim, J.; Kumar, A.; Negi, Y.S. Nanoporous Sodium Carboxymethyl Cellulose-g-Poly (Sodium Acrylate)/FeCl3 Hydrogel Beads: Synthesis and Characterization. *Gels* **2020**, *6*, 49, doi:10.3390/gels6040049.
287. Hu, Y.; Jeong, D.; Kim, Y.; Kim, S.; Jung, S. Preparation of Succinoglycan Hydrogel Coordinated With Fe3+ Ions for Controlled Drug Delivery. *Polymers* **2020**, *12*, 977, doi:10.3390/polym12040977.
288. Parhi, R.; Sahoo, S.K.; Das, A. Applications of Polysaccharides in Topical and Transdermal Drug Delivery: A Recent Update of Literature. *Braz. J. Pharm. Sci.* **2022**, *58*, e20802, doi:10.1590/s2175-97902022e20802.
289. Torres, C.A.V.; Ferreira, A.R.V.; Freitas, F.; Reis, M.A.M.; Coelhoso, I.; Sousa, I.; Alves, V.D. Rheological Studies of the Fucose-Rich Exopolysaccharide FucoPol. *Int. J. Biol. Macromol.***2015**, *79*, 611–617, doi:10.1016/j.ijbiomac.2015.05.029.
290. Guerreiro, B.; Silva, J.; Lima, J.; Reis, M.; Freitas, F. Antioxidant Potential of the Bio-Based Fucose-Rich Polysaccharide FucoPol Supports Its Use in Oxidative Stress-Inducing Systems. *Polymers* **2021**, *13*, 3020, doi:10.3390/polym13183020.
291. Concórdio-Reis, P.; Pereira, C.V.; Batista, M.P.; Sevrin, C.; Grandfils, C.; Marques, A.C.; Fortunato, E.; Gaspar, F.B.; Matias, A.A.; Freitas, F.; et al. Silver Nanocomposites Based on the Bacterial Fucose-Rich Polysaccharide Secreted by Enterobacter A47 for Wound Dressing Applications: Synthesis, Characterization and in Vitro Bioactivity. *Int. J. Biol. Macromol.***2020**, *163*, 959–969, doi:10.1016/j.ijbiomac.2020.07.072.

292. Fialho, L.; Araújo, D.; Alves, V.D.; Roma-Rodrigues, C.; Baptista, P.V.; Fernandes, A.R.; Freitas, F.; Reis, M.A.M. Cation-Mediated Gelation of the Fucose-Rich Polysaccharide FucoPol: Preparation and Characterization of Hydrogel Beads and Their Cytotoxicity Assessment. *Int. J. Polym. Mater. Polym. Biomater.* **2021**, *70*, 90–99, doi:10.1080/00914037.2019.1695205.

293. Concórdio-Reis, P.; Pereira, J.R.; Torres, C.A.V.; Sevrin, C.; Grandfils, C.; Freitas, F. Effect of Mono- and Dipotassium Phosphate Concentration on Extracellular Polysaccharide Production by the Bacterium Enterobacter A47. *Process Biochemistry* **2018**, *75*, 16–21, doi:10.1016/j.procbio.2018.09.001.

294. Fernandes, A.R.; Mendonça-Martins, I.; Santos, M.F.A.; Raposo, L.R.; Mendes, R.; Marques, J.; Romão, C.C.; Romão, M.J.; Santos-Silva, T.; Baptista, P.V. Improving the Anti-Inflammatory Response via Gold Nanoparticle Vectorization of CO-Releasing Molecules. *ACS Biomater. Sci. Eng.* **2020**, *6*, 1090–1101, doi:10.1021/acsbiomaterials.9b01936.

295. Livak, K.J.; Schmittgen, T.D. Analysis of Relative Gene Expression Data Using Real-Time Quantitative PCR and the 2−ΔΔCT Method. *Methods* **2001**, *25*, 402–408, doi:10.1006/meth.2001.1262.

296. Narayanan, R.P.; Melman, G.; Letourneau, N.J.; Mendelson, N.L.; Melman, A. Photodegradable Iron(III) Cross-Linked Alginate Gels. *Biomacromolecules* **2012**, *13*, 2465–2471, doi:10.1021/bm300707a.

297. Li, M.; Wu, Q.; Moon, R.J.; Hubbe, M.A.; Bortner, M.J. Rheological Aspects of Cellulose Nanomaterials: Governing Factors and Emerging Applications. *Adv. Mater.* **2021**, *33*, 2006052, doi:10.1002/adma.202006052.

298. Stojkov, G.; Niyazov, Z.; Picchioni, F.; Bose, R.K. Relationship between Structure and Rheology of Hydrogels for Various Applications. *Gels* **2021**, *7*, 255, doi:10.3390/gels7040255.

299. Shukla, S.; Favata, J.; Srivastava, V.; Shahbazmohamadi, S.; Tripathi, A.; Shukla, A. Effect of Polymer and Ion Concentration on Mechanical and Drug Release Behavior of Gellan Hydrogels Using Factorial Design. *Journal of Polymer Science* **2020**, *58*, 1365–1379, doi:10.1002/pol.20190205.

300. Ambebila, E.N.; Santamaría, E.; Maestro, A.; Gutiérrez, J.M.; González, C. Gellan Hydrogels: Preparation, Rheological Characterization and Application in Encapsulation of Curcumin. *Food Biophysics* **2019**, *14*, 154–163, doi:10.1007/s11483-019-09568-0.

301. Lu, L.; Tian, T.; Wu, S.; Xiang, T.; Zhou, S. A pH-Induced Self-Healable Shape Memory Hydrogel with Metal-Coordination Cross-Links. *Polym. Chem.* **2019**, *10*, 1920–1929, doi:10.1039/C9PY00015A.

302. Yang, C.; Zhang, Y.; Tang, P.; Zheng, T.; Zhang, X.; Zhang, Y.; Li, G. Collagen-Based Hydrogels Cross-Linked via Laccase - Mediated System Incorporated with Fe3+ for Wound Dressing. *Colloids and Surfaces B: Biointerfaces* **2022**, *219*, 112825, doi:10.1016/j.colsurfb.2022.112825.

303. Li, N.; Sun, D.; Su, Z.; Hao, X.; Li, M.; Ren, J.; Peng, F. Rapid Fabrication of Xylan-Based Hydrogel by Graft Polymerization via a Dynamic Lignin-Fe3+ Plant Catechol System. *Carbohydr. Polym.* **2021**, *269*, 118306, doi:10.1016/j.carbpol.2021.118306.

304. Yu, P.; Li, Y.; Sun, H.; Ke, X.; Xing, J.; Zhao, Y.; Xu, X.; Qin, M.; Xie, J.; Li, J. Cartilage-Inspired Hydrogel with Mechanical Adaptability, Controllable Lubrication, and Inflammation Regulation Abilities. *ACS Appl. Mater. Interfaces* **2022**, *14*, 27360–27370, doi:10.1021/acsami.2c04609.

305. Araújo, D.; Rodrigues, T.; Roma-Rodrigues, C.; Alves, V.D.; Fernandes, A.R.; Freitas, F. Chitin-Glucan Complex Hydrogels: Physical-Chemical Characterization, Stability, In Vitro Drug Permeation, and Biological Assessment in Primary Cells. *Polymers* **2023**, *15*, 791, doi:10.3390/polym15040791.
306. Pathak, T.S.; Yun, J.-H.; Lee, J.; Paeng, K.-J. Effect of Calcium Ion (Cross-Linker) Concentration on Porosity, Surface Morphology and Thermal Behavior of Calcium Alginates Prepared from Algae (Undaria Pinnatifida). *Carbohydr. Polym.* **2010**, *81*, 633–639, doi:10.1016/j.carbpol.2010.03.025.
307. Tran, V.T.; Mredha, Md.T.I.; Jeon, I. High-Water-Content Hydrogels Exhibiting Superior Stiffness, Strength, and Toughness. *Extreme Mechanics Letters* **2020**, *37*, 100691, doi:10.1016/j.eml.2020.100691.
308. Araújo, D.; Concórdio-Reis, P.; Marques, A.C.; Sevrin, C.; Grandfils, C.; Alves, V.D.; Fortunato, E.; Reis, M.A.M.; Freitas, F. Demonstration of the Ability of the Bacterial Polysaccharide FucoPol to Flocculate Kaolin Suspensions. *Environmental Technology* **2020**, *41*, 287–295, doi:10.1080/09593330.2018.1497710.
309. Sthoer, A.; Adams, E.M.; Sengupta, S.; Corkery, R.W.; Allen, H.C.; Tyrode, E.C. La3+ and Y3+ Interactions with the Carboxylic Acid Moiety at the Liquid/Vapor Interface: Identification of Binding Complexes, Charge Reversal, and Detection Limits. *Journal of Colloid and Interface Science* **2022**, *608*, 2169–2180, doi:10.1016/j.jcis.2021.10.052.
310. Gao, H.-L.; Ding, B.; Yi, L.; Cheng, P.; Liao, D.-Z.; Yan, S.-P.; Jiang, Z.-H. Syntheses and Structures of 1D and 2D Coordination Polymers Derived from Pyridine-2,4,6-Tricarboxylic Acid. *Inorganic Chemistry Communications* **2005**, *8*, 151–154, doi:10.1016/j.inoche.2004.11.023.
311. Hu, X.; Guo, J.; Wang, Y.; Liu, C. Synthesis, Infrared Spectra, Thermal Analyses and Structural Studies of Half-Sandwich Fe(III)/Fe(II) Complex Containing Pyridine-2,6-Dicarboxylate and 1,10-Phenanthroline. *Spectrochimica Acta Part A: Molecular and Biomolecular Spectroscopy* **2009**, *74*, 48–51, doi:10.1016/j.saa.2009.04.027.
312. Inam, M.; Khan, R.; Park, D.; Lee, Y.-W.; Yeom, I. Removal of Sb(III) and Sb(V) by Ferric Chloride Coagulation: Implications of Fe Solubility. *Water* **2018**, *10*, 418, doi:10.3390/w10040418.
313. Vázquez-González, Y.; Prieto, C.; Stojanovic, M.; Torres, C.A.V.; Freitas, F.; Ragazzo-Sánchez, J.A.; Calderón-Santoyo, M.; Lagaron, J.M. Preparation and Characterization of Electrospun Polysaccharide FucoPol-Based Nanofiber Systems. *Nanomaterials* **2022**, *12*, 498, doi:10.3390/nano12030498.
314. Alosmanov, R.; Imanova, J.; Wolski, K.; Ziemmermann, R.; Fiejdasz, S.; Przewoźnik, J.; Goc, K.; Kapusta, C.; Zapotoczny, S.; Szuwarzyński, M. Fabrication of Functional Carbon/Magnetic Nanocomposites as A Promising Model of Utilization of Used Crosslinked Polymers. *Materials* **2018**, *11*, 2595, doi:10.3390/ma11122595.
315. Bothara, S.B.; Singh, S. Thermal Studies on Natural Polysaccharide. *Asian Pacific Journal of Tropical Biomedicine* **2012**, *2*, S1031–S1035, doi:10.1016/S2221-1691(12)60356-6.
316. You, S.; Xiang, Y.; Qi, X.; Mao, R.; Cai, E.; Lan, Y.; Lu, H.; Shen, J.; Deng, H. Harnessing a Biopolymer Hydrogel Reinforced by Copper/Tannic Acid Nanosheets for Treating Bacteria-Infected Diabetic Wounds. *Materials Today Advances* **2022**, *15*, 100271, doi:10.1016/j.mtadv.2022.100271.

317. Murakawa, K.; King, D.R.; Sun, T.; Guo, H.; Kurokawa, T.; Gong, J.P. Polyelectrolyte Complexation via Viscoelastic Phase Separation Results in Tough and Self-Recovering Porous Hydrogels. *J. Mater. Chem. B* **2019**, *7*, 5296–5305, doi:10.1039/C9TB01376H.
318. Cao, Z.; Zhang, Y.; Luo, K.; Wu, Y.; Gao, H.; Cheng, J.; Liu, C.; Tao, G.; Guan, Q.; Zhang, L. Preparation and Properties of Polyacrylamide/Sodium Alginate Hydrogel and the Effect of Fe Adsorption on Its Mechanical Performance. *Journal of Renewable Materials* **2021**, *9*, 1447–1462, doi:10.32604/jrm.2021.015593.
319. Popov, S.; Paderin, N.; Chistiakova, E.; Ptashkin, D. Serosal Adhesion Ex Vivo of Hydrogels Prepared from Apple Pectin Cross-Linked with Fe3+ Ions. *IJMS* **2023**, *24*, 1248, doi:10.3390/ijms24021248.
320. Kang, X.; Deng, L.; Yi, L.; Ruan, C.-Q.; Zeng, K. A Facile Method for Preparation of Green and Antibacterial Hydrogel Based on Chitosan and Water-Soluble 2,3-Dialdehyde Cellulose. *Cellulose* **2021**, *28*, 6403–6416, doi:10.1007/s10570-021-03879-7.
321. Li, H.; Wang, J.; Luo, Y.; Bai, B.; Cao, F. pH-Responsive Eco-Friendly Chitosan–Chlorella Hydrogel Beads for Water Retention and Controlled Release of Humic Acid. *Water* **2022**, *14*, 1190, doi:10.3390/w14081190.
322. Roy, N.; Saha, N.; Saha, P. Stability Study of Novel Medicated Hydrogel Wound Dressings. *Int. J. Polym. Mater. Polym. Biomater.* **2013**, *62*, 150–156, doi:10.1080/00914037.2011.641697.
323. Tanan, W.; Panichpakdee, J.; Saengsuwan, S. Novel Biodegradable Hydrogel Based on Natural Polymers: Synthesis, Characterization, Swelling/Reswelling and Biodegradability. *European Polymer Journal* **2019**, *112*, 678–687, doi:10.1016/j.eurpolymj.2018.10.033.
324. Li, Z.; You, S.; Mao, R.; Xiang, Y.; Cai, E.; Deng, H.; Shen, J.; Qi, X. Architecting Polyelectrolyte Hydrogels with Cu-Assisted Polydopamine Nanoparticles for Photothermal Antibacterial Therapy. *Materials Today Bio* **2022**, *15*, 100264, doi:10.1016/j.mtbio.2022.100264.
325. Bueno, V.B.; Bentini, R.; Catalani, L.H.; Petri, D.F.S. Synthesis and Swelling Behavior of Xanthan-Based Hydrogels. *Carbohydr. Polym.* **2013**, *92*, 1091–1099, doi:10.1016/j.carbpol.2012.10.062.
326. Wu, Y.; Wang, L.; Qing, Y.; Yan, N.; Tian, C.; Huang, Y. A Green Route to Prepare Fluorescent and Absorbent Nano-Hybrid Hydrogel for Water Detection. *Sci Rep* **2017**, *7*, 4380, doi:10.1038/s41598-017-04542-7.
327. Awasthi, S.; Singhal, R. A Mathematical Study on Effect of 2-Hydroxyl Ethyl Acrylate on Controlled Drug Diffusion from Smart Hydrogels Based on Poly(Acrylamide-Co-Hydroxy Ethyl Acrylate-Co-Acrylic Acid). *Journal of Macromolecular Science, Part A* **2012**, *49*, 397–413, doi:10.1080/10601325.2012.671760.
328. Peppas, N.A. *Hydrogels in Medicine and Pharmacy. Volume I, Fundamentals*; First edition.; CRC Press: Boca Raton, 2019; ISBN 978-0-429-28509-7.
329. Naeem, F.; Khan, S.; Jalil, A.; Ranjha, N.M.; Riaz, A.; Haider, M.S.; Sarwar, S.; Saher, F.; Afzal, S. pH Responsive Cross-Linked Polymeric Matrices Based on Natural Polymers: Effect of Process Variables on Swelling Characterization and Drug Delivery Properties. *Bioimpacts* **2017**, *7*, 177–192, doi:10.15171/bi.2017.21.
330. Nicoletta, F.P.; De Filpo, G.; Formoso, P. Hydrogel Membranes. In *Encyclopedia of Membranes*; Drioli, E., Giorno, L., Eds.; Springer Berlin Heidelberg: Berlin, Heidelberg, 2015; pp. 1–4 ISBN 978-3-642-40872-4.

331. Trombino, S.; Sole, R.; Curcio, F.; Cassano, R. Polymeric Based Hydrogel Membranes for Biomedical Applications. *Membranes* **2023**, *13*, 576, doi:10.3390/membranes13060576.
332. Liu, H.; Wang, C.; Li, C.; Qin, Y.; Wang, Z.; Yang, F.; Li, Z.; Wang, J. A Functional Chitosan-Based Hydrogel as a Wound Dressing and Drug Delivery System in the Treatment of Wound Healing. *RSC Adv.* **2018**, *8*, 7533–7549, doi:10.1039/C7RA13510F.
333. Do, N.H.N.; Pham, T.H.; Le, P.K.; Ha, A.C. Thermo-Responsive Chitosan/β-Glycerophosphate Hydrogels Directly Post-Loading Anti-Inflammatory Diclofenac Sodium. *J Sol-Gel Sci Technol* **2023**, *105*, 451–460, doi:10.1007/s10971-022-06020-7.
334. Bhattarai, N.; Gunn, J.; Zhang, M. Chitosan-Based Hydrogels for Controlled, Localized Drug Delivery. *Advanced Drug Delivery Reviews* **2010**, *62*, 83–99, doi:10.1016/j.addr.2009.07.019.
335. Tan, L.S.; Tan, H.L.; Deekonda, K.; Wong, Y.Y.; Muniyandy, S.; Hashim, K.; Pushpamalar, J. Fabrication of Radiation Cross-Linked Diclofenac Sodium Loaded Carboxymethyl Sago Pulp/Chitosan Hydrogel for Enteric and Sustained Drug Delivery. *Carbohydrate Polymer Technologies and Applications* **2021**, *2*, 100084, doi:10.1016/j.carpta.2021.100084.
336. Awachat, A.; Shukla, D.; Bhola, N.D. Efficacy of Diclofenac Transdermal Patch in Therapeutic Extractions: A Literature Review. *Cureus* **2022**, doi:10.7759/cureus.30411.
337. Suhail, M.; Wu, P.-C.; Minhas, M.U. Using Carbomer-Based Hydrogels for Control the Release Rate of Diclofenac Sodium: Preparation and In Vitro Evaluation. *Pharmaceuticals* **2020**, *13*, 399, doi:10.3390/ph13110399.
338. Muchová, M.; Münster, L.; Capáková, Z.; Mikulcová, V.; Kuřitka, I.; Vícha, J. Design of Dialdehyde Cellulose Crosslinked Poly(Vinyl Alcohol) Hydrogels for Transdermal Drug Delivery and Wound Dressings. *Materials Science and Engineering: C* **2020**, *116*, 111242, doi:10.1016/j.msec.2020.111242.
339. Luo, L.; Lane, M.E. Topical and Transdermal Delivery of Caffeine. *International Journal of Pharmaceutics* **2015**, *490*, 155–164, doi:10.1016/j.ijpharm.2015.05.050.
340. Völker, J.M.; Koch, N.; Becker, M.; Klenk, A. Caffeine and Its Pharmacological Benefits in the Management of Androgenetic Alopecia: A Review. *Skin Pharmacol Physiol* **2020**, *33*, 153–169, doi:10.1159/000508228.
341. Shatalebi, M.; Ahmadraji, F. Evaluation of the Clinical Efficacy and Safety of an Eye Counter Pad Containing Caffeine and Vitamin K in Emulsified Emu Oil Base. *Adv Biomed Res* **2015**, *4*, 10, doi:10.4103/2277-9175.148292.
342. Lourenço, I. Utilization of FucoPol for commercial inocula immobilization for bioremediation applications, 2021.
343. Gherman, S.P.; Biliuță, G.; Bele, A.; Ipate, A.M.; Baron, R.I.; Ochiuz, L.; Șpac, A.F.; Zavastin, D.E. Biomaterials Based on Chitosan and Polyvinyl Alcohol as a Drug Delivery System with Wound-Healing Effects. *Gels* **2023**, *9*, 122, doi:10.3390/gels9020122.
344. Kincl, M.; Meleh, M.; Veber, M.; Vrečer, F. STUDY OF PHYSICOCHEMICAL PARAMETERS AFFECTING THE RELEASE OF DICLOFENAC SODIUM FROM LIPOPHILIC MATRIX TABLETS. *Acta Chim. Slov.* **2004**.
345. Araújo, D.; Martins, M.; Concórdio-Reis, P.; Roma-Rodrigues, C.; Morais, M.; Alves, V.D.; Fernandes, A.R.; Freitas, F. Novel Hydrogel Membranes Based on the Bacterial Polysaccharide FucoPol: Design, Characterization and Biological Properties. *Pharmaceuticals* **2023**, *16*, 991, doi:10.3390/ph16070991.

346. Rodrigues, N.V.S.; Cardoso, E.M.; Andrade, M.V.O.; Donnici, C.L.; Sena, M.M. Analysis of Seized Cocaine Samples by Using Chemometric Methods and FTIR Spectroscopy. *Journal of the Brazilian Chemical Society* **2013**, doi:10.5935/0103-5053.20130066.
347. Chee, B.S.; Goetten de Lima, G.; Devine, D.M.; Nugent, M.J.D. Investigation of the Effects of Orientation on Freeze/Thawed Polyvinyl Alcohol Hydrogel Properties. *Materials Today Communications* **2018**, *17*, 82–93, doi:10.1016/j.mtcomm.2018.08.005.
348. Basu, A.; Lindh, J.; Ålander, E.; Strømme, M.; Ferraz, N. On the Use of Ion-Crosslinked Nanocellulose Hydrogels for Wound Healing Solutions: Physicochemical Properties and Application-Oriented Biocompatibility Studies. *Carbohydr. Polym.* **2017**, *174*, 299–308, doi:10.1016/j.carbpol.2017.06.073.
349. Huang, J.; Xu, Y.; Qi, S.; Zhou, J.; Shi, W.; Zhao, T.; Liu, M. Ultrahigh Energy-Dissipation Elastomers by Precisely Tailoring the Relaxation of Confined Polymer Fluids. *Nat Commun* **2021**, *12*, 3610, doi:10.1038/s41467-021-23984-2.
350. Soares, G.A.; Castro, A.D. de; Cury, B.S.F.; Evangelista, R.C. Blends of Cross-Linked High Amylose Starch/Pectin Loaded with Diclofenac. *Carbohydr. Polym.* **2013**, *91*, 135–142, doi:10.1016/j.carbpol.2012.08.014.
351. Russo, J.; Fiegel, J.; Brogden, N.K. Effect of Salt Form on Gelation and Drug Delivery Properties of Diclofenac-Loaded Poloxamer Gels for Delivery to Impaired Skin. *Pharm Res* **2022**, *39*, 2515–2527, doi:10.1007/s11095-022-03356-1.
352. Kamaly, N.; Yameen, B.; Wu, J.; Farokhzad, O.C. Degradable Controlled-Release Polymers and Polymeric Nanoparticles: Mechanisms of Controlling Drug Release. *Chem. Rev.* **2016**, *116*, 2602–2663, doi:10.1021/acs.chemrev.5b00346.
353. Schnell, C.N.; Galván, M.V.; Zanuttini, M.A.; Mocchiutti, P. Hydrogels from Xylan/Chitosan Complexes for the Controlled Release of Diclofenac Sodium. *Cellulose* **2020**, *27*, 1465–1481, doi:10.1007/s10570-019-02850-x.
354. Lin, X.; Yang, H.; Su, L.; Yang, Z.; Tang, X. Effect of Size on the in Vitro / in Vivo Drug Release and Degradation of Exenatide-Loaded PLGA Microspheres. *J. Drug Deliv. Sci. Technol.* **2018**, *45*, 346–356, doi:10.1016/j.jddst.2018.03.024.
355. Zand-Rajabi, H.; Madadlou, A. Caffeine-Loaded Whey Protein Hydrogels Reinforced with Gellan and Enriched with Calcium Chloride. *International Dairy Journal* **2016**, *56*, 38–44, doi:10.1016/j.idairyj.2015.12.011.
356. Mahdavinia, G.R.; Etemadi, H. In Situ Synthesis of Magnetic CaraPVA IPN Nanocomposite Hydrogels and Controlled Drug Release. *Materials Science and Engineering: C* **2014**, *45*, 250–260, doi:10.1016/j.msec.2014.09.023.
357. Hashmi, S.; Nadeem, S.; García-Peñas, A.; Ahmed, R.; Zahoor, A.; Vatankhah-Varnoosfaderani, M.; Stadler, F.J. Study the Effects of Supramolecular Interaction on Diffusion Kinetics in Hybrid Hydrogels of Zwitterionic Polymers and CNTs. *Macro Chemistry & Physics* **2022**, *223*, 2100348, doi:10.1002/macp.202100348.
358. Qiao, Z.; Tran, L.; Parks, J.; Zhao, Y.; Hai, N.; Zhong, Y.; Ji, H. Highly Stretchable Gelatin-polyacrylamide Hydrogel for Potential Transdermal Drug Release. *Nano Select* **2021**, *2*, 107–115, doi:10.1002/nano.202000087.
359. Donnelly, R.F.; Singh, T.R.R.; Garland, M.J.; Migalska, K.; Majithiya, R.; McCrudden, C.M.; Kole, P.L.; Mahmood, T.M.T.; McCarthy, H.O.; Woolfson, A.D. Hydrogel-Forming Microneedle Arrays for Enhanced Transdermal Drug Delivery. *Adv. Funct. Mater.* **2012**, *22*, 4879–4890, doi:10.1002/adfm.201200864.

360. Gerstel, M.S.; Place, V.A.A. Drug Delivery Device 1976.

361. Henry, S.; McAllister, D.V.; Allen, M.G.; Prausnitz, M.R. Microfabricated Microneedles: A Novel Approach to Transdermal Drug Delivery. *Journal of Pharmaceutical Sciences* **1998**, *87*, 922–925, doi:10.1021/js980042+.

362. Cleary, G.W. Microneedles for Drug Delivery. *Pharm Res* **2011**, *28*, 1–6, doi:10.1007/s11095-010-0307-3.

363. Han, T.; Das, D.B. Potential of Combined Ultrasound and Microneedles for Enhanced Transdermal Drug Permeation: A Review. *Eur. J. Pharm. Biopharm.* **2015**, *89*, 312–328, doi:10.1016/j.ejpb.2014.12.020.

364. Tuan-Mahmood, T.-M.; McCrudden, M.T.C.; Torrisi, B.M.; McAlister, E.; Garland, M.J.; Singh, T.R.R.; Donnelly, R.F. Microneedles for Intradermal and Transdermal Drug Delivery. *European Journal of Pharmaceutical Sciences* **2013**, *50*, 623–637, doi:10.1016/j.ejps.2013.05.005.

365. Kulkarni, D.; Gadade, D.; Chapaitkar, N.; Shelke, S.; Pekamwar, S.; Aher, R.; Ahire, A.; Avhale, M.; Badgule, R.; Bansode, R.; et al. Polymeric Microneedles: An Emerging Paradigm for Advanced Biomedical Applications. *Sci. Pharm.* **2023**, *91*, 27, doi:10.3390/scipharm91020027.

366. Indermun, S.; Luttge, R.; Choonara, Y.E.; Kumar, P.; Du Toit, L.C.; Modi, G.; Pillay, V. Current Advances in the Fabrication of Microneedles for Transdermal Delivery. *J. Control. Release* **2014**, *185*, 130–138, doi:10.1016/j.jconrel.2014.04.052.

367. Ita, K. Transdermal Delivery of Drugs with Microneedles—Potential and Challenges. *Pharmaceutics* **2015**, *7*, 90–105, doi:10.3390/pharmaceutics7030090.

368. Demir, Y.K.; Akan, Z.; Kerimoglu, O. Characterization of Polymeric Microneedle Arrays for Transdermal Drug Delivery. *PLoS ONE* **2013**, *8*, e77289, doi:10.1371/journal.pone.0077289.

369. Wang, M.; Hu, L.; Xu, C. Recent Advances in the Design of Polymeric Microneedles for Transdermal Drug Delivery and Biosensing. *Lab Chip* **2017**, *17*, 1373–1387, doi:10.1039/C7LC00016B.

370. Yang, S.; Wu, F.; Liu, J.; Fan, G.; Welsh, W.; Zhu, H.; Jin, T. Phase-Transition Microneedle Patches for Efficient and Accurate Transdermal Delivery of Insulin. *Adv. Funct. Mater.* **2015**, *25*, 4633–4641, doi:10.1002/adfm.201500554.

371. Matteucci, M.; Fanetti, M.; Casella, M.; Gramatica, F.; Gavioli, L.; Tormen, M.; Grenci, G.; De Angelis, F.; Di Fabrizio, E. Poly Vinyl Alcohol Re-Usable Masters for Microneedle Replication. *Microelectronic Engineering* **2009**, *86*, 752–756, doi:10.1016/j.mee.2009.01.068.

372. Cha, K.J.; Kim, T.; Park, S.J.; Kim, D.S. Simple and Cost-Effective Fabrication of Solid Biodegradable Polymer Microneedle Arrays with Adjustable Aspect Ratio for Transdermal Drug Delivery Using Acupuncture Microneedles. *J. Micromech. Microeng.* **2014**, *24*, 115015, doi:10.1088/0960-1317/24/11/115015.

373. Chen, M.-C.; Ling, M.-H.; Lai, K.-Y.; Pramudityo, E. Chitosan Microneedle Patches for Sustained Transdermal Delivery of Macromolecules. *Biomacromolecules* **2012**, *13*, 4022–4031, doi:10.1021/bm301293d.

374. Jin, J.; Reese, V.; Coler, R.; Carter, D.; Rolandi, M. Chitin Microneedles for an Easy-to-Use Tuberculosis Skin Test. *Adv. Healthcare Mater.* **2014**, *3*, 349–353, doi:10.1002/adhm.201300185.

375. Raja, W.K.; MacCorkle, S.; Diwan, I.M.; Abdurrob, A.; Lu, J.; Omenetto, F.G.; Kaplan, D.L. Transdermal Delivery Devices: Fabrication, Mechanics and Drug Release from Silk. *Small* **2013**, *9*, 3704–3713, doi:10.1002/smll.201202075.
376. Liu, S.; Jin, M.; Quan, Y.; Kamiyama, F.; Kusamori, K.; Katsumi, H.; Sakane, T.; Yamamoto, A. Transdermal Delivery of Relatively High Molecular Weight Drugs Using Novel Self-Dissolving Microneedle Arrays Fabricated from Hyaluronic Acid and Their Characteristics and Safety after Application to the Skin. *Eur. J. Pharm. Biopharm.* **2014**, *86*, 267–276, doi:10.1016/j.ejpb.2013.10.001.
377. Bhatia, S. *Natural Polymer Drug Delivery Systems*; Springer International Publishing: Cham, 2016; ISBN 978-3-319-41128-6.
378. Caballero-George, C.; Marin; Briceño Critical Evaluation of Biodegradable Polymers Used in Nanodrugs. *IJN* **2013**, 3071, doi:10.2147/IJN.S47186.
379. Castilla-Casadiego, D.A.; Miranda-Muñoz, K.A.; Roberts, J.L.; Crowell, A.D.; Gonzalez-Nino, D.; Choudhury, D.; Aparicio-Solis, F.O.; Servoss, S.L.; Rosales, A.M.; Prinz, G.; et al. Biodegradable Microneedle Patch for Delivery of Meloxicam for Managing Pain in Cattle. *PLoS ONE* **2022**, *17*, e0272169, doi:10.1371/journal.pone.0272169.
380. Olatunji, O.; Igwe, C.C.; Ahmed, A.S.; Alhassan, D.O.A.; Asieba, Gg.O.; Diganta, B.D. Microneedles from Fish Scale Biopolymer. *J. Appl. Polym. Sci.* **2014**, *131*, n/a-n/a, doi:10.1002/app.40377.
381. Olatunji, O.; Olsson, R. Microneedles from Fishscale-Nanocellulose Blends Using Low Temperature Mechanical Press Method. *Pharmaceutics* **2015**, *7*, 363–378, doi:10.3390/pharmaceutics7040363.
382. Medhi, P.; Olatunji, O.; Nayak, A.; Uppuluri, C.T.; Olsson, R.T.; Nalluri, B.N.; Das, D.B. Lidocaine-Loaded Fish Scale-Nanocellulose Biopolymer Composite Microneedles. *AAPS PharmSciTech* **2017**, *18*, 1488–1494, doi:10.1208/s12249-017-0758-5.
383. Lee, J.; Jang, E.H.; Kim, J.H.; Park, S.; Kang, Y.; Park, S.; Lee, K.; Kim, J.-H.; Youn, Y.-N.; Ryu, W. Highly Flexible and Porous Silk Fibroin Microneedle Wraps for Perivascular Drug Delivery. *J. Control. Release* **2021**, *340*, 125–135, doi:10.1016/j.jconrel.2021.10.024.
384. Ono, A.; Ito, S.; Sakagami, S.; Asada, H.; Saito, M.; Quan, Y.-S.; Kamiyama, F.; Hirobe, S.; Okada, N. Development of Novel Faster-Dissolving Microneedle Patches for Transcutaneous Vaccine Delivery. *Pharmaceutics* **2017**, *9*, 27, doi:10.3390/pharmaceutics9030027.
385. Park, Y.-H.; Ha, S.K.; Choi, I.; Kim, K.S.; Park, J.; Choi, N.; Kim, B.; Sung, J.H. Fabrication of Degradable Carboxymethyl Cellulose (CMC) Microneedle with Laser Writing and Replica Molding Process for Enhancement of Transdermal Drug Delivery. *Biotechnol Bioproc E* **2016**, *21*, 110–118, doi:10.1007/s12257-015-0634-7.
386. Yu, W.; Jiang, G.; Zhang, Y.; Liu, D.; Xu, B.; Zhou, J. Polymer Microneedles Fabricated from Alginate and Hyaluronate for Transdermal Delivery of Insulin. *Materials Science and Engineering: C* **2017**, *80*, 187–196, doi:10.1016/j.msec.2017.05.143.
387. Miyano, T.; Tobinaga, Y.; Kanno, T.; Matsuzaki, Y.; Takeda, H.; Wakui, M.; Hanada, K. Sugar Micro Needles as Transdermic Drug Delivery System. *Biomed Microdevices* **2005**, *7*, 185–188, doi:10.1007/s10544-005-3024-7.
388. Lee, K.; Lee, C.Y.; Jung, H. Dissolving Microneedles for Transdermal Drug Administration Prepared by Stepwise Controlled Drawing of Maltose. *Biomaterials* **2011**, *32*, 3134–3140, doi:10.1016/j.biomaterials.2011.01.014.

389. Zhang, Y.; Jiang, G.; Yu, W.; Liu, D.; Xu, B. Microneedles Fabricated from Alginate and Maltose for Transdermal Delivery of Insulin on Diabetic Rats. *Materials Science and Engineering: C* **2018**, *85*, 18–26, doi:10.1016/j.msec.2017.12.006.
390. Donnelly, R.F.; Morrow, D.I.J.; Singh, T.R.R.; Migalska, K.; McCarron, P.A.; O'Mahony, C.; Woolfson, A.D. Processing Difficulties and Instability of Carbohydrate Microneedle Arrays. *Drug Dev. Ind. Pharm.* **2009**, *35*, 1242–1254, doi:10.1080/03639040902882280.
391. Turner, J.G.; White, L.R.; Estrela, P.; Leese, H.S. Hydrogel-Forming Microneedles: Current Advancements and Future Trends. *Macromolecular Bioscience* **2021**, *21*, 2000307, doi:10.1002/mabi.202000307.
392. Zhou, Z.; Xing, M.; Zhang, S.; Yang, G.; Gao, Y. Process Optimization of Ca2+ Cross-Linked Alginate-Based Swellable Microneedles for Enhanced Transdermal Permeability: More Applicable to Acidic Drugs. *International Journal of Pharmaceutics* **2022**, *618*, 121669, doi:10.1016/j.ijpharm.2022.121669.
393. Wei, H.; Liu, S.; Tong, Z.; Chen, T.; Yang, M.; Guo, Y.; Sun, H.; Wu, Y.; Chu, Y.; Fan, L. Hydrogel-Based Microneedles of Chitosan Derivatives for Drug Delivery. *Reactive and Functional Polymers* **2022**, *172*, 105200, doi:10.1016/j.reactfunctpolym.2022.105200.
394. Yin, Z.; Kuang, D.; Wang, S.; Zheng, Z.; Yadavalli, V.K.; Lu, S. Swellable Silk Fibroin Microneedles for Transdermal Drug Delivery. *Int. J. Biol. Macromol.* **2018**, *106*, 48–56, doi:10.1016/j.ijbiomac.2017.07.178.
395. Chang, H.; Zheng, M.; Yu, X.; Than, A.; Seeni, R.Z.; Kang, R.; Tian, J.; Khanh, D.P.; Liu, L.; Chen, P.; et al. A Swellable Microneedle Patch to Rapidly Extract Skin Interstitial Fluid for Timely Metabolic Analysis. *Advanced Materials* **2017**, *29*, 1702243, doi:10.1002/adma.201702243.
396. Karim, Z.; Karwa, P.; Hiremath, S.R.R. Polymeric Microneedles for Transdermal Drug Delivery- a Review of Recent Studies. *J. Drug Deliv. Sci. Technol.* **2022**, *77*, 103760, doi:10.1016/j.jddst.2022.103760.
397. Yang, J.; Zhang, H.; Hu, T.; Xu, C.; Jiang, L.; Shrike Zhang, Y.; Xie, M. Recent Advances of Microneedles Used towards Stimuli-Responsive Drug Delivery, Disease Theranostics, and Bioinspired Applications. *Chemical Engineering Journal* **2021**, *426*, 130561, doi:10.1016/j.cej.2021.130561.
398. Eum, J.; Kim, Y.; Um, D.; Shin, J.; Yang, H.; Jung, H. Solvent-Free Polycaprolactone Dissolving Microneedles Generated via the Thermal Melting Method for the Sustained Release of Capsaicin. *Micromachines* **2021**, *12*, 167, doi:10.3390/mi12020167.
399. Kim, M.; Kim, T.; Kim, D.; Chung, W. Curved Microneedle Array-Based sEMG Electrode for Robust Long-Term Measurements and High Selectivity. *Sensors* **2015**, *15*, 16265–16280, doi:10.3390/s150716265.
400. DeMuth, P.C.; Garcia-Beltran, W.F.; Ai-Ling, M.L.; Hammond, P.T.; Irvine, D.J. Composite Dissolving Microneedles for Coordinated Control of Antigen and Adjuvant Delivery Kinetics in Transcutaneous Vaccination. *Adv. Funct. Mater.* **2013**, *23*, 161–172, doi:10.1002/adfm.201201512.
401. Haj-Ahmad, R.; Khan, H.; Arshad, M.; Rasekh, M.; Hussain, A.; Walsh, S.; Li, X.; Chang, M.-W.; Ahmad, Z. Microneedle Coating Techniques for Transdermal Drug Delivery. *Pharmaceutics* **2015**, *7*, 486–502, doi:10.3390/pharmaceutics7040486.
402. Ingrole, R.S.J.; Gill, H.S. Microneedle Coating Methods: A Review with a Perspective. *J Pharmacol Exp Ther* **2019**, *370*, 555–569, doi:10.1124/jpet.119.258707.

403. Lee, K.J.; Jeong, S.S.; Roh, D.H.; Kim, D.Y.; Choi, H.-K.; Lee, E.H. A Practical Guide to the Development of Microneedle Systems – In Clinical Trials or on the Market. *International Journal of Pharmaceutics* **2020**, *573*, 118778, doi:10.1016/j.ijpharm.2019.118778.

404. Dalton, B.; Bhagabati, P.; De Micco, J.; Padamati, R.B.; O'Connor, K. A Review on Biological Synthesis of the Biodegradable Polymers Polyhydroxyalkanoates and the Development of Multiple Applications. *Catalysts* **2022**, *12*, 319, doi:10.3390/catal12030319.

405. Anjum, A.; Zuber, M.; Zia, K.M.; Noreen, A.; Anjum, M.N.; Tabasum, S. Microbial Production of Polyhydroxyalkanoates (PHAs) and Its Copolymers: A Review of Recent Advancements. *Int. J. Biol. Macromol.***2016**, *89*, 161–174, doi:10.1016/j.ijbiomac.2016.04.069.

406. Chan, C.M.; Vandi, L.-J.; Pratt, S.; Halley, P.; Ma, Y.; Chen, G.-Q.; Richardson, D.; Werker, A.; Laycock, B. Understanding the Effect of Copolymer Content on the Processability and Mechanical Properties of Polyhydroxyalkanoate (PHA)/Wood Composites. *Composites Part A: Applied Science and Manufacturing* **2019**, *124*, 105437, doi:10.1016/j.compositesa.2019.05.005.

407. Pereira, J.R.; Rafael, A.M.; Esmail, A.; Morais, M.; Matos, M.; Marques, A.C.; Reis, M.A.M.; Freitas, F. Preparation of Porous Scaffold Based on Poly(3-Hydroxybutyrate-Co-3-Hydroxyvalerate-Co-3-Hydroxyhexanoate) and FucoPol. *Polymers* **2023**, *15*, 2945, doi:10.3390/polym15132945.

408. Bonartsev, A.P.; Bonartseva, G.A.; Reshetov, I.V.; Shaitan, K.V.; Kirpichnikov, M.P. Application of Polyhydroxyalkanoates in Medicine and the Biological Activity of Natural Poly(3-Hydroxybutyrate). *Acta Naturae* **2019**, *11*, 4–16, doi:10.32607/20758251-2019-11-2-4-16.

409. Kaniuk, Ł.; Stachewicz, U. Development and Advantages of Biodegradable PHA Polymers Based on Electrospun PHBV Fibers for Tissue Engineering and Other Biomedical Applications. *ACS Biomater. Sci. Eng.* **2021**, *7*, 5339–5362, doi:10.1021/acsbiomaterials.1c00757.

410. Koller, M. Biodegradable and Biocompatible Polyhydroxy-Alkanoates (PHA): Auspicious Microbial Macromolecules for Pharmaceutical and Therapeutic Applications. *Molecules* **2018**, *23*, 362, doi:10.3390/molecules23020362.

411. Zhang, X.; Liu, X.-Y.; Yang, H.; Chen, J.-N.; Lin, Y.; Han, S.-Y.; Cao, Q.; Zeng, H.-S.; Ye, J.-W. A Polyhydroxyalkanoates-Based Carrier Platform of Bioactive Substances for Therapeutic Applications. *Front. Bioeng. Biotechnol.* **2022**, *9*, 798724, doi:10.3389/fbioe.2021.798724.

412. Silvestre, S.L.; Araújo, D.; Marques, A.C.; Pires, C.; Matos, M.; Alves, V.; Martins, R.; Freitas, F.; Reis, M.A.M.; Fortunato, E. Microneedle Arrays of Polyhydroxyalkanoate by Laser-Based Micromolding Technique. *ACS Appl. Bio Mater.* **2020**, *3*, 5856–5864, doi:10.1021/acsabm.0c00570.

413. Cruz, M.V.; Sarraguça, M.C.; Freitas, F.; Lopes, J.A.; Reis, M.A.M. Online Monitoring of P(3HB) Produced from Used Cooking Oil with near-Infrared Spectroscopy. *Journal of Biotechnology* **2015**, *194*, 1–9, doi:10.1016/j.jbiotec.2014.11.022.

414. Esmail, A.; Pereira, J.R.; Sevrin, C.; Grandfils, C.; Menda, U.D.; Fortunato, E.; Oliva, A.; Freitas, F. Preparation and Characterization of Porous Scaffolds Based on Poly(3-Hydroxybutyrate) and Poly(3-Hydroxybutyrate-Co-3-Hydroxyvalerate). *Life* **2021**, *11*, 935, doi:10.3390/life11090935.

415. Silva, F.; Matos, M.; Pereira, B.; Ralo, C.; Pequito, D.; Marques, N.; Carvalho, G.; Reis, M.A.M. An Integrated Process for Mixed Culture Production of 3-Hydroxyhexanoate-Rich

Polyhydroxyalkanoates from Fruit Waste. *Chemical Engineering Journal* **2022**, *427*, 131908, doi:10.1016/j.cej.2021.131908.

416. De Meneses, L.; Pereira, J.R.; Sevrin, C.; Grandfils, C.; Paiva, A.; Reis, M.A.M.; Freitas, F. Pseudomonas Chlororaphis as a Multiproduct Platform: Conversion of Glycerol into High-Value Biopolymers and Phenazines. *New Biotechnology* **2020**, *55*, 84–90, doi:10.1016/j.nbt.2019.10.002.
417. Morais, C.; Freitas, F.; Cruz, M.V.; Paiva, A.; Dionísio, M.; Reis, M.A.M. Conversion of Fat-Containing Waste from the Margarine Manufacturing Process into Bacterial Polyhydroxyalkanoates. *Int. J. Biol. Macromol.* **2014**, *71*, 68–73, doi:10.1016/j.ijbiomac.2014.04.044.
418. Larrañeta, E.; Moore, J.; Vicente-Pérez, E.M.; González-Vázquez, P.; Lutton, R.; Woolfson, A.D.; Donnelly, R.F. A Proposed Model Membrane and Test Method for Microneedle Insertion Studies. *International Journal of Pharmaceutics* **2014**, *472*, 65–73, doi:10.1016/j.ijpharm.2014.05.042.
419. Silva, A.C.Q.; Pereira, B.; Lameirinhas, N.S.; Costa, P.C.; Almeida, I.F.; Dias-Pereira, P.; Correia-Sá, I.; Oliveira, H.; Silvestre, A.J.D.; Vilela, C.; et al. Dissolvable Carboxymethylcellulose Microneedles for Noninvasive and Rapid Administration of Diclofenac Sodium. *Macromolecular Bioscience* **2023**, *23*, 2200323, doi:10.1002/mabi.202200323.
420. Chotchindakun, K.; Pathom-Aree, W.; Dumri, K.; Ruangsuriya, J.; Pumas, C.; Pekkoh, J. Low Crystallinity of Poly(3-Hydroxybutyrate-Co-3-Hydroxyvalerate) Bioproduction by Hot Spring Cyanobacterium Cyanosarcina Sp. AARL T020. *Plants* **2021**, *10*, 503, doi:10.3390/plants10030503.
421. Lemechko, P.; Le Fellic, M.; Bruzaud, S. Production of Poly(3-Hydroxybutyrate-Co-3-Hydroxyvalerate) Using Agro-Industrial Effluents with Tunable Proportion of 3-Hydroxyvalerate Monomer Units. *Int. J. Biol. Macromol.* **2019**, *128*, 429–434, doi:10.1016/j.ijbiomac.2019.01.170.
422. Abbasi, M.; Pokhrel, D.; Coats, E.R.; Guho, N.M.; McDonald, A.G. Effect of 3-Hydroxyvalerate Content on Thermal, Mechanical, and Rheological Properties of Poly(3-Hydroxybutyrate-Co-3-Hydroxyvalerate) Biopolymers Produced from Fermented Dairy Manure. *Polymers* **2022**, *14*, 4140, doi:10.3390/polym14194140.
423. Bagatella, S.; Ciapponi, R.; Ficara, E.; Frison, N.; Turri, S. Production and Characterization of Polyhydroxyalkanoates from Wastewater via Mixed Microbial Cultures and Microalgae. *Sustainability* **2022**, *14*, 3704, doi:10.3390/su14063704.
424. Meléndez-Rodríguez, B.; Torres-Giner, S.; Reis, M.A.M.; Silva, F.; Matos, M.; Cabedo, L.; Lagarón, J.M. Blends of Poly(3-Hydroxybutyrate-Co-3-Hydroxyvalerate) with Fruit Pulp Biowaste Derived Poly(3-Hydroxybutyrate-Co-3-Hydroxyvalerate-Co-3-Hydroxyhexanoate) for Organic Recycling Food Packaging. *Polymers* **2021**, *13*, 1155, doi:10.3390/polym13071155.
425. Guho, N.M.; Pokhrel, D.; Abbasi, M.; McDonald, A.G.; Alfaro, M.; Brinkman, C.K.; Coats, E.R. Pilot-Scale Production of Poly-3-Hydroxybutyrate-Co-3-Hydroxyvalerate from Fermented Dairy Manure: Process Performance, Polymer Characterization, and Scale-up Implications. *Bioresour. Technol. Reports* **2020**, *12*, 100588, doi:10.1016/j.biteb.2020.100588.
426. Eesaee, M.; Ghassemi, P.; Nguyen, D.D.; Thomas, S.; Elkoun, S.; Nguyen-Tri, P. Morphology and Crystallization Behaviour of Polyhydroxyalkanoates-Based Blends and

Composites: A Review. *Biochemical Engineering Journal* **2022**, *187*, 108588, doi:10.1016/j.bej.2022.108588.

427. Wang, Y.; Chen, R.; Cai, J.; Liu, Z.; Zheng, Y.; Wang, H.; Li, Q.; He, N. Biosynthesis and Thermal Properties of PHBV Produced from Levulinic Acid by Ralstonia Eutropha. *PLoS ONE* **2013**, *8*, e60318, doi:10.1371/journal.pone.0060318.
428. Bhubalan, K.; Rathi, D.-N.; Abe, H.; Iwata, T.; Sudesh, K. Improved Synthesis of P(3HB-Co-3HV-Co-3HHx) Terpolymers by Mutant Cupriavidus Necator Using the PHA Synthase Gene of Chromobacterium Sp. USM2 with High Affinity towards 3HV. *Polymer Degradation and Stability* **2010**, *95*, 1436–1442, doi:10.1016/j.polymdegradstab.2009.12.018.
429. Zhao, W.; Chen, G.-Q. Production and Characterization of Terpolyester Poly(3-Hydroxybutyrate-Co-3-Hydroxyvalerate-Co-3-Hydroxyhexanoate) by Recombinant Aeromonas Hydrophila 4AK4 Harboring Genes phaAB. *Process Biochemistry* **2007**, *42*, 1342–1347, doi:10.1016/j.procbio.2007.07.006.
430. Yuan, W.; Xiaoyun Hong; Zaozhan Wu; Lizhu Chen; Liu, Z.; Fei Wu; Liangming Wei, L. Dissolving and Biodegradable Microneedle Technologies for Transdermal Sustained Delivery of Drug and Vaccine. *DDDT* **2013**, 945, doi:10.2147/DDDT.S44401.
431. Wu, L.; Shrestha, P.; Iapichino, M.; Cai, Y.; Kim, B.; Stoeber, B. Characterization Method for Calculating Diffusion Coefficient of Drug from Polylactic Acid (PLA) Microneedles into the Skin. *J. Drug Deliv. Sci. Technol.* **2021**, *61*, 102192, doi:10.1016/j.jddst.2020.102192.
432. Kang, S.; Song, J.E.; Jun, S.-H.; Park, S.-G.; Kang, N.-G. Sugar-Triggered Burst Drug Releasing Poly-Lactic Acid (PLA) Microneedles and Its Fabrication Based on Solvent-Casting Approach. *Pharmaceutics* **2022**, *14*, 1758, doi:10.3390/pharmaceutics14091758.
433. Aldawood, F.K.; Andar, A.; Desai, S. A Comprehensive Review of Microneedles: Types, Materials, Processes, Characterizations and Applications. *Polymers* **2021**, *13*, 2815, doi:10.3390/polym13162815.
434. Khosraviboroujeni, A.; Mirdamadian, S.Z.; Minaiyan, M.; Taheri, A. Preparation and Characterization of 3D Printed PLA Microneedle Arrays for Prolonged Transdermal Drug Delivery of Estradiol Valerate. *Drug Deliv. and Transl. Res.* **2022**, *12*, 1195–1208, doi:10.1007/s13346-021-01006-4.
435. Shah, S.A.; Oakes, R.S.; Kapnick, S.M.; Jewell, C.M. Mapping the Mechanical and Immunological Profiles of Polymeric Microneedles to Enable Vaccine and Immunotherapy Applications. *Front. Immunol.* **2022**, *13*, 843355, doi:10.3389/fimmu.2022.843355.
436. Wu, L.; Park, J.; Kamaki, Y.; Kim, B. Optimization of the Fused Deposition Modeling-Based Fabrication Process for Polylactic Acid Microneedles. *Microsyst Nanoeng* **2021**, *7*, 58, doi:10.1038/s41378-021-00284-9.
437. Park, J.-H.; Prausnitz, M. Analysis of Mechanical Failure of Polymer Microneedles by Axial Force. *J. Korean Phy. Soc.* **2010**, *56*, 1223–1227, doi:10.3938/jkps.56.1223.
438. Zhang, H.-F.; Ma, L.; Wang, Z.-H.; Chen, G.-Q. Biosynthesis and Characterization of 3-Hydroxyalkanoate Terpolyesters with Adjustable Properties by *Aeromonas Hydrophila*. *Biotechnol. Bioeng.* **2009**, *104*, 582–589, doi:10.1002/bit.22409.
439. Du, G.; Zhang, Z.; He, P.; Zhang, Z.; Sun, X. Determination of the Mechanical Properties of Polymeric Microneedles by Micromanipulation. *Journal of the Mechanical Behavior of Biomedical Materials* **2021**, *117*, 104384, doi:10.1016/j.jmbbm.2021.104384.

440. Zhang, L.; Chen, Y.; Tan, J.; Feng, S.; Xie, Y.; Li, L. Performance Enhancement of PLA-Based Blend Microneedle Arrays through Shish-Kebab Structuring Strategy in Microinjection Molding. *Polymers* **2023**, *15*, 2234, doi:10.3390/polym15102234.
441. Fonseca, D.F.S.; Vilela, C.; Pinto, R.J.B.; Bastos, V.; Oliveira, H.; Catarino, J.; Faísca, P.; Rosado, C.; Silvestre, A.J.D.; Freire, C.S.R. Bacterial Nanocellulose-Hyaluronic Acid Microneedle Patches for Skin Applications: In Vitro and in Vivo Evaluation. *Materials Science and Engineering: C* **2021**, *118*, 111350, doi:10.1016/j.msec.2020.111350.
442. Sabri, A.H.; Cater, Z.; Ogilvie, J.; Scurr, D.J.; Marlow, M.; Segal, J. Characterisation of Mechanical Insertion of Commercial Microneedles. *J. Drug Deliv. Sci. Technol.* **2020**, *58*, 101766, doi:10.1016/j.jddst.2020.101766.
443. Czekalla, C.; Schönborn, K.H.; Lademann, J.; Meinke, M.C. Noninvasive Determination of Epidermal and Stratum Corneum Thickness in Vivo Using Two-Photon Microscopy and Optical Coherence Tomography: Impact of Body Area, Age, and Gender. *Skin Pharmacol Physiol* **2019**, *32*, 142–150, doi:10.1159/000497475.
444. Wang, Q.L.; Zhu, D.D.; Chen, Y.; Guo, X.D. A Fabrication Method of Microneedle Molds with Controlled Microstructures. *Materials Science and Engineering: C* **2016**, *65*, 135–142, doi:10.1016/j.msec.2016.03.097.
445. Dawud, H.; Abu Ammar, A.A. Rapidly Dissolving Microneedles for the Delivery of Steroid-Loaded Nanoparticles Intended for the Treatment of Inflammatory Skin Diseases. *Pharmaceutics* **2023**, *15*, 526, doi:10.3390/pharmaceutics15020526.
446. Detamornrat, U.; Parrilla, M.; Domínguez-Robles, J.; Anjani, Q.K.; Larrañeta, E.; De Wael, K.; Donnelly, R.F. Transdermal On-Demand Drug Delivery Based on an Iontophoretic Hollow Microneedle Array System. *Lab Chip* **2023**, *23*, 2304–2315, doi:10.1039/D3LC00160A.
447. Rodgers, A.M.; McCrudden, M.T.C.; Vincente-Perez, Eva.M.; Dubois, A.V.; Ingram, R.J.; Larrañeta, E.; Kissenpfennig, A.; Donnelly, R.F. Design and Characterisation of a Dissolving Microneedle Patch for Intradermal Vaccination with Heat-Inactivated Bacteria: A Proof of Concept Study. *International Journal of Pharmaceutics* **2018**, *549*, 87–95, doi:10.1016/j.ijpharm.2018.07.049.
448. Chen, Y.; Chen, B.Z.; Wang, Q.L.; Jin, X.; Guo, X.D. Fabrication of Coated Polymer Microneedles for Transdermal Drug Delivery. *J. Control. Release* **2017**, *265*, 14–21, doi:10.1016/j.jconrel.2017.03.383.
449. Vrdoljak, A.; McGrath, M.G.; Carey, J.B.; Draper, S.J.; Hill, A.V.S.; O'Mahony, C.; Crean, A.M.; Moore, A.C. Coated Microneedle Arrays for Transcutaneous Delivery of Live Virus Vaccines. *J. Control. Release* **2012**, *159*, 34–42, doi:10.1016/j.jconrel.2011.12.026.
450. Keirouz, A.; Mustafa, Y.L.; Turner, J.G.; Lay, E.; Jungwirth, U.; Marken, F.; Leese, H.S. Conductive Polymer-Coated 3D Printed Microneedles: Biocompatible Platforms for Minimally Invasive Biosensing Interfaces. *Small* **2023**, *19*, 2206301, doi:10.1002/smll.202206301.
451. Vallhov, H.; Xia, W.; Engqvist, H.; Scheynius, A. Bioceramic Microneedle Arrays Are Able to Deliver OVA to Dendritic Cells in Human Skin. *J. Mater. Chem. B* **2018**, *6*, 6808–6816, doi:10.1039/C8TB01476K.
452. Zhou, Z.; Zhang, S.; Yang, G.; Gao, Y. Enhanced Delivery Efficiency and Sustained Release of Biopharmaceuticals by Complexation-Based Gel Encapsulated Coated Microneedles:

rhIFNα-1b Example. *Asian Journal of Pharmaceutical Sciences* **2021**, *16*, 612–622, doi:10.1016/j.ajps.2021.05.002.

453. Carvalho, J.P.F.; Silva, A.C.Q.; Bastos, V.; Oliveira, H.; Pinto, R.J.B.; Silvestre, A.J.D.; Vilela, C.; Freire, C.S.R. Nanocellulose-Based Patches Loaded with Hyaluronic Acid and Diclofenac towards Aphthous Stomatitis Treatment. *Nanomaterials* **2020**, *10*, 628, doi:10.3390/nano10040628.

APPENDIX

A.1

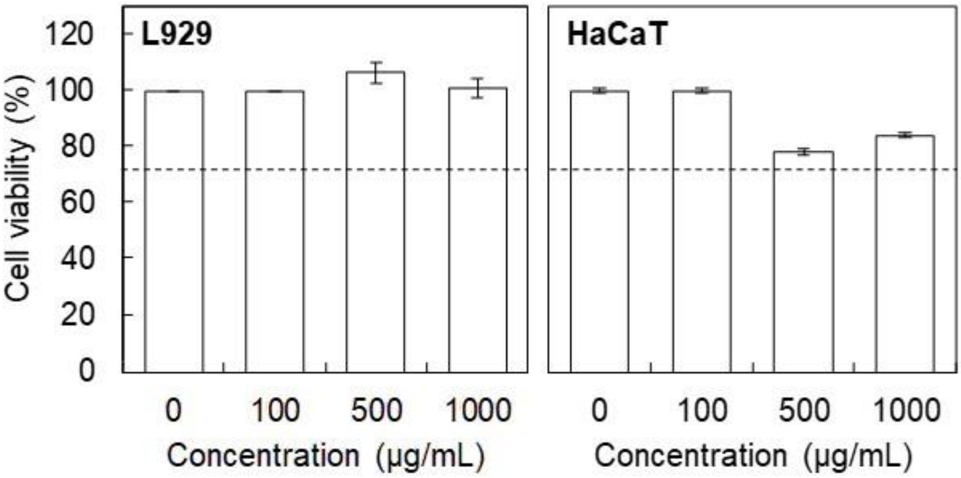

A1. L929 fibroblasts and HaCaT keratinocytes viability when exposed to different concentrations of NaOH, for 24 h. The dotted line at 70% represents the viability limits for non-toxic condition (ISO 10993-5, 2009).

A.2

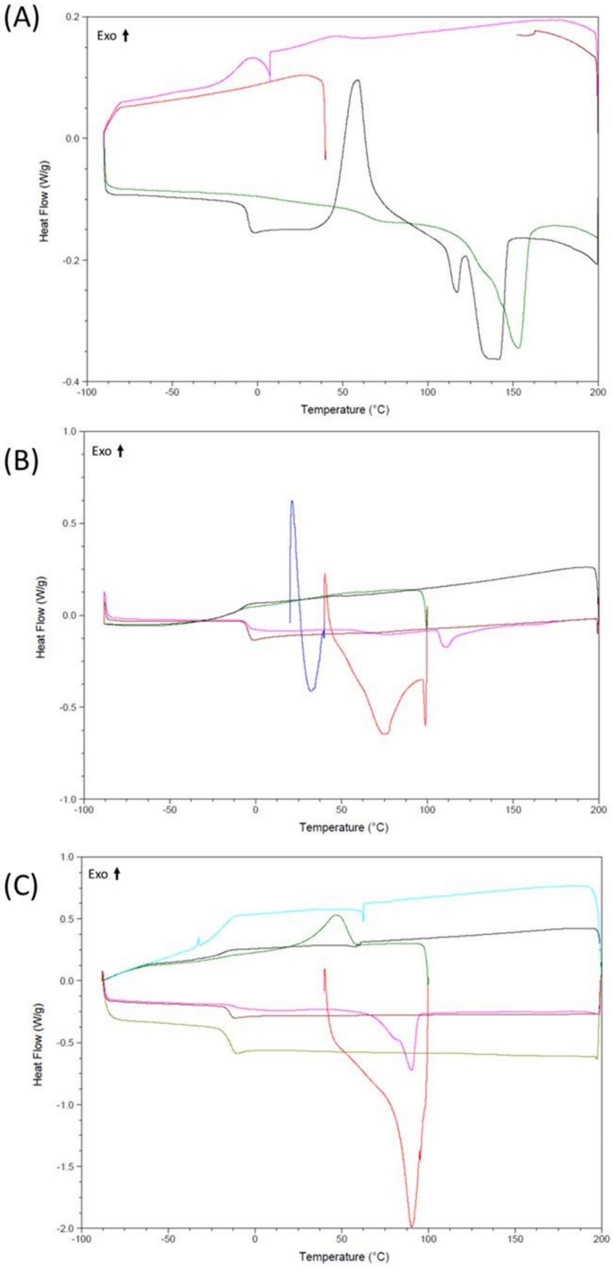

A2. Differential scanning calorimetry (DSC) thermogram of polymers (A) PHBV$_{14}$, (B) PHBV$_{43}$ and (C) PHBV$_{87}$.

TRANSDERMAL DELIVERY SYSTEMS BASED ON NATURAL POLYMERIC BIOMATERIALS

DIANA FILIPA VIEIRA ARAÚJO

2023